ULSAN NATIONAL INSTITUTE OF
SCIENCE AND TECHNOLOGY

Doctoral Thesis

Combined Molecular Design, Morphology Control, and Device Engineering Towards Superior Organic Semiconductors

Jungho Lee

Department of Energy Engineering
(Energy Engineering)

Graduate School of UNIST

2020

Combined Molecular Design, Morphology Control, and Device Engineering Towards Superior Organic Semiconductors

Jungho Lee

Department of Energy Engineering
(Energy Engineering)

Graduate School of UNIST

Combined Molecular Design, Morphology Control, and Device Engineering Towards Superior Organic Semiconductors

A dissertation
submitted to the Graduate School of UNIST
in partial fulfillment of the
requirements for the degree of
Doctor of Philosophy

Jungho Lee

12. 23. 2019 of submission
Approved by

Advisor
Changduk Yang

Combined Molecular Design, Morphology Control, and Device Engineering Towards Superior Organic Semiconductors

Jungho Lee

This certifies that the thesis/dissertation of Jungho Lee is approved.

12. 30. 2019 of submission

signature

Advisor: Prof. Changduk Yang

signature

Prof. Jin Young Kim: Thesis Committee Member #1

signature

SungYouHong.

Prof. Sung You Hong: Thesis Committee Member #2

signature

Prof. Hyesung Park: Thesis Committee Member #3

signature

Prof. BongSoo Kim: Thesis Committee Member #4;

Abstract

Owing to the valuable features of organic polymers, such as inexpensive materials, ease of mass production, light-flexible properties, in recent days, the organic semiconductors have attracted significant research interests of challenging scientists in conducting and semiconducting organic polymers. The main concept of the conjugation of conducting organic polymers has occurred from the continuously connected p_z-orbitals of sp^2(or sp)-hybridized carbon atoms from the alternating sequence of single and multi-bonds (double and triple bonds) in the polymeric backbone. Based on the concept of conjugation structure, until now, many π-conjugated organic polymers and small molecules have been designed with great expectation for various advents of the electronic application, like as organic light-emitting diodes (OLEDs), organic photovoltaics (OPVs), and organic field-effect transistors (OFETs).

Over the past decades, many pioneering research groups have paid attention to the design and development of novel organic semiconductors for next generated optoelectronic devices due to the aforementioned advantages of organic semiconductors. Moreover, many research interests have been concentrated on not only the invention of completely brand-new molecular structures but also fine-tuning of the existing molecular structures with marginal trade-off their outstanding own properties. In particular, the fine-tuning approaches are quite effective methods because the parent molecules had exhibited remarkable performances in optoelectronic devices. Therefore, the modified molecules usually have shown comparable or much better performances compared to parent molecules.

In terms of modification of backbone, I present the article describes the synthesis and characterization as well as OFET characteristics of a collection of TBIG-based polymers with varied compositions between TBIG and IIG accepting segments and bithiophene counterpart donor.

Secondly, based on the designed and synthesized with 2-ethylhexyl and 5-ethylnonyl side chains on the CPDT core, I demonstrated its effectiveness of side-chain engineering for the CPDT-based polymers and CPDT-based small molecules on the OFET performance and semi-transparent OPV performance, respectively.

Finally, to fine-tuning of molecular properties, the substituents have been used without the sacrificial of the mainstream of organic semiconductors. The most universal substituent, fluorine with single proton, I investigated the constitutional isomeric effects on the photovoltaic performances via atomic level insight from the computational simulation and nano-second transient absorption spectroscopy.

Table of Contents

List of Figures

List of Schemes

List of Tables

Glossary of Abbreviations

AAMD	All-atom molecular dynamics
AFM	Atomic force microscopy
AVT	Average visible transmittance
BDT	Bezodithiophene
BHJ	Bulk heterojunction
CCL	Crystalline correlation length
CDT	Cyclopentadithiophene
CdTe	Cadmium telluride
CF	Chloroform
CGMD	Coarse-grained molecular dynamics
CIGS	Copper indium germanium selenide
***c*-Si**	Crystalline silicon
CV	Cyclic voltammetry
D-A	Donor-acceptor
DCI	1,1-Dicyanomethylene-3-indanone
DCM	Dichloromethane
DFT	Density functional theory
DIO	1,8-Diiodooctane
DPP	Diketopyrrolopyrole
DSC	Differential scanning calorimetry
EA	Elemental analysis
EDX	Energy-dispersive X-ray spectroscopy
E_g	Bandgap
EQE	External quantum efficiency
ETL	Electron transporting layer
FF	Fill factor
GIXD	Grazing incident X-ray diffraction
HDMS	Hexamethyldisilazane

HOMO	Highest occupied molecular orbital
HTL	Hole transporting layer
HT-GPC	High-temperature gel-permeation chromatography
ICT	Internal charge transfer
IDT	Indacenodithiophene
IIG	Isoindigo
ITO	Indium tin oxide
J_{SC}	Short-circuit current
LUMO	Lowest unoccupied molecular orbital
M_n	Number average molecular weight
MS	Mass spectrometry
NDI	Naphtalenediimide
NMR	Nuclear magnetic resonance
***o*-DCB**	*o*-Dichlorobenzene
OFETs	Organic field-effect transistors
OLED	Organic light-emitting diodes
OPVs	Organic photovoltaics
$PC_{71}BM$	[6,6]-Phenyl C_{71}-butyric acid methyl ester
PCE	Power conversion efficiency
PDI	Polydispersity index
PEDOT:PSS	Poly(3,4-ethlenedioxythiophene):poly(styrene sulfonate)
RDF	Radial distribution function
TA	Transient absorption
TBIG	Thieno-benzo-isoindigo
TEM	Transmission electron microscopy
TGA	Thermal gravimetric analysis
THF	Tetrahydrofuran
TIG	Thienoisoindigo
TiO_x	Titanium oxide
V_{OC}	Open-circuit voltage
UPS	Ultraviolet photoelectron spectra
ZnO	Zinc oxide

Chapter 1. Introduction

1.1 Organic semiconductors

In the 1970s, Alan MacDiarmid and Alan Heeger gave a passion for the investigation of electrical properties of inorganic polymeric sulfur nitride $(SN)_X$ and they found that the drop the bromine atoms as a dopant similar to that used in silicon transistors increase 10-fold conductivity of $(SN)_X$. Then, they come up with the Hideki Shirakawa's polyacetylene, instead of $(SN)_X$, firstly inventing the conducting organic polymers and the capability to dope these organic polymers over the full range from insulator to metal.[1] Owing to the valuable features of organic polymers, such as inexpensive materials, ease of mass production, light-flexible properties, it is the day opening the floodgate of research interests of challenging scientists in conducting and semiconducting organic polymers.[2-10] Finally, they got the honor of the 2000 Nobel Prize in Chemistry "For the discovery and development of electrically conductive polymers". The main concept of the conjugation of conducting organic polymers has occurred from the continuously connected p_z-orbitals of sp^2(or sp)-hybridized carbon atoms from the alternating sequence of single and multi-bonds (double or triple bonds) in the polymeric backbone (**Figure 1.1.1**). Based on the concept of conjugation structure, until now, many π-conjugated organic semiconductors have been designed with great expectation for various advents of the electronic application, like as organic light-emitting diodes (OLEDs),[11-16] organic photovoltaics (OPVs),[4, 10, 17-20] and organic field-effect transistors (OFETs).[21-24]

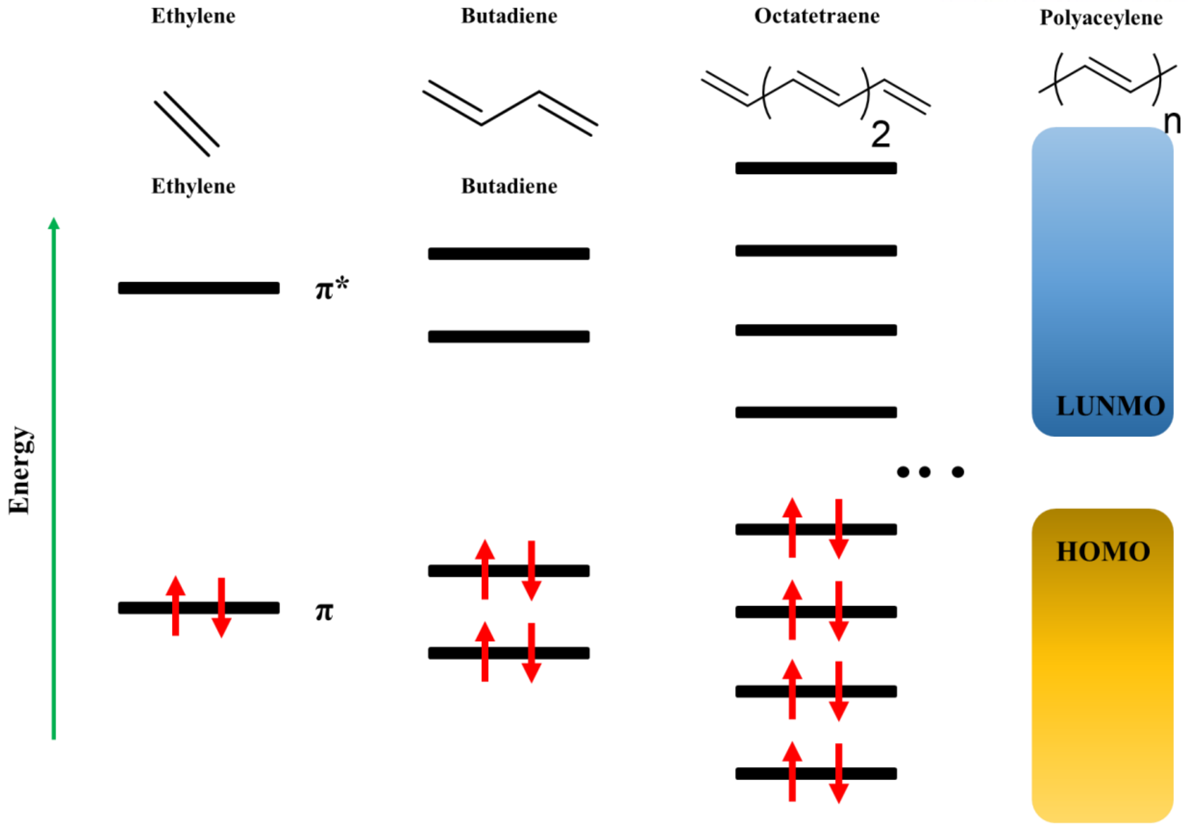

Figure 1.1.1. Schematic of energy-level splitting with increasing conjugation length.

Through the π-conjugated systems, the organic semiconductors have similar charge-transfer mechanisms with inorganic semiconductors. It is the same as the inorganic semiconductors; electrons can freely pass through the overlapped π-electrons clouds by a hopping and tunneling mechanisms.[25] On the other hand, at the initial stage of usual organic semiconductors, they have no dominant packing orientation between neighboring molecules. Therefore, the main transportation of charge carriers is a hopping mechanism which relies upon the disparity of energy gap between the highest occupied molecular orbital (HOMO) and the lowest unoccupied molecular orbital (LUMO). With the development of planar structures of molecular designs and elongated conjugated backbones, many key factors have been important related to the charge carrier mobility, such as intermolecular packing states, disorder by impurities, circumstantial temperatures, and so on. Especially, intermolecular packing state including molecular packing orientations and intermolecular spacing is of great significance to adjust the energy barriers at molecular boundaries owing to their electively weak intermolecular electronic couplings.

Over the past decades, many pioneering research groups have paid attention to the design and development of novel organic semiconductors for next generated optoelectronic devices due to the aforementioned advantages of organic semiconductors. From the organic dyes-based molecules (e.g.

isoindigo (IIG),[26-31] diketopyrrolopyrole (DPP),[32-36] and naphtalenediimide (NDI)[37-41]) to ladder-type backbone (e.g. indacenodithiophene (IDT),[42-46] cyclopentadithiophene (CDT),[47-52] and bezodithiophene (BDT)[53-58]), various kinds of novel materials have been investigated as high-performance organic candidates promising the decent electron-withdrawing (or donating) abilities, unique absorption ranges, and swift charge transportation. (**Figure 1.1.2**) Moreover, many research interests have been concentrated on not only the invention of completely brand-new molecular structures but also fine-tuning of the existing molecular structures with marginal trade-off their outstanding own properties. In particular, the fine-tuning approaches are quite effective methods because the parent molecules had exhibited remarkable performances in optoelectronic devices. Therefore, the modified molecules usually have shown comparable or much better performances compared to parent molecules.

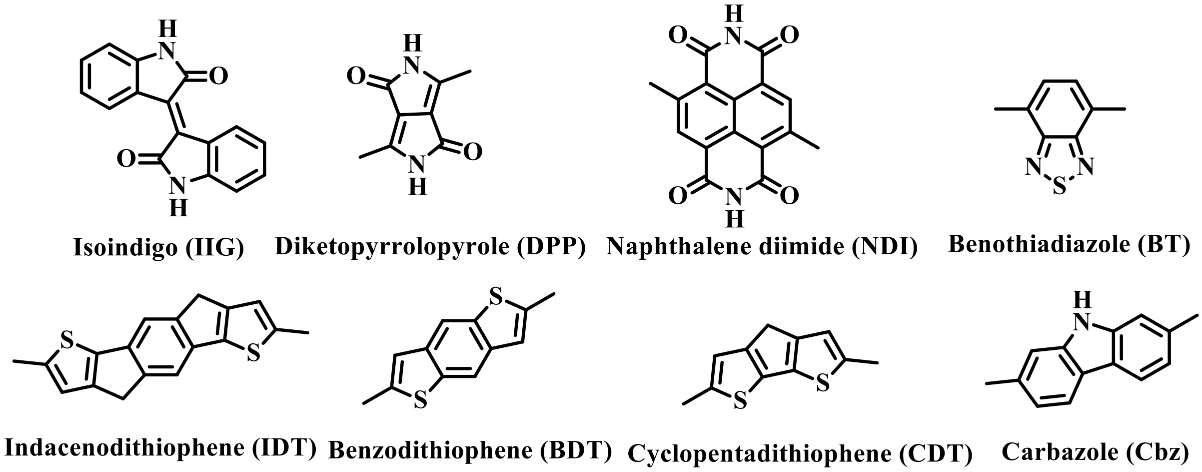

Isoindigo (IIG) **Diketopyrrolopyrole (DPP)** **Naphthalene diimide (NDI)** **Benothiadiazole (BT)**

Indacenodithiophene (IDT) **Benzodithiophene (BDT)** **Cyclopentadithiophene (CDT)** **Carbazole (Cbz)**

Figure 1.1.2. The representative conjugated molecular backbones.

Herein, in this chapter, I will briefly provide the background of the principles of OPVs and OFETs as representative applied optoelectronic devices. Furthermore, according to the molecular modifications, I divided the discussion part into three main categories; i) Molecular backbone modification, ii) Side-chain engineering, and iii) Single atoms substitution.

1.2 Organic optoelectronic applications

The field of organic optoelectronics has been developed in the past 20 years by the discovery of electroluminescence in molecular crystals and conducting organic polymers. The attractive properties such as facile fabrication, cost-effective for large areas, and remarkable physical strengths intensify a lot of research efforts. As a result, the devoted efforts have enlarged diverse types of organic optoelectronics like OPVs, OFETs, OLEDs, sensors, and photorefractive devices. Among these optoelectronics, particularly, OPVs and OFETs have been intensively examined for the understanding of blends of various multi-components and high-performing single-component, respectively. In this chapter, I focus on these two applications (OPVs and OFETs) with their background and corresponding organic semiconductors.

1.2.1 Organic photovoltaics (OPVs)

Research background

Fossil fuels are the current major energy resources that have been used cosmopolitanly, but the issues of fossil fuels such as non-renewable resources and serious air pollution always remind the requirement of next-generated energy resources. The photovoltaic cells, which mine electricity from sunlight, are one of the most promising technologies to solve the worldwide energy demands. Currently, inorganic photovoltaics (e.g. crystalline silicon (c-Si), cadmium telluride (CdTe), or copper indium germanium selenide (CIGS)) are already commercialized devices stably producing a relatively high power conversion efficiency (PCE) of around 15–20%. However, huge cost consumption of inorganic photovoltaics and environmental issue from the disposal of used devices are obstacles to be worldwide energy resources.

In 1986, Tang et al. firstly is successful in the usage of dyes in OPVs based on the bilayer structure yielding 1% of PCE in sunlight.[59] After the first success in OPVs, the concept of the bulk heterojunction (BHJ) was brought to work out the limited exciton (tightly bound electron-hole pair) within diffusion length (less than 10 nm) in bilayer OPVs. In the BHJ OPVs, the photo-active donor and acceptor materials are formed from the homogenous solution for the bi-continuous interpenetrating architecture with large interfacial areas between donor and acceptor for efficient exciton dissociation. Until now, the BHJ embedded OPVs have been well known as the stereotype of OPVs. Therefore, herein, I will explain OPVs which is presupposed as BHJ embedded devices.

Architecture of BHJ-OPV devices

In supposing only single layer BHJ-OPVs except for the concept of the tandem structure of OPVs, the architectures of BHJ-OPV are classified as conventional or inverted devices depending on the orientation of the electrode. **(Figure 1.2.1**) Generally, in the case of conventional architecture, the anode layer is composed of a thin layer of indium tin oxide (ITO) coated with a hole transporting layer (HTL) of poly(3,4-ethlenedioxythiophene):poly(styrene sulfonate) (PEDOT:PSS). The ITO is commonly used owing to its promising conductivity, transparency, and high-work function. As a HTL, PEDOT:PSS prevent the pinholes in the ITO film, as well as form the Ohmic contact with the photoactive layer. On the contrary to this, the cathode layer is constructed from low-work function metals such as calcium, lithium fluoride, and aluminum. However, the low-work function materials as the outer loop easily cause the problem of real-time oxidation when exposed to air, and acidity of PEDOT:PSS gradually damage on the photoactive layers.[60] As the above-mentioned problems of conventional architecture, the inverted architecture also has been evolved via the introductions of more stable and high work-function materials like molybdenum oxide, gold, and silver as the loop-top anode. Instead of PEDOT:PSS HTL, low work-function and solution-processable materials are selected (e.g. titanium oxide (TiO_X), zinc oxide (ZnO)) as the electron transporting layer (ETL).[61-63]

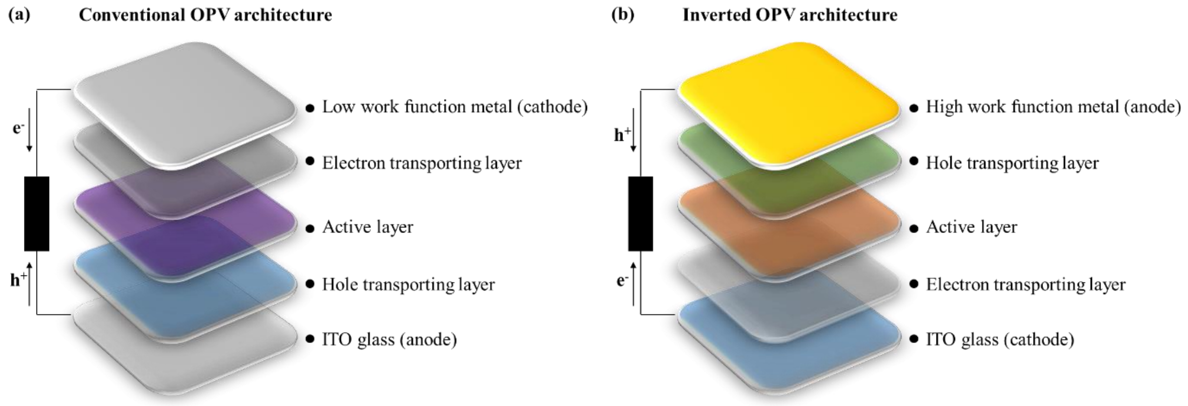

Figure 1.2.1. The illustrations of (a) conventional OPV architecture and (b) inverted OPV architecture.

Principle of BHJ-OPVs

From the Sunlight to the photocurrent, there are four steps of energy harvesting progress in OPVs (**Figure 1.2.2**).[64] The four-step process of OPVs is influenced by the photovoltaic performance and external quantum efficiency (EQE) of the device. The EQE can be estimated by the following equation:[65]

$$\mathrm{EQE} = \eta_{\mathrm{A}} \times \eta_{\mathrm{D}} \times \eta_{\mathrm{CT}} \times \eta_{\mathrm{CC}}$$

(i) Light absorption (η_{A})

With the irradiation of sunlight which has enough energy to excite the electrons of photoactive materials, the electrons bound to HOMO can be easily excited to LUMO level. In this state, the pair of excited electrons and the vacancy (so-called hole) is named as an exciton. To further produce the exciton in the photoactive layer, the broaden absorption spectra is a key factor to determine the capacity of sunlight irradiation. Also, the most energy distribution of sunlight leans too much towards to visible range (400 - 700 nm) and near-infrared (700 - 2500 nm), so the ideal absorption range should be long-wavelength region.

(ii) Exciton diffusion (η_{D})

Right after the birth of excitons by light absorption, the excitons are diffused to the donor-acceptor interface to yield the free charge carrier. Since the limit of exciton diffusion length (L_d) is ~10 nm, the required diffusion distance (L_i) between new-birth exciton location and donor-acceptor interface should be smaller than L_d to avoid radiative or non-radiative recombination.[66]

(iii) Exciton dissociation and charge transport (η_{CT})

At the donor-acceptor interfaces, the excitons are dissociated into the corresponding electrode in the form of free charge carriers. On this occasion, the minimum exciton binding energy (~0.3 eV) is required to dissociate, and the required potential is gotten from the offset of LUMO energy levels of donor and acceptor.[67] On the other hand, the resulted open-circuit voltage (V_{OC}) is determined by the gap of LUMO of acceptor and HOMO of the donor. Therefore, the optimum of LUMO energy levels of donor and acceptor is demanded enhanced OPVs performance.

(iv) Collection of charge carriers (η_{CC})

The generated free charge carriers resulted from the exciton dissociation are collected in the corresponded electrodes. The driving force to transfer the free charge carriers are affected by the well-aligned energy level of the photo-active layer and the work function of electrodes. Moreover, the free charge carriers could be easily diminished by non-germinate recombination, the fast charge carrier mobilities within the donor-acceptor layers can increase the possibility of collection of free charge carriers.

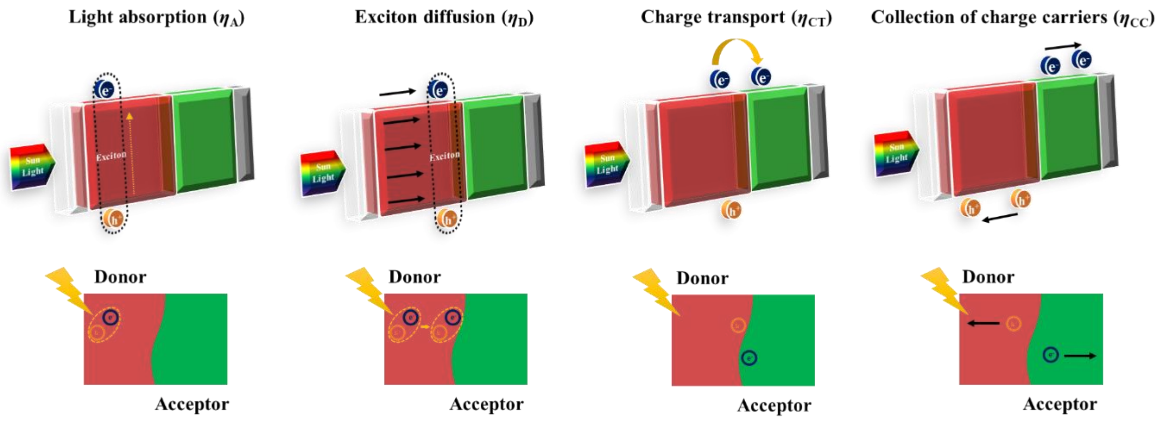

Figure 1.2.2. The working mechanism of OPVs operation.

As a result of four steps photocurrent generation of OPVs, the PCE is calculated by the following equation:

$$\mathrm{PCE} = J_{SC} \times V_{OC} \times FF \times 100\% / P_{in}$$

where P_{in} is the incident light power density, J_{SC} is the short-circuit current density, V_{OC} is the open-circuit voltage, and FF is the fill factor (**Figure 1.2.3**). The P_{in} is determined the input power of the cell, normally air mass 1.5G condition as 1 sun. The J_{SC} is obtained when the solar cell is short-circuited (i.e., the voltage across the solar cell is zero), and largely influenced by the capability of light absorption in the photoactive organic materials. Thus, the formation of a wide range of absorption bands of organic materials with a high absorption coefficient, as well as appropriate active layer thickness is crucial factors to get the optimal PCEs.[68-72] In the case of the V_{OC}, it could be presented with the absence of external electric current flow between the terminals. In addition, the disparity between the HOMO of donor and LUMO of the acceptor is the chief parameter to settle for manifested V_{OC} considering the exciton dissociation energy (~ 0.3 eV) and radiative and non-radiative energy loss.[73, 74] On the assumption that the maximum power is estimated by product of J_{SC} and V_{OC}, the *FF* is the ratio of the actual device operation compared to this maximum power. The *FF* is manifoldly concerned in the carrier mobilities of photo-active layers, shunt resistance (R_{SH}) originating from poor diode contact, and series resistance (R_S) occurred at the contact of bulk semiconductors.[75, 76]

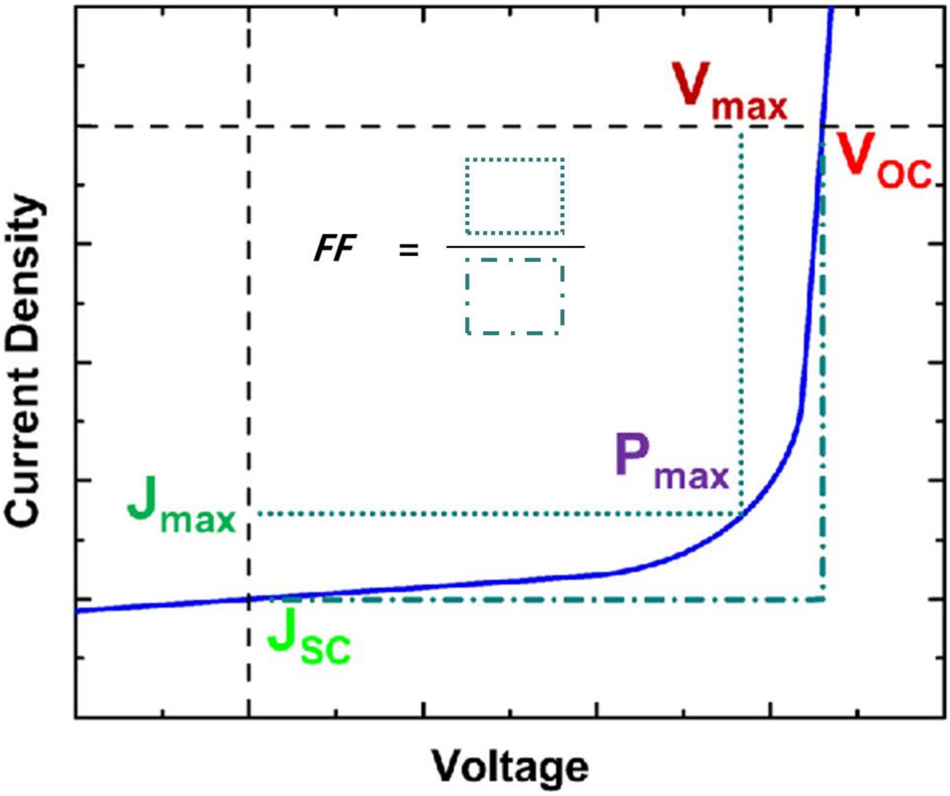

Figure 1.2.3. The typical current density-voltage (J-V) profiles of the OPVs.

1.2.2 Organic field-effect transistors (OFETs)

Research background

The first application of organic semiconductor, polythiophene, to the transistor in 1986 by Tsumura et al. have inspired the utilities of organic semiconductors in OFETs.[77] OFETs are constituted by five parts which are gate electrode (G), source and drain electrodes (S/D), gate insulator (GI), and organic semiconductor (OSC). With regards to the configuration of the gate electrode, source, and drain electrodes, OFETs can be categorized as four architectures: bottom-gate and top-contact (BG-TC), bottom-gate and bottom contact (BG-BC), top-gate and top-contact (TG-TC), and top-gate and bottom contact (TG-BC) (**Figure 1.2.4**). In the perspective of the gate electrode, the bottom-gate architecture facilitates to stabilize the OSC layer because both the gate electrode and gate insulator are pre-deposited before the organic semiconductor casting. Moreover, the pre-deposition process makes a room for diverse treatment for gate electrodes and gate insulators, eliminating the possibility to damage on the OSC layer. On the contrary, the top-gate architecture has merits of chances to modify the pattern of source and drain electrodes and ease fabrications of the gate insulator simply protecting layer for OSC. However, the difficulty to control the roughness of the loop top of the OSC layer, resultingly, leads to the degradation in charge carrier transport. In terms of contact electrodes, top-contact architecture has been usually exhibited better performance than bottom-contact due to enlarged charge injection area lessening the contact resistance. As mentioned earlier, each of these architectures coexist the merits and demerits, either in technical demand of fabrication or in OFET performances.

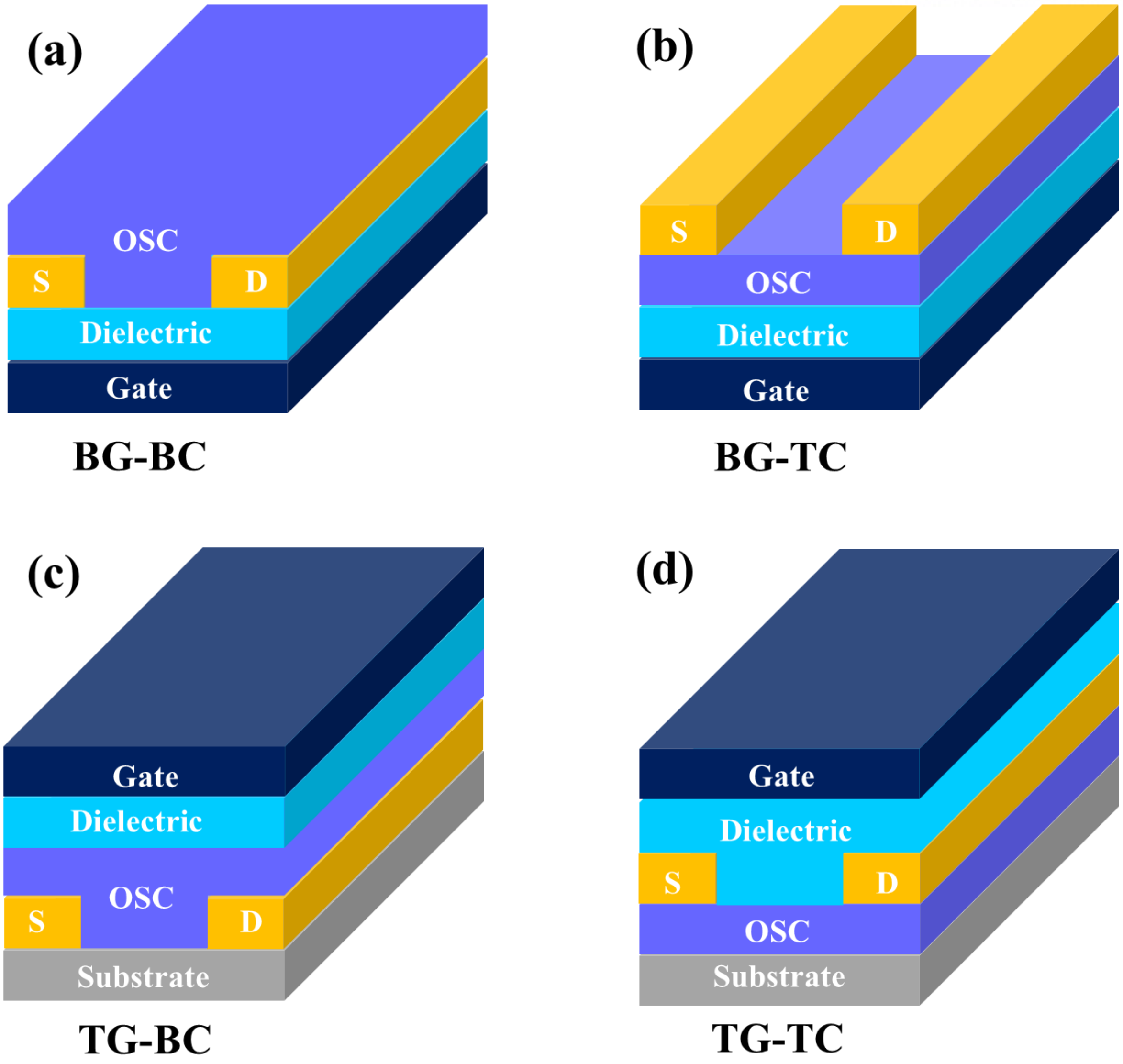

Figure 1.2.4. The illustrations of OFET architectures (a) bottom-gate and bottom contact (BG-BC), (b) bottom-gate and top-contact (BG-TC), (c) top-gate and bottom contact (TG-BC), and (d) bottom-gate and bottom contact (BG-BC).

Principle of OFETs

In **Figure 1.2.5**, the operation of OFETs is described with bottom-gate and bottom-contact configuration. The gate electrode and drain electrode manage the operation of OFETs, with the source electrode is maintained at the ground connection. For the more convenient description of the operation of OFETs in the following discussion, the model of OFETs is presumed assumed as a p-type, where the holes are majority charge carriers. With no gate-source voltage (V_{GS} = 0 V), none of the free charge carriers are existed in the conduction channel, and the source-drain current will naturally be closed to zero (so-called "off" state). If a negative gate voltage ($V_{GS} < 0$ V) is applied, positive charges (p-channel) will be constructed in the near of the semiconductor/dielectric interface, and source-drain current (J_{DS}) is rapidly increased (so-called "on" state). At this moment, the applied drain-source voltage (V_{DS}) translocate the accumulated charge carriers from the source electrode to the drain electrode, as a result the drain current (I_D) is measured. Consequently, the charge density in the channel is adjusted by the magnitude of V_{GS}. Au fond, the only small negative V_{GS} is necessary to first fill the charge traps at the semiconductor-dielectric interface to ready for charge carrier accumulation. At this time, the applied potential (i.e. trap-filling potential) is known as the threshold voltage (V_{th}) which is stems from the factors such as crystal defects, impurities, or interfacial roughness.[7, 78]

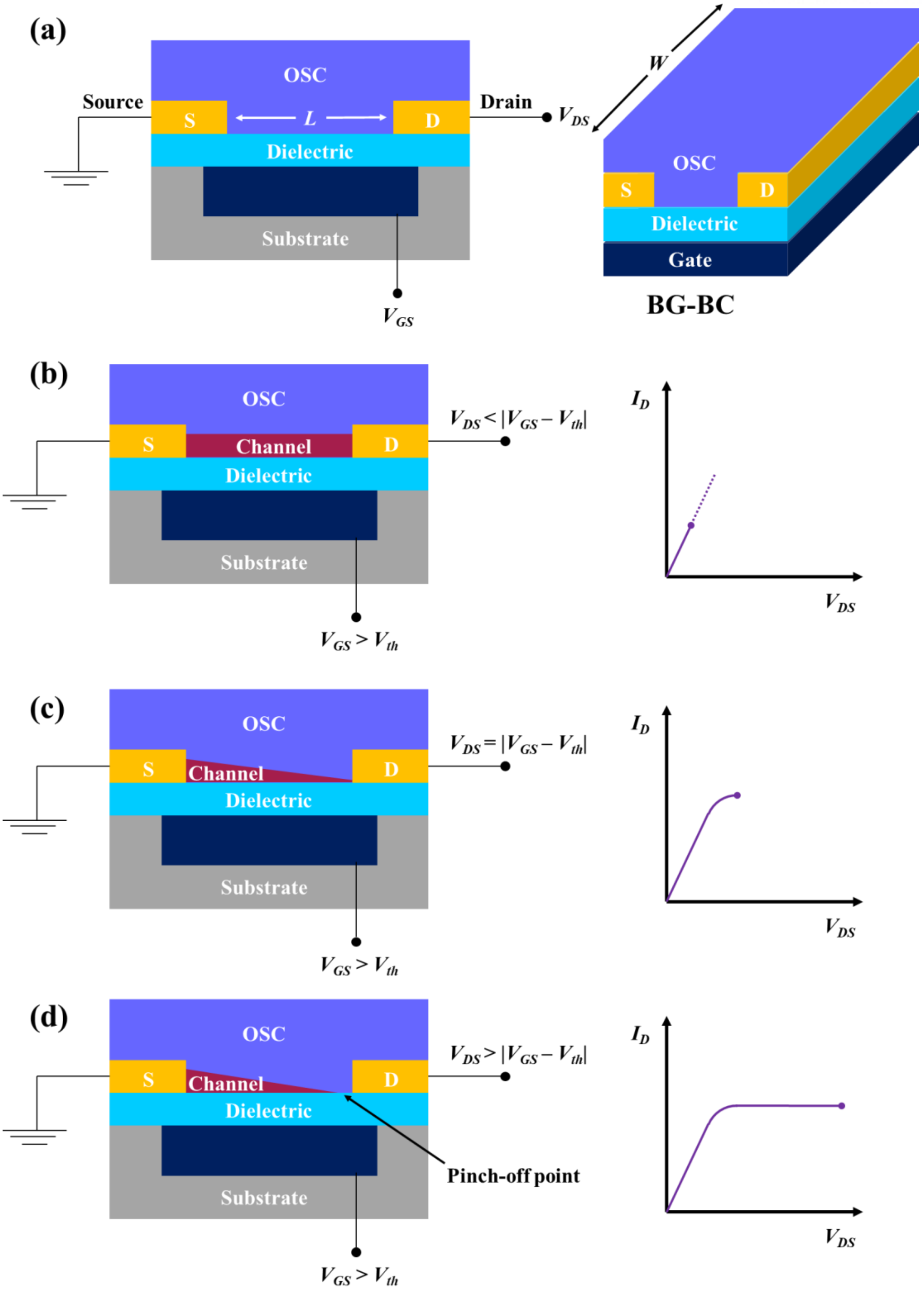

Figure 1.2.5. (a) Schematic structure of a field-effect transistor with BG-BC architecture: (L) channel length, (W) channel width, (V_{DS}) drain voltage, (V_{GS}) gate voltage, (V_{th}) threshold voltage and (I_D) drain current. (b-d) illustration of operating regimes of field-effect transistors: (b) linear regime; (c) start of saturation regime at pinch-off; (d) saturation regime and corresponding current-voltage characteristics.

Along with the increase of V_{DS}, the drawn OFET characteristics are divided into two regions. The first region is the linear regime when $V_{DS} < |V_{GS} - V_{th}|$, the I_D is in directly proportional to the V_{DS} and the device is under the control of the gate-voltage variable. As VDS being almost equalized to the VGS, the output profile of OFET is transformed owing to the two interacting potentials. Eventually, where $V_{DS} = |V_{GS} - V_{th}|$, it's denoted as the critical point, the free charge carriers are exhausted near the vicinity of the drain electrode and become pinched off. The applied electric field leads to the charge carriers from the pinch-off point to the drain electrode while the space-charge limited current flows across the depletion region. After the critical point, additional increased V_{DS} cause not only the migration of charges from source to drain but also the expanding depletion zone near the drain with the saturation of I_D, thus, this region is named as saturation region. Within the saturation region, the field-effect mobility, μ, is a value how quickly charge carriers transport regarding to an external electric field. The μ can be estimated from the transfer characteristic using the following equation:

$$I_{DS} = \frac{\mu C_{diel} W}{2L} (V_{GS} - V_{th})^2$$

where W is the channel width, L is the channel length, C_{diel} is the dielectric capacitance, μ is the field-effect mobility.[79]

1.3 Design of organic semiconductors

1.3.1 Aryl-aryl coupling reactions

The aryl-aryl couplings have been advanced together with the progress of organic semiconductors. In this respect, the knowledge of numerous coupling reactions is essential to propose and synthesize organic semiconductors. Typically, there are two kinds of coupling reactions relying on the number of employed monomers: homo-coupling with only one monomer and cross-coupling of the plural different monomers. Meanwhile, the state-of-the-art proposed molecular design becomes more complex, accordingly the miscellaneous type of synthetic route for the coupling of π-conjugated systems have been evolved under the diverse circumstances of reactions. Among them, most of the coupling reactions have employed organometallic catalysts such as palladium-, nickel-, and copper-based ones (**Table 1.3.1**).[80]

Table 1.3.1 The overview of coupling reactions.

Reaction	Reactant A		Reactant B		Catalyst	Note
Wurtz reaction	R-X	sp^3	R-X	sp^3	-	Na
Glaser coupling	$RC\equiv CH$	sp	$RC\equiv CH$	sp	Cu	O_2
Ulmann reaction	Ar-X	sp^2	Ar-X	sp^2	Cu	-
Gomberg-Bachmann reaction	Ar-H	sp^2	$Ar\text{-}N_2X$	sp^2	-	Base
Caito-Chodkiwicz coupling	$RC\equiv CH$	sp	$RC\equiv CX$	sp	Cu	Base
Castro-Stephens coupling	$RC\equiv CH$	sp	Ar-X	sp^2	Cu	-
Gilman reagent coupling	R_2CuLi	-	R-X	-	-	
Cassar reaction	$RC=CH_2$	sp^2	R-X	sp^3	Pd	Base
Kumada coupling	Ar-MgBr	sp^2, sp^3	Ar-X	sp^2	Pd or Ni, or Fe	Base
Heck reaction	$RC=CH_2$	sp^2	R-X	sp^2	Pd or Ni	Base
Sonogashira coupling	$RC\equiv CH$	sp	R-X	sp^2, sp^3	Pd and Ni	Base
Negishi coupling	R-Zn-X	sp, sp^2, sp^3	R-X	sp^2, sp^3	Pd or Ni	-
Stille cross coupling	$R\text{-}SnR_3$	sp, sp^2, sp^3	R-X	sp^2, sp^3	Pd	-
Suzuki reaction	$R\text{-}B(OR)_2$	sp^2	R-X	sp^2, sp^3	Pd or Ni	Base
Hiyama coupling	$R\text{-}SiR_3$	sp^2	R-X	sp^2, sp^3	Pd	Base
Buchwald-Hartwig reaction	$R_2N\text{-}H$	sp	R-X	sp^2	Pd	N-C coupling
Fukuyama coupling	R-Zn-I	sp^3	RCO(SEt)	sp^2	Pd	-

Research background

Generally, the mechanisms of organometallic based coupling reaction are three-step processes, oxidative addition, trans-metalation, and reductive elimination steps follow in order (**Figure 1.3.1**). The starting point of the coupling reaction is oxidative addition initiating with the combination of the organic electrophile and organometallic catalyst. At this moment, the reactivity of the leaving groups on the organic electrophile can manage the rate of reaction. After the oxidative addition, the combined seed goes through the trans-metalation putting the leaving groups aside together with bringing in other counterparts on the seed. In the final step of the coupling, the reductive elimination undergoes rearrangement by switching of ligand and counterpart, and the adjacent coupling partners go out the seed with the regeneration of the catalyst for the next coupling reaction.

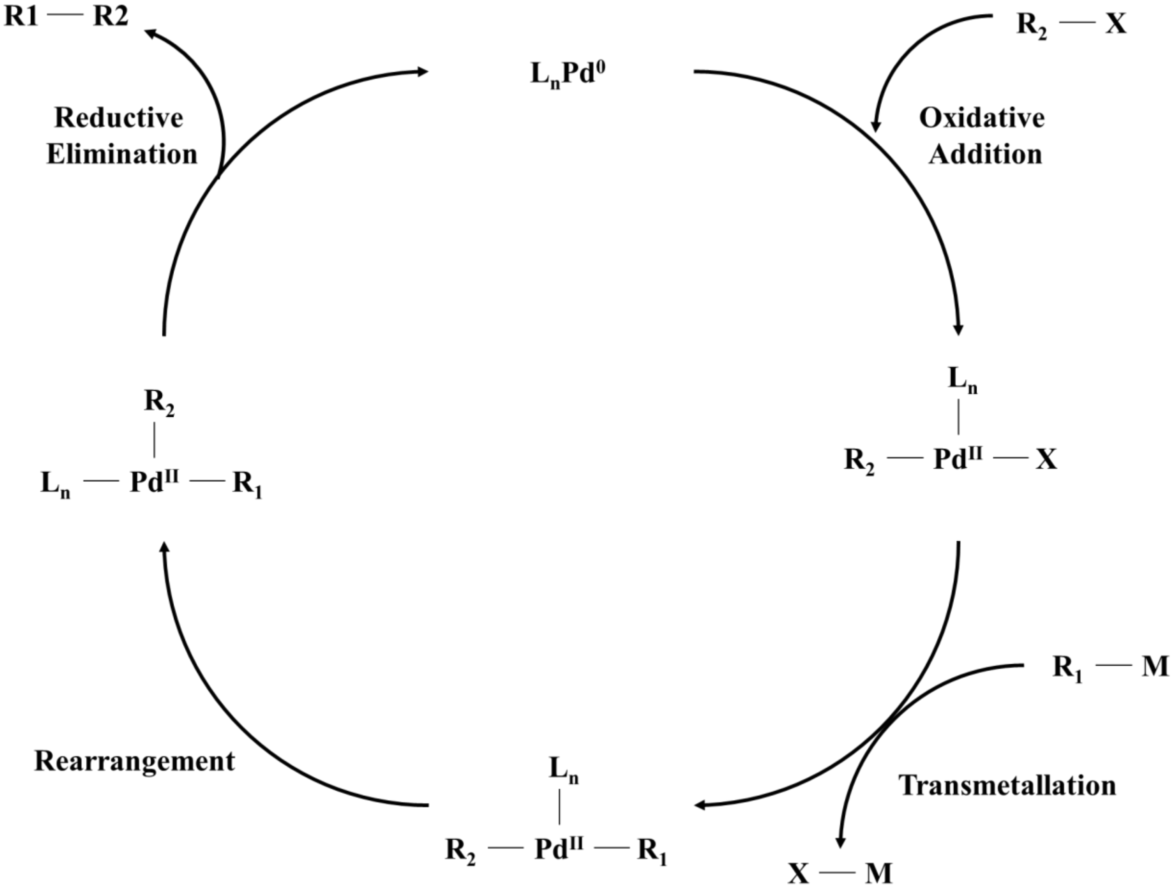

Figure 1.3.1. Typical palladium-catalyzed cross-coupling reaction mechanism.

In the undermentioned discussion, for the handy talk about the approaches to modify the conjugated polymer and small molecules, I arbitrarily divided into three methods as following; molecular backbone modification, side-chain engineering, and single atoms substitution.

1.3.2 Molecular backbone modification

The conjugated backbone is the heart of constituent of materials because it has the strongest discretion to features of resulting materials from the physical properties such as the energy levels of frontier orbitals and bandgap to inter/intra molecular interactions. Until the present, there are over hundreds of different backbones have been born in many research groups, however, the design of brand-new conjugated backbones is usually adventurous because only a few candidates can demonstrate their success to achieve high performances in optoelectronic devices. Therefore, the rational approach to the design of a new conjugated backbone is paramount for further advances.

Ordinarily, the compositions of building blocks for low bandgap conjugated materials are a pair of donor-acceptor (D-A) units. The repeating unit of D-A configuration consisted of an electron-rich unit D (so-called donor) and electron-deficient unit A (so-called acceptor). The internal charge transfer (ICT) between the D and A units from the concept of push-pull architecture contributes to a more desirable double bond characteristic rather single bond. As a result, the conjugated backbone adopts a more planar structure to promote the π-electrons delocalization along the conjugated backbone, implying the formation of the smaller bandgap of conjugated materials. In addition, in accordance with the factors of how the strength of D/A units are employed for resulting conjugated backbones, the aligned HOMO and LUMO level could be under the control.

From now on, under the D-A configuration, each independent property of D and A units are considered not only in terms of molecular planarity related to intermolecular interaction, but also the electrical properties. The fused structure of the conjugated backbone is the most popular design for promising the flat conformation, tunability of electrical properties via aromaticity, and handy elongation of effective conjugation length. Meanwhile, if the fused ring is the above-ideal level of elongation, the conjugated backbone has a high possibility to get in trouble because of the instability of the high level of fusion and poor solubility by the too rigidity of backbone. In **Figure 1.3.2**, there are representative fused ring structures of D and A units.

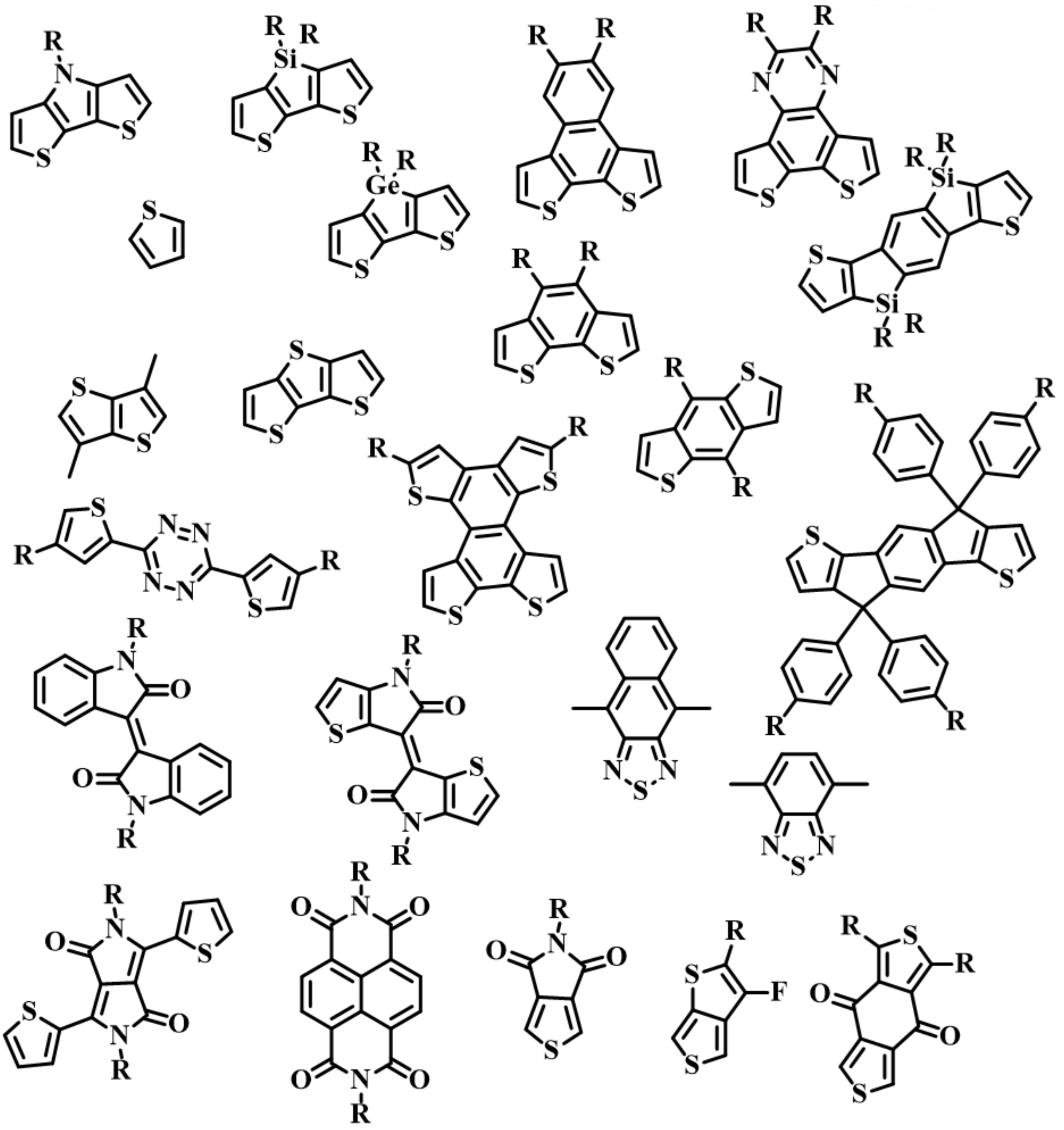

Figure 1.3.2. The representative building blocks of conjugated materials.

1.3.3 Side-chain engineering

The careful selection of the side-chains is as important as choosing the appropriate conjugated backbones for portraiting optimal conjugated materials. On the contrary to molecular backbones, the side chins have a vital role in solubility associated with processability, as well as intermolecular interaction to allow the closed packing and orientation in thin-film state. Moreover, recent researches in functional side chains (e.g. organic/inorganic hybrid functionality, induction of the hydrogen bonding) reveled the reinforcement of physical properties, as well as amphiphilicity of conjugated materials.

Based on the aforementioned role of side chains, the use of side chains is mandatory to the state-of-the-art organic semiconductors. Withal, the docking position of side-chains on the conjugated backbone is one of the considerations owing to the attachment of side chains consequently arousing the steric hindrance and twisting the conjugated backbone. And there are issues of momentous steric hindrance between these aromatic units on the conjugated backbone, too long side-chain inhibits the fast charge carrier transport via increase of population of insulating side-chains in total conduction platform. Therefore, abundant research results have been reported in regard to exploring the suitable position of side chain considering the regio-regularity and tailoring of the length of side chains. In **Figure 1.3.3**, there are representative side-chains.

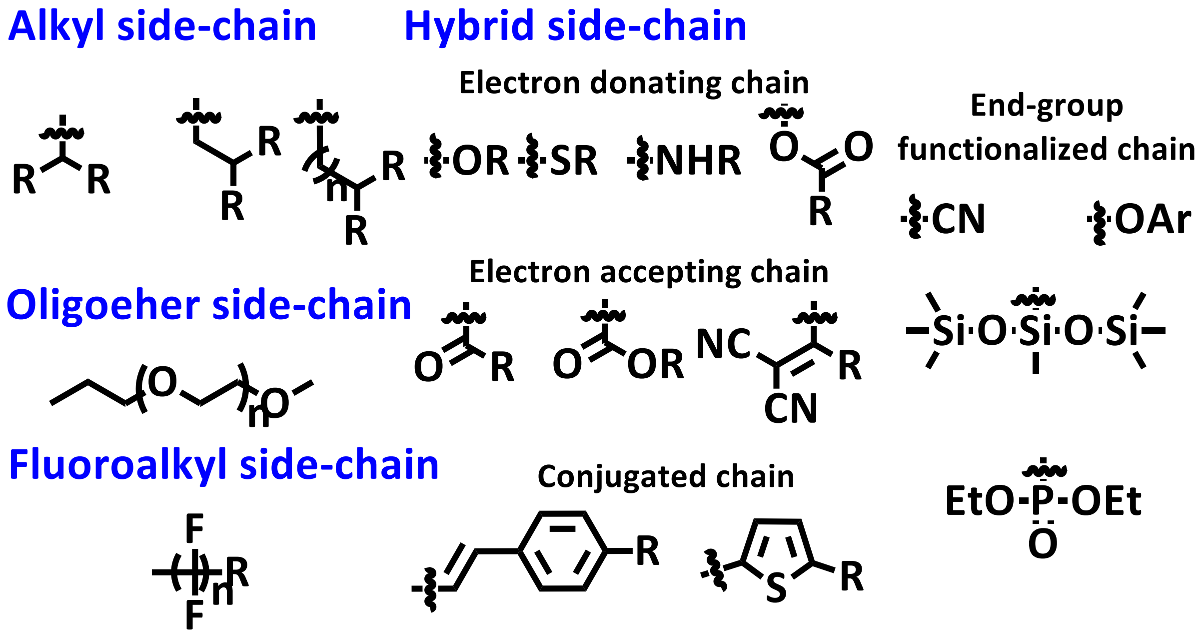

Figure 1.3.3. The overview of various side-chains.

1.3.4 Single atoms substitution

Nevertheless, both molecular backbone modification and side-chain engineering promptly have huge impacts on the resulting organic semiconductors based on the above-mentioned factors, it is somewhat not efficient to finely tune the properties of organic semiconductors. Thence, as a bypass to fine-tuning of molecular properties, the substituents have been used without the sacrificial of the mainstream of organic semiconductors. With advanced molecular structures and qualified candidate backbones, the small changes via substituents gradually have been spotlighted due to their fluid applicability on any kind of molecules.

The most universal substituents are halogen atoms with single proton, among them, the fluorine substitution is the most famous case. The reasons why the fluorine substitution is popular are easily found from the characteristics of fluorine atom as following: i) The comparable size of an atom which is only 1.35 Å of van de Waals radius. ii) The Pauling electronegativity of 4.0 implies most electron-withdrawing group iii) There is a great influence on inter- and intramolecular interactions via C−F···H, F···S, and C−F···π_F interaction. On top of that, the other halogen atoms chlorine, bromine, and iodine have occasionally been used as a substituent, but these always accompany competition of side reaction due to their reactivity as an active cite during the Ar-Ar coupling reactions. Besides, another representative electron-withdrawing substituent is cyano (-CN) group, but the difficulty and limit of substitution on the conjugated backbone hinder the vigorous researches works.

1.4 Toolbox of characterization of organic semiconductors

During the whole process from the proposal of brand-new organic semiconductors to finalize the synthesis of target molecules, each step of synthetic schemes is required to fully characterize the molecular structure. Moreover, based on the synthesized molecules, numerous investigations for the understanding of optoelectronic properties and nano-scaled morphologies are fulfilled to grasp the resulting performances in applied devices. Therefore, before handling the main discussion, I will provide brief introduction of commonly used tools for characterizations in this section.

1.4.1 Material characterization

Nuclear magnetic resonance (NMR)

Nuclear magnetic resonance (NMR) spectroscopy is a simple, yet powerful tool to analyze the molecular structure as well as the dynamics of macromolecules. The versatility of NMR spectroscopy is demonstrated by a variety of utilization from macromolecular science to supramolecular systems. Depending on the advances of magnetic field and timescale, NMR spectroscopy may allow to elucidate the inter/intra molecular interactions or arrangement in solid-state and disclose the precise investigation of complicated structures such as end-group of conjugated polymers. Leaving the powerful ability of NMR spectroscopy, unfortunately, the following discussion will only deal with the molecular characterization via ^{1}H and ^{13}C isotopes due to the confines of the facility.

Elemental analysis (EA)

Elemental analysis (EA) is performed on the basis of carbon, hydrogen and nitrogen atoms to characterize the elemental composition of organic sample. Under the thermally mineralization over 990 °C, the organic substance undergoes oxidative decomposition and subsequently leading the reduction of nitrogen and sulfur oxides with the production of the final products such as water, carbon dioxide, elemental nitrogen, and sulfur dioxide. The product gas mixture flows through a detection tunnel, resulting in a quantitative analysis of the ratio of components. The EA is confined to elements C,H,N, and S, hence the analysis usually is used for supporting the other characterization and guarantee of purity.

Mass spectrometry (MS)

The mass spectrometry (MS) analyzes the measure the mass-to-charge ratio (m/z) in the gas phase, and the corresponding measurement is presented as a mass spectrum. The MS is usually used to verify the purity of the sample as well as the population of complex mixtures. On the contrary to EA measurement, there is no limitation of the kind of organic sample excluding with too high molecular weight, so the precise characterization of the organic sample is secured in case of the known molecular formula. Together with NMR and EA measurement, MS is supplementary data of the molecular structures with basic information of target molecules.

1.4.2 Analysis of optoelectronic properties

Absorption spectroscopy

The absorption spectroscopy is a useful method to identify the specific substances via the wavelength-dependent absorption characteristics. The sample molecules are normally prepared as a dilute solution or thin-film state and exposed under the light for excitation of the ground-state electrons to a higher energy orbital. Concerning the organic semiconductors, the comparison of absorption profiles during the phase transition from diluted solution to solid-state mostly gives a hand to elucidate the molecular optoelectronic properties. For example, the absorption onset point from the solid-state spectrum can help to estimate the optical bandgap via photon energy calculation. On the other hand, the changes during the phase transition can depict the intermolecular aggregation in a roundabout way including the aggregation types.

Cyclic voltammetry

The voltammetry provides the information of the analyte originated in the measurement of current as a function of applied potential. In terms of the cyclic voltammetry, it means that the potential is swept back and forth past the formal potential of an analyte, and the corresponding current flows through the electrode that either oxidizes or reduces the analyte. Conventionally, the cyclic voltammetry uses the three-electrode system consisting of working, reference and counter electrodes sinking in the specific electrolyte solution. On account of sweep back and forth the potential, the oxidation and reduction potential are acquired independently yielding the HOMO and LUMO energy level with the corresponding bandgap. During the several times of sweep reiterations, the electrochemical stability of materials subsidiarily could be predicted by the reversible or irreversible profiles of cyclic voltammetry.

1.4.3 Observation of thin film morphology

Transmission electron microscopy (TEM)

The transmission electron microscopy (TEM) is one of the microscopy techniques which observe the transmission of the electron beam passing through the sample on the grid. The samples are normally less than 100 nm thickness and the images are the portrait by results of the transmissions from the interaction between the electrons and samples. Thus, via TEM images, the nano-scaled morphologies of organic semiconductors reflect to inform the molecular aggregations and crystallinity. Moreover, together with energy-dispersive X-ray spectroscopy (EDX) of TEM, the molecular mapping of the distribution of specific elements (e.g. fluorine, chlorine, silicon, and so forth) is described.

Atomic force microscopy (AFM)

The atomic force microscopy (AFM) is also a powerful tool for observing the microstructure of organic semiconductors, but the gained images are extricated from the interaction between sample and cantilever/tip (so-called probe). Therefore, unlike the TEM images, AFM images can deliver more vivid images and higher-resolution to study of nano-scaled morphologies of organic semiconductors. Especially, when studying about the bi-molecular thin films obtained from BHJ active layers, the AFM can help to examine the corresponding films via profiling of phase transition images.

One-dimensional and two-dimensional X-ray diffraction (1D/2D XRD)

On the contrary to above-introduced microscopies, the X-ray diffraction is connected to the evaluation of the intermolecular distance instead of thin-film morphologies. Because of the resolution of X-ray penetration through the packed intermolecular space of organic semiconductors, more precise measurement is available from the diffraction pattern and Bragg's equation. In addition, by means of expansion from the one-dimension to two-dimension, the 2D-XRD diffraction gives light on the intermolecular distance, as well as is enabled to figure out the orientation of molecular packing. Depending on the direction of orientation of organic semiconductor, there are two kinds of descriptions as following: i) edge-on orientation implying the packed molecules are arranged in perpendicular to the substrate ii) face-on orientation indicating oriented packed molecules is laying on the substrate. Each of those orientations may have favorable to facilitate fact charge carrier transport according to applied device architecture.

1.5 References

1. Shirakawa, H.; Louis, E. J.; MacDiarmid, A. G.; Chiang, C. K.; Heeger, A. J., Synthesis of electrically conducting organic polymers: halogen derivatives of polyacetylene,(CH) x. *J. Chem. Soc. Chem. Commun.* **1977,** (16), 578-580.

2. Cheng, Y.-J.; Yang, S.-H.; Hsu, C.-S., Synthesis of conjugated polymers for organic solar

cell applications. *Chem. Rev.* **2009,** *109* (11), 5868-5923.

3. Günes, S.; Neugebauer, H.; Sariciftci, N. S., Conjugated polymer-based organic solar cells. *Chem. Rev.* **2007,** *107* (4), 1324-1338.

4. Yu, G.; Gao, J.; Hummelen, J. C.; Wudl, F.; Heeger, A. J., Polymer photovoltaic cells: enhanced efficiencies via a network of internal donor-acceptor heterojunctions. *Science* **1995,** *270* (5243), 1789-1791.

5. Forrest, S. R., The path to ubiquitous and low-cost organic electronic appliances on plastic. *Nature* **2004,** *428* (6986), 911.

6. Arias, A. C.; MacKenzie, J. D.; McCulloch, I.; Rivnay, J.; Salleo, A., Materials and applications for large area electronics: solution-based approaches. *Chem. Rev.* **2010,** *110* (1), 3-24.

7. Dimitrakopoulos, C. D.; Malenfant, P. R., Organic thin film transistors for large area electronics. *Adv. Mater.* **2002,** *14* (2), 99-117.

8. Li, Y.; Wu, Y.; Ong, B. S., Polyindolo [3, 2-b] carbazoles: a new class of p-channel semiconductor polymers for organic thin-film transistors. *Macromolecules* **2006,** *39* (19), 6521-6527.

9. Li, G.; Zhu, R.; Yang, Y., Polymer solar cells. *Nat. Photonics* **2012,** *6* (3), 153.

10. Lu, L.; Zheng, T.; Wu, Q.; Schneider, A. M.; Zhao, D.; Yu, L., Recent advances in bulk heterojunction polymer solar cells. *Chem. Rev.* **2015,** *115* (23), 12666-12731.

11. Burroughes, J. H.; Bradley, D. D.; Brown, A.; Marks, R.; Mackay, K.; Friend, R. H.; Burns, P.; Holmes, A., Light-emitting diodes based on conjugated polymers. *Nature* **1990,** *347* (6293), 539.

12. Kobayashi, H.; Kanbe, S.; Seki, S.; Kigchi, H.; Kimura, M.; Yudasaka, I.; Miyashita, S.; Shimoda, T.; Towns, C. R.; Burroughes, J. H., A novel RGB multicolor light-emitting polymer display. *Syn. Met.* **2000,** *111*, 125-128.

13. Bernius, M. T.; Inbasekaran, M.; O'Brien, J.; Wu, W., Progress with light-emitting polymers. *Adv. Mater.* **2000,** *12* (23), 1737-1750.

14. Friend, R.; Gymer, R.; Holmes, A.; Burroughes, J.; Marks, R.; Taliani, C.; Bradley, D.; Dos Santos, D.; Bredas, J.; Lögdlund, M., Electroluminescence in conjugated polymers. *Nature* **1999,** *397* (6715), 121.

15. Dai, L.; Winkler, B.; Dong, L.; Tong, L.; Mau, A. W., Conjugated Polymers for Light-Emitting Applications. *Adv. Mater.* **2001,** *13* (12-13), 915-925.

16. Fukuda, Y.; Watanabe, T.; Wakimoto, T.; Miyaguchi, S.; Tsuchida, M., An organic LED display exhibiting pure RGB colors. *Syn. Met.* **2000,** *111*, 1-6.

17. Kim, J. Y.; Lee, K.; Coates, N. E.; Moses, D.; Nguyen, T.-Q.; Dante, M.; Heeger, A. J., Efficient tandem polymer solar cells fabricated by all-solution processing. *Science* **2007,** *317* (5835),

222-225.

18. Park, S. H.; Roy, A.; Beaupré, S.; Cho, S.; Coates, N.; Moon, J. S.; Moses, D.; Leclerc, M.; Lee, K.; Heeger, A. J., Bulk heterojunction solar cells with internal quantum efficiency approaching 100%. *Nat. Photonics* **2009,** *3* (5), 297.

19. Wang, C.; Dong, H.; Hu, W.; Liu, Y.; Zhu, D., Semiconducting π-conjugated systems in field-effect transistors: a material odyssey of organic electronics. *Chem. Rev.* **2011,** *112* (4), 2208-2267.

20. Dou, L.; Liu, Y.; Hong, Z.; Li, G.; Yang, Y., Low-bandgap near-IR conjugated polymers/molecules for organic electronics. *Chem. Rev.* **2015,** *115* (23), 12633-12665.

21. Garnier, F.; Hajlaoui, R.; Yassar, A.; Srivastava, P., All-polymer field-effect transistor realized by printing techniques. *Science* **1994,** *265* (5179), 1684-1686.

22. Facchetti, A.; Deng, Y.; Wang, A.; Koide, Y.; Sirringhaus, H.; Marks, T. J.; Friend, R. H., Tuning the Semiconducting Properties of Sexithiophene by α, ω-Substitution—α, ω-Diperfluorohexylsexithiophene: The First n-Type Sexithiophene for Thin-Film Transistors. *Angew. Chem. Int. Ed.* **2000,** *112* (24), 4721-4725.

23. Murphy, A. R.; Fréchet, J. M., Organic semiconducting oligomers for use in thin film transistors. *Chem. Rev.* **2007,** *107* (4), 1066-1096.

24. Yan, H.; Chen, Z.; Zheng, Y.; Newman, C.; Quinn, J. R.; Dötz, F.; Kastler, M.; Facchetti, A., A high-mobility electron-transporting polymer for printed transistors. *Nature* **2009,** *457* (7230), 679.

25. Hirsch, J., Hopping transport in disordered aromatic solids: a re-interpretation of mobility measurements on PKV and TNF. *J. Phys. C* **1979,** *12* (2), 321.

26. Mei, J.; Kim, D. H.; Ayzner, A. L.; Toney, M. F.; Bao, Z., Siloxane-terminated solubilizing side chains: bringing conjugated polymer backbones closer and boosting hole mobilities in thin-film transistors. *J. Am. Chem. Soc.* **2011,** *133* (50), 20130-20133.

27. Stalder, R.; Puniredd, S. R.; Hansen, M. R.; Koldemir, U.; Grand, C.; Zajaczkowski, W.; Müllen, K.; Pisula, W.; Reynolds, J. R., Ambipolar Charge Transport in Isoindigo-Based Donor–Acceptor Polymers. *Chem. Mater.* **2016,** *28* (5), 1286-1297.

28. Lei, T.; Dou, J. H.; Pei, J., Influence of Alkyl Chain Branching Positions on the Hole Mobilities of Polymer Thin-Film Transistors. *Adv. Mater.* **2012,** *24* (48), 6457-6461.

29. Kim, G.; Han, A.-R.; Lee, H. R.; Lee, J.; Oh, J. H.; Yang, C., Acceptor–acceptor type isoindigo-based copolymers for high-performance n-channel field-effect transistors. *Chem. Commun.* **2014,** *50* (17), 2180-2183.

30. Grand, C.; Zajaczkowski, W.; Deb, N.; Lo, C. K.; Hernandez, J. L.; Bucknall, D. G.; Müllen, K.; Pisula, W.; Reynolds, J. R., Morphology control in films of isoindigo polymers by side-

chain and molecular weight effects. *ACS Appl. Mater. Interfaces* **2017,** *9* (15), 13357-13368.

31. Ashraf, R. S.; Kronemeijer, A. J.; James, D. I.; Sirringhaus, H.; McCulloch, I., A new thiophene substituted isoindigo based copolymer for high performance ambipolar transistors. *Chem. Commun.* **2012,** *48* (33), 3939-3941.

32. Lim, B.; Sun, H.; Lee, J.; Noh, Y.-Y., High performance solution processed organic field effect transistors with novel diketopyrrolopyrrole-containing small molecules. *Sci. Rep.* **2017,** *7* (1), 164.

33. Lee, S. M.; Lee, H. R.; Dutta, G. K.; Lee, J.; Oh, J. H.; Yang, C., Furan-flanked diketopyrrolopyrrole-based chalcogenophene copolymers with siloxane hybrid side chains for organic field-effect transistors. *Polym. Chem.* **2019,** *10* (22), 2854-2862.

34. Kaur, M.; Shin, J.; Lee, T. W.; Choi, K.; Cho, M. J.; Choi, D. H., A novel tellurophene-containing conjugated polymer with a dithiophenyl diketopyrrolopyrrole unit for use in organic thin film transistors. *Chem. Commun.* **2013,** *49* (48), 5495-5497.

35. Kang, S.-H.; Lee, H. R.; Dutta, G. K.; Lee, J.; Oh, J. H.; Yang, C., A role of side-chain regiochemistry of thienylene–vinylene–thienylene (TVT) in the transistor performance of isomeric polymers. *Macromolecules* **2017,** *50* (3), 884-890.

36. Huang, Y.-F.; Chang, S.-T.; Wu, K.-Y.; Wu, S.-L.; Ciou, G.-T.; Chen, C.-Y.; Liu, C.-L.; Wang, C.-L., Influences of Conjugation Length on Organic Field-Effect Transistor Performances and Thin Film Structures of Diketopyrrolopyrrole-Oligomers. *ACS Appl. Mater. Interfaces* **2018,** *10* (10), 8869-8876.

37. Sung, M. J.; Luzio, A.; Park, W. T.; Kim, R.; Gann, E.; Maddalena, F.; Pace, G.; Xu, Y.; Natali, D.; de Falco, C., High-Mobility Naphthalene Diimide and Selenophene-Vinylene-Selenophene-Based Conjugated Polymer: n-Channel Organic Field-Effect Transistors and Structure–Property Relationship. *Adv. Funct. Mater.* **2016,** *26* (27), 4984-4997.

38. Nakano, M.; Osaka, I.; Hashizume, D.; Takimiya, K., α-Modified Naphthodithiophene Diimides Molecular Design Strategy for Air-Stable n-Channel Organic Semiconductors. *Chem. Mater.* **2015,** *27* (18), 6418-6425.

39. Kim, Y.; Long, D. X.; Lee, J.; Kim, G.; Shin, T. J.; Nam, K.-W.; Noh, Y.-Y.; Yang, C., A balanced face-on to edge-on texture ratio in naphthalene diimide-based polymers with hybrid siloxane chains directs highly efficient electron transport. *Macromolecules* **2015,** *48* (15), 5179-5187.

40. Fukutomi, Y.; Nakano, M.; Hu, J.-Y.; Osaka, I.; Takimiya, K., Naphthodithiophenediimide (NDTI): synthesis, structure, and applications. *J. Am. Chem. Soc.* **2013,** *135* (31), 11445-11448.

41. Fan, W.; Liu, C.; Li, Y.; Wang, Z., Fluoroalkyl-modified naphthodithiophene diimides.

Chem. Commun. **2017,** *53* (1), 188-191.

42. Chan, S.-H.; Chen, C.-P.; Chao, T.-C.; Ting, C.; Lin, C.-S.; Ko, B.-T., Synthesis, characterization, and photovoltaic properties of novel semiconducting polymers with thiophene− phenylene− thiophene (TPT) as coplanar units. *Macromolecules* **2008,** *41* (15), 5519-5526.

43. Chen, C.-P.; Chan, S.-H.; Chao, T.-C.; Ting, C.; Ko, B.-T., Low-bandgap poly (thiophene-phenylene-thiophene) derivatives with broaden absorption spectra for use in high-performance bulk-heterojunction polymer solar cells. *J. Am. Chem. Soc.* **2008,** *130* (38), 12828-12833.

44. Chen, Y.-C.; Yu, C.-Y.; Fan, Y.-L.; Hung, L.-I.; Chen, C.-P.; Ting, C., Low-bandgap conjugated polymer for high efficient photovoltaic applications. *Chem. Commun.* **2010,** *46* (35), 6503-6505.

45. Zhang, Y.; Zou, J.; Yip, H.-L.; Chen, K.-S.; Zeigler, D. F.; Sun, Y.; Jen, A. K.-Y., Indacenodithiophene and quinoxaline-based conjugated polymers for highly efficient polymer solar cells. *Chem. Mater.* **2011,** *23* (9), 2289-2291.

46. Sun, Y.; Chien, S.-C.; Yip, H.-L.; Zhang, Y.; Chen, K.-S.; Zeigler, D. F.; Chen, F.-C.; Lin, B.; Jen, A. K.-Y., High-mobility low-bandgap conjugated copolymers based on indacenodithiophene and thiadiazolo [3, 4-c] pyridine units for thin film transistor and photovoltaic applications. *J. Mater. Chem.* **2011,** *21* (35), 13247-13255.

47. Zhu, Z.; Waller, D.; Gaudiana, R.; Morana, M.; Mühlbacher, D.; Scharber, M.; Brabec, C., Panchromatic conjugated polymers containing alternating donor/acceptor units for photovoltaic applications. *Macromolecules* **2007,** *40* (6), 1981-1986.

48. Soci, C.; Hwang, I. W.; Moses, D.; Zhu, Z.; Waller, D.; Gaudiana, R.; Brabec, C. J.; Heeger, A. J., Photoconductivity of a low-bandgap conjugated polymer. *Adv. Funct. Mater.* **2007,** *17* (4), 632-636.

49. Bijleveld, J. C.; Shahid, M.; Gilot, J.; Wienk, M. M.; Janssen, R. A., Copolymers of Cyclopentadithiophene and Electron-Deficient Aromatic Units Designed for Photovoltaic Applications. *Adv. Funct. Mater.* **2009,** *19* (20), 3262-3270.

50. Zhang, M.; Tsao, H. N.; Pisula, W.; Yang, C.; Mishra, A. K.; Müllen, K., Field-effect transistors based on a benzothiadiazole− cyclopentadithiophene copolymer. *J. Am. Chem. Soc.* **2007,** *129* (12), 3472-3473.

51. Yamashita, Y.; Hinkel, F.; Marszalek, T.; Zajaczkowski, W.; Pisula, W.; Baumgarten, M.; Matsui, H.; Müllen, K.; Takeya, J., Mobility exceeding 10 cm2/(V· s) in donor–acceptor polymer transistors with band-like charge transport. *Chem. Mater.* **2016,** *28* (2), 420-424.

52. Hinkel, F.; Marszalek, T.; Zajaczkowski, W.; Puniredd, S. R.; Baumgarten, M.; Pisula, W.; Müllen, K., Tuning Packing and Solubility of Donor (D)–Acceptor (A) Polymers by cis–

trans Isomerization within Alkenyl Side Chains. *Chem. Mater.* **2014,** *26* (16), 4844-4848.

53. Liang, Y.; Feng, D.; Wu, Y.; Tsai, S.-T.; Li, G.; Ray, C.; Yu, L., Highly efficient solar cell polymers developed via fine-tuning of structural and electronic properties. *J. Am. Chem. Soc.* **2009,** *131* (22), 7792-7799.

54. Hou, J.; Chen, H.-Y.; Zhang, S.; Chen, R. I.; Yang, Y.; Wu, Y.; Li, G., Synthesis of a low band gap polymer and its application in highly efficient polymer solar cells. *J. Am. Chem. Soc.* **2009,** *131* (43), 15586-15587.

55. Son, H. J.; Wang, W.; Xu, T.; Liang, Y.; Wu, Y.; Li, G.; Yu, L., Synthesis of fluorinated polythienothiophene-co-benzodithiophenes and effect of fluorination on the photovoltaic properties. *J. Am. Chem. Soc.* **2011,** *133* (6), 1885-1894.

56. Zhou, J.; Zuo, Y.; Wan, X.; Long, G.; Zhang, Q.; Ni, W.; Liu, Y.; Li, Z.; He, G.; Li, C., Solution-processed and high-performance organic solar cells using small molecules with a benzodithiophene unit. *J. Am. Chem. Soc.* **2013,** *135* (23), 8484-8487.

57. Qin, T.; Zajaczkowski, W.; Pisula, W.; Baumgarten, M.; Chen, M.; Gao, M.; Wilson, G.; Easton, C. D.; Müllen, K.; Watkins, S. E., Tailored donor–acceptor polymers with an A–D1–A–D2 structure: controlling intermolecular interactions to enable enhanced polymer photovoltaic devices. *J. Am. Chem. Soc.* **2014,** *136* (16), 6049-6055.

58. Tang, A.; Zhan, C.; Yao, J., Series of quinoidal methyl-dioxocyano-pyridine based π-extended narrow-bandgap oligomers for solution-processed small-molecule organic solar cells. *Chem. Mater.* **2015,** *27* (13), 4719-4730.

59. Tang, C. W., Two-layer organic photovoltaic cell. *Appl. Phys. Lett.* **1986,** *48* (2), 183-185.

60. Jørgensen, M.; Norrman, K.; Krebs, F. C., Stability/degradation of polymer solar cells. *Sol. Energy Mater. Sol. Cells* **2008,** *92* (7), 686-714.

61. Sun, Y.; Seo, J. H.; Takacs, C. J.; Seifter, J.; Heeger, A. J., Inverted polymer solar cells integrated with a low-temperature-annealed sol-gel-derived ZnO film as an electron transport layer. *Adv. Mater.* **2011,** *23* (14), 1679-1683.

62. Hau, S. K.; Yip, H.-L.; Leong, K.; Jen, A. K.-Y., Spraycoating of silver nanoparticle electrodes for inverted polymer solar cells. *Org. Electron.* **2009,** *10* (4), 719-723.

63. Kim, G.; Yeom, H. R.; Cho, S.; Seo, J. H.; Kim, J. Y.; Yang, C., Easily attainable phenothiazine-based polymers for polymer solar cells: advantage of insertion of S, S-dioxides into its polymer for inverted structure solar cells. *Macromolecules* **2012,** *45* (4), 1847-1857.

64. Nunzi, J.-M., Organic photovoltaic materials and devices. *Comptes Rendus Physique* **2002,** *3* (4), 523-542.

65. Saunders, B. R.; Turner, M. L. J. A. i. c.; science, i., Nanoparticle–polymer photovoltaic cells.

Adv. Colloid Interface Sci. **2008,** *138* (1), 1-23.

66. Heremans, P.; Cheyns, D.; Rand, B. P., Strategies for increasing the efficiency of heterojunction organic solar cells: material selection and device architecture. *Acc. Chem. Res.* **2009,** *42* (11), 1740-1747.

67. Ameri, T.; Dennler, G.; Lungenschmied, C.; Brabec, C. J., Organic tandem solar cells: A review. *Energy Environ. Sci.* **2009,** *2* (4), 347-363.

68. van Duren, J. K.; Yang, X.; Loos, J.; Bulle-Lieuwma, C. W.; Sieval, A. B.; Hummelen, J. C.; Janssen, R. A., Relating the morphology of poly (p-phenylene vinylene)/methanofullerene blends to solar-cell performance. *Adv. Funct. Mater.* **2004,** *14* (5), 425-434.

69. Hoppe, H.; Glatzel, T.; Niggemann, M.; Schwinger, W.; Schaeffler, F.; Hinsch, A.; Lux-Steiner, M. C.; Sariciftci, N., Efficiency limiting morphological factors of MDMO-PPV: PCBM plastic solar cells. *Thin Solid Films* **2006,** *511*, 587-592.

70. Hoppe, H.; Niggemann, M.; Winder, C.; Kraut, J.; Hiesgen, R.; Hinsch, A.; Meissner, D.; Sariciftci, N. S., Nanoscale morphology of conjugated polymer/fullerene-based bulk-heterojunction solar cells. *Adv. Funct. Mater.* **2004,** *14* (10), 1005-1011.

71. Gebeyehu, D.; Brabec, C.; Padinger, F.; Fromherz, T.; Hummelen, J.; Badt, D.; Schindler, H.; Sariciftci, N., The interplay of efficiency and morphology in photovoltaic devices based on interpenetrating networks of conjugated polymers with fullerenes. *Syn. Met.* **2001,** *118* (1-3), 1-9.

72. Martens, T.; D'Haen, J.; Munters, T.; Beelen, Z.; Goris, L.; Manca, J.; D'Olieslaeger, M.; Vanderzande, D.; De Schepper, L.; Andriessen, R., Disclosure of the nanostructure of MDMO-PPV: PCBM bulk hetero-junction organic solar cells by a combination of SPM and TEM. *Syn. Met.* **2003,** *138* (1-2), 243-247.

73. Brabec, C. J.; Cravino, A.; Meissner, D.; Sariciftci, N. S.; Fromherz, T.; Rispens, M. T.; Sanchez, L.; Hummelen, J. C., Origin of the open circuit voltage of plastic solar cells. *Adv. Funct. Mater.* **2001,** *11* (5), 374-380.

74. Scharber, M. C.; Mühlbacher, D.; Koppe, M.; Denk, P.; Waldauf, C.; Heeger, A. J.; Brabec, C. J., Design rules for donors in bulk-heterojunction solar cells—Towards 10% energy-conversion efficiency. *Adv. Mater.* **2006,** *18* (6), 789-794.

75. Riedel, I.; Dyakonov, V., Influence of electronic transport properties of polymer-fullerene blends on the performance of bulk heterojunction photovoltaic devices. *Phys. Status Solidi A* **2004,** *201* (6), 1332-1341.

76. Schilinsky, P.; Waldauf, C.; Hauch, J.; Brabec, C. J., Simulation of light intensity dependent current characteristics of polymer solar cells. *J. Appl. Phys.* **2004,** *95* (5), 2816-2819.

77. Tsumura, A.; Koezuka, H.; Ando, T., Macromolecular electronic device: Field-effect

transistor with a polythiophene thin film. *Appl. Phys. Lett.* **1986,** *49* (18), 1210-1212.

78. Newman, C. R.; Frisbie, C. D.; da Silva Filho, D. A.; Brédas, J.-L.; Ewbank, P. C.; Mann, K. R., Introduction to organic thin film transistors and design of n-channel organic semiconductors. *Chem. Mater.* **2004,** *16* (23), 4436-4451.

79. Guo, X.; Facchetti, A.; Marks, T. J., Imide-and amide-functionalized polymer semiconductors. *Chem. Rev.* **2014,** *114* (18), 8943-9021.

80. Hassan, J.; Sevignon, M.; Gozzi, C.; Schulz, E.; Lemaire, M., Aryl− aryl bond formation one century after the discovery of the Ullmann reaction. *Chem. Rev.* **2002,** *102* (5), 1359-1470.

Chapter 2. TBIG based backbone modification with random polymerization

Chapter 2 is reproduced in part with permission of "Controlling the ambipolarity of thieno-benzo-isoindigo polymer-based transistors: the balance of face-on and edge-on populations" from J. Lee *et al. J. Mater. Chem. C*, **2019**, DOI: 10.1039/c9tc05641f.

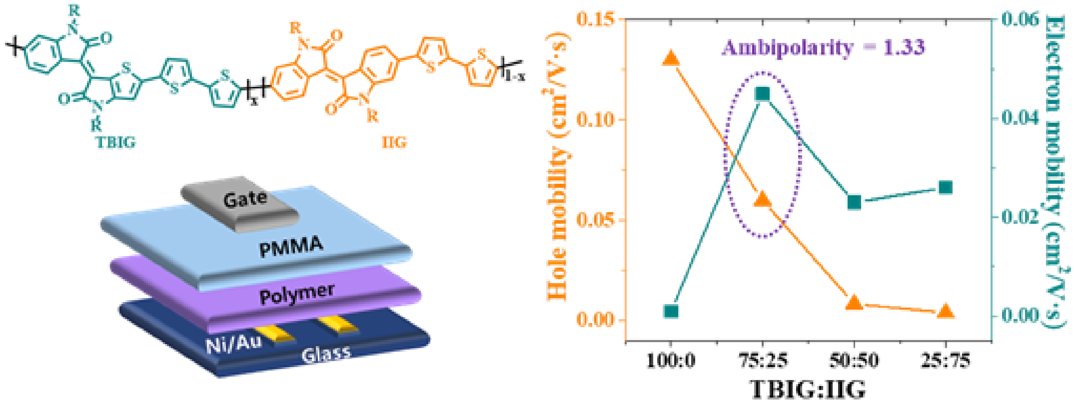

2.1 Introduction

Organic field-effect transistors (OFETs) based on π-conjugated polymers are of particular interest as the basic elements for circuits used in flexible active-matrix displays, radio frequency identification (RFID) tags, electronic papers, and other printed electronic devices.[1-6] With current rapid progress in the development of state-of-the-art π-conjugated polymers, high-performance p-channel, n-channel, and even ambipolar OFETs with excellent mobility and stability have been reported.[7-11] Many studies demonstrate that appropriate connection of donor-acceptor moieties is a viable approach to create high-performance polymers in OFETs by taking advantage of intermolecular donor and acceptor interactions that are preferable for charge carrier transport through intermolecular hopping mechanism.[12] The incorporation of 'symmetric' dyes with polar cyclic amide and diimide structures, such as diketopyrrolopyrrole (DPP),[13-17] isoindigo (IIG),[8, 18-22] and thienoisoindigo (TIG),[10, 23-25] naphthalenediimide (NDI),[26-30] and perylenediimides (PDI)[31-34] have been established as a very effective way to combine strong accepting properties with a tendency to provide close intermolecular packing through dipolar interactions. Such dyes-containing successful polymers have been reported, showing impressive hole and electron OFET mobilities and even excellent ambipolar behaviors.[7-10]

Very recently, Fréchet and co-workers reported the synthesis of a brand-new thieno-benzo-isoindigo (TBIG) dye in which one single phenyl ring of IIG is replaced with thiophene, and its-containing polymers.[25] Similar to the aforementioned dyes, the TBIG is a polar cyclic amide structure as a thiophene analogue of IIG, yet 'asymmetric' unit, and combines the dual properties of IIG and TIG. Despite having such unique structure features, up to now, TBIG-based polymers have been very little reported for use in optoelectronic devices.[25, 35-38]

The present article describes the synthesis and characterization as well as OFET characteristics of a collection of TBIG-based polymers (PTBIG-100, PTBIG-75, PTBIG-50, and PTBIG-25) with varied compositions between TBIG and IIG accepting segments and bithiophene counterpart donor. We found that the essential properties including not only absorptions, aggregation type, frontier energy levels, morphology, and molecular orientation but also the carrier mobility and dominant polarity in OFETs to be strongly related to the loading ratios of TBIG and IIG. Concretely, PTBIG-100 film (no IIG unit) has a large propensity to form J-aggregate and face-on orientation, showing the highest hole mobility of up to 0.13 cm^2/V·s but rather low electron mobility, whereas introduction of IIG into the backbone leads to the favourable H-aggregate and increased edge-on population and electron mobility. Besides, it is worthy to note that PTBIG-75 has an almost half-and-half ratio of the face-on and edge-on orientations, affording the highly balanced hole and electron mobilities ($\mu_{\mathrm{FET,\ h}}$ = 0.06 cm^2/V·s and $\mu_{\mathrm{FET,\ e}}$ 0.045 cm^2/V·s). Overall, these results reveal that the degree of face-on and edge-on orientation can highly contribute to the dominant polarity and balanced ambipolar nature of the conjugated polymers.

2.2 Result and discussion

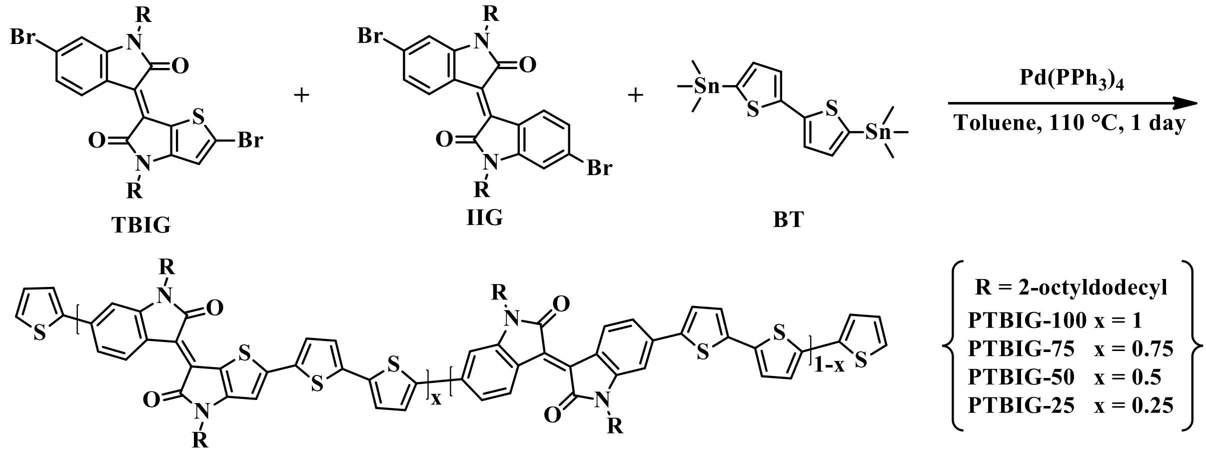

Scheme 2.1. Synthetic scheme of TBIG-based polymers.

Two dibrominated TBIG and IIG monomers were prepared according to the previous literature.[25] As shown in **Scheme 2.1**, all the polymers were prepared via Stille coupling by using the catalyst Pd(PPh$_3$)$_4$ with bis(trimethylstannyl)bithiophene (BT) as a counterpart donor co-monomer in toluene for 1 day. To investigate the relationship between the composition and properties of the resulting polymers, the feed ratios of TBIG to IIG in the polymer backbone are varied as 100%, 75%, 50%, 25%, denoted as PTBIG-100, PTBIG-75, PTBIG-50, and PTBIG-25. All the polymers were purified via sequential Soxhlet extraction using methanol, acetone, and *n*-hexane to remove the oligomers and other impurities. Then, the chloroform was employed to elute the refined polymers and re-precipitation into methanol, yielded the desired products. The more detailed polymerization procedures and characterizations are described in the Experimental Section. The average molecular weights (M_n) and polydispersity index (PDI) were determined using high-temperature gel-permeation chromatography (HT-GPC) at 100 °C with 1,2,4-trichlorobenzene as the eluent. PTBIG-100, PTBIG-75, PTBIG-50, and PTBIG-25 revealed M_n of 18.6, 18.0, 29.8, and 26.4 kDa, respectively with narrow PDI values of 1.81 – 2.45. All the polymers have high solubility in common organic solvents such as chloroform and chlorobenzene.

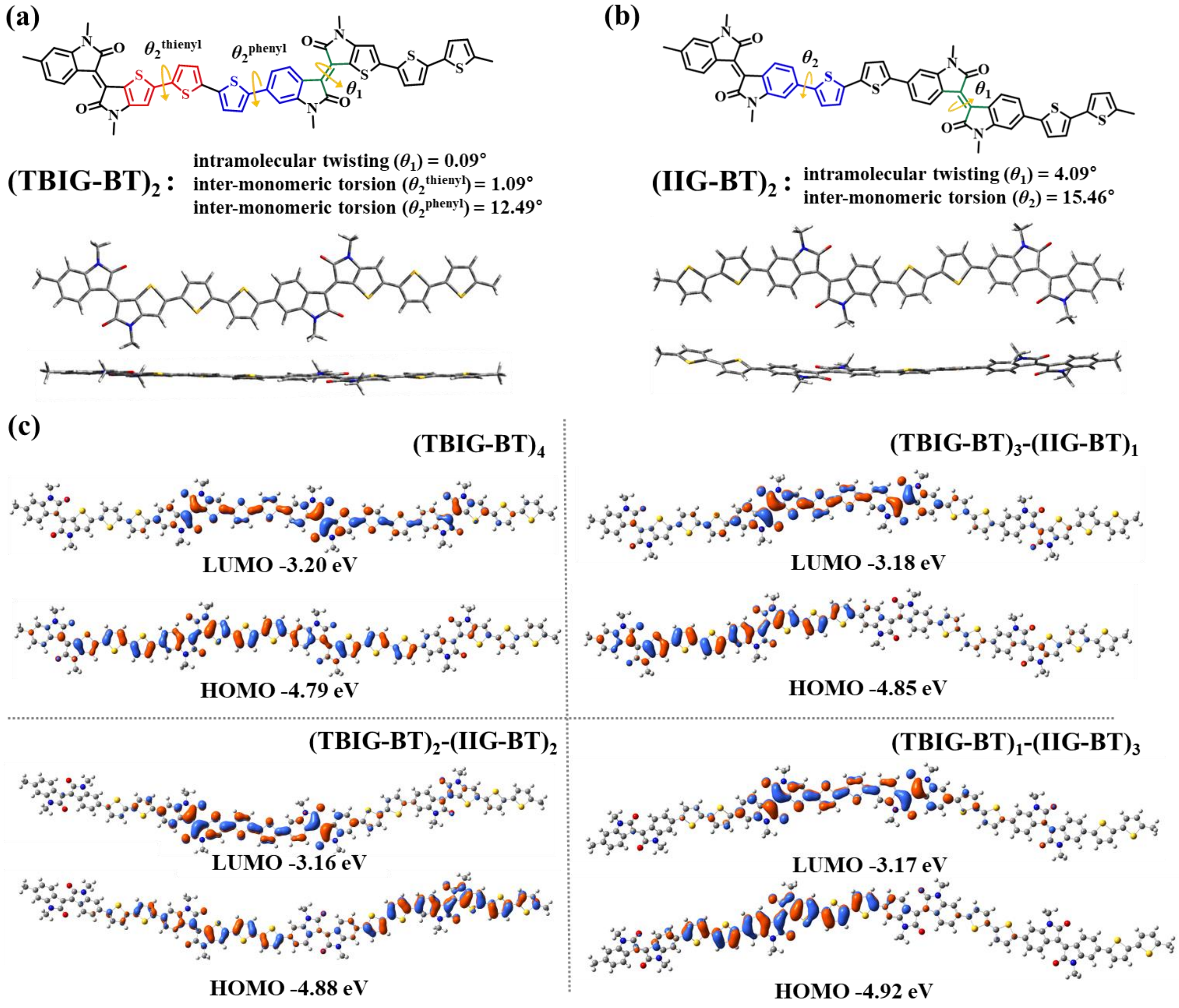

Figure 2.1. The intramolecular twisting and inter-monomeric torsion angles with front/side geometries from the DFT calculations at the B3LYP/6-31G* level based on (a) (TBIG-BT)$_2$ and (b) (IIG-BT)$_2$; (c) Optimized molecular geometries of tetramers of TBIG and IIG segments with calculated LUMOs and HOMOs of (TBIG-BT)$_4$, (TBIG-BT)$_3$-(IIG-BT)$_1$, (TBIG-BT)$_2$-(IIG-BT)$_2$, and (TBIG-BT)$_1$-(IIG-BT)$_3$.

To simulate the geometry-optimized structures, density functional theory (DFT) calculations for two models with alternative sequence ((TBIG-BT)$_2$ and (IIG-BT)$_2$) were performed using Gaussian 09 using a hybrid B3LYP correlation functional and 6-31G* basis set (**Figure 2.1a** and **2.1b**), where the methyl groups were used instead of 2-octyldodecyl chains to reduce the computational time. For (IIG-BT)$_2$, the intramolecular twisting angle (θ_1) within IIG segment and inter-monomeric torsion angle (θ_2) between IIG and BT subunits is 4.09° and 15.46°, respectively, while the much smaller dihedral angels (θ_1 = 0.09° and $\theta_2^{thienyl}$ and θ_2^{pheyl} = 1.09° and 12.49°) were observed in (TBIG-BT)$_2$. Note that in the case of (TBIG-BT)$_2$, the presence of two inter-monomeric torsion angles is a result of the asymmetric structure of TBIT; $\theta_2^{thienyl}$ and θ_2^{pheyl} are the torsion angles between thienyl and phenyl substitutions of TBIG and BT, respectively. These results suggest that the backbone co-planarity of the synthesized polymers can be increased with increasing the TBIG content, expecting the benefits on OFET performance (*i.e.*, tight molecular packing and extended effective conjugation length).

In addition, to explore the electron density distributions and energy levels as a function of different ratios of TBIG and IIG units in the polymer backbone, we also carried out the DFT calculations of the tetrameric models ((TBIG-BT)$_4$, (TBIG-BT)$_3$-(IIG-BT)$_1$, (TBIG-BT)$_2$-(IIG-BT)$_2$, and (TBIG-BT)$_1$-(IIG-BT)$_3$ (see **Figure 2.1c**). HOMO/LUMO energies of (TBIG-BT)$_4$, (TBIG-BT)$_3$-(IIG-BT)$_1$, (TBIG-BT)$_2$-(IIG-BT)$_2$, and (TBIG-BT)$_1$-(IIG-BT)$_3$ were calculated to be -4.79/-3.20, -4.85/-3.18, -4.88/-3.16, and -4.92/-3.17 eV, respectively. Notably, it is apparent that the electron densities of HOMO and LUMO are more delocalized along the entire conjugated backbones with increasing TBIG-BT fractions, which is beneficial for charge carrier transport.

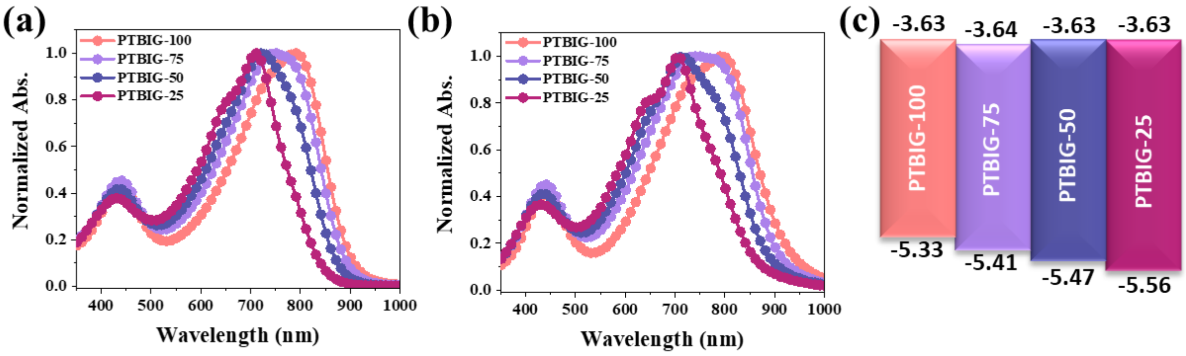

Figure 2.2. UV-vis absorption spectra of TBIG-based polymers (a) in dilute chloroform solution and (b) in films; (c) Molecular energy level diagrams of the materials in this work.

Table 2.1 Optical properties of TBIG-based polymers.

	$\lambda_{max}^{sol.}$ [nm]	λ_{max}^{film} [nm]	λ_{onset} [nm]	E_g^{opt} [eV]
PTBIG-100	**790**	**798**	**931**	**1.33**
PTBIG-75	**750**	**742**	**904**	**1.37**
PTBIG-50	**722**	**716**	**886**	**1.40**
PTBIG-25	**712**	**706**	**862**	**1.44**

To investigate the optical properties of the TBIG-based polymers, UV-vis absorption spectra were measured in dilute chloroform solution (**Figure 2.2a**) and films (**Figure 2.2b**), and relevant data are collected in **Table 2.1**. All the absorption spectra of TBIG-based polymers exhibited two distinctive absorption bands between 350–500 nm and 600–900 nm; the former one is known as π-π^* transitions and the latter one is the intramolecular charge transfer (ICT) between D and A segments. Increasing the TBIG concentration results in a gradual red shift of the absorption maximum (λ_{max}) of the ICT band, indicating the higher backbone co-planarity of TBIG relative to IIG, which is well-consistent with the DFT calculations above.

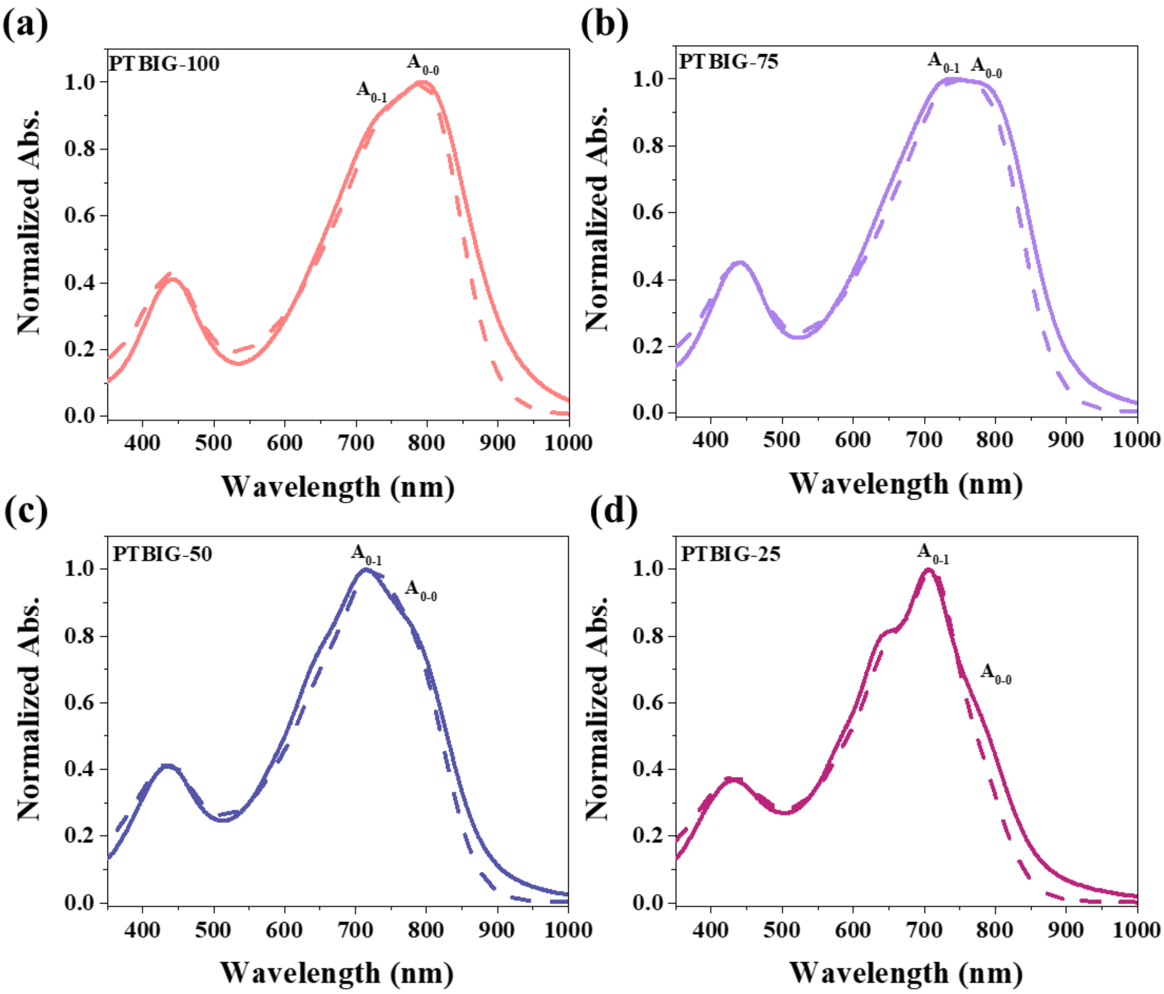

Figure 2.3. Normalized absorption spectra of (a) PTBIG-100, (b) PTBIG-75, (c) PTBIG-50, and (d) PTBIG-25 in chloroform solution (dashed line) and thin films (continuous line).

In addition, it should be interestingly to note that from solution to solid-state, the PTBIG-100 polymer with alternating sequence shows a slightly red shift (8 nm), while the others with random sequence present somewhat blue shifts (6 – 8 nm), being attributed to two different packing motifs with predominant with J- and H-aggregates in solid states, respectively.[16, 39] **Figure 2.3** shows the distinct A_{0-0} and A_{0-1} vibronic peaks of each TBIG-based polymer and the A_{0-0}/A_{0-1} ratios are dependent on the aggregate types. PTBIG-100 exhibits the A_{0-0}/A_{0-1} ratio larger than unity, implying the predominant J-type aggregation, while the others show the A_{0-0}/A_{0-1} smaller than unity, mainly forming the H-type aggregation.[40] One can conclude that the composition and sequence of monomer building blocks can play a crucial role in determining the aggregate types. The optical bandgaps (E_g^{opt}) of the polymers were estimated from the onset of the ICT bands in the films, providing the following trend: PTBIG-100 (1.33 eV) < PTBIG-75 (1.37 eV) < PTBIG-50 (1.40 eV) < PTBIG-25 (1.44 eV).

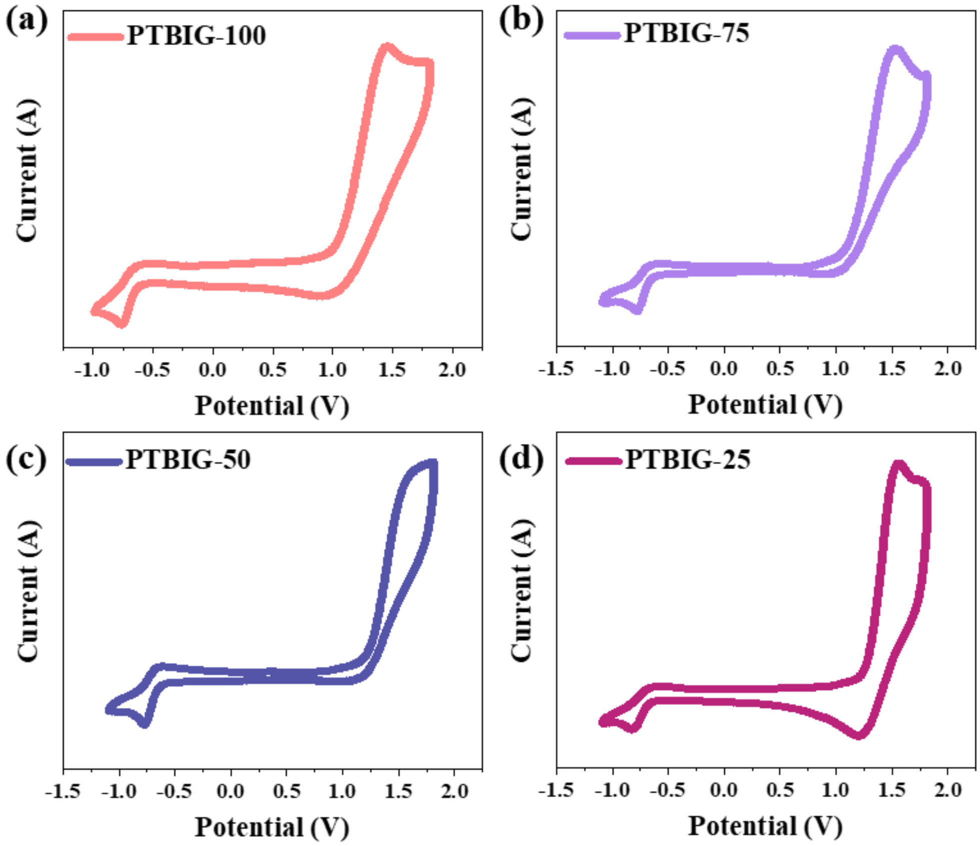

Figure 2.4. Cyclic voltammograms of (a) PTBIG-100, (b) PTBIG-75, (c) PTBIG-50, and (d) PTBIG-25.

The electrochemical behaviours and electronic energy levels of the polymers were investigated by cyclic voltammetry (CV) (**Figure 2.4**). The polymer films were coated on a platinum working electrode, and their CV diagrams were recorded in an acetonitrile solution containing 0.1 M n-Bu_4NPF_6 under an inert atmosphere versus the Ag/Ag^+ redox couple. The HOMO and LUMO energy levels of polymers were obtained from the equation E_{HOMO} (eV) = $-(E_{(ox)}^{onset} - E_{(ferrocene)}^{onset} + 4.8)$ and E_{LUMO} (eV) = $-(E_{(red)}^{onset} - E_{(ferrocene)}^{onset} + 4.8)$, respectively. The estimated HOMO/LUMO energy levels of the polymers are depicted as energy level diagrams in **Figure 2.2c** It is apparent that although composition variations of TBIG and IIG subunits have little impact on LUMO values of the polymers, the HOMO values rise gradually with increasing TBIG portion, resulting from the increased electron donating characteristics and co-planarity when phenyl rings in IIG are replaced by more electron-rich and less sterically demanding thiophene unit in TBIG.[25] The electrochemical bandgaps (E_g^{CV}s) gathered from CV measurements are in good agreement with the E_g^{opt}s' trends discussed above.

The top-gate/bottom-contact configuration of OFETs was made by the TBIG-based polymers, with pre-patterned Au/Ni electrodes and PMMA dielectric layer was deposited by spin-coating onto the active layer. All the OFET devices were annealed at the optimized temperature of 250 °C for 30 min. The more detailed fabrication processes are provided in the **Experimental Section**. The representative transfer curves of OFETs based on the series of TBIG-based polymers for p-type and n-type operations were shown in **Figure 2.5a** and **Figure 2.5b** respectively. All the device parameters extracted from the saturation regime (V_D= - 80 V) are summarized in **Table 2.2**. The modulation of charge transport characteristics occurred in accordance with the increased portion of the IIG segment in the polymer backbone. The OFET performed with PTBIG-100 showed the highest hole mobility ($\mu_{FET,\,h}$) up to 0.13 $cm^2/V \cdot s$, whereas the electron mobility ($\mu_{FET,\,e}$) exhibited rather worse OFET performance with 0.009 $cm^2/V \cdot s$. Very interestingly, incorporating IIG unit into the backbone caused the dramatical enhancement of the electron mobilities, accompanied with decreased hole mobilities. As a result, PTBIG-50 and PTBIG-25 showed the inversed dominant polarity (*i.g.*, n-channel dominant OFETs) with the significantly improved electron mobilities of 0.023 $cm^2/V \cdot s$ and 0.026 $cm^2/V \cdot s$ compared to PTBIG-100, respectively. In the meantime, PTBIG-75 achieved the most balanced ambipolar mobilities ($\mu_{FET,\,h}$ = 0.06 $cm^2/V \cdot s$ and $\mu_{FET,\,e}$ 0.045 $cm^2/V \cdot s$) with ambipolarity ($\mu_{FET,\,h}/\mu_{FET,\,e}$) up to 1.33.

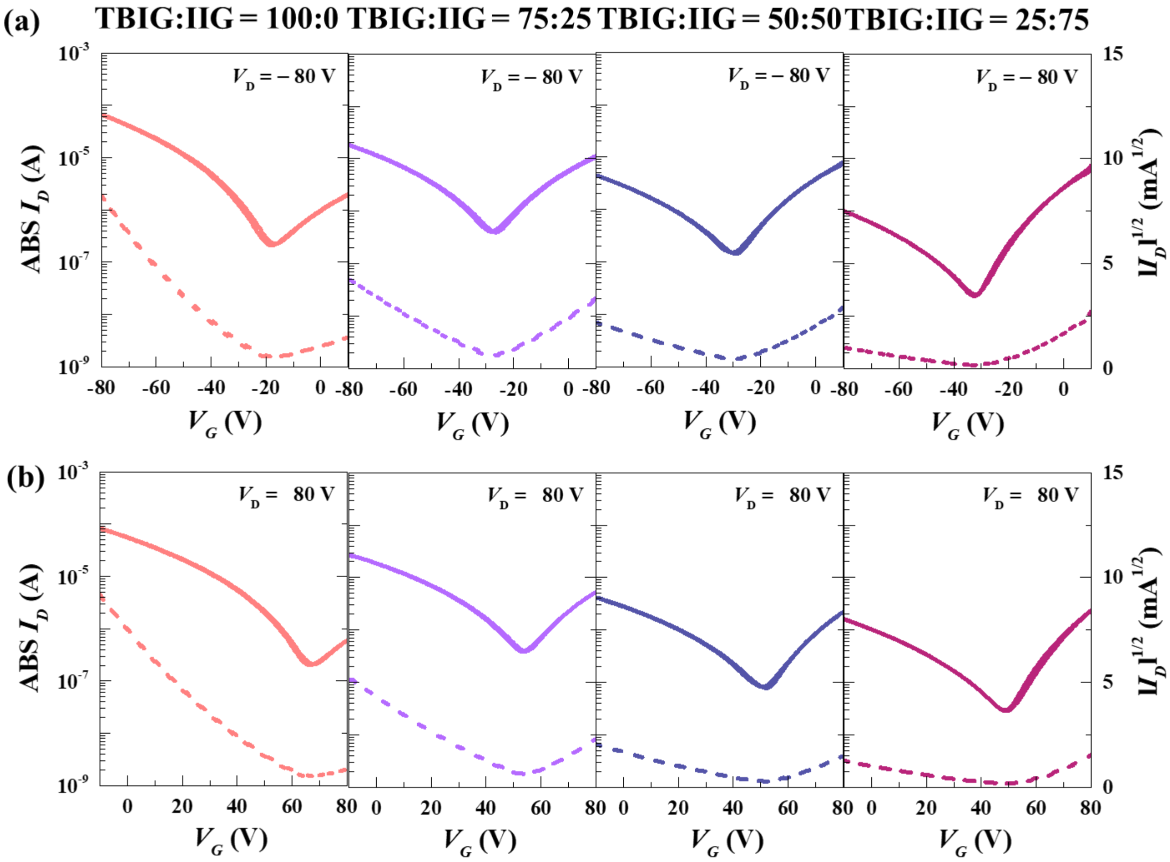

Figure 2.5. Transfer characteristics of (a) p- type and (b) n-type for TBIG:IIG ratio of 100:0, 75:25, 50:50, and 25:75 in OFETs.

Table 2.2 Summary of parameters for PTBIG-based OFETs.

Polymer	$\mu_{\mathrm{FET,h}}$ [cm^2/V·s]	$\mu_{\mathrm{FET,h}}$ [cm^2/V·s]	Ambipolarity [$\mu_{\mathrm{FET,h}}$/ $\mu_{\mathrm{FET,e}}$]	$V_{T,\mathrm{h}}$ [V]	$V_{T,\mathrm{e}}$ [V]	Rc·W$_\mathrm{h}$ [MΩ·cm]	Rc· W$_\mathrm{e}$ [MΩ·cm]	EA [meV]
PTBIG-100	0.13 ± 0.05	0.009 ± 0.002	14.44	47.8	50.0	0.36	762	115.05
PTBIG-75	0.06 ± 0.02	0.045 ± 0.010	1.33	35.5	55.8	0.58	147	122.20
PTBIG-50	0.008 ± 0.003	0.023 ± 0.007	0.35	30.5	52.8	5.1	257	173.12
PTBIG-25	0.004 ± 0.001	0.026 ± 0.005	0.015	28.4	52.3	41.6	550	192.60

For the investigation of the device stability, the bias stress and air stability were measured for TBIG-based OFETs in p-type characteristics (**Figure 2.6a and 2.6b**). The drain current versus function of time depending on the TBIG/IIG ratio shows dramatically degradation of drain current in bias stress. The contact resistance (R_C) between the S/D electrodes and the TBIG-based polymer films can be evaluated by the output characteristics in the linear regime and Y-function method (**Figure 2.7**).[41, 42] As the ratio of IIG segment increases, the $R_{C,h}$ is increased by 100 times from 0.36 MΩ·cm of PTBIG-100 to 41.6 MΩ·cm of PTBIG-25, and the lowest $R_{C,h}$ value of PTBIG-100 is one of the clear reasons for the highest hole mobility in OFETs. These results are consistent with the correlation between the energy level of the gold electrode and the HOMO levels according to the ratio change of TBIG and IIG.

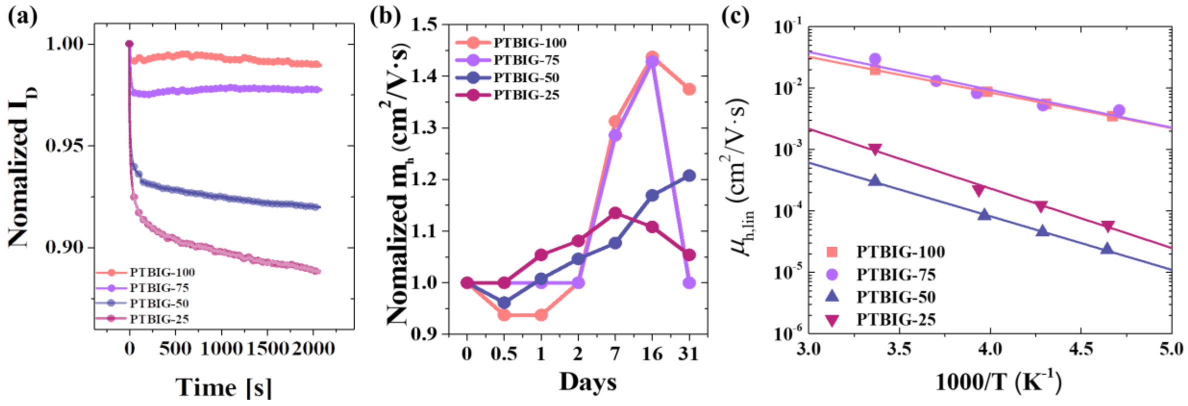

Figure 2.6. (a) Normalized bias stability and (b) air stability of TBIG-based polymers OFETs; (c) Field-effect mobility in the linear regime versus temperature of PTBIG- based polymers.

To obtain more understanding of the effects on charge transport, we performed low- temperature measurements based on all series of TBIG-based polymers OFETs. Because the charge carrier mobilities of conjugated polymers occurred through thermally activated hopping in the localized state, thus the activation energy (E_A) can be calculated as follows:

$$\mu(T) = \mu' \exp\left(-\frac{E_A}{k_B T}\right)$$

where μ' is the charge carrier mobility in the trap-free states, k_B is the Boltzmann constant, and T is the absolute temperature.[43] **Figure 2.6c** shows the temperature dependence of the linear mobility (μ_{lin}) of TBIG-based polymers OFETs. According to the ratio of TBIG:IIG segment in the resulting polymer, the activation energy is clearly different, which means that the structure of the acceptor segments (e.g., IIG and TBIG) has a great influence on the activation energy. The lower activation energy can allow to let the effective hopping transfer between localized site in films, thus the lowest activation energy of 115.05 meV of PTBIG-100 is a good agreement with the highest hole mobility performance. In addition, in comparison with PTBIG-50 and PTBIG-25, the PTBIG-75 is of almost similar activation energy (~122.20 meV), which demonstrates the decent trade-off from marginally sacrificial hole mobility resulting in the most balanced ambipolarity.

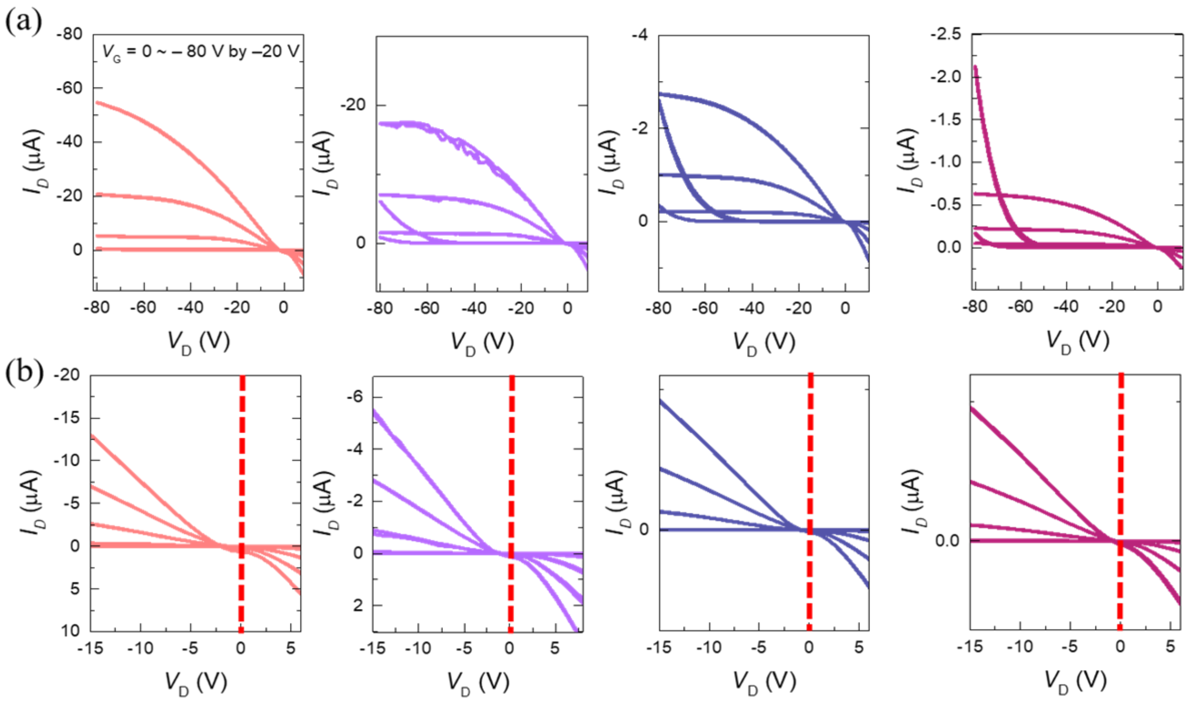

Figure 2.7. (a) Output characteristics for TBIG:IIG OFETs with 100:0, 75:25, 50:50, and 25:75; (b) Enlarged figure of output curves in linear regime.

To investigate the molecular ordering and crystalline property of the TBIG-based polymers, the atomic force microscope (AFM) and 2D-grazing incidence X-ray diffraction (2D-GIXD) were carried out. The AFM images with phase mode were measured to confirm surface morphologies for films with all ratio of TBIG:IIG. All the films showed smooth surfaces, but the root means square roughness of films is increased a little bit as increasing IIG segment from 0.47 nm to 0.81 nm (**Figure 2.8**).

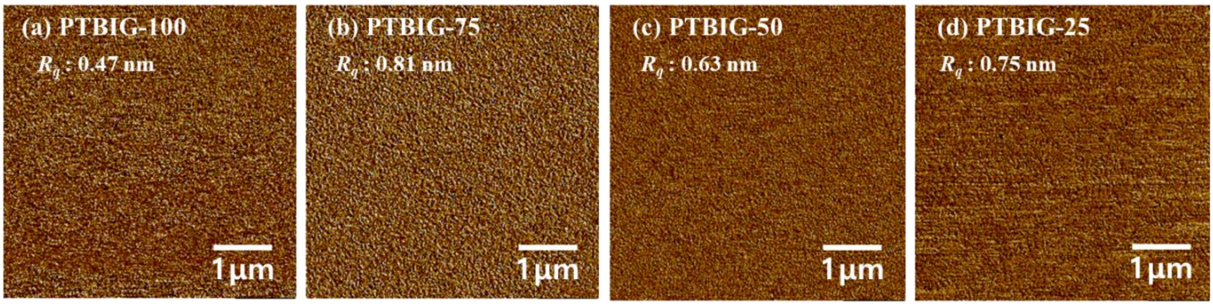

Figure 2.8. The AFM height images of (a) PTBIG-100, (b) PTBIG-75, (c) PTBIG-50, and (d) PTBIG-25.

Figure 2.9a and **Figure 2.10** shows 2D-GIXD patterns and 1D-profiles polymer films based-on PTBIG series with thermal annealing treatment for 10 minutes at 250 °C. All the PTBIG series show the similar diffraction peaks along the out-of-plane and in-plane direction, as well as the similar lamella *d*-spacing distances and π-π stacking distances. The lamella *d*-spacing distances are calculated from the (100) peak at $q \approx 0.29$ Å^{-1} in out of plane as 22.2 Å, and the π-π stacking distances are derived from the (010) peak at $q \approx 1.67$ Å^{-1} in out of plane as 3.76 Å. Interestingly, the strong (010) diffraction peak in out of plane observed from PTBIG-100 gradually faded with growing the portion of IIG segment in the polymer backbone. On the contrary to this, the lamellar (*h*00) peaks in out of plane are vivid steadily with IIG segment climb against the TBIG segment. From these results, we can expect the changes of crystallinity structure from strong face-on orientation to edge-on dominant textures as the increasing ratio of IIG segment.

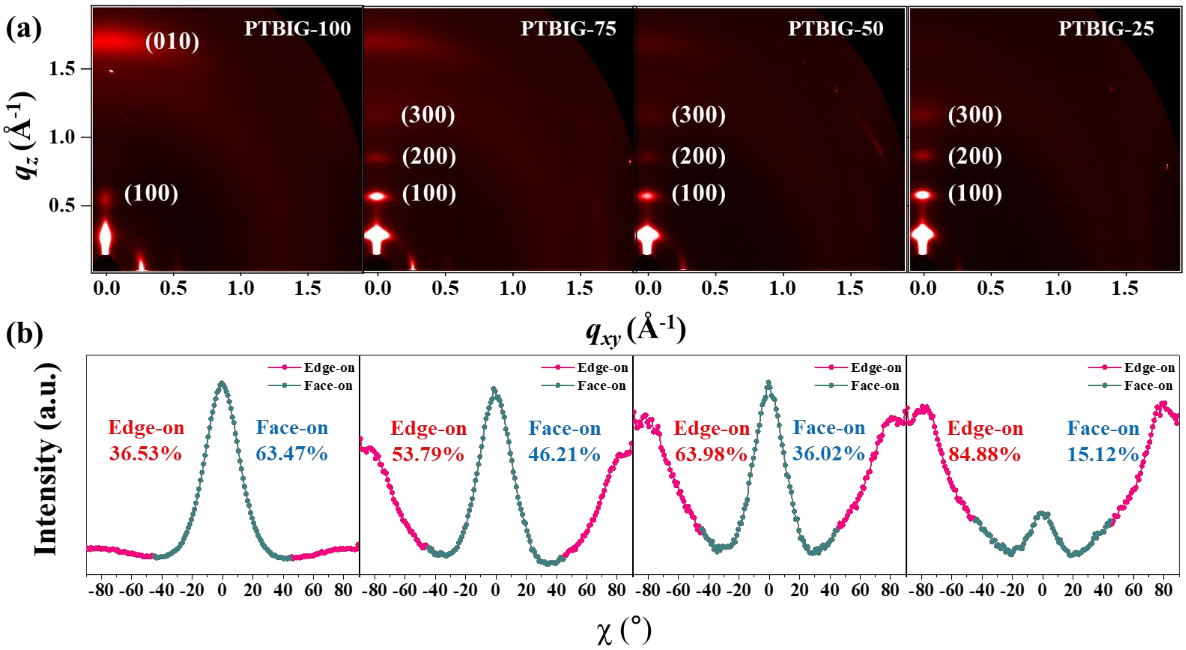

Figure 2.9. (a) 2D-GIXD image of TBIG-based polymers films; (b) Pole figure extracted from (010) diffraction peaks of PTBIG-based polymers films.

Intensity-corrected pole figure plot on the (010) diffraction peaks is used to investigated crystallite orientation distribution in **Figure 2.9b**. The area can be divided by $\chi = 0° \pm 45°$ and $\chi = \pm 45° \pm 90°$ to calculated quantitatively face-on and edge-on crystallinity structure, respectively. The PTBIG-100 clearly show the face-on dominant distribution (face-on: 63.47% and edge-on: 36.53%), but the PTBIG-50 and PTBIG-25 exhibit the edge-on dominant distribution. On the other hand, the PTBIG-75 film is of almost half-and-half of face-on and edge-on packing orientations, which might make a room for the three-dimensional charge conduction channel for electron and hole resulting most balanced ambipolarity in OFET performances. These findings suggest that the polymer chain orientation plays a crucial role in determining the balanced ambipolarity of polymers.

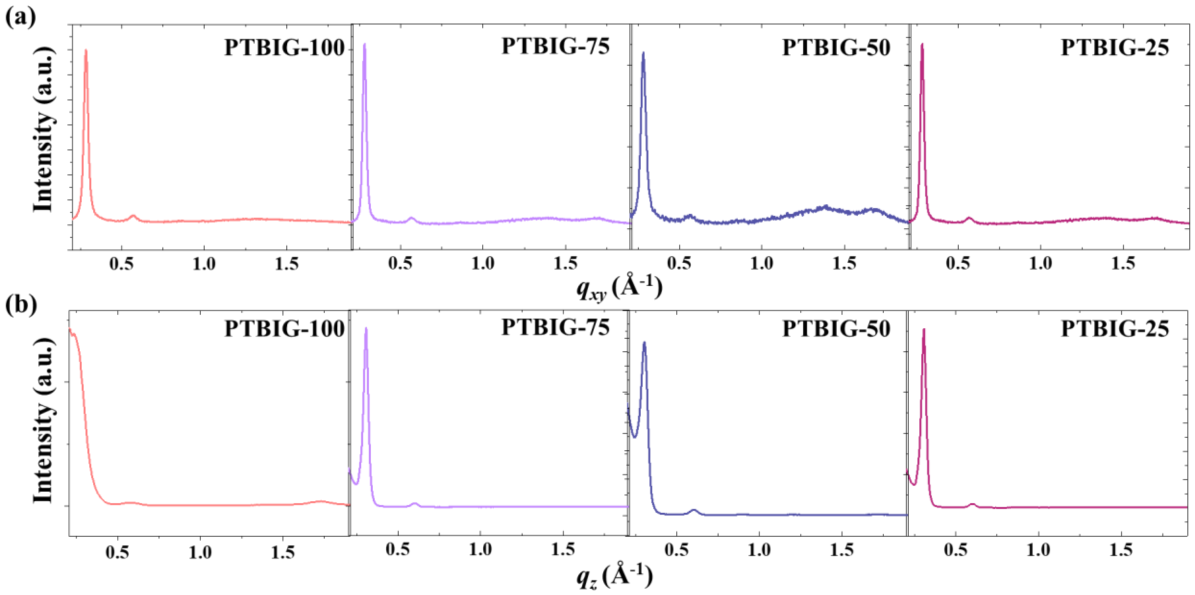

Figure 2.10.1-D profile for TBIG-based polymers films (a) in plane and (b) out of plane.

2.3 Conclusion

In summary, we have synthesized and characterized a series of TBIG-based polymers (PTBIG-100, PTBIG-75, PTBIG-50, and PTBIG-25) composed of different feed ratios between TBIG and IIG accepting segments and bithiophene counterpart donating unit. The resultant polymers with higher TBIG contents exhibit increased backbone co-planarity, red-shifted absorptions, and higher-lying HOMO levels. Besides, in the solid state, IIG-containing polymers have a propensity to form H-aggregate, while J-aggregation is more dominant in PTBIG-100 polymer (no IIG unit). The 2D-GIXD pattern images and intensity-corrected pole figure plot elucidate striking changes of dominant packing orientation from face-on to edge-on depending on the composition between TBIG and IIG units; the edge-on crystallite populations relative to face-on ones are in order of PTBIG-100 < PTBIG-75 < PTBIG-50 < PTBIG-25. In OFET tests, all the polymers display ambipolar behaviors; PTBIG-100 with a higher face-on alignment shows a best hole mobility of 0.13 cm^{2}/V·s yet rather low electron mobility, while PTBIG-25 with a higher edge-on alignment displays a best electron mobility of 0.026 cm^{2}/V·s yet the reduced hole mobility. More interestingly, we find that the PTBIG-75 with adopting almost half-and-half of face-on and edge-on packing orientations shows the highly balanced hole and electron mobility ($\mu_{\mathrm{FET,\,h}} = 0.06$ cm^{2}/V·s and $\mu_{\mathrm{FET,\,e}}$ 0.045 cm^{2}/V·s). Consequently, these findings provide relevant study subjects for establishing a correlation between molecular orientation and ambipolar device performance.

2.4 Experimental section

Materials and Characterization

All starting materials were purchased from Aldrich and Acros and used without further purification. All solvents are of ACS grade unless otherwise noted. ^{1}H NMR and ^{13}C NMR spectra were recorded on a VNMRS 400 MHz spectrophotometer using $CDCl_3$ as solvent and tetramethylsilane (TMS) as the internal standard. UV-vis spectra were recorded on a Cary 5000 (Varian USA) spectrophotometer. The optical bandgaps were estimated from absorption onset of the as-cast thin films. Number-average (M_n) and weight average (M_w) molecular weights, and polydispersity index (PDI) of the polymer products were determined by gel permeation chromatography (GPC) with Waters 150C GPC using a series of mono disperse polystyrene as standards in 1,2,4-trichlorobenzene (HPLC grade) at 100 °C. Cyclic voltammetry (CV) measurements were performed on Solartron electrochemical station (METEK, Versa STAT3) with a three-electrode cell in a 0.1 M tetra-*n*-butylammonium hexafluorophosphate (n-Bu_4NPF_6) solution in acetonitrile at a scan rate of 100 mV s^{-1} at room temperature under argon. An Ag/Ag^+ electrode, a platinum wire, and a platinum electrode were used as the reference electrode, counter electrode, and working electrode, respectively. The Ag/Ag^+ reference electrode was calibrated using a ferrocene/ferrocenium redox couple as an external standard, whose oxidation potential is set at 4.8 eV with respect to a zero vacuum level. The HOMO energy levels were obtained from the equation HOMO (eV) = $-(E_{(ox)}^{onset} - E_{(ferrocene)}^{onset} + 4.8)$. The LUMO levels of polymers were obtained from the equation LUMO (eV) = $-(E_{(red)}^{onset} - E_{(ferrocene)}^{onset} + 4.8)$. The OFETs with top-gate/bottom-contact configuration were fabricated on glass substrates with a prepatterned Au/Ni electrode by using conventional photolithography process. The glass substrates were cleaned by deionized water, acetone and isopropanol solution for 10min in an ultrasonic bath, respectively. The solutions of all PTBIG-100, 75, 50 and 25 were prepared by dichlorobenzene solvent with 5 mg/ml concentration and were spin coated at 2000 rpm for 60 s on substrates. In an N_2-filled glove box, all the coated films were thermally annealed at 250 °C for 30 min. and Polymethylmethacrylate (PMMA, Aldrich, M_w = 120 kDa) polymer in n-butyl acetate with 80 mg/ml was filtered using 0.45 μm polytetrafluoroethylene syringe filter and spin coated on the PTBIG polymer at 2000 rpm for 60 s as a dielectric later in an N_2-filled glove box. After then all samples were thermally annealed at 80 °C for 2 h in same atmosphere. For gate electrode, Al was deposited on the active position with shadow mask using thermal evaporation (~50 nm thick). The electrical characteristics of the OFETs were measured using semiconductor characterization system (Keithley 4200-SCS) in N_2-filled glove box. The field-effect mobility (μ_{FET}) and threshold voltage (V_T) were calculated by equations for classical silicon metal-oxide-semiconductor field-effect transistors in saturation regime. For low temperature measurement system, same system with electrical characteristics and vacuum chamber were used and the liquified nitrogen gas used to reduce temperature. The surface morphology of TBIG:IIG semiconducting polymer were investigated using atomic force microscopy (AFM) with tapping-mode (Nanoscope Ⅲ, Veeco Instruments, Inc.), and 2D-grazing incidence X-ray diffraction (2D-GIXD) performed using 11.17 keV X-rays at Beamline 9A in Pohang Accelerator Laboratory. All films were prepared under the same conditions as the above device fabrication.

Polymerization methods

General Procedure for Polymers by Using Stille Coupling: In a long Schlenk flask, TBIG (a mol), IIG (b mol), and BT (a + b mol) were dissolved in anhydrous toluene (4 mL), and purged with argon for 15 min. Then, $Pd(PPh_3)_4$ (0.02 equiv. of BT) was added and purged again with argon for 10 min. After that, the reaction mixture was stirred at 110 °C for 1 day. Afterward, small amounts of 2-bromothiophene and 2-(trimethylstannyl)thiophene were used as the end-capping agent, respectively. And then, the mixture was cooled down and precipitated to methanol. The precipitated crude product was purified via sequential Soxhlet extraction with methanol, acetone, *n*-hexane, and chloroform. The chloroform fraction was concentrated and precipitated to methanol. The purified polymers were collected by using membrane filter (pore size, 0.45 μm) and dried under high vacuum oven.

Synthesis of PTBIG-100: On basis of the procedure described above, the reference PTBIG-100 polymer was prepared by using TBIG (197 mg, 0.2 mmol) and BT (98.2 mg, 0.2 mmol). Yield = 78.7%. Elemental analysis: anal. calcd C, 75.10; H, 9.16; N, 2.82; S, 9.69. Found: C, 75.19; H, 9.14; N, 2.79; S, 9.67. M_n = 18.6 kDa, M_w = 37.1 kDa, PDI = 1.99.

Synthesis of PTBIG-75: On basis of the procedure described above, the PTBIG-75 polymer was prepared by using TBIG (148 mg, 0.15 mmol), IIG (49.1mg, 0.05 mmol) and BT (98.2 mg, 0.2 mmol). Yield = 88.6%. Elemental analysis: anal. calcd C, 75.83; H, 9.23; N, 2.82; S, 8.89. Found: C, 75.69; H, 9.19; N, 2.78; S, 8.67. M_n = 18.0 kDa M_w = 32.6 kDa, PDI = 1.81.

Synthesis of PTBIG-50: On basis of the procedure described above, the PTBIG-50 polymer was prepared by using TBIG (98.7 mg, 0.10 mmol), IIG (98.1mg, 0.10 mmol) and BT (98.2 mg, 0.2 mmol). Yield = 86.5%. Elemental analysis: anal. calcd C, 76.54; H, 9.30; N, 2.83; S, 8.10. Found: C, 76.56; H, 9.22; N, 2.81; S, 8.07. M_n = 29.8 kDa, M_w = 72.9 kDa, PDI = 2.45.

Synthesis of PTBIG-25: On basis of the procedure described above, the PTBIG-25 polymer was prepared by using TBIG (49.4 mg, 0.05 mmol), IIG (147 mg, 0.15 mmol) and BT (98.2 mg, 0.2 mmol). Yield = 87.1%. Elemental analysis: anal. calcd C, 77.27; H, 9.35; N, 2.84; S, 7.30. Found: C, 77.45; H, 9.27; N, 2.82; S, 7.27. M_n = 26.4 kDa, M_w = 53.7 kDa, PDI = 2.03.

2.5 References

1. Yao, Y.; Dong, H.; Hu, W., Charge transport in organic and polymeric semiconductors for flexible and stretchable devices. *Adv. Mater.* **2016,** *28* (22), 4513-4523.

2. Yan, H.; Chen, Z.; Zheng, Y.; Newman, C.; Quinn, J. R.; Dötz, F.; Kastler, M.; Facchetti, A., A high-mobility electron-transporting polymer for printed transistors. *Nature* **2009,** *457* (7230), 679.

3. Someya, T.; Bao, Z.; Malliaras, G. G., The rise of plastic bioelectronics. *Nature* **2016,** *540* (7633), 379.

4. Lee, W. Y.; Wu, H. C.; Lu, C.; Naab, B. D.; Chen, W. C.; Bao, Z., n‐Type Doped Conjugated Polymer for Nonvolatile Memory. *Adv. Mater.* **2017,** *29* (16), 1605166.

5. Gelinck, G.; Heremans, P.; Nomoto, K.; Anthopoulos, T. D., Organic transistors in optical displays and microelectronic applications. *Adv. Mater.* **2010,** *22* (34), 3778-3798.

6. Beaujuge, P. M.; Fréchet, J. M., Molecular design and ordering effects in π-functional materials for transistor and solar cell applications. *J. Am. Chem. Soc.* **2011,** *133* (50), 20009-20029.

7. Sun, B.; Hong, W.; Yan, Z.; Aziz, H.; Li, Y., Record high electron mobility of 6.3 cm2V− 1s− 1 achieved for polymer semiconductors using a new building block. *Adv. Mater.* **2014,** *26* (17), 2636-2642.

8. Mei, J.; Kim, D. H.; Ayzner, A. L.; Toney, M. F.; Bao, Z., Siloxane-terminated solubilizing side chains: bringing conjugated polymer backbones closer and boosting hole mobilities in thin-film transistors. *J. Am. Chem. Soc.* **2011,** *133* (50), 20130-20133.

9. Lee, J.; Han, A.-R.; Yu, H.; Shin, T. J.; Yang, C.; Oh, J. H., Boosting the ambipolar performance of solution-processable polymer semiconductors via hybrid side-chain engineering. *J. Am. Chem. Soc.* **2013,** *135* (25), 9540-9547.

10. Kim, G.; Kang, S.-J.; Dutta, G. K.; Han, Y.-K.; Shin, T. J.; Noh, Y.-Y.; Yang, C., A thienoisoindigo-naphthalene polymer with ultrahigh mobility of 14.4 cm2/V· s that substantially exceeds benchmark values for amorphous silicon semiconductors. *J. Am. Chem. Soc.* **2014,** *136* (26), 9477-9483.

11. Huang, J.; Chen, Z.; Mao, Z.; Gao, D.; Wei, C.; Lin, Z.; Li, H.; Wang, L.; Zhang, W.; Yu, G., Tuning Frontier Orbital Energetics of Azaisoindigo‐Based Polymeric Semiconductors to Enhance the Charge‐Transport Properties. *Adv. Electron. Mater.* **2017,** *3* (11), 1700078.

12. Scher, H.; Lax, M., Stochastic transport in a disordered solid. I. Theory. *Phys. Rev. B* **1973,** *7* (10), 4491.

13. Lim, B.; Sun, H.; Lee, J.; Noh, Y.-Y., High performance solution processed organic field effect transistors with novel diketopyrrolopyrrole-containing small molecules. *Sci. Rep.* **2017,** *7* (1), 164.

14. Lee, S. M.; Lee, H. R.; Dutta, G. K.; Lee, J.; Oh, J. H.; Yang, C., Furan-flanked

diketopyrrolopyrrole-based chalcogenophene copolymers with siloxane hybrid side chains for organic field-effect transistors. *Polym. Chem.* **2019,** *10* (22), 2854-2862.

15. Kaur, M.; Shin, J.; Lee, T. W.; Choi, K.; Cho, M. J.; Choi, D. H., A novel tellurophene-containing conjugated polymer with a dithiophenyl diketopyrrolopyrrole unit for use in organic thin film transistors. *Chem. Commun.* **2013,** *49* (48), 5495-5497.

16. Kang, S.-H.; Lee, H. R.; Dutta, G. K.; Lee, J.; Oh, J. H.; Yang, C., A role of side-chain regiochemistry of thienylene–vinylene–thienylene (TVT) in the transistor performance of isomeric polymers. *Macromolecules* **2017,** *50* (3), 884-890.

17. Huang, Y.-F.; Chang, S.-T.; Wu, K.-Y.; Wu, S.-L.; Ciou, G.-T.; Chen, C.-Y.; Liu, C.-L.; Wang, C.-L., Influences of Conjugation Length on Organic Field-Effect Transistor Performances and Thin Film Structures of Diketopyrrolopyrrole-Oligomers. *ACS Appl. Mater. Interfaces* **2018,** *10* (10), 8869-8876.

18. Stalder, R.; Puniredd, S. R.; Hansen, M. R.; Koldemir, U.; Grand, C.; Zajaczkowski, W.; Müllen, K.; Pisula, W.; Reynolds, J. R., Ambipolar Charge Transport in Isoindigo-Based Donor–Acceptor Polymers. *Chem. Mater.* **2016,** *28* (5), 1286-1297.

19. Lei, T.; Dou, J. H.; Pei, J., Influence of Alkyl Chain Branching Positions on the Hole Mobilities of Polymer Thin-Film Transistors. *Adv. Mater.* **2012,** *24* (48), 6457-6461.

20. Kim, G.; Han, A.-R.; Lee, H. R.; Lee, J.; Oh, J. H.; Yang, C., Acceptor–acceptor type isoindigo-based copolymers for high-performance n-channel field-effect transistors. *Chem. Commun.* **2014,** *50* (17), 2180-2183.

21. Grand, C.; Zajaczkowski, W.; Deb, N.; Lo, C. K.; Hernandez, J. L.; Bucknall, D. G.; Müllen, K.; Pisula, W.; Reynolds, J. R., Morphology control in films of isoindigo polymers by side-chain and molecular weight effects. *ACS Appl. Mater. Interfaces* **2017,** *9* (15), 13357-13368.

22. Ashraf, R. S.; Kronemeijer, A. J.; James, D. I.; Sirringhaus, H.; McCulloch, I., A new thiophene substituted isoindigo based copolymer for high performance ambipolar transistors. *Chem. Commun.* **2012,** *48* (33), 3939-3941.

23. Kim, G.; Kim, H.; Jang, M.; Jung, Y. K.; Oh, J. H.; Yang, C., Ultra-narrow-bandgap thienoisoindigo polymers: Structure–property correlations in field-effect transistors. *J. Mater. Chem. C* **2016,** *4* (40), 9554-9560.

24. Dutta, G. K.; Han, A. R.; Lee, J.; Kim, Y.; Oh, J. H.; Yang, C., Visible-Near Infrared Absorbing Polymers Containing Thienoisoindigo and Electron-Rich Units for Organic Transistors with Tunable Polarity. *Adv. Funct. Mater.* **2013,** *23* (42), 5317-5325.

25. Chen, M. S.; Niskala, J. R.; Unruh, D. A.; Chu, C. K.; Lee, O. P.; Fréchet, J. M., Control of polymer-packing orientation in thin films through synthetic tailoring of backbone coplanarity.

Chem. Mater. **2013,** *25* (20), 4088-4096.

26. Sung, M. J.; Luzio, A.; Park, W. T.; Kim, R.; Gann, E.; Maddalena, F.; Pace, G.; Xu, Y.; Natali, D.; de Falco, C., High-Mobility Naphthalene Diimide and Selenophene-Vinylene-Selenophene-Based Conjugated Polymer: n-Channel Organic Field-Effect Transistors and Structure–Property Relationship. *Adv. Funct. Mater.* **2016,** *26* (27), 4984-4997.

27. Nakano, M.; Osaka, I.; Hashizume, D.; Takimiya, K., α-Modified Naphthodithiophene Diimides Molecular Design Strategy for Air-Stable n-Channel Organic Semiconductors. *Chem. Mater.* **2015,** *27* (18), 6418-6425.

28. Kim, Y.; Long, D. X.; Lee, J.; Kim, G.; Shin, T. J.; Nam, K.-W.; Noh, Y.-Y.; Yang, C., A balanced face-on to edge-on texture ratio in naphthalene diimide-based polymers with hybrid siloxane chains directs highly efficient electron transport. *Macromolecules* **2015,** *48* (15), 5179-5187.

29. Fukutomi, Y.; Nakano, M.; Hu, J.-Y.; Osaka, I.; Takimiya, K., Naphthodithiophenediimide (NDTI): synthesis, structure, and applications. *J. Am. Chem. Soc.* **2013,** *135* (31), 11445-11448.

30. Fan, W.; Liu, C.; Li, Y.; Wang, Z., Fluoroalkyl-modified naphthodithiophene diimides. *Chem. Commun.* **2017,** *53* (1), 188-191.

31. Tilley, A. J.; Guo, C.; Miltenburg, M. B.; Schon, T. B.; Yan, H.; Li, Y.; Seferos, D. S., Thionation Enhances the Electron Mobility of Perylene Diimide for High Performance n-Channel Organic Field Effect Transistors. *Adv. Funct. Mater.* **2015,** *25* (22), 3321-3329.

32. Samanta, S. K.; Song, I.; Yoo, J. H.; Oh, J. H., Organic n-Channel Transistors Based on [1] Benzothieno [3, 2-b] benzothiophene–Rylene Diimide Donor–Acceptor Conjugated Polymers. *ACS Appl. Mater. Interfaces* **2018,** *10* (38), 32444-32453.

33. Khim, D.; Baeg, K.-J.; Kim, J.; Kang, M.; Lee, S.-H.; Chen, Z.; Facchetti, A.; Kim, D.-Y.; Noh, Y.-Y., High performance and stable N-channel organic field-effect transistors by patterned solvent-vapor annealing. *ACS Appl. Mater. Interfaces* **2013,** *5* (21), 10745-10752.

34. Jones, B. A.; Facchetti, A.; Wasielewski, M. R.; Marks, T. J., Effects of arylene diimide thin film growth conditions on n-channel OFET performance. *Adv. Funct. Mater.* **2008,** *18* (8), 1329-1339.

35. You, L.; Chaudhry, S. T.; Zhao, Y.; Liu, J.; Zhao, X.; He, J.; Mei, J., Direct arylation polymerization of asymmetric push–pull aryl halides. *Polym. Chem.* **2017,** *8* (16), 2438-2441.

36. Luo, X.; Tran, D. T.; Kadlubowski, N. M.; Ho, C. H. Y.; Riley, P.; So, F.; Mei, J., Side-Chain Sequence Enabled Regioisomeric Acceptors for Conjugated Polymers. *Macromolecules* **2018,** *51* (21), 8486-8492.

37. James, D. I.; Wang, S.; Ma, W.; Hedström, S.; Meng, X.; Persson, P.; Fabiano, S.;

Crispin, X.; Andersson, M. R.; Berggren, M., High-Performance Hole Transport and Quasi-Balanced Ambipolar OFETs Based on D–A–A Thieno-benzo-isoindigo Polymers. *Adv. Electron. Mater.* **2016,** *2* (4), 1500313.

38. Ide, M.; Saeki, A.; Koizumi, Y.; Koganezawa, T.; Seki, S., Molecular engineering of benzothienoisoindigo copolymers allowing highly preferential face-on orientations. *J. Mater. Chem. A* **2015,** *3* (43), 21578-21585.

39. Más-Montoya, M.; Janssen, R. A., The Effect of H-and J-Aggregation on the Photophysical and Photovoltaic Properties of Small Thiophene–Pyridine–DPP Molecules for Bulk-Heterojunction Solar Cells. *Adv. Funct. Mater.* **2017,** *27* (16), 1605779.

40. Spano, F. C., The spectral signatures of Frenkel polarons in H-and J-aggregates. *Acc. Chem. Res.* **2009,** *43* (3), 429-439.

41. Xu, Y.; Minari, T.; Tsukagoshi, K.; Chroboczek, J.; Ghibaudo, G., Direct evaluation of low-field mobility and access resistance in pentacene field-effect transistors. *J. Appl. Phys.* **2010,** *107* (11), 114507.

42. Darmawan, P.; Minari, T.; Xu, Y.; Li, S. L.; Song, H.; Chan, M.; Tsukagoshi, K., Optimal Structure for High-Performance and Low-Contact-Resistance Organic Field-Effect Transistors Using Contact-Doped Coplanar and Pseudo-Staggered Device Architectures. *Adv. Funct. Mater.* **2012,** *22* (21), 4577-4583.

43. Blom, P.; De Jong, M.; Van Munster, M., Electric-field and temperature dependence of the hole mobility in poly (p-phenylene vinylene). *Phys. Rev. B* **1997,** *55* (2), R656.

Chapter 3. CPDT based polymer and small molecules with side-chain engineering

Chapter 3.1 is reproduced in part with permission of "Improvement in solubility and molecular assembly of cyclopentadithiophene-benzothiadiazole polymer" from J. Lee *et al. Macromolecular Chem. Phys.*, **2015,** *216*, 1244.

3.1. Improvement in solubility and molecular assembly of cyclopentadithiophene-benzothiadiazole polymer

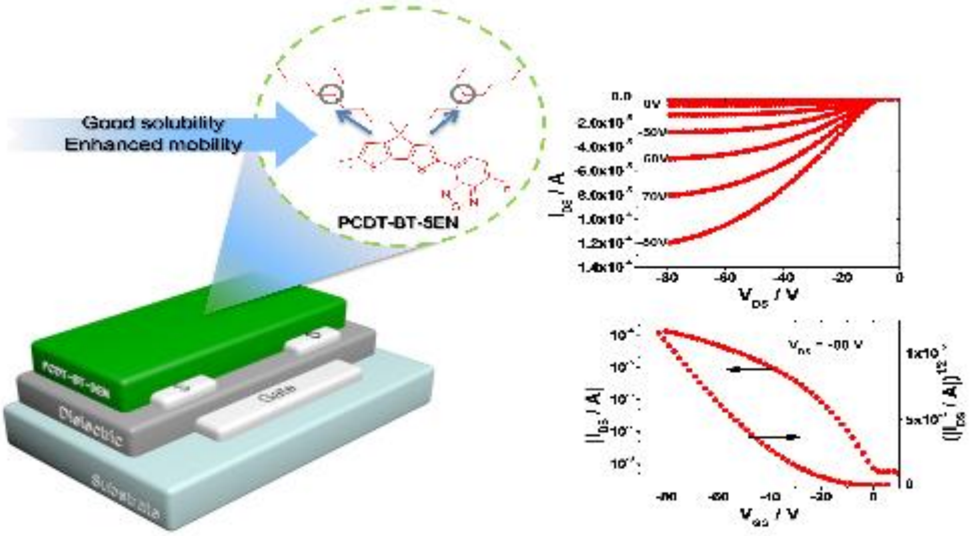

3.1.1 Introduction

Organic field-effect transistors (OFETs) based on semiconducting polymers have attracted noticeable research attention in recent years because of their potential application in ultralow-cost, large-area, lightweight, and flexible electronic devices.[1-4] The most important parameter for OFETs is the charge carrier mobility that describes how fast the injected carriers travel through the π-orbital overlap of the molecules within the transistor channel.[5, 6] Therefore, it is crucial to control the π–π interaction of the polymer backbones to achieve higher mobilities in semiconducting polymer-based OFETs.[7-12] A promising strategy to induce good π-stacking and highly ordered structures with optimally oriented domains is the inclusion of fused-ring aromatic compounds into the conjugated polymer backbone,[13-23] since they have a strong tendency to form π-stacks with a large π-orbital overlapping area. Among known fused-ring structures, cyclopentadithiophene (CDT) as such fused heterocycle has received recently considerable interest.

Described by Müllen and co-workers,[24] a cyclopentadithiophene–benzothiadiazole (PCDT-BT-C_{16}) polymer with linear hexadecyl side chains (C_{16}) on the CDT moiety exhibited an ability to self-assemble into a lamellar superstructure, reaching excellent mobility in the range of 0.1–3 $cm^2 V^{-1} s^{-1}$. However, hexadecyl side chains are not sufficient to ensure a high solubility, which reduces the versatility of this polymer for use in various other optoelectronic devices. Thereby, branched 2-ethylhexyl chains (2EH) have been used to replace the linear chains C_{16} to generate better solubility of the CDT-BT polymer family, denoted here as **PCDT-BT-2EH**. On the other hand, the mobility of **PCDT-BT-2EH** is more than three to four orders of magnitude lower than that exhibited for PCDT-BT-C_{16} since the branched 2EH group causes large π-stacking distance due to the steric hindrance of the side chains.[25-27] In order to maintain good solubilizing capability without disrupting the π–π interactions, in this work, we introduce a 5-ethylnonyl solubilizing group (5EN) as a side chain that shifted the branching point further away from the backbone and demonstrate its effectiveness for the CDT-BT polymer on both self-assembly and OFET performance.[28-34]

3.1.2 Result and Discussion

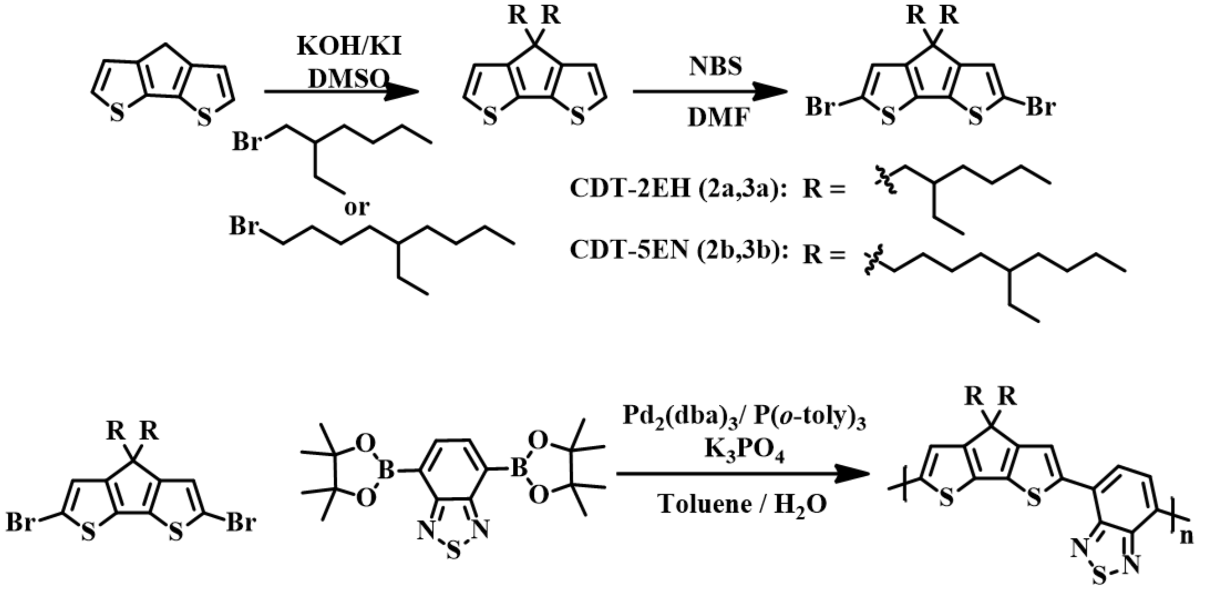

Scheme 3.1.1 Synthesis of CDT-BT-based polymers.

Scheme 3.1.1 shows the synthetic procedures and structures of intermediates and polymers; the details and characterization data are described in the experimental section. First, the synthesis of 5-ethylnonyl-bromide as the key branched chain involves a multistep synthesis starting from 2-ethylhexyl-bromide as shown in our previous paper.[35] Each of the branched alkyl substituents (2EH and 5EN) was introduced into the CDT system in the presence of KOH/KI, followed by bromination with NBS. All compounds were purified by silica column chromatography in each step and confirmed by ^{1}H and ^{13}C NMR spectra in the experimental section. The CDT-5EN monomer was employed in the synthesis of the target **PCDT-BT-5EN** polymer with diboronic ester benzothiadiazole (BT) comonomer under Suzuki conditions. In addition, we prepared **PCDT-BT-2EH** as the reference polymer by using the same polymerization condition. Both polymers were purified by precipitation into methanol followed by Soxhlet extraction using acetone, hexane, and chloroform. For the chloroform fraction of each polymer, gel-permeation chromatography (GPC) analysis against a polystyrene standard in THF exhibited a number average molecular mass (M_n) of 21.0 and 38.0 kDa and polydispersity indices (PDI) of 1.60 and 2.03 for **PCDT-BT-2EH** and **PCDT-BT-5EN**, respectively. The relatively improved solubility of **PCDT-BT-5EN** might allow us to achieve its higher M_n value than that of **PCDT-BT-2EH**. **PCDT-BT-5EN** shows good thermal stability up to 370 °C (Figure S2, Supporting Information), while no phase transition was observed by differential scanning calorimetry (DSC) in the range of 35−270 °C in both cases (**Figure 3.1.1**).

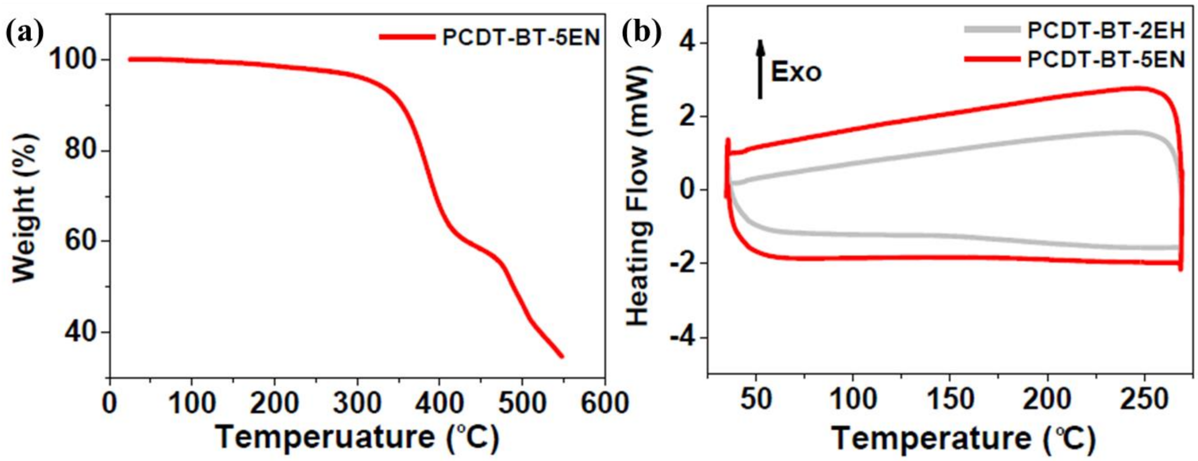

Figure 3.1.1 (a) Thermal gravimetric analysis (TGA) of **PCDT-BT-5EN** with a ramping rate of 5°C/min in nitrogen condition. (b) Differential scanning calorimetry (DSC) traces of polymers (scan rate: 10 °C/min) results of **PCDT-BT-2EH** (grey) and **PCDT-BT-5EN** (red).

The absorption spectra were obtained for each polymer in dilute chloroform solution and thin film (**Figure 3.1.2a** and **3.1.2b**). Both polymers showed similar dual characteristic bands in the absorption spectra, where the absorption peaks at ≈400 nm can be ascribed to π–π* transitions of the backbone, while the absorption bands centered at the range of 650−830 nm can be related to internal charge transfer (ICT) effects. The film absorption spectra of these polymers redshifted compared to those measured in the solution, which correlated well with polymer packing in solid state. Interestingly, in both solution and film, the ICT bands of **PCDT-BT-5EN** (λ_{max}^{sol} = 708 nm and λ_{max}^{film} = 753 nm) showed redshift compared to those of **PCDT-BT-2EH** (λ_{max}^{sol} = 687 nm and λ_{max}^{film} = 715 nm). This suggests that moving the branching point further away from the CDT core can allow stronger π–π stacking and higher molecular weight, ultimately leading to enhanced molecular assembly in both solution and solid state. The optical bandgaps of **PCDT-BT-2EH** and **PCDT-BT-5EN** are 1.48 and 1.33 eV, respectively, as estimated from the absorption onset in film.

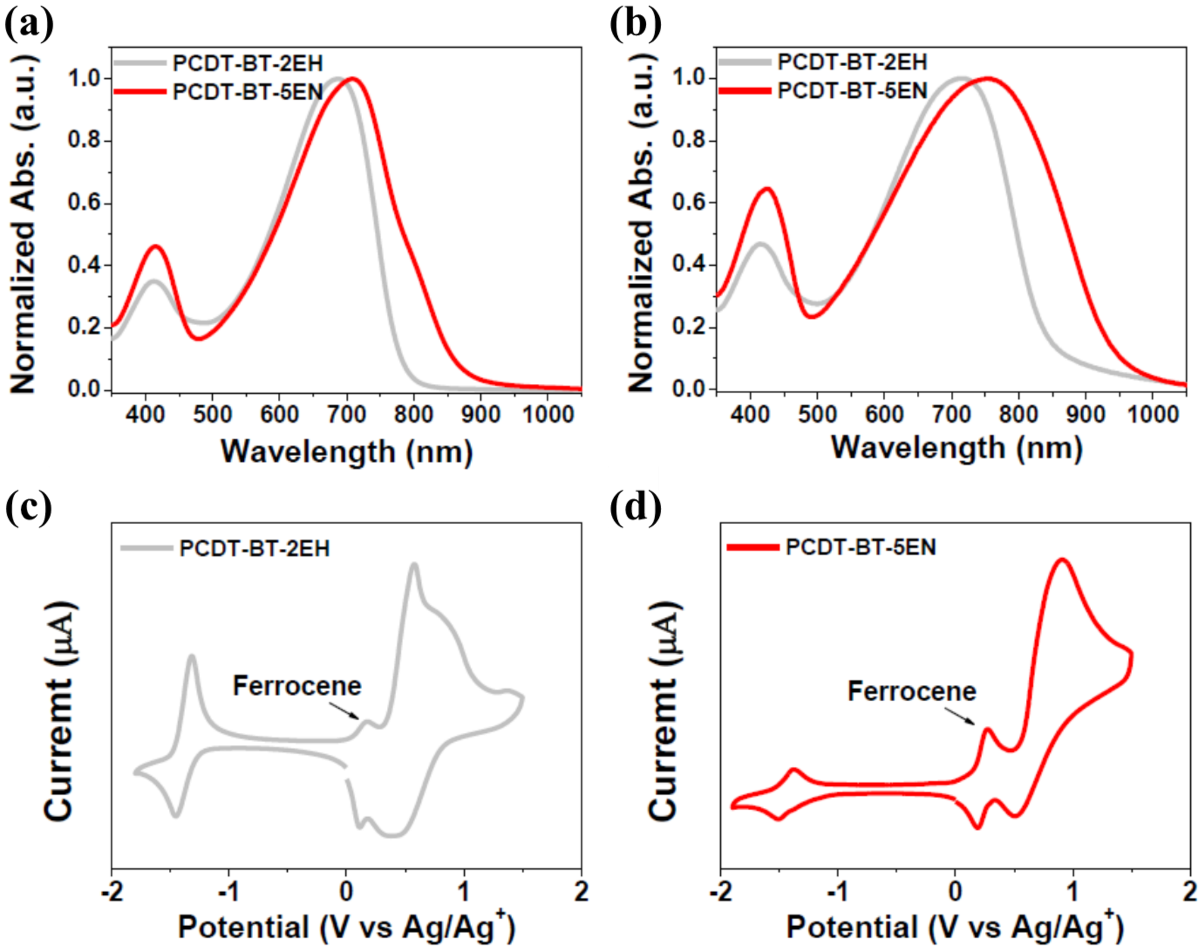

Figure 3.1.2 UV-Vis absorption spectra and cyclic voltammograms of **PCDT-BT-2EH** (gray) and **PCDT-BT-5EN** (red). (a) Chloroform solution at room temperature and (b) films cast from chloroform solution, (c) **PCDT-BT-2EH** and (d) **PCDT-BT-5EN** films drop-cast on a platinum electrode in n-Bu_4NPF_6/CH_3CN solution.

Cyclic voltammetry (CV) was measured in a three-electrode cell system using 0.1 m tetrabutylammonium hexafluorophosphate (Bu_4NPF_6) in acetonitrile as the electrolyte. Ag/Ag^+ 0.1 m of $AgNO_3$ in acetonitrile as a reference electrode, a platinum counter electrode, and a polymer-coated platinum working electrode were used to evaluate electronic energy levels of the polymers (see **Figure 3.1.2c** and **3.1.2d**). The HOMO/LUMO levels are calculated from the equation

HOMO (eV) = $-(E_{(ox)}^{onset} - E_{(ferrocene)}^{onset} + 4.8)$ and LUMO (eV) = $-(E_{(red)}^{onset} - E_{(ferrocene)}^{onset} + 4.8)$. The obtained HOMO/LUMO levels are −5.01/−3.38 eV for **PCDT-BT-2EH** and −5.13/−3.54 eV for **PCDT-BT-5EN**, respectively. The observed energy level differences are indicative for packing effects in the solid state, which is in good agreement with the absorption features described above.

To probe how the side-chain engineering affects the charge carrier transport over macroscopic dimensions, we fabricated bottom contact, bottom gate OFETs under the same conditions for both polymers. The 300 nm thick SiO_2 dielectric covering the highly doped Si acting as the gate electrode was functionalized with hexamethyldisilazane (HMDS) to minimize interfacial trapping sites. Polymer thin films were deposited by drop-casting 2 mg mL^{-1} $CHCl_3$ solution on FET substrates in nitrogen atmosphere, followed by annealing at 200 °C for 1 h. The channel lengths and widths are 10 and 700 μm, respectively. All the electrical measurements were performed in a glove box under nitrogen atmosphere. **Figure 3.1.3** exhibits the output and transfer characteristics for OFETs based on both polymer films annealed at 200 °C for 1 h. The maximum mobility of **PCDT-BT-5EN**-based devices was determined as high as 0.09 $cm^2\ V^{-1}\ s^{-1}$ with an on/off ratio of 10^4, while **PCDT-BT-2EH** exhibited significantly lower charge carrier mobility with μ_{max} = 0.004 $cm^2\ V^{-1}\ s^{-1}$. This result implies that **PCDT-BT-5EN** has a stronger tendency to form inter-chain aggregates in the solid state relative to **PCDT- BT-2EH** films by virtue of strong π–π stacking, which leads to enhanced charge transport in devices.[36, 37]

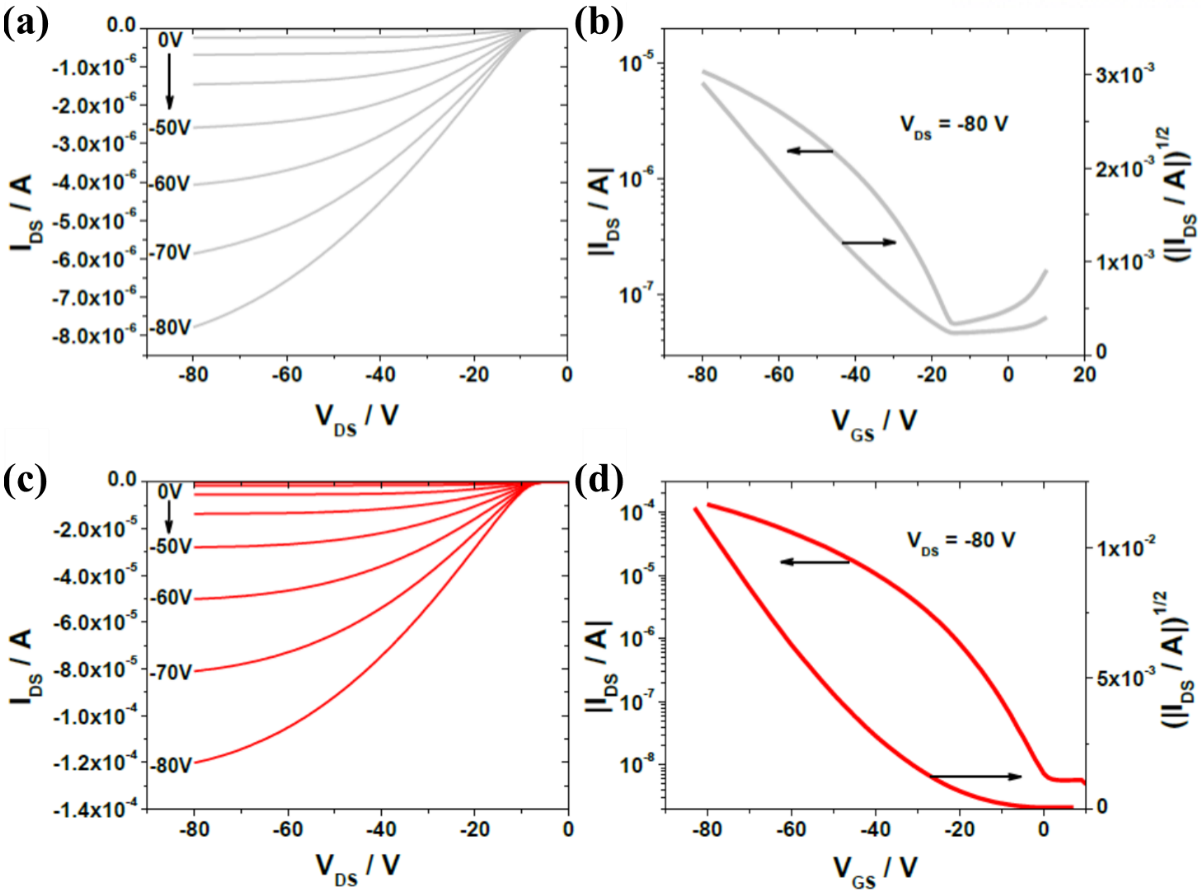

Figure 3.1.3 Output and transfer characteristics of (a), (b) **PCDT-BT-2EH** and (c), (d) **PCDTBT-5EN**.

To find the correlation between order, surface organization, and charge carrier mobility, grazing incidence wide-angle x-ray scattering (GIWAXS) measurements were performed for films. The GIWAX samples were prepared as thin film with the same procedure as it was used in OFETs fabrication. The GIWAXS patterns indicate significant differences in the surface arrangement between both the polymers, **PCDT-BT-2EH** and **PCDT-BT-5EN** (**Figure 3.1.4**). For PCDT-BT-2EH, the main meridional reflection at q_z = 5.7 Å^{-1} for q_{xy} = 0 Å^{-1} is assigned to an interlayer distance of 1.10 nm (**Figure 3.1.4a**). However, the isotropic distribution of this peak suggests that the polymer layers are randomly arranged on the substrate. The position of the off-equatorial reflection at q_z = 0.27 Å^{-1} and q_{xy} = 0.54 Å^{-1} suggests a monoclinic lattice in which the polymer backbones are shifted toward each other by ≈6 Å. This value is in agreement with the length of the CDT unit of 6.1 Å as calculated by Cerius^2. The lateral shift of the backbones toward each other was previously observed for PCDT-BT with branched decyl-tetradecyl side chains.[25-27] Thereby, the polymer backbones perform a translational shift in the range between 1.0 and 3.0 Å as confirmed by the solid-state NMR experiment. In the case discussed in the current work, the 2EH seem to affect the shift to a greater extent. Scattering intensities related to the π-stacking are not observed for **PCDT-BT-2EH**, suggesting a disordered packing of the polymer chains within the layer structures.

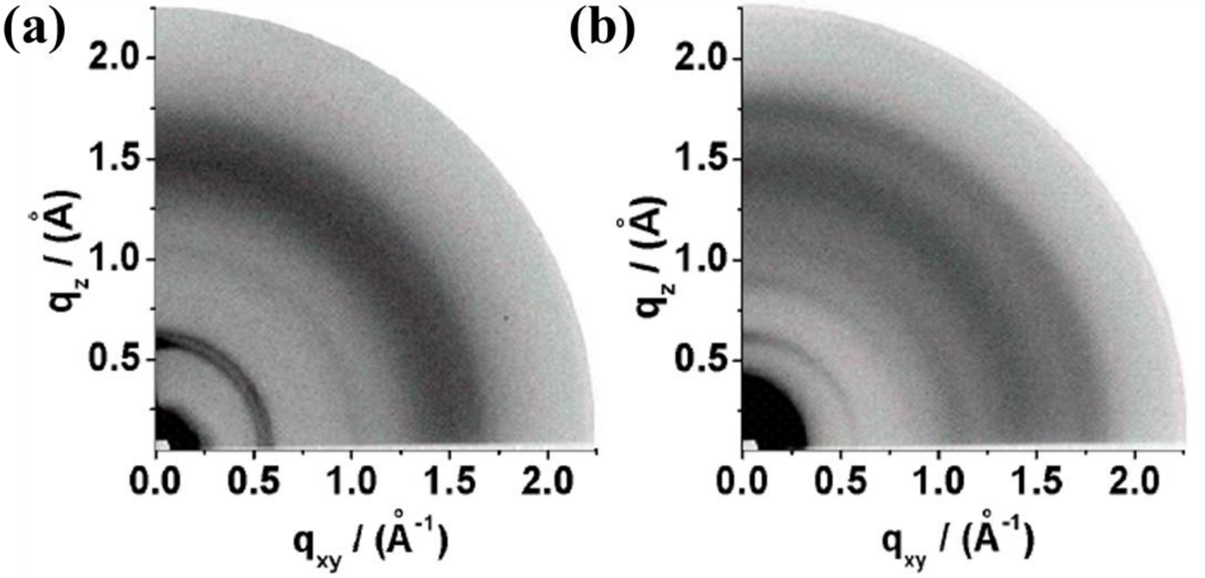

Figure 3.1.4 GIWAXS patterns of (a) **PCDT-BT-2EH** and (b) **PCDT-BT-5EN** films.

On the other hand, the GIWAXS pattern of **PCDT-BT-5EN** suggests higher order than for **PCDT-BT-2EH** (**Figure 3.1.4b**), as evident from reflections up to third order appearing on the meridional plane. From the first-order peak at $q_z = 3.1$ Å^{-1} for $q_{xy} = 0$ Å^{-1} a larger interlayer distance of 2.00 nm is determined due to longer alkyl side chains. Two reflections are additionally observed at the wide-angle range that is related to the CDT length of 0.57 nm and to the π-stacking distance of 0.365 nm. Analogous to **PCDT-BT-2EH**, the isotropic intensity distribution of the π-stacking reflection for **PCDT-BT-5EN** is a characteristic for the random organization of the polymer chains with respect to the surface. Based on the material characterization above, we can conclude that applying 5EN side chains in PCDT-BT results in improved supra-molecular organization that promotes charge mobility, while maintaining good solution processability.

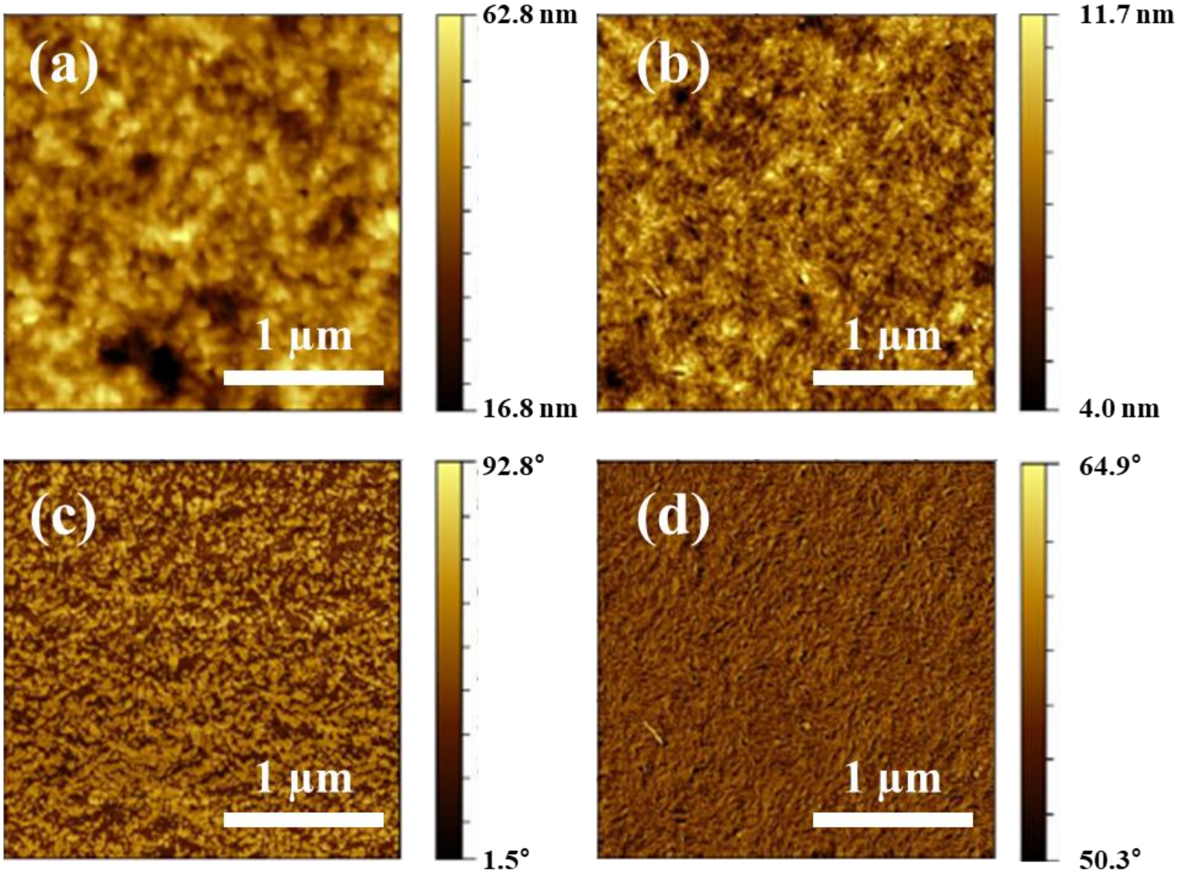

Figure 3.1.5 Height and phase AFM images of (a,c) **PCDT-BT-2EH** and (b, d) **PCDT-BT-5EN** films.

The morphology of drop-cast **PCDT-BT-2EH** and **PCDT-BT-5EN** films has been explored by atomic force microscopy (AFM). As evident from the AFM images in **Figure 3.1.5**, the film morphology is strongly dependent on the attached substituents. Polymer **PCDT-BT-2EH** possesses a lower solubility leading to the formation of −80 nm to 200 nm large aggregates (**Figure 3.1.5a** and **3.1.5c**). In the case of **PCDT-BT-5EN**, a nanofiber network is observed implying directed self-assembly of the polymer (**Figure 3.1.5b** and **3.1.5d**). The **PCDT-BT-5EN** nanofibers show diameters of ≈10 nm and lengths of ≈100 nm. The morphology studies of the drop-cast films clearly prove that not only the supramolecular order is improved for **PCDT-BT-5EN** but also the microstructure is strongly enhanced leading to a pronounced nanofiber network. In the case of large aggregates of **PCDT-BT-2EH**, the charge carrier transport can seriously be disturbed by distinct grain boundaries. In contrast, the nanofibers of **PCDT-BT-5EN** serve as pathways for the charge carriers allowing a 2D migration due to the network formation. The fiber evolution can be attributed to enhanced π-stacking interactions between **PCDT-BT-5EN** polymer backbones by reducing the steric demand of the peripheral side chains.

3.1.3 Conclusion

In summary, we have demonstrated that the use of branched 5EN chains in PCDT-BT polymer has a large effect on the optical and electrochemical properties. Apart from its sufficient solubility for solution processing, **PCDT-BT-5EN** organizes in ordered layer structures that in turn can further facilitate the charge carrier transport along the layer stacks ($\mu \cong 0.1$ cm^2 V^{-1} s^{-1}), in comparison to the reference polymer **PCDT-BT-2EH**. On the basis of our results, it is predicted that **PCDT-BT-5EN** should attract particular interest in the OPV community.

3.1.4 Experimental section

All chemicals and solvents were purchased from Sigma-Aldrich and Acros chemical companies and used as received without further purification. ^{1}H and ^{13}C NMR were recorded on Varian VNRS 400 MHz spectrophotometer using the deuterated chloroform (CDCl$_3$) with TMS as an internal standard. To investigate molecular weight and polydispersity index (PDI) of the new polymers, gel-permeation chromatography (GPC) was carried out with Agilent 1200 series and miniDAWN TREOS using THF as a solvent against PS as a standard. UV–vis absorption spectra were recorded on a Varian Carry 5000 spectrophotometer at room temperature. The electrochemical data were obtained from VersaSTAT3 Princeton Applied Research Potentiostat.

Synthetic Details

Synthesis of 4,4-Bis(5-ethylnonyl)-4H-cyclopenta[1,2-b;3,4-b']dithiophene (2b): To a suspension solution of compound 1 (1 g, 5.6 mmol) in 20 mL of DMSO, 5-ehtylnonyl bromide (2.9 g, 12.3 mmol, 2.2 equiv.) and potassium iodide (15 mg) were added at room temperature. The reaction mixture was cooled with ice bath and potassium hydroxide (0.95 g, 16.9 mmol, 3.0 equiv.) was added in one portion. The resulting solution was stirred for overnight at room temperature and then quenched with water and extracted with diethyl ether (3 × 100 mL). The combined organic layer was dried over MgSO$_4$. After removing the solvent by the rotary evaporator, the residue was purified by column chromatography on silica gel (hexane) to give as pale yellow oil **2b** (2.12 g, 78%). ^{1}H NMR (400 MHz, CDCl$_3$, δ): 7.14 (d, J = 4.0 Hz, 2H), 6.93 (d, J = 4.0 Hz, 2H), 1.83(m, 4H), 1.35–1.03(m, 24H), 0.98–0.81(m, 12H), 0.77(t, J = 8.0 Hz, 6H). ^{13}C NMR (100 MHz, CDCl$_3$, δ): 158.22, 136.59, 124.52, 121.77, 53.40, 38.97, 37.98, 33.20, 32.96, 29.09, 27.35, 25.98, 25.19, 23.28, 14.32, 11.00. Elemental analysis: C, 76.48; H, 10.35; S, 13.17 found: C: 76.30; H: 10.11; S: 13.09. MALDI-TOF-MS *m*/*z*: [M]$^{+\cdot}$= 487.19; calcd, 488.35.

Synthesis of 2,6-Dibromo-4,4-bis(5-ethylnonyl)-4H-cyclopenta[1,2-b;3,4-b']dithiophene (3b): To a solution of **2b** (2 g, 4.1 mmol) in DMF 50 mL was added *N*-bromosuccinimide (1.54 g, 8.6 mmol 2.1 equiv.) in the dark. The resulting solution was stirred for overnight at room temperature and then was extracted with diethyl ether (3 × 100 mL) with water. The combined organic layer was dried over $MgSO_4$. After removing the solvent by the rotary evaporator, the residue was purified by column chromatography on silica gel (hexane) to give as pale yellow oil **3b** (1.9 g, 72%). ^1H NMR (400 MHz, $CDCl_3$, δ): 6.93 (s, 2H), 1.77 (m, 4H), 1.33–1.05 (m, 24H), 0.94–0.82 (m, 12H), 0.78 (t, J = 8.0 Hz, 6H). ^{13}C NMR (100 MHz, $CDCl_3$, δ): 156.08, 136.48, 124.78, 111.25, 55.20, 38.98, 37.80, 33.13, 32.96, 29.12, 27.29, 25.97, 25.07, 23.27, 14.32, 11.03. Elemental analysis: C, 57.76; H, 7.51; S, 9.95 found: C: 57.57; H: 7.33; S: 9.85. MALDI-TOF-MS m/z: $[M]^{+\cdot}$= 644.01; calcd, 644.17.

Synthesis of Poly[2,6-(4,4-bis-(2-ethylhexyl)-4H-cyclopenta[2,1-b;3,4-b']dithiophene)-alt-4,7(2,1,3-benzothiadiazole)] (PCDT-BT-2EH): **3a** (150 mg, 0.268 mmol) and **4** (104 mg, 0.268 mmol) were dissolved in anhydrous toluene (10 mL) and argon-bubbled for 10 min in a tube-type Schlenk flask. $Pd_2(dba)_3$ (7.35 mg, 3 mol%, 8.03 μmol), P(o-toly)$_3$ (9.77 mg, 32.1 μmol), K_3PO_4 (227 mg, 1.07 mmol), and distilled water (3 mL) were sequentially added to the flask. The reaction mixture was stirred and refluxed for 48 h. After it was cooled down, the mixture was poured into MeOH. The precipitate was collected and then purified by Soxhlet extraction with acetone, hexane, and chloroform in sequence. The chloroform fraction was concentrated to a small volume, which was followed by reprecipitation in MeOH. Finally, the precipitate was collected by suction filtration and completely dried in a vacuum oven to afford deep green polymer powder (120 mg, 79%). M_n = 21 kDa, PDI = 1.60. ^1H NMR (400 MHz, $CDCl_3$, δ): 8.4–7.0 (br, 4H), 2.4–1.8 (br, 4H), 1.6–0.4 (br, 30H). Elemental analysis: C, 69.62; H, 7.16; N, 5.24; S, 17.99 found: C: 69.31; H: 7.28; N: 5.06; S: 17.72.

Synthesis of Poly[2,6-(4,4-bis-(5-ethylnonyl)-4H-cyclopenta[2,1-b;3,4-b']dithiophene)-alt-4,7(2,1,3-benzothiadiazole)] (PCDT-BT-5EN): **3b** (150 mg, 0.233 mmol) and **4** (90.4 mg, 0.233 mmol) were dissolved in anhydrous toluene (10 mL) and argon-bubbled for 10 min in a tube-type Schlenk flask. $Pd_2(dba)_3$ (6.39 mg, 3 mol%, 6.98 μmol), P(o-toly)$_3$ (8.50 mg, 27.9 μmol), K_3PO_4 (247 mg, 1.17 mmol), and distilled water (3 mL) were sequentially added to the flask. The reaction mixture was stirred and refluxed for 48 h. After it was cooled down, the mixture was poured into MeOH. The precipitate was collected and then purified by Soxhlet extraction with acetone, hexane, and chloroform in sequence. The chloroform fraction was concentrated to a small volume, which was followed by reprecipitation in MeOH. Finally, the precipitate was collected by suction filtration and completely dried in a vacuum oven to afford deep green polymer powder (100 mg, 69%). M_n = 38 kDa, PDI = 2.03. ^1H NMR (400 MHz, $CDCl_3$, δ): 8.2–7.8 (br, 4H), 2.2–1.8 (br, 4H), 1.7–0.6 (br, 42H). Elemental analysis: C, 71.79; H, 8.14; N, 4.53; S, 15.54 found: C: 71.21; H: 8.62; N: 4.26; S: 15.31.

3.1.5 References

1. Huitema, H.; Gelinck, G.; van der Putten, J.; Kuijk, K.; Hart, C.; Cantatore, E.;

Herwig, P.; van Breemen, A.; de Leeuw, D., Plastic transistors in active-matrix displays. *Nature* **2001,** *414*, 599.

2. Dimitrakopoulos, C. D.; Malenfant, P. R., Organic thin film transistors for large area electronics. *Adv. Mater.* **2002,** *14* (2), 99-117.

3. Li, Y.; Wu, Y.; Ong, B. S., Polyindolo [3, 2-b] carbazoles: a new class of p-channel semiconductor polymers for organic thin-film transistors. *Macromolecules* **2006,** *39* (19), 6521-6527.

4. Arias, A. C.; MacKenzie, J. D.; McCulloch, I.; Rivnay, J.; Salleo, A., Materials and applications for large area electronics: solution-based approaches. *Chem. Rev.* **2010,** *110* (1), 3-24.

5. Sirringhaus, H.; Brown, P.; Friend, R.; Nielsen, M. M.; Bechgaard, K.; Langeveld-Voss, B.; Spiering, A.; Janssen, R. A.; Meijer, E.; Herwig, P., Two-dimensional charge transport in self-organized, high-mobility conjugated polymers. *Nature* **1999,** *401* (6754), 685.

6. Skotheim, T. A.; Reynolds, J., *Handbook of conducting polymers, 2 volume set*. CRC press: 2007.

7. Giri, G.; Verploegen, E.; Mannsfeld, S. C.; Atahan-Evrenk, S.; Kim, D. H.; Lee, S. Y.; Becerril, H. A.; Aspuru-Guzik, A.; Toney, M. F.; Bao, Z., Tuning charge transport in solution-sheared organic semiconductors using lattice strain. *Nature* **2011,** *480* (7378), 504.

8. Chen, H.; Guo, Y.; Yu, G.; Zhao, Y.; Zhang, J.; Gao, D.; Liu, H.; Liu, Y., Highly π-Extended Copolymers with Diketopyrrolopyrrole Moieties for High-Performance Field-Effect Transistors. *Adv. Mater.* **2012,** *24* (34), 4618-4622.

9. Li, J.; Zhao, Y.; Tan, H. S.; Guo, Y.; Di, C.-A.; Yu, G.; Liu, Y.; Lin, M.; Lim, S. H.; Zhou, Y., A stable solution-processed polymer semiconductor with record high-mobility for printed transistors. *Sci. Rep.* **2012,** *2*, 754.

10. Lee, J.; Han, A.-R.; Kim, J.; Kim, Y.; Oh, J. H.; Yang, C., Solution-processable ambipolar diketopyrrolopyrrole–selenophene polymer with unprecedentedly high hole and electron mobilities. *J. Am. Chem. Soc.* **2012,** *134* (51), 20713-20721.

11. Lee, J.; Han, A.-R.; Yu, H.; Shin, T. J.; Yang, C.; Oh, J. H., Boosting the ambipolar performance of solution-processable polymer semiconductors via hybrid side-chain engineering. *J. Am. Chem. Soc.* **2013,** *135* (25), 9540-9547.

12. Kim, G.; Kang, S.-J.; Dutta, G. K.; Han, Y.-K.; Shin, T. J.; Noh, Y.-Y.; Yang, C., A thienoisoindigo-naphthalene polymer with ultrahigh mobility of 14.4 cm2/V· s that substantially exceeds benchmark values for amorphous silicon semiconductors. *J. Am. Chem. Soc.* **2014,** *136* (26), 9477-9483.

13. Chen, C.-P.; Chan, S.-H.; Chao, T.-C.; Ting, C.; Ko, B.-T., Low-bandgap poly (thiophene-phenylene-thiophene) derivatives with broaden absorption spectra for use in high-

performance bulk-heterojunction polymer solar cells. *J. Am. Chem. Soc.* **2008,** *130* (38), 12828-12833.

14. Dennler, G.; Scharber, M. C.; Brabec, C. J., Polymer-fullerene bulk-heterojunction solar cells. *Adv. Mater.* **2009,** *21* (13), 1323-1338.

15. Hou, J.; Chen, H.-Y.; Zhang, S.; Li, G.; Yang, Y., Synthesis, characterization, and photovoltaic properties of a low band gap polymer based on silole-containing polythiophenes and 2, 1, 3-benzothiadiazole. *J. Am. Chem. Soc.* **2008,** *130* (48), 16144-16145.

16. Moulé, A. J.; Tsami, A.; Bünnagel, T. W.; Forster, M.; Kronenberg, N. M.; Scharber, M.; Koppe, M.; Morana, M.; Brabec, C. J.; Meerholz, K., Two novel cyclopentadithiophene-based alternating copolymers as potential donor components for high-efficiency bulk-heterojunction-type solar cells. *Chem. Mater.* **2008,** *20* (12), 4045-4050.

17. Guo, X.; Kim, F. S.; Jenekhe, S. A.; Watson, M. D., Phthalimide-based polymers for high performance organic thin-film transistors. *J. Am. Chem. Soc.* **2009,** *131* (21), 7206-7207.

18. Steckler, T. T.; Zhang, X.; Hwang, J.; Honeyager, R.; Ohira, S.; Zhang, X.-H.; Grant, A.; Ellinger, S.; Odom, S. A.; Sweat, D., A spray-processable, low bandgap, and ambipolar donor– acceptor conjugated polymer. *J. Am. Chem. Soc.* **2009,** *131* (8), 2824-2826.

19. Kulkarni, A. P.; Zhu, Y.; Babel, A.; Wu, P.-T.; Jenekhe, S. A., New Ambipolar Organic Semiconductors. 2. Effects of Electron Acceptor Strength on Intramolecular Charge Transfer Photophysics, Highly Efficient Electroluminescence, and Field-Effect Charge Transport of Phenoxazine-Based Donor– Acceptor Materials. *Chem. Mater.* **2008,** *20* (13), 4212-4223.

20. McCulloch, I.; Heeney, M.; Bailey, C.; Genevicius, K.; MacDonald, I.; Shkunov, M.; Sparrowe, D.; Tierney, S.; Wagner, R.; Zhang, W., Liquid-crystalline semiconducting polymers with high charge-carrier mobility. *Nat. Mater.* **2006,** *5* (4), 328.

21. Tsao, H. N.; Cho, D.; Andreasen, J. W.; Rouhanipour, A.; Breiby, D. W.; Pisula, W.; Müllen, K., The influence of morphology on high-performance polymer field-effect transistors. *Adv. Mater.* **2009,** *21* (2), 209-212.

22. Osaka, I.; Abe, T.; Shinamura, S.; Miyazaki, E.; Takimiya, K., High-mobility semiconducting naphthodithiophene copolymers. *J. Am. Chem. Soc.* **2010,** *132* (14), 5000-5001.

23. Kim, J.; Han, A.-R.; Seo, J. H.; Oh, J. H.; Yang, C., β-Alkyl substituted Dithieno [2, 3-d; 2′, 3′-d′] benzo [1, 2-b; 4, 5-b′] dithiophene Semiconducting Materials and Their Application to Solution-Processed Organic Transistors. *Chem. Mater.* **2012,** *24* (17), 3464-3472.

24. Wang, S.; Kappl, M.; Liebewirth, I.; Müller, M.; Kirchhoff, K.; Pisula, W.; Müllen, K., Organic field-effect transistors based on highly ordered single polymer fibers. *Adv. Mater.* **2012,** *24* (3), 417-420.

25. Pisula, W.; Tsao, H.; Dudenko, D.; Cho, D.; Puniredd, S.; Zhao, Y.; Mavrinskiy, A.;

Shu, J.; Hansen, M.; Baumgarten, M., Solid-State Organization and Ambipolar Field-Effect Transistors of Benzothiadiazole-Cyclopentadithiophene Copolymer with Long Branched Alkyl Side Chains. *Polymers* **2013,** *5* (2), 833-846.

26. Oh, H. S.; Kim, T.-D.; Koh, Y.-H.; Lee, K.-S.; Cho, S.; Cartwright, A.; Prasad, P. N., Synthesis and characterization of dithienylbenzobis (thiadiazole)-based low band-gap polymers for organic electronics. *Chem. Commun.* **2011,** *47* (31), 8931-8933.

27. Horie, M.; Kettle, J.; Yu, C.-Y.; Majewski, L. A.; Chang, S.-W.; Kirkpatrick, J.; Tuladhar, S. M.; Nelson, J.; Saunders, B. R.; Turner, M. L., Cyclopentadithiophene-benzothiadiazole oligomers and polymers; synthesis, characterisation, field-effect transistor and photovoltaic characteristics. *J. Mater. Chem.* **2012,** *22* (2), 381-389.

28. Meager, I.; Ashraf, R. S.; Mollinger, S.; Schroeder, B. C.; Bronstein, H.; Beatrup, D.; Vezie, M. S.; Kirchartz, T.; Salleo, A.; Nelson, J., Photocurrent enhancement from diketopyrrolopyrrole polymer solar cells through alkyl-chain branching point manipulation. *J. Am. Chem. Soc.* **2013,** *135* (31), 11537-11540.

29. Zhang, F.; Hu, Y.; Schuettfort, T.; Di, C.-a.; Gao, X.; McNeill, C. R.; Thomsen, L.; Mannsfeld, S. C.; Yuan, W.; Sirringhaus, H., Critical role of alkyl chain branching of organic semiconductors in enabling solution-processed n-channel organic thin-film transistors with mobility of up to 3.50 cm2 V–1 s–1. *J. Am. Chem. Soc.* **2013,** *135* (6), 2338-2349.

30. Li, Y.; Zou, J.; Yip, H.-L.; Li, C.-Z.; Zhang, Y.; Chueh, C.-C.; Intemann, J.; Xu, Y.; Liang, P.-W.; Chen, Y., Side-chain effect on cyclopentadithiophene/fluorobenzothiadiazole-based low band gap polymers and their applications for polymer solar cells. *Macromolecules* **2013,** *46* (14), 5497-5503.

31. Fu, B.; Baltazar, J.; Sankar, A. R.; Chu, P. H.; Zhang, S.; Collard, D. M.; Reichmanis, E., Enhancing field-effect mobility of conjugated polymers through rational design of branched side chains. *Adv. Funct. Mater.* **2014,** *24* (24), 3734-3744.

32. Lu, R.-Q.; Xuan, W.; Zheng, Y.-Q.; Zhou, Y.-N.; Yan, X.-Y.; Dou, J.-H.; Chen, R.; Pei, J.; Weng, W.; Cao, X.-Y., A corannulene-based donor–acceptor polymer for organic field-effect transistors. *RSC Advances* **2014,** *4* (100), 56749-56755.

33. Dou, J. H.; Zheng, Y. Q.; Lei, T.; Zhang, S. D.; Wang, Z.; Zhang, W. B.; Wang, J. Y.; Pei, J., Systematic Investigation of Side-Chain Branching Position Effect on Electron Carrier Mobility in Conjugated Polymers. *Adv. Funct. Mater.* **2014,** *24* (40), 6270-6278.

34. Li, J.; Qiao, X.; Xiong, Y.; Li, H.; Zhu, D., Five-ring fused tetracyanothienoquinoids as high-performance and solution-processable n-channel organic semiconductors: effect of the branching position of alkyl chains. *Chem. Mater.* **2014,** *26* (19), 5782-5788.

35. Lee, K. C.; Song, S.; Lee, J.; Kim, D. S.; Kim, J. Y.; Yang, C., A Roundabout Approach to Control Morphological Orientation and Solar-Cell Performance by Modulating Side-Chain Branching Position in Benzodithiophene-Based Polymers. *ChemPhysChem* **2015,** *16* (6), 1305-1314.

36. Li, Y.; Sonar, P.; Singh, S. P.; Soh, M. S.; van Meurs, M.; Tan, J., Annealing-Free High-Mobility Diketopyrrolopyrrole– Quaterthiophene Copolymer for Solution-Processed Organic Thin Film Transistors. *J. Am. Chem. Soc.* **2011,** *133* (7), 2198-2204.

37. Zhang, M.; Tsao, H. N.; Pisula, W.; Yang, C.; Mishra, A. K.; Müllen, K., Field-effect transistors based on a benzothiadiazole– cyclopentadithiophene copolymer. *J. Am. Chem. Soc.* **2007,** *129* (12), 3472-3473.

Chapter 3.2 is reproduced in part with permission of "Semi-Transparent Low-Donor Content Organic Solar Cells Employing Cyclopentadithiophene-Based Conjugated Molecules" from J. Lee *et al. J. Mater. Chem. C*, **2018,** *6*, 10532.

3.2 Semi-Transparent Low-Donor Content Organic Solar Cells Employing Cyclopentadithiophene-Based Conjugated Molecules

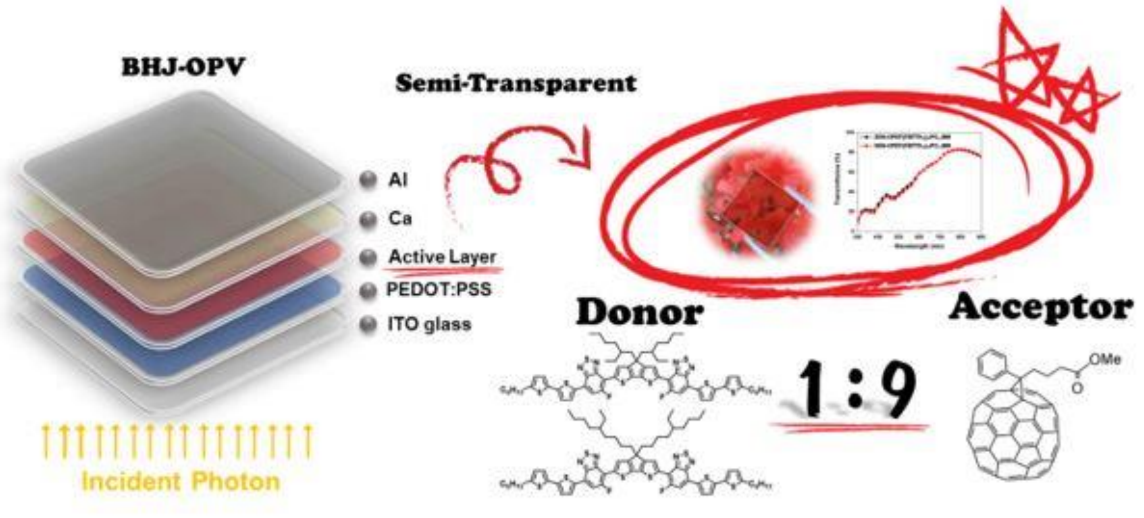

3.2.1 Introduction

Polymer-based organic solar cells (OSCs) have attracted significant attention in academia and industry owing to their potential value in the global solar energy market.[1-3] Recent advancements that have combined narrow band gap donor–acceptor polymer donors with soluble acceptors in a bulk heterojunction architecture have yielded power conversion efficiency (PCE) values over 10%.[4-9] Recently, OSCs based on conjugated molecules have emerged as an alternative to the polymer counterparts owing to their well-defined structures without batch-to-batch variations, easy control of energy levels by designing a chemical structure, and relatively simple synthesis and purification.[10-12] One of the most successful OSC conjugated molecular skeletons can be described as containing a central donor core flanked by acceptor units and terminated with π-conjugated end-capping groups.[13-15]

Cyclopentadithiophene (CPDT), a fused ring bithiophene derivative, has attracted significant attention as a donor block for the construction of state-of-the-art narrow band gap donor–acceptor polymer donors. This is due to its efficient electron-donating nature and high co-planarity with strong intermolecular π–π interactions, as well as its facile synthesis from commercially available reagents and simple side-chain manipulation for solubility.[16, 17] In fact, the Si or Ge analogues (*e.g.*, dithienosilole and dithienogermole building blocks) have been used for the successful synthesis of OSC molecular frameworks,[18-23] however they have tedious multiple synthetic routes and difficulty in tuning side-chains. Therefore, a vast library of CPDT-containing polymers is reported in the field of organic electronics including OSCs and organic field-effect transistors. However, little attention has been paid to the design of discrete CPDT-based conjugated molecules.[24, 25]

In this work, two conjugated molecules, 2EH-CPDT(FBTTh$_2$)$_2$ and 5EN-CPDT(FBTTh$_2$)$_2$, were designed and synthesized with 2-ethylhexyl and 5-ethylnonyl side chains on the CPDT core, respectively, where they are affixed by the external 5-fluorobenzo[*c*][1,2,5]thiadiazole (FBT) and bithiophene moieties. While optimizing the OSCs, a surprisingly low 2EH-CPDT(FBTTh$_2$)$_2$: PC$_{71}$BM weight ratio of 1 : 9 was found to provide the highest performance, yielding an average PCE of 3.2%, which lead to active materials that are transparent across the visible spectrum. We believe that this study contributes to a better understanding of the structure–property relationships in conjugated molecule-based OSCs and facilitates the design of new compounds for advanced high-performance transparent and semi-transparent photovoltaic devices.

3.2.2 Results and discussion

The synthesis of 2EH-CPDT(FBTTh$_2$)$_2$ and 5EN-CPDT(FBTTh$_2$)$_2$ was carried out *via* a series of Migita–Kosugi–Stille cross-coupling reactions. The synthetic routes and structures are shown in **Scheme 3.2.1**, and the detailed procedures and spectroscopic characterization are given in the Experimental section.

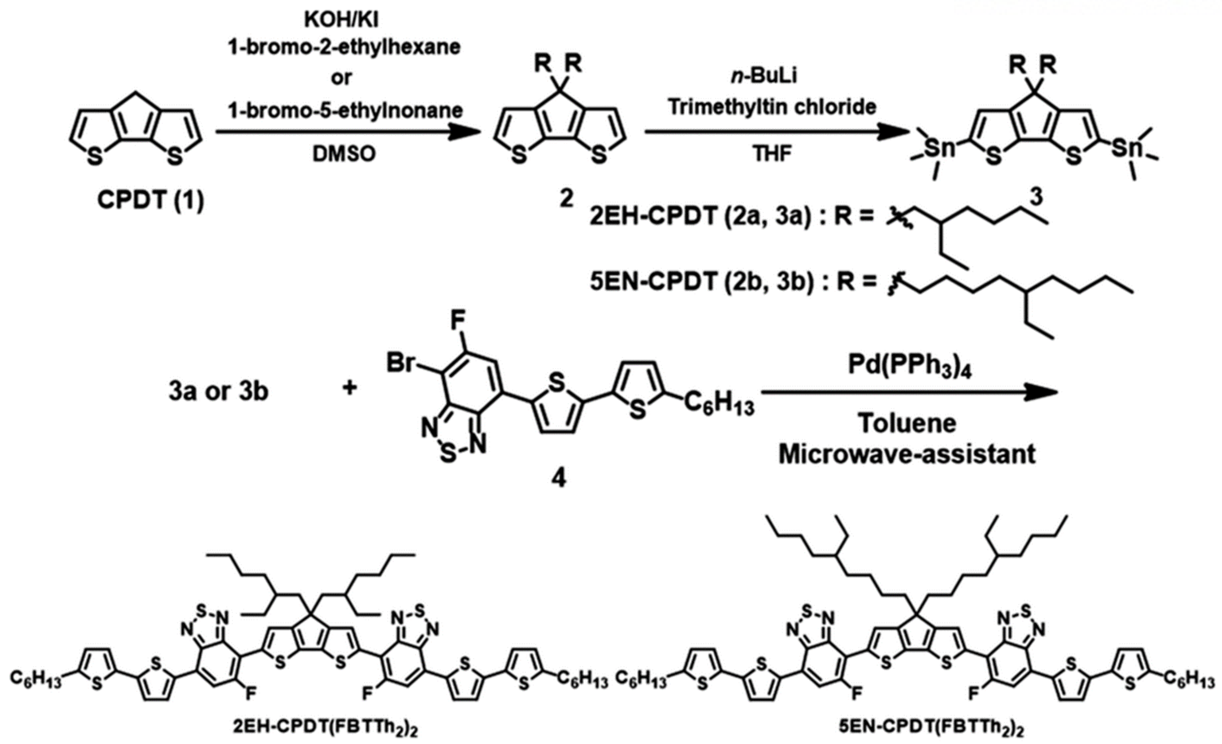

Scheme 3.2.1. Synthetic route for 2EH-CPDT(FBTTh$_2$)$_2$ and 5EN-CPDT(FBTTh$_2$)$_2$.

The initial step during the synthesis involves a dialkylation onto the bridging methylene group of the CPDT core under basic conditions (KOH/KI). 5-Ethylnonyl-bromide was obtained by the following synthetic sequence: the coupling reaction of an alkyl halide with a Grignard reagent, hydroboration–oxidation, and bromination.[26] Additionally, the different reactivities of the two bromide functionalities in 4,7-dibromo-5-fluorobenzo[*c*][1,2,5]thiadiazole enabled access to the desired regioisomers where the two fluorine atoms are in a symmetric proximal/proximal configuration with respect to the central CPDT core.[18-22] Both products exhibit high solubility in most organic solvents and were structurally characterized using elemental analysis, solution NMR spectroscopy, and mass spectrometry.

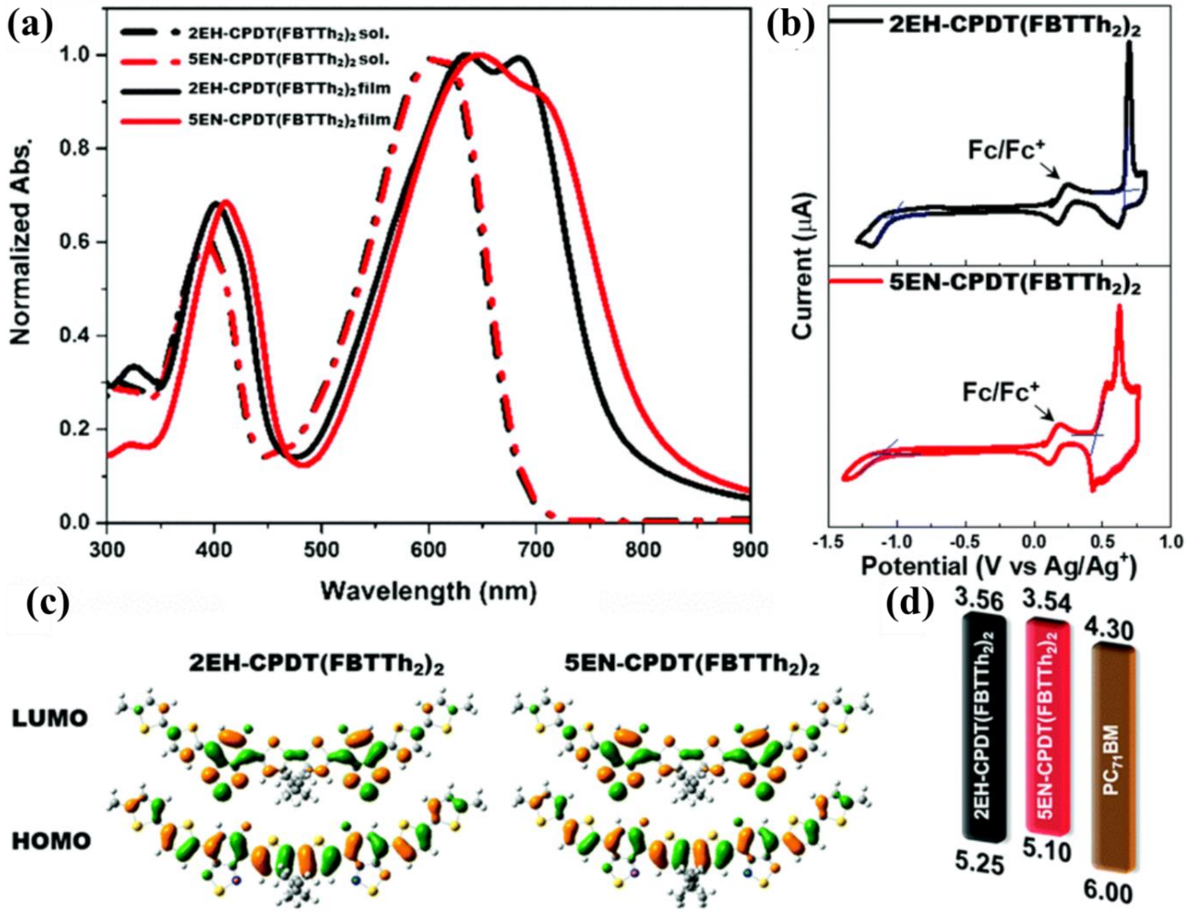

Figure 3.2.1. (a) Normalized UV-vis absorption spectra of 2EH-CPDT(FBTTh$_2$)$_2$ and 5EN-CPDT(FBTTh$_2$)$_2$ in chloroform solution (dashed-dotted line) and film (solid line). (b) Cyclic voltammograms of 2EH-CPDT(FBTTh$_2$)$_2$ and 5EN-CPDT(FBTTh$_2$)$_2$ films with a ferrocene/ferrocenium couple (Fc/Fc$^+$) as an internal standard. (c) DFT calculated HOMO/LUMO geometry (top view) of 2EH-CPDT(FBTTh$_2$)$_2$ and 5EN-CPDT(FBTTh$_2$)$_2$. (d) Energy diagrams of 2EH-CPDT(FBTTh$_2$)$_2$, 5EN-CPDT(FBTTh$_2$)$_2$ and PC$_{71}$BM.

Figure 3.2.1 depicts the normalized UV-vis absorbance spectra of neat 2EH-CPDT(FBTTh$_2$)$_2$ and 5EN-CPDT(FBTTh$_2$)$_2$ in chloroform solution and thin films. Both 2EH-CPDT(FBTTh$_2$)$_2$ and 5EN-CPDT(FBTTh$_2$)$_2$ display dual absorption bands with distinct high and low energy bands attributed to localized π–π* and internal charge transfer transitions, respectively.[15, 18] Such absorption profiles are typically possessed by donor–acceptor type π-conjugated molecules. Their solution absorption spectra reveal a remarkable similarity, while a red shift of both the absorption onset (λ_{onset}) and maximum (λ_{max}) in the film absorption spectra of 5EN-CPDT(FBTTh$_2$)$_2$ relative to 2EH-CPDT(FBTTh$_2$)$_2$ is observed. The optical band gap is reduced by 0.10 eV for 5EN-CPDT(FBTTh$_2$)$_2$ in comparison with that of 2EH-CPDT(FBTTh$_2$)$_2$. A rational explanation for this observation is the greater molecular ordering of 5EN-

CPDT($FBTTh_2$)$_2$ in the solid state, which results in an improved inter-chromophore electronic coupling. This notion is consistent with the literature findings where moving the alkyl chain branching point away from conjugated backbones potentially allows the backbones to come closer and facilitates charge transport through intermolecular contact.[27-29] The highest occupied molecular orbital (HOMO) and lowest unoccupied molecular orbital (LUMO) energies of the conjugated molecules were determined from thin film cyclic voltammetry (CV) measurements, showing quasi-reversible oxidation and non-reversible reduction waves (**Figure 3.2.1b**). The LUMO levels (−3.54 to −3.56 eV) are nearly identical for both molecules, while the HOMO level (−5.10 eV) for 5EN-CPDT($FBTTh_2$)$_2$ is 0.15 eV higher than that of 2EH-CPDT($FBTTh_2$)$_2$ (−5.25 eV). Furthermore, we also measured the ultraviolet photoelectron spectra (UPS) of the two material films (**Figure 3.2.2**). The UPS-derived HOMO levels show a similar trend and agree with the CV results. From these CV and UPS results, we can conclude that the oxidation is more facile and readily accommodated by the closer backbone packing induced by moving the alkyl branch site away from the CPDT backbone. Density functional theory calculations were also performed at the B3LYP/6-31G level using Gaussian 09. For computational simplicity, the 2-ethylhexyl and 5-ethylnonyl chains on the CPDT core were replaced with 2-methylpropyl and 5-methylhexyl units, and the terminal hexyl chains were changed to methyl groups. Both the models displayed almost identical molecular geometries and distributions of the HOMO and LUMO energies (**Figure 3.2.1c** and **3.2.1d**).

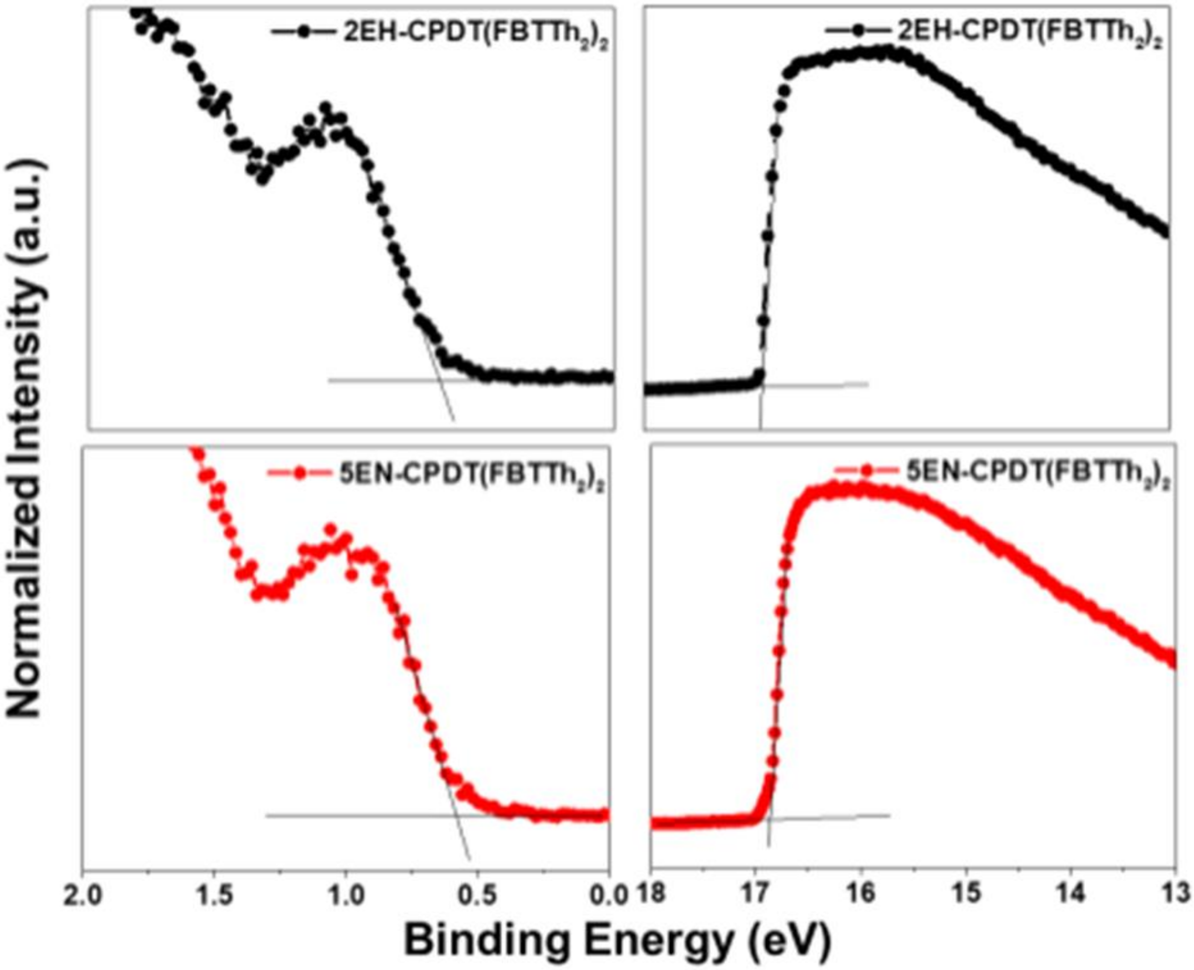

Figure 3.2.2. Ultraviolet photoelectron spectra of 2EH-CPDT(FBTTh2)2 and 5EN-CPDT(FBTTh2)2 using HeI emission (hv = 21.2 eV) as a light source. The calculated HOMO levels of 2EHCPDT(FBTTh2)2 and 5EN-CPDT(FBTTh2)2 are -5.02 eV and -4.92 eV, respectively.

The photovoltaic properties of the donor molecules were evaluated in a conventional BHJ configuration (ITO/PEDOT:PSS/donor:(6,6)-phenyl-C_{71}-butyric acid methyl ester ($PC_{71}BM$)/Ca/Al) under an inert atmosphere. The detailed procedures for the device fabrication are described in the Experimental section. We carefully optimized the OSC performance *via* controlling the donor:acceptor blend ratio within the active layer. **Figure 3.2.3a-c** show the short circuit current density (J_{SC}), open circuit voltage (V_{OC}), fill factor (FF), and PCE as a function of the donor:acceptor weight ratio for 2EH-CPDT(FBTTh$_2$)$_2$ and 5EN-CPDT(FBTTh$_2$)$_2$ OSCs. The best performance was found with a donor : acceptor ratio of 1 : 9, which gave the highest J_{SC}, V_{OC}, and FF values among the tested systems. Although the PCE values in the proposed study are lower in comparison to state of the art OSCs, it is worth noting that both donor molecules show the best-performing OSCs with extremely low-donor content in the active layer, which, to the best of our knowledge, is rarely seen for other conjugated donor materials.[15, 18, 30-32] Interestingly, thermal and solvent-additive (1,8-diiodooctane) treatments decreased the device performance and therefore, the devices functioned the best without such post processing treatments.[13, 31, 33-36] **Figure 3.2.3d** shows the current density *versus* voltage (J–V) characteristics and the corresponding external quantum efficiencies (EQE) for the best-performing OSCs (a donor : acceptor ratio of 1 : 9), while the photovoltaic parameters are detailed in **Table 3.2.1**. The 2EH-CPDT(FBTTh$_2$)$_2$-based devices without any post treatments demonstrated an average PCE of 3.2%, which was more than twice that of those based on 5EN-CPDT(FBTTh$_2$)$_2$. The enhancement in PCE is mainly due to the improved J_{SC} and V_{OC}. While the slightly deeper-lying HOMO of 2EH-CPDT(FBTTh$_2$)$_2$ does support the improvement in V_{OC}, we believe that there is still scatter in the data due to the other factors. In addition, it is also clear that, in comparison to devices based on 5EN-CPDT(FBTTh$_2$), 2EH-CPDT(FBTTh$_2$)-based devices show higher photo-conversion efficiency in the wavelength range from 300 to 750 nm, with the highest monochromatic EQE value over 60% at around 400 nm. A low donor OSC is beneficial because due to strong PCBM absorption at short wavelengths, the active layer can be made to be highly transparent; the optimized 2EH-CPDT(FBTTh$_2$):PC$_{71}$BM film displays over 65% transparency at long wavelengths beyond 650 nm and its average visible transmittance (AVT) calculated from the whole visible region (370–740 nm) is 50.4% (**Figure 3.2.4a**).[37] To demonstrate the proposed application of this type of OSC, **Figure 3.2.4b** shows an image of this optimized and nearly transparent film with the flowers behind clearly visible.

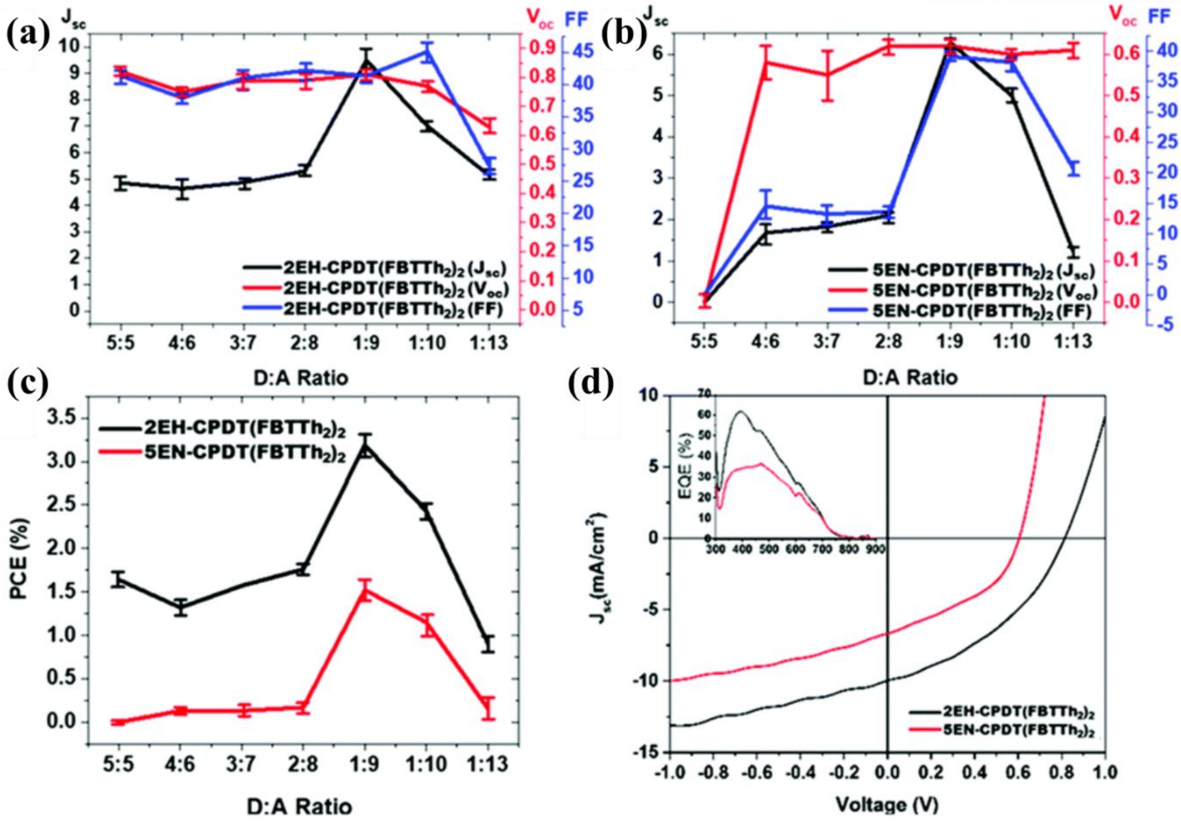

Figure 3.2.3. The OSC parameters as a function of donor:acceptor blend ratios. (a) 2EH-CPDT(FBTTh$_2$)$_2$ and (b) 5EN-CPDT(FBTTh$_2$)$_2$ with PC$_{71}$BM. (c) The PCE as a function of the D : A ratio for both 2EH-CPDT(FBTTh$_2$)$_2$ and 5EN-CPDT(FBTTh$_2$)$_2$ with PC$_{71}$BM. (d) *J*–*V* curves of optimized solar cells composed of 2EH-CPDT(FBTTh$_2$)$_2$:PC$_{71}$BM (black line) and 5EN-CPDT(FBTTh$_2$)$_2$:PC$_{71}$BM (red line) under AM 1.5G irradiation at 100 mW cm^{-2}.

Table 3.2.1. The optimized OSC results of 2EH-CPDT(FBTTh$_2$)$_2$ and 5EN-CPDT(FBTTh$_2$)$_2$ under AM1.5G illumination at 100 mW cm$^{-2\,a}$.

	J_{SC} [mA cm^{-2}]	V_{OC} [V]	*FF* [%]	PCE [%]
2EH-CPDT(FBTTh$_2$)$_2$	9.5 ± 0.6	0.81 ± 0.01	41.4 ± 3.1	3.2 ± 0.2
5EN-CPDT(FBTTh$_2$)$_2$	6.3 ± 0.3	0.62 ± 0.02	39.1 ± 1.1	1.5 ± 0.1

[a] Average values of each parameter are gained over 6 devices.

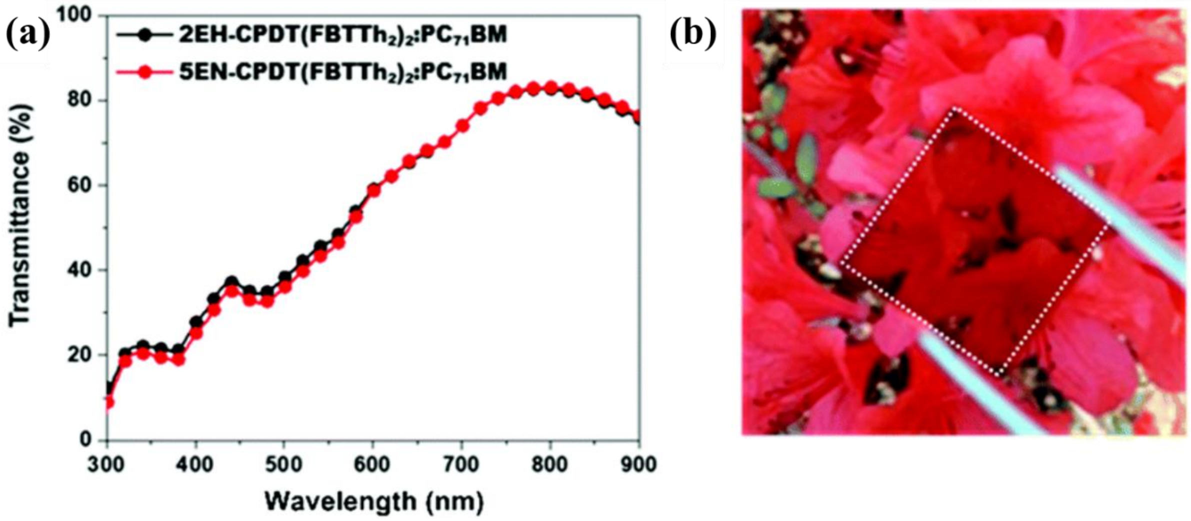

Figure 3.2.4. (a) The transmittance spectra of blend films with 1 : 9 2EH-CPDT(FBTTh$_2$)$_2$: PC$_{71}$BM and 5EN-CPDT(FBTTh$_2$)$_2$: PC$_{71}$BM weight ratios. (b) Photograph of a film composed of 1 : 9 2EH-CPDT(FBTTh$_2$)$_2$: PC$_{71}$BM weight ratio.

To understand the texture and molecular packing of the active layer morphology, grazing-incidence wide-angle X-ray scattering (GIWAXS) was collected for the neat and optimized blend films, as shown in **Figure 3.2.5**. In addition to the observation of many diffraction spots induced by multiple degrees of crystalline order, both neat films exhibited preferential edge-on π-stacking with respect to the substrate with the evidence of a strong (100) lamellar peak along q_z and a (010) π–π peak along q_{xy}. In comparison with 2EH-CPDT(FBTTh$_2$)$_2$, the neat 5EN-CPDT(FBTTh$_2$)$_2$ film showed more intense diffraction peaks, a strong enhancement of higher-order lamellar peaks, and a higher crystalline correlation length (CCL$_{010}$), which was determined using the Scherrer relation (7.7 nm for 2EH-CPDT(FBTTh$_2$)$_2$ *vs.* 16.9 nm for 5EN-CPDT(FBTTh$_2$)$_2$).[38] These observations suggest a greater extent of order and packing within 5EN-CPDT(FBTTh$_2$)$_2$, which is consistent with the UV-vis absorption results above.

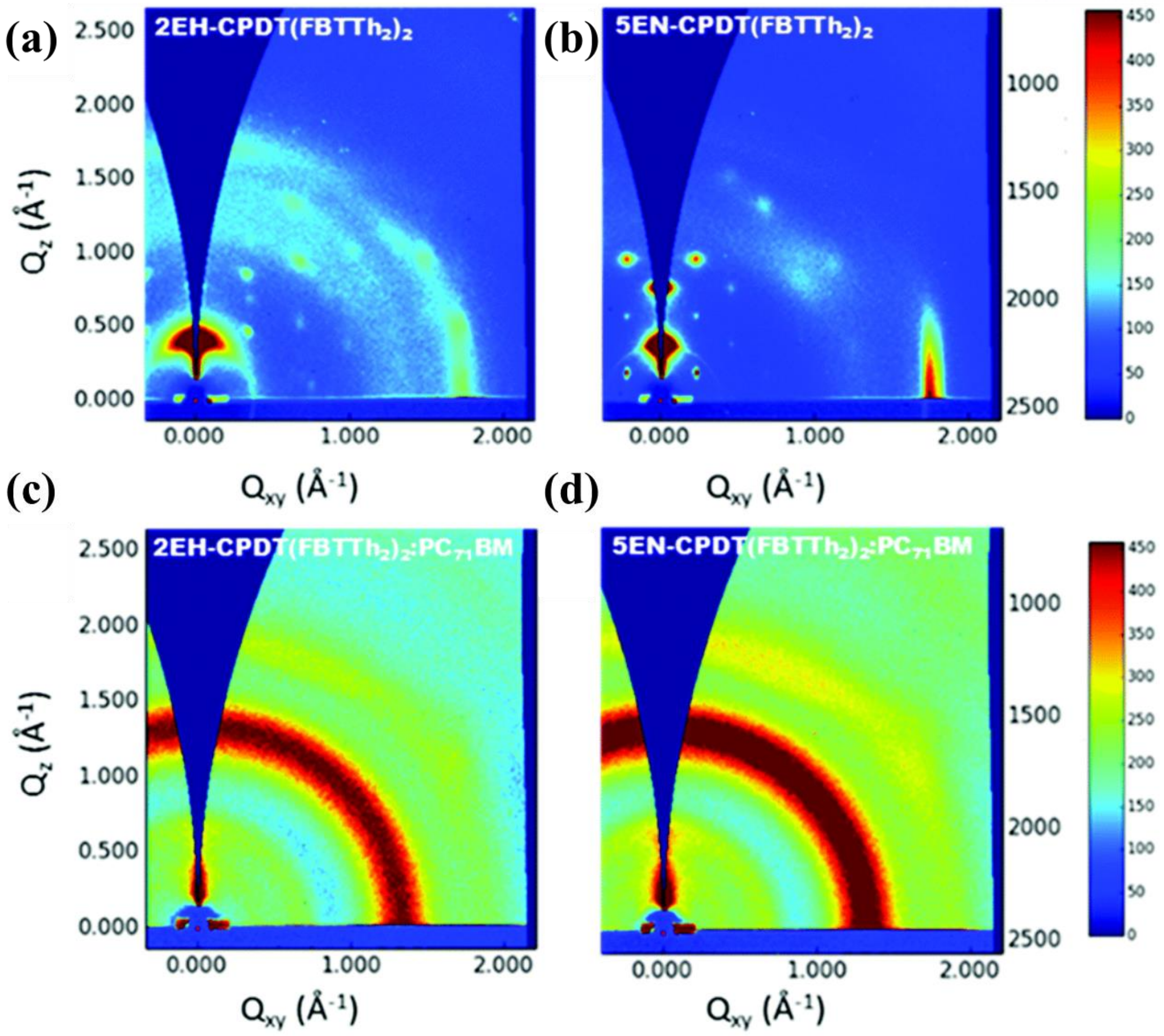

Figure 3.2.5. 2D GIWAXS images of films composed of (a) 2EH-CPDT(FBTTh$_2$)$_2$, (b) 5EN-CPDT(FBTTh$_2$)$_2$, (c) 2EH-CPDT(FBTTh$_2$)$_2$: PC$_{71}$BM (1 : 9) and (d) 5EN-CPDT(FBTTh$_2$)$_2$: PC$_{71}$BM (1 : 9).

In contrast, for both BHJ films, there were scarcely any distinct diffraction peaks in both the q_z and q_{xy} directions, except for a symmetric circle at ~1.38 Å^{-1} corresponding to the intramolecular PC$_{71}$BM distances. This signifies that the donor conjugated molecules are just dispersed into the PC$_{71}$BM matrix without properly forming crystalline structures, which is most likely due to their very low content in the blend system. The amorphous and featureless textures of both the blend films are further supported by the atomic force microscopy (AFM) images, which show very fine and smooth surfaces with a small root-mean-square roughness (below 1 nm) (**Figure 3.2.6**). It is noteworthy that the 5EN-CPDT(FBTTh$_2$)$_2$ blend showed small indents with some pinholes, indicating poor film quality, which could explain the lower performance of this blend compared to that with 2EH-

CPDT(FBTTh2)2.

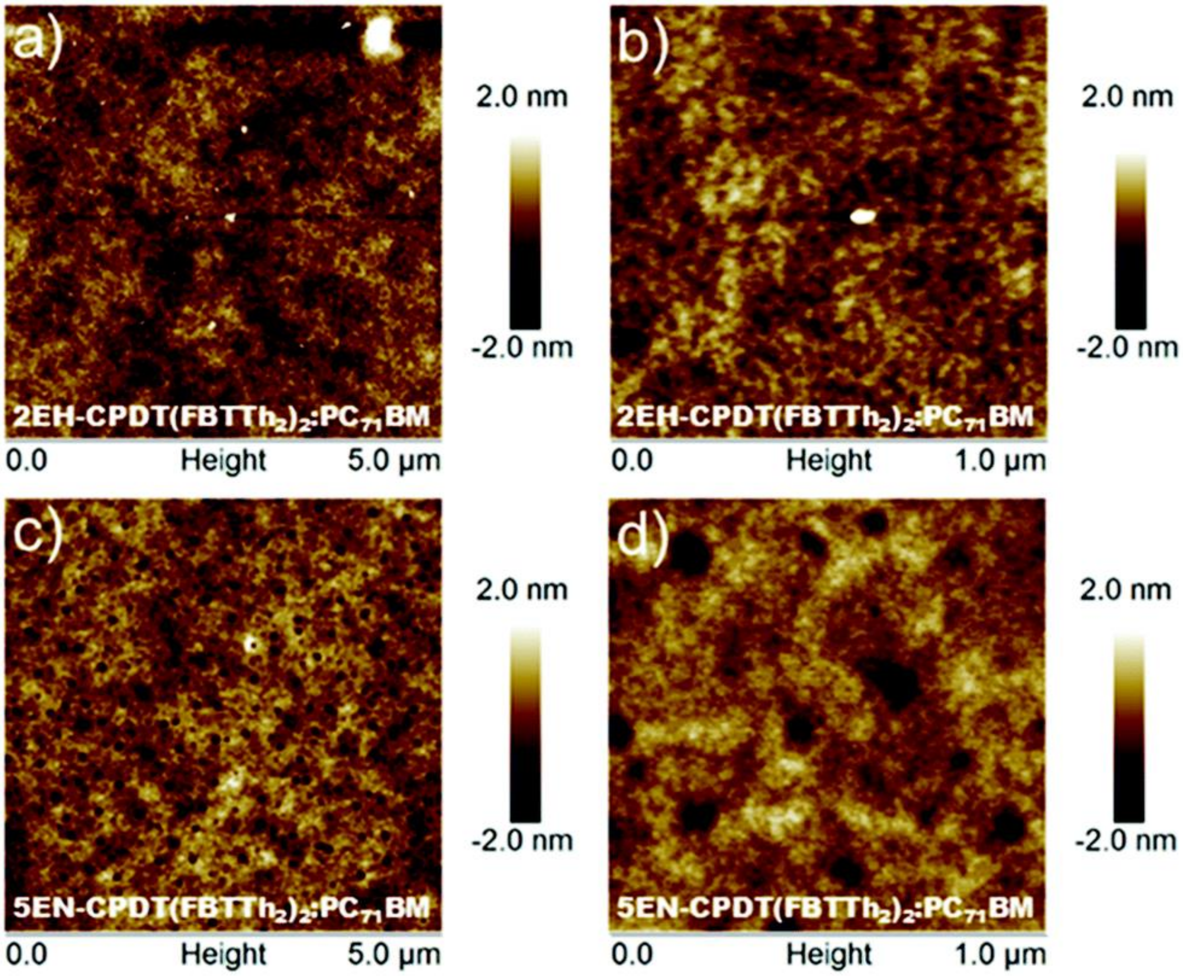

Figure 3.2.6. AFM images of BHJ films of 2EH-CPDT(FBTTh$_2$)$_2$: PC$_{71}$BM (1 : 9) and 5EN-CPDT(FBTTh$_2$)$_2$: PC$_{71}$BM (1 : 9), taken (a) and (c) at 5 by 5 μm, (b) and (d) at 1 by 1 μm.

3.2.3 Conclusion

In this study, we synthesized two novel discrete conjugated molecules, 2EH-CPDT(FBTTh$_2$)$_2$ and 5EN-CPDT(FBTTh$_2$)$_2$, based on an alternating donor–acceptor architecture for OSC applications by utilizing the easily accessible CPDT building core and modifying the branching position of the side-chains. With a branch point shifted away from the CPDT backbone, 5EN-CPDT(FBTTh$_2$)$_2$ showed a red-shifted absorption spectrum for the film and a higher-lying HOMO level with respect to 2EH-CPDT(FBTTh$_2$)$_2$. The best OSC based on 2EH-CPDT(FBTTh$_2$)$_2$:PC$_{71}$BM without additional post processing exhibited a more than 2-fold higher average PCE value than that of the 5EN-CPDT(FBTTh$_2$)$_2$-based OSC. Interestingly, unlike other conjugated donor materials, the optimized OSCs in this study were determined to have an extremely low donor content within the active layer (a donor : acceptor ratio of 1 : 9), which enabled the fabrication of a highly transparent film (a high AVT of 50.4%). These results indicate that CPDT-based molecules are effective for use in transparent and semitransparent OSCs.

3.2.4 Experimental section

All starting materials were purchased from Aldrich and Acros and used without further purification. All solvents are of ACS grade unless otherwise noted. ^{1}H NMR and ^{13}C NMR spectra were recorded on a VNMRS 400 MHz spectrophotometer using $CDCl_3$ as solvent and tetramethylsilane (TMS) as the internal standard. UV-vis spectra were recorded on a Cary 5000 (Varian USA) spectrophotometer. Cyclic voltammetry (CV) measurements were performed on Solartron electrochemical station (METEK, Versa STAT3) with a three-electrode cell in a 0.1 M tetra-*n*-butylammonium hexafluorophosphate (*n*-Bu_4NPF_6) solution in acetonitrile at a scan rate of 100 mV s^{-1} at room temperature under argon. A Ag/Ag$^+$ electrode, a platinum wire, and a platinum electrode were used as the reference electrode, counter electrode, and working electrode, respectively. The Ag/Ag$^+$ reference electrode was calibrated using a ferrocene/ferrocenium redox couple as an external standard, whose oxidation potential is set at −4.8 eV with respect to a zero vacuum level. The HOMO energy levels were obtained from the equation HOMO (eV) = $-(E^{\text{onset}}_{(\text{ox})} - E^{\text{onset}}_{(\text{ferrocene})} + 4.8)$. The LUMO levels of polymers were obtained from the equation LUMO (eV) = $-(E^{\text{onset}}_{(\text{red})} - E^{\text{onset}}_{(\text{ferrocene})} + 4.8)$. AFM was collected using a Bruker Dimension Icon Atomic Force Microscope with an RTESP-150 probe in the standard tapping mode.

4,4-Bis(2-ethylhexyl)-2,6-bis(trimethylstannyl)-4H-cyclopenta[1,2-b:5,4-b']dithiophene (3a): **2a** (1 g, 2.5 mmol) was dissolved in anhydrous THF (25 ml) and kept at −78 °C under nitrogen flow. Then, *n*-butyllithium (2.2 ml, 5.5 mmol, 2.5 M in hexane) was slowly added. Subsequently, after stirring at −78 °C for 1 h, a trimethyltin chloride solution (5.5 ml, 5.5 mmol, 1.0 M in THF) was added. The reaction mixture was then slowly warmed to room temperature and stirred overnight. The mixture was quenched by adding water and extracted with diethyl ether 3 times. The organic layer was dried over anhydrous $MgSO_4$ and concentrated under reduced pressure. The final product was obtained by column chromatography (AlO_x, *n*-hexane contained 10% of trimethylamine) to give **3a** (1.4 g, 77%) as a pale yellow oil. ^{1}H NMR (400 MHz, $CDCl_3$, δ) 6.98 (m, 2H), 1.85 (m, 4H), 1.30 (m, 2H), 0.92 (m, 16H), 0.78 (t, 6H), 0.62 (t, 6H), 0.38 (m, 18H).

4,4-Bis(5-ethylnonyl)-2,6-bis(trimethylstannyl)-4H-cyclopenta[1,2-b:5,4-b']dithiophene (3b): **3b** was prepared by the same method as that used for the synthesis of **3a**. **2b** (1g, 2.1 mmol), *n*-butyllithium (1.8 ml, 4.6 mmol, 2.5 M in hexane) and a trimethyltin chloride solution (4.6 ml, 4.6 mmol, 1.0 M in THF) were used to give **3b** (1.2g, 72%) as a pale yellow oil. ^{1}H NMR (400 MHz, $CDCl_3$, δ) 6.98 (s, 2H), 1.85 (m, 4H), 1.30 (m, 24H), 0.92 (m, 12H), 0.78 (t, 6H), 0.38 (m, 18H).

7,7'-(4,4-Bis(2-ethylhexyl)-4H-cyclopenta[1,2-b:5,4-b']dithiophene-2,6-diyl)bis(6-fluoro-4-(5'-hexyl-

[2,2'-bithiophene]-5-yl)benzo[c][1,2,5]thiadiazole) (2EH-CPDT(FBTTh$_2$)$_2$): **3a** (300 mg, 0.41 mmol), **4** (397 mg, 0.82 mmol) and Pd(PPh_3)$_4$ (10 mg, 0.008 mmol) were dissolved in anhydrous toluene (10 ml) under nitrogen flow. The reaction mixture was heated to 100 °C for 1 minute, 125 °C for 1 minute, 140 °C for 10 minutes, and 160 °C for 10 minutes in a microwave reactor. The reaction mixture was evaporated under reduced pressure and purified by column chromatography using *n*-hexane/chloroform gradient several times to give 2EH-CPDT(FBTTh$_2$)$_2$ (250 mg, 50%) as a dark purple solid. ^{1}H NMR (400 MHz, $CDCl_3$, δ) 8.24 (t, 2H), 8.05 (m, 2H), 7.76 (d, 2H), 7.20 (d, 2H), 7.14(d, 2H), 6.74 (d, 2H), 2.83 (t, 4H), 2.07 (m, 4H), 1.71 (m, 4H), 1.25 (m, 12H) 1.10 (m, 18H), 0.91 (m, 6H,), 0.64 (m, 12H); ^{13}C NMR (100 MHz, $CDCl_3$, δ) 158.88, 157.00, 153.15, 153.03, 149.64, 146.29, 140.76, 140.22, 136.00, 134.40, 133.87, 128.85, 125.00, 123.95, 123.76, 116.11, 115.81, 112.00, 54.03, 43.14, 35.25, 34.27, 31.59, 31.56, 30.25, 28.80, 28.53, 27.51, 22.87, 22.60, 14.11, 14.05, 10.72; elemental analysis calc for $C_{65}H_{72}F_2N_4S_8$ C, 64.85; H, 6.03; N, 4.65; S, 21.31; found: C, 64.81; H, 5.86; N, 4.63; S, 21.31. MALDI-TOF-MS *m/z*: $[M]^+ = 1204.33$; calcd 1203.81.

7,7'-(4,4-Bis(5-ethylnonyl)-4H-cyclopenta[1,2-b:5,4-b']dithiophene-2,6-diyl)bis(6-fluoro-4-(5'-hexyl-[2,2'-bithiophene]-5-yl)benzo[c][1,2,5]thiadiazole) (5EN-CPDT(FBTTh$_2$)$_2$): **3b** (300mg, 0.37 mmol), **4** (356 mg, 0.74 mmol) and Pd(PPh_3)$_4$ (8.5 mg, 0.0074 mmol) were dissolved in anhydrous toluene (9 ml) under nitrogen flow. The reaction mixture was heated to 100 °C for 1 minute, 125 °C for 1 minute, 140 °C for 10 minutes, and 160 °C for 10 minutes in a microwave reactor. The reaction mixture was evaporated under reduced pressure and purified by column chromatography using *n*-hexane/chloroform gradient several times to give 5EN-CPDT(FBTTh$_2$)$_2$ (230 mg, 48%) as a dark purple solid. ^{1}H NMR (400 MHz, $CDCl_3$, δ) 8.24 (s, 2H), 8.03 (m, 2H), 7.74 (d, 2H), 7.18 (d, 2H), 7.12 (d, 2H), 6.74 (d, 2H), 2.83 (t, 4H), 2.04 (m, 4H), 1.71 (m, 4H), 1.34 (m, 28H) 1.13 (m, 14H), 0.80 (m, 6H,), 0.74 (m, 12H); ^{13}C NMR (100 MHz, $CDCl_3$, δ) 159.33, 157.00, 152.99, 152.92, 149.52, 146.22, 140.57, 140.16, 135.89, 134.45, 133.65, 128.79, 124.93, 124.35, 123.88, 115.88, 115.56, 111.81, 53.92, 38.85, 37.81, 33.13, 32.82, 31.63, 31.56, 30.27, 28.97, 28.87, 27.38, 25.85, 25.34, 23.15, 22.64, 14.18, 14.15, 10.90; elemental analysis calc. for $C_{71}H_{84}F_2N_4S_8$ C, 66.21; H, 6.57; N, 4.35; S, 19.92; found: C, 65.94; H, 6.65; N, 4.34; S, 19.94. MALDI-TOF-MS *m/z*: $[M]^+ = 1288.47$; calcd 1287.97.

GIWAXS measurements were carried out on beamline 11-3 at the Stanford Synchrotron Radiation Light source (SSRL) with the help of Dr Chris Tassone. The beam was kept at an energy of 12.7 keV with an incidence angle of 0.13°. A LaB_6 standard sample was used to calibrate the instrument and software WxDiff ver 1.20 was used to reduce the 2d scattering data into the corrected 1d integration plots (*I vs. q*).[39] Neat films and bulk-heterojunction films were coated on top of PEDOT:PSS (Clevios P VP AI 4083)/Si.

OSC device fabrication: Pre-patterned indium tin oxide (ITO) was sonicated for 5 minutes each in a solution of sodium dodecyl sulfate (SDS) purchased from Sigma Aldrich in 18 MΩ water obtained from a Millipore Direct Q 3 UV system, then acetone, and then isopropanol. The ITO was then UV-ozone cleaned for 10 minutes. PEDOT:PSS (Clevios P VP AI 4083) was filtered with a 13 mm 0.45 μm Nylon syringe, spun coat on cleaned ITO at 5000 rpm for 50 seconds, and then dried on a 120 °C hotplate in air for 10 minutes. Solutions of either 2EH-CPDT(FBTTh$_2$)$_2$ or 5EN-CPDT(FBTTh$_2$)$_2$ with PC$_{71}$BM (15 mg ml^{-1} total solid concentration) were spin coated on PEDOT:PSS/ITO at 800 rpm for 50 seconds in an Ar filled glove box. The top electrode was formed by sequential deposition of 10 nm Ca followed by 100 nm Al in a thermal evaporator at a pressure of 10^{-5} mbar. Devices were tested with a Newport ABB class solar simulator attached to a Keithley 2410 SMU source meter for AM 1.5G measurements calibrated to 100 mW cm^{-2}. The device active area is 0.08 cm^2, which is defined by the overlapping area of the top and bottom electrodes.

3.5 References

1. Wang, C.; Dong, H.; Hu, W.; Liu, Y.; Zhu, D., Semiconducting π-conjugated systems in field-effect transistors: a material odyssey of organic electronics. *Chem. Rev.* **2011,** *112* (4), 2208-2267.
2. Lu, L.; Zheng, T.; Wu, Q.; Schneider, A. M.; Zhao, D.; Yu, L., Recent advances in bulk heterojunction polymer solar cells. *Chem. Rev.* **2015,** *115* (23), 12666-12731.
3. Dou, L.; Liu, Y.; Hong, Z.; Li, G.; Yang, Y., Low-bandgap near-IR conjugated polymers/molecules for organic electronics. *Chem. Rev.* **2015,** *115* (23), 12633-12665.
4. Zhao, W.; Qian, D.; Zhang, S.; Li, S.; Inganäs, O.; Gao, F.; Hou, J., Fullerene-free polymer solar cells with over 11% efficiency and excellent thermal stability. *Adv. Mater.* **2016,** *28* (23), 4734-4739.
5. Ye, L.; Zhang, S.; Zhao, W.; Yao, H.; Hou, J., Highly efficient 2D-conjugated benzodithiophene-based photovoltaic polymer with linear alkylthio side chain. *Chem. Mater.* **2014,** *26* (12), 3603-3605.
6. Liu, Y.; Zhao, J.; Li, Z.; Mu, C.; Ma, W.; Hu, H.; Jiang, K.; Lin, H.; Ade, H.; Yan, H., Aggregation and morphology control enables multiple cases of high-efficiency polymer solar cells. *Nat. Commun.* **2014,** *5*, 5293.
7. Lim, K.-G.; Choi, M.-R.; Lee, T.-W., Improvement of both efficiency and stability in organic photovoltaics by using water-soluble anionic conjugated polyelectrolyte interlayer. *Mat. Today Energy* **2017,** *5*, 66-71.
8. Kim, H.; Byun, J.; Bae, S. H.; Ahmed, T.; Zhu, J. X.; Kwon, S. J.; Lee, Y.; Min, S. Y.; Wolf, C.; Seo, H. K., On-Fabrication Solid-State N-Doping of Graphene by an Electron-Transporting Metal Oxide Layer for Efficient Inverted Organic Solar Cells. *Adv. Energy Mater.* **2016,** *6*

(12), 1600172.

9. Lim, K.-G.; Ahn, S.; Lee, T.-W., Energy level alignment of dipolar interface layer in organic and hybrid perovskite solar cells. *J. Mater. Chem. C* **2018,** *6* (12), 2915-2924.

10. Zade, S. S.; Zamoshchik, N.; Bendikov, M., From short conjugated oligomers to conjugated polymers. Lessons from studies on long conjugated oligomers. *Acc. Chem. Res* **2010,** *44* (1), 14-24.

11. Kim, C.; Liu, J.; Lin, J.; Tamayo, A. B.; Walker, B.; Wu, G.; Nguyen, T.-Q., Influence of structural variation on the solid-state properties of diketopyrrolopyrrole-based oligophenylenethiophenes: Single-crystal structures, thermal properties, optical bandgaps, energy levels, film morphology, and hole mobility. *Chem. Mater.* **2012,** *24* (10), 1699-1709.

12. Henson, Z. B.; Müllen, K.; Bazan, G. C., Design strategies for organic semiconductors beyond the molecular formula. *Nat. Chem.* **2012,** *4* (9), 699.

13. Wang, K.; Liang, R. Z.; Wolf, J.; Saleem, Q.; Babics, M.; Wucher, P.; Abdelsamie, M.; Amassian, A.; Hansen, M. R.; Beaujuge, P. M., Donor and Acceptor Unit Sequences Influence Material Performance in Benzo [1, 2-b: 4, 5-b′] dithiophene–6, 7-Difluoroquinoxaline Small Molecule Donors for BHJ Solar Cells. *Adv. Funct. Mater.* **2016,** *26* (39), 7103-7114.

14. Tang, A.; Zhan, C.; Yao, J., Comparative Study of Effects of Terminal Non-Alkyl Aromatic and Alkyl Groups on Small-Molecule Solar Cell Performance. *Adv. Energy Mater.* **2015,** *5* (13), 1500059.

15. Sun, Y.; Welch, G. C.; Leong, W. L.; Takacs, C. J.; Bazan, G. C.; Heeger, A. J., Solution-processed small-molecule solar cells with 6.7% efficiency. *Nat. Mater.* **2012,** *11* (1), 44.

16. Yamashita, Y.; Hinkel, F.; Marszalek, T.; Zajaczkowski, W.; Pisula, W.; Baumgarten, M.; Matsui, H.; Müllen, K.; Takeya, J., Mobility exceeding 10 cm2/(V· s) in donor–acceptor polymer transistors with band-like charge transport. *Chem. Mater.* **2016,** *28* (2), 420-424.

17. Hinkel, F.; Marszalek, T.; Zajaczkowski, W.; Puniredd, S. R.; Baumgarten, M.; Pisula, W.; Müllen, K., Tuning Packing and Solubility of Donor (D)–Acceptor (A) Polymers by cis–trans Isomerization within Alkenyl Side Chains. *Chem. Mater.* **2014,** *26* (16), 4844-4848.

18. Moon, M.; Walker, B.; Lee, J.; Park, S. Y.; Ahn, H.; Kim, T.; Lee, T. H.; Heo, J.; Seo, J. H.; Shin, T. J.; Kim, J.; Yang, C., Dithienogermole-Containing Small-Molecule Solar Cells with 7.3% Efficiency: In-Depth Study on the Effects of Heteroatom Substitution of Si with Ge. *Adv. Energy Mater.* **2015,** *5* (9), 1402044.

19. Van Der Poll, T. S.; Love, J. A.; Nguyen, T. Q.; Bazan, G. C., Non-basic high-performance molecules for solution-processed organic solar cells. *Adv, Mater.* **2012,** *24* (27), 3646-3649.

20. Han, D.; Kumari, T.; Jung, S.; An, Y.; Yang, C., A Comparative Investigation of Cyclohexyl-End-Capped Versus Hexyl-End-Capped Small-Molecule Donors on Small Donor/Polymer

Acceptor Junction Solar Cells. *Solar RRL* **2018,** *2* (5), 1800009.

21. Walker, B.; Han, D.; Moon, M.; Park, S. Y.; Kim, K.-H.; Kim, J. Y.; Yang, C., Effect of Heterocyclic Anchoring Sequence on the Properties of Dithienogermole-Based Solar Cells. *ACS Appl. Mater. Interfaces* **2017,** *9* (8), 7091-7099.

22. Han, D.; Lee, J.; Lee, S. M.; Seo, J. H.; Park, S. H.; Yang, C., Regioregular dithienosilole-and dithienogermole-based small molecules with symmetric distal/distal orientation of F atoms. *Dyes Pigm.* **2018,** *155*, 7-13.

23. Kumari, T.; Moon, M.; Kang, S.-H.; Yang, C., Improved efficiency of dtge (fbtth2) 2-based solar cells by using macromolecular additives: How macromolecular additives versus small additives influence nanoscale morphology and photovoltaic performance. *Nano Energy* **2016,** *24*, 56-62.

24. Zhang, M.; Tsao, H. N.; Pisula, W.; Yang, C.; Mishra, A. K.; Müllen, K., Field-effect transistors based on a benzothiadiazole− cyclopentadithiophene copolymer. *J. Am. Chem. Soc.* **2007,** *129* (12), 3472-3473.

25. Li, Z.; Tsang, S. W.; Du, X.; Scoles, L.; Robertson, G.; Zhang, Y.; Toll, F.; Tao, Y.; Lu, J.; Ding, J., Alternating Copolymers of Cyclopenta [2, 1-b; 3, 4-b′] dithiophene and Thieno [3, 4-c] pyrrole-4, 6-dione for High-Performance Polymer Solar Cells. *Adv. Funct. Mater.* **2011,** *21* (17), 3331-3336.

26. Lee, J.; Marszalek, T.; Lee, K. C.; Kim, J.; Pisula, W.; Yang, C., Improvement in Solubility and Molecular Assembly of Cyclopentadithiophene–Benzothiadiazole Polymer. *Macromol. Chem. Phys.* **2015,** *216* (11), 1244-1250.

27. Mei, J.; Kim, D. H.; Ayzner, A. L.; Toney, M. F.; Bao, Z., Siloxane-terminated solubilizing side chains: bringing conjugated polymer backbones closer and boosting hole mobilities in thin-film transistors. *J. Am. Chem. Soc.* **2011,** *133* (50), 20130-20133.

28. Lei, T.; Dou, J. H.; Pei, J., Influence of Alkyl Chain Branching Positions on the Hole Mobilities of Polymer Thin-Film Transistors. *Adv, Mater.* **2012,** *24* (48), 6457-6461.

29. Lee, J.; Han, A.-R.; Yu, H.; Shin, T. J.; Yang, C.; Oh, J. H., Boosting the ambipolar performance of solution-processable polymer semiconductors via hybrid side-chain engineering. *J. Am. Chem. Soc.* **2013,** *135* (25), 9540-9547.

30. Wang, J. L.; Yin, Q. R.; Miao, J. S.; Wu, Z.; Chang, Z. F.; Cao, Y.; Zhang, R. B.; Wang, J. Y.; Wu, H. B.; Cao, Y., Rational Design of Small Molecular Donor for Solution-Processed Organic Photovoltaics with 8.1% Efficiency and High Fill Factor via Multiple Fluorine Substituents and Thiophene Bridge. *Adv. Funct. Mater.* **2015,** *25* (23), 3514-3523.

31. Wang, H.; Liu, F.; Bu, L.; Gao, J.; Wang, C.; Wei, W.; Russell, T. P., The Role of Additive in Diketopyrrolopyrrole-Based Small Molecular Bulk Heterojunction Solar Cells. *Adv, Mater.*

2013, *25* (45), 6519-6525.

32. Cui, C.; Guo, X.; Min, J.; Guo, B.; Cheng, X.; Zhang, M.; Brabec, C. J.; Li, Y., High-Performance Organic Solar Cells Based on a Small Molecule with Alkylthio-Thienyl-Conjugated Side Chains without Extra Treatments. *Adv, Mater.* **2015,** *27* (45), 7469-7475.

33. Wessendorf, C. D.; Schulz, G. L.; Mishra, A.; Kar, P.; Ata, I.; Weidelener, M.; Urdanpilleta, M.; Hanisch, J.; Mena-Osteritz, E.; Lindén, M., Efficiency Improvement of Solution-Processed Dithienopyrrole-Based A-D-A Oligothiophene Bulk-Heterojunction Solar Cells by Solvent Vapor Annealing. *Adv. Energy Mater.* **2014,** *4* (14), 1400266.

34. Wang, J. L.; Xiao, F.; Yan, J.; Wu, Z.; Liu, K. K.; Chang, Z. F.; Zhang, R. B.; Chen, H.; Wu, H. B.; Cao, Y., Difluorobenzothiadiazole-Based Small-Molecule Organic Solar Cells with 8.7% Efficiency by Tuning of π-Conjugated Spacers and Solvent Vapor Annealing. *Adv. Funct. Mater.* **2016,** *26* (11), 1803-1812.

35. Li, L.; Xiao, L.; Qin, H.; Gao, K.; Peng, J.; Cao, Y.; Liu, F.; Russell, T. P.; Peng, X., High-efficiency small molecule-based bulk-heterojunction solar cells enhanced by additive annealing. *ACS Appl. Mater. Interfaces* **2015,** *7* (38), 21495-21502.

36. Deng, D.; Zhang, Y.; Yuan, L.; He, C.; Lu, K.; Wei, Z., Effects of Shortened Alkyl Chains on Solution-Processable Small Molecules with Oxo-Alkylated Nitrile End-Capped Acceptors for High-Performance Organic Solar Cells. *Adv. Energy Mater.* **2014,** *4* (17), 1400538.

37. Chen, K.-S.; Salinas, J.-F.; Yip, H.-L.; Huo, L.; Hou, J.; Jen, A. K.-Y., Semi-transparent polymer solar cells with 6% PCE, 25% average visible transmittance and a color rendering index close to 100 for power generating window applications. *Energy Environ. Sci.* **2012,** *5* (11), 9551-9557.

38. Smilgies, D.-M., Scherrer grain-size analysis adapted to grazing-incidence scattering with area detectors. *J. Appl. Crystallogr.* **2009,** *42* (6), 1030-1034.

39. Mannsfeld, S., WxDiff. Stanford Synchrotron Radiation Light-Source: 2009.

Chapter 4. Insight into the isomeric effect of fullerene-free acceptor via fluorine substitution

Chapter 4 is reproduced in part with permission of “Insights into Constitutional Isomeric Effects on Donor-Acceptor Intermolecular Arrangements in Non-fullerene Organic Solar Cells” from J. Lee *et al.* *J. Mater. Chem. A*, **2019,** *7*, 18468.
Copyright 2019 Royal Society of Chemistry (RSC)

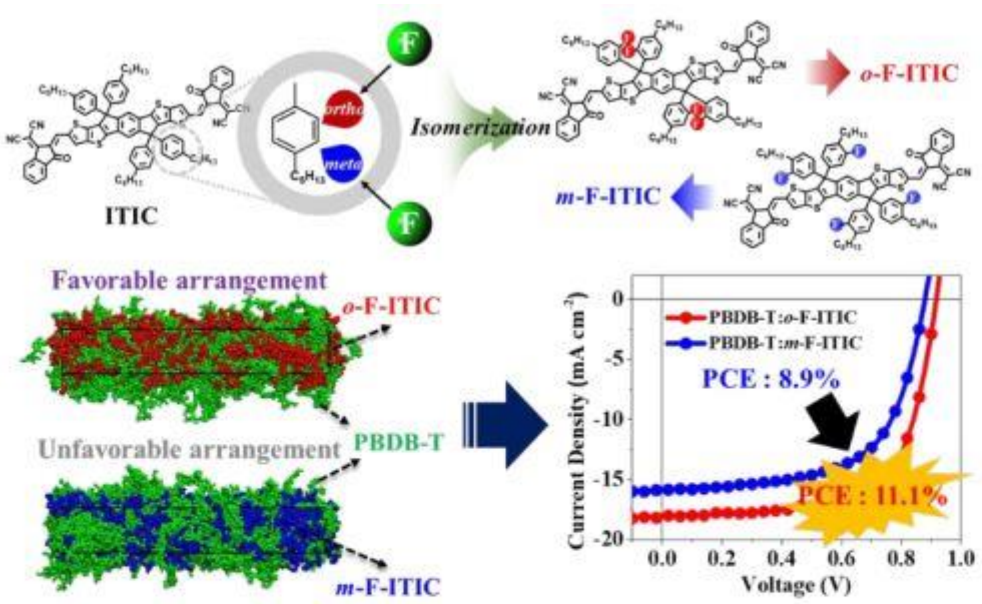

4.1 Introduction

Bulk-heterojunction (BHJ) organic solar cells (OSCs) comprising a blend active layer of a *p*-type electron donor and an *n*-type electron acceptor offer the prospect of low-cost, light-weight, and environmentally benign solar energy production.[1-3] Mainly benefiting from the development of highly efficient donor materials, power conversion efficiencies (PCEs) of BHJ OSCs based on fullerene derivative acceptors have exceeded 10%.[4-9] However, further improvements in fullerene-based OSCs are limited owing to the intrinsic shortcomings of the fullerene acceptors, such as synthetic difficulty in tuning their optical/electronic properties and their poor light absorbing capability. Therefore, non-fullerene small molecules have emerged as very promising electron acceptors in OSCs to overcome the above-mentioned issues, and PCEs beyond the fullerene-based OSCs have been achieved in OSCs based on fused-ring-type non-fullerene acceptors.[10-15] Among them, the most successful and representative acceptor is ITIC that contains the indacenodithieno[3,2-*b*]thiophene (IDT) core and 1,1-dicyanomethylene-3-indanone (DCI) terminal groups.[10, 16-21] Therefore, considerable efforts have been devoted to modifying the structure of ITIC to adjust the absorption spectra and energy levels to further improve PCEs, for example, by changing the side chain type,[22] bulkiness,[23-26] and length;[27] extending the conjugation length of the core and terminal groups;[28-32] functionalizing the terminal groups (e.g., methylation, fluorination, and chlorination),[13-15, 32-34] and utilizing thienyl-fused DCI terminal analogs.[35-39]

It is well documented that the favorable donor–acceptor intermolecular interactions and/or arrangements present in the blend active layer of OSCs can play a major role in exciton dissociation, charge separation, and charge recombination processes.[40-45] In line with this consideration, herein, we assume that subtle changes in the positioning of a single atom in ITIC (popularly called constitutional isomerism effect) can strongly affect the intermolecular interactions and/or arrangements in the OSCs, which are one of the crucial factors that govern their efficient operation. Although considerate research efforts have been devoted to modifying ITIC-series including the modification of core units, terminal units, heteroatoms, and the bridges between the core and terminal units within ITIC-related backbones,[46-48] the constitutional isomerism effect within the side chains remains unexplored.

In this study, to establish the structure–property relationship induced by constitutional isomerism, we synthesized two new ITIC-based isomeric acceptors (*o*-F-ITIC and *m*-F-ITIC) with *ortho* and *meta* positions of fluorine atoms in the side chains and did a comparative investigation on their photovoltaic properties. The *o*-F-ITIC OSC exhibits a PCE as high as 11.11%, significantly higher than that of *m*-F-ITIC OSC (PCE = 8.90%), when employing poly[(2,6-(4,8-bis(5-(2-ethylhexyl)thiophen-2-yl)-benzo[1,2-*b*:4,5-*b'*]dithiophene))-*alt*-(5,5-(1',3'-di-2-thienyl-5',7'-bis(2-ethylhexyl)benzo[1',2'-*c*:4',5'-*c*']dithiophene-4,8-dione))] (named as PBDB-T) as a donor counterpart of the active layer. A detailed simulation analysis demonstrates different donor–acceptor intermolecular complexes formed between the F-ITIC acceptors and PBDB-T donor, which not only supports our hypothesis but also provides a possible explanation for the significant difference between the OSCs based on the two isomers. Moreover, experimental studies (e.g., electrical and morphological properties as well as exciton generation and charge transfer behaviors) through a broad range of techniques further elucidate the varied intermolecular complexes, as observed from the theoretical study. The results obtained from a combination of theoretical and experimental studies here advance the understanding of the role of constitutional isomerism in intermolecular interactions, thereby facilitating a molecular design of non-fullerene acceptors.

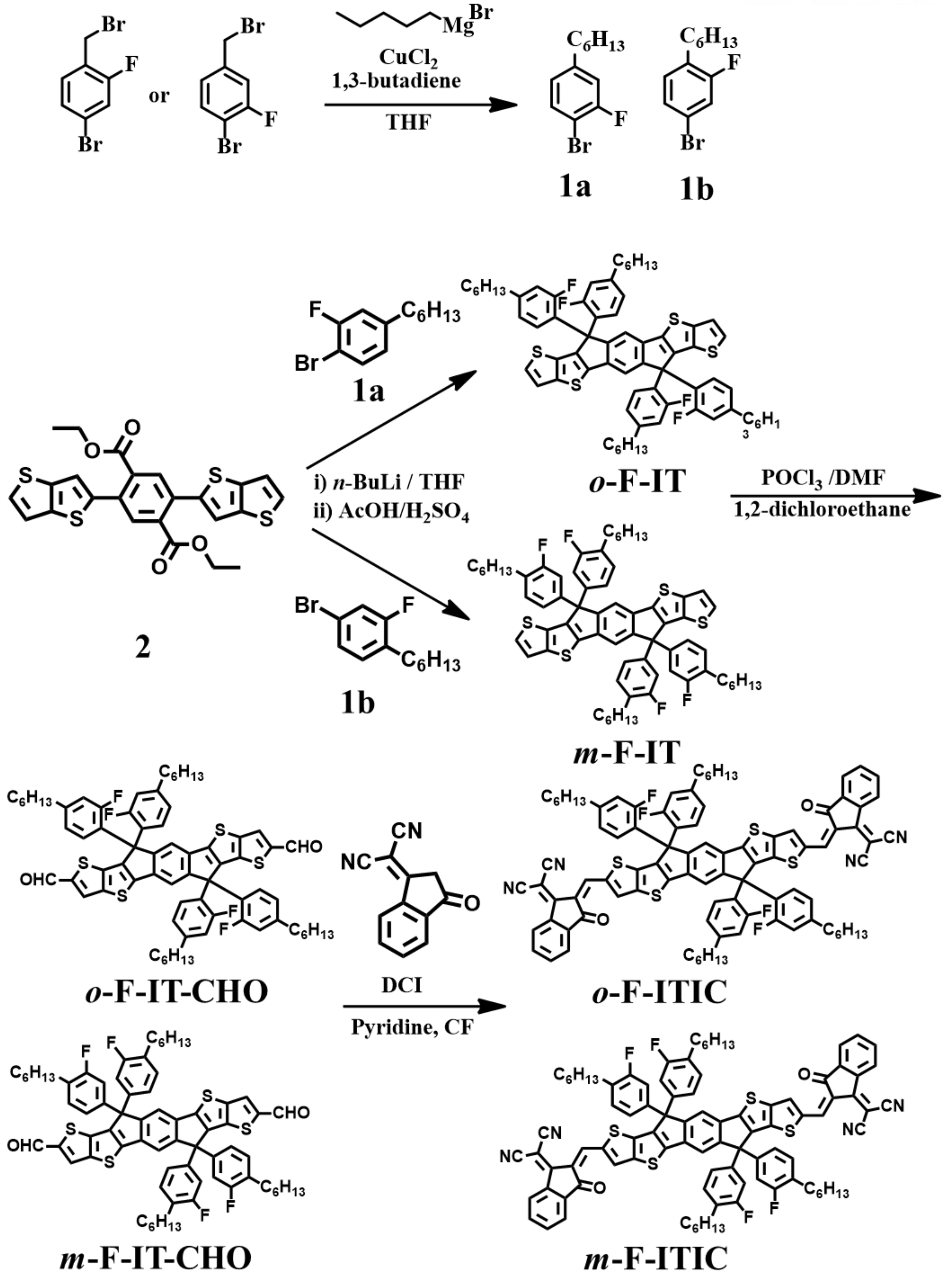

Scheme 4.1. Synthetic routes of *o*-F-ITIC and *m*-F-ITIC.

4.2 Results and Discussion

Material Design, Characterization, and Photovoltaic Properties

The chemical structures and synthetic routes of *o*-F-ITIC and *m*-F-ITIC are illustrated in **Scheme 4.1**. First, 1-bromo-2-fluoro-4-hexylbenzene (**1a**) and 4-bromo-2-fluro-1-hexylbenzene (**1b**) were used the key isomeric side chains prepared through copper-catalyzed alkyl-alkyl cross-coupling reaction with the commercially available chemicals (1-bromo-4-(bromomethyl)-2-fluorobenzene and 4-bromo-1-(bromomethyl)-2-fluorobenzene), respectively.[49] A double nucleophilic addition between each of the freshly lithiated isomeric side chains and the ester groups of diethyl-2,5-bis(thieno[3,2-*b*]thiophene-2-yl)terephthalate (**2**) was performed, which was followed by an acid-mediated Friedel-Crafts-type ring closing reaction, leading to the seven-ring fused cores based on IDT (*o*-F-IT and *m*-F-IT). Finally, the target F-ITIC acceptor isomers with DCI as the terminal groups (*o*-F-ITIC and *m*-F-ITIC) were synthesized by the well-documented means of subsequent Vilsmeier-Haack and Knoevenagel condensation reactions. Their chemical structures and qualities were analyzed through ^{1}H and ^{13}C NMR spectroscopy, elemental analysis, and mass spectroscopy (see the Experimental section).

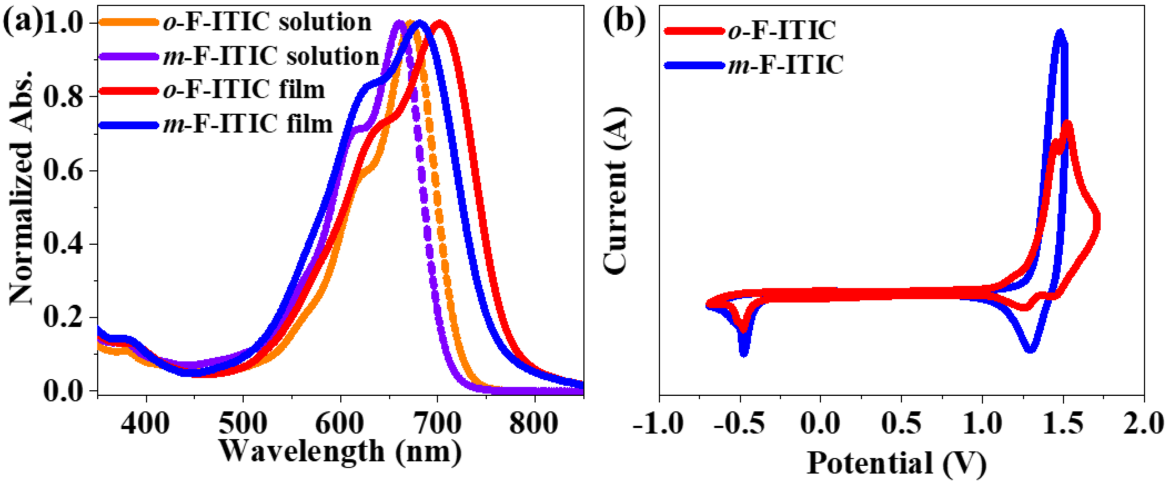

Figure 4.1. (a) Solution and film UV-vis absorption spectra of F-ITICs. (b) Cyclic voltammograms of *o*-F-ITIC and *m*-F-ITIC.

Table 4.1. Optical and electrochemical properties of F-ITIC acceptors.

	$\lambda_{\text{max,sol.}}$ [nm]	$\lambda_{\text{max,film}}$ [nm]	$E_{\text{HOMO}}{}^{a}$ [eV]	$E_{\text{LUMO}}{}^{a}$ [eV]	$E_{g}{}^{\text{elec.}}$ [eV]	IP^{b} [eV]
o-F-ITIC	672	702	-5.66	-3.94	1.72	5.74
m-F-ITIC	661	681	-5.69	-3.96	1.73	5.77

[a]Thin films in CH3CN/n-Bu4NPF6, versus Fc/Fc+ at 0.1 V s−1. HOMO and LUMO estimated from the onset oxidation and reduction potentials, respectively, assuming the absolute energy level of ferrocene/ferrocenium to be 4.8 eV below vacuum; [b]Measured by an ambient ultraviolet photoelectron spectroscopy (UPS) technique.

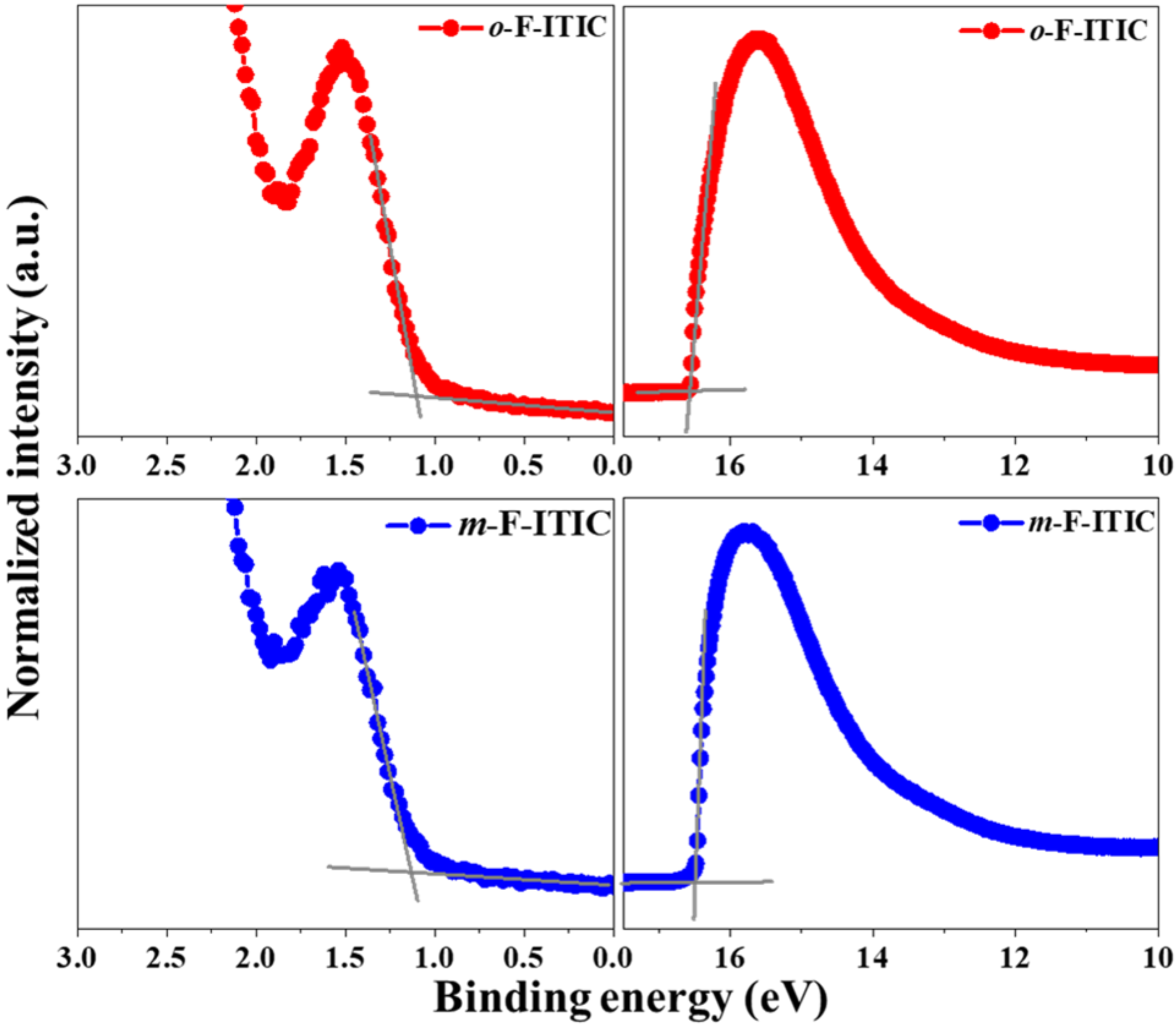

Figure 4.2. Ultraviolet photoelectron spectra of *o*-F-ITIC and *m*-F-ITIC using HeI emission (hv =21.2 eV) as a light source. The calculated HOMO levels of o-F-ITIC and m-F-ITIC are -5.74 eV and -5.77 eV, respectively.

The optical properties of F-ITIC isomers were measured in chloroform solution and as a thin-film state; the relevant data are provided in **Figure 4. 1a** and **Table 4.1**. Both *o*-F-ITIC and *m*-F-ITIC show strong absorption bands from 550 nm to 730 nm in chloroform solution as well as redshifts of 20–30 nm in the film as a result of their solid-state packing. It is very interesting to note that, relative to *m*-F-ITIC, *o*-F-ITIC displays a more red-shifted absorption spectrum in both the solution and the film and a slight lower optical bandgap (E_g^{opt}) [1.58 eV (*o*-F-ITIC) versus 1.62 eV (*m*-F-ITIC)], which indicates its stronger chain aggregation property. As shown in **Figure 4.1b**, the cyclic voltammetry (CV)-derived highest occupied molecular orbital (HOMO) and lowest unoccupied molecular orbital (LUMO) energies show little variation for *o*-F-ITIC (−5.66/−3.94 eV) and *m*-F-ITIC (−5.69/−3.96 eV). Additionally, their ultraviolet photoelectron spectroscopy-derived HOMOs deviate within only a small margin from the CV data (**Figure 4.2**). Collectively, the optical and electrochemical data demonstrate that different positioning of the fluorine atoms within the side chains can change the absorption profile by manipulating the molecular self-organization with minimal impact on the redox property.

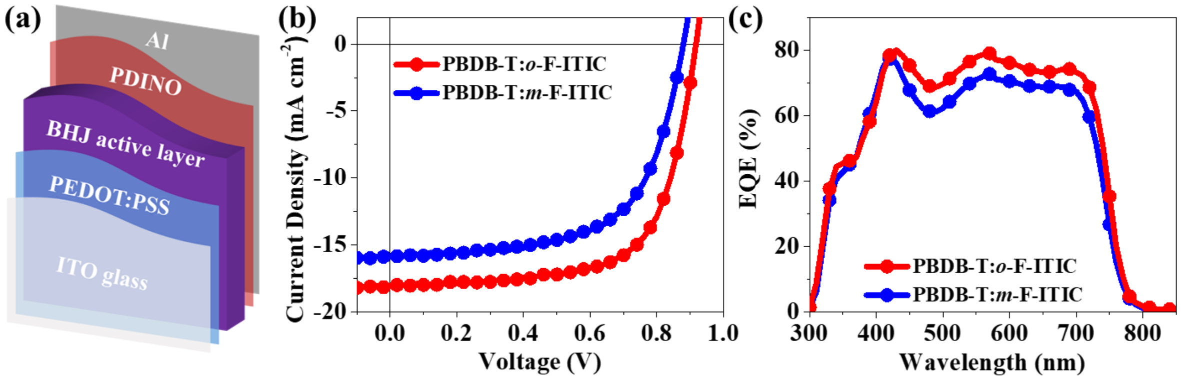

Figure 4.3. (a) Conventional device architecture. (b) *J*-*V* curves of the devices with PBDB-T:*o*-F-ITIC and PBDB-T:*m*-F-ITIC with optimal fabrication condition. (c) The corresponding EQE curves.

Table 4.2. Photovoltaic parameters of the devices based on PBDB-T:*o*-ITIC and PBDB-T:*m*-F-ITIC with optimal fabrication conditions.[a]

	V_{OC} [V]	J_{SC} [mA cm^{-2}]	*FF* [%]	PCE [%]	J_{SC}[b] [mA cm^{-2}]
o-F-ITIC	0.918 (0.914 ± 0.004)	18.07 (17.65 ± 0.43)	66.97 (67.30 ± 0.44)	11.11 (10.89 ± 0.21)	17.16
m-F-ITIC	0.883 (0.878 ± 0.006)	15.80 (15.72 ± 0.18)	63.79 (63.91 ± 0.33)	8.90 (8.82 ± 0.08)	15.76

[a] The photovoltaic properties were averaged over eight devices and the average values and standard deviation were given in parentheses. [b] The short-circuit current densities are integrated from the EQE spectra.

A well-known wide-bandgap polymer PBDB-T was selected as a counter donor to fabricate BHJ OSCs because it has well-complementary absorption associated with appropriate energy levels that can pair with the F-ITIC acceptors synthesized in this study. The device structure was ITO/PEDOT:PSS/active layer/PDINO/Al, where PDINO was used as the cathode interlayer material (**Figure 4.3a**). The optimization involved varying the donor/acceptor ratio, amount of 1,8-diiodoctane (DIO) additive, and thermal annealing temperature. We found that, for the both blends (PBDB-T:*o*-F-ITIC and PBDB-T:*m*-F-ITIC), the optimal device performances were obtained by employing chlorobenzene with a donor:acceptor weight ratio of 1.3:1 and 0.5 vol% of DIO additive, followed by thermal annealing at 60 °C for 10 min. The current density–voltage (J–V) curves of the optimized devices (AM1.5G, 100 mW cm^{-2}) are shown in **Figure 4.3b**, and the corresponding photovoltaic parameters are listed in **Table 4.2**. The PBDB-T:*m*-F-ITIC device showed a short-circuit current (J_{SC}) of 15.80 mA cm^{-2}, an open-circuit voltage (V_{OC}) of 0.883 V, and a fill factor (FF) of 63.79%, yielding a PCE of 8.90%. For the PBDB-T:*o*-F-ITIC device, all photovoltaic parameters (J_{SC} = 18.07 mA cm^{-2}, V_{OC} = 0.918 V, and FF = 66.97%) were improved, which resulted in a remarkably higher PCE of 11.11%. Note that PBDB-T:ITIC-based device (F-free ITIC reference acceptor) yielded the PCE of 9.69% under the same device condition, implying that rather than its density, the positioning of the fluorine atom plays role in determining the device performance.

As shown in **Figure 4.3c**, in addition to a good agreement between the J_{SC} values obtained from the J–V measurement and those calculated by integrating the external quantum efficiency (EQE) spectra, the PBDB-T:*o*-F-ITIC-based device showed higher EQE values in the most photo-response range from 300 to 800 nm compared to the PBDB-T:*m*-F-ITIC-based device. It is also noted that relative to both *m*-F-ITIC- and ITIC-based ones, *o*-F-ITIC-based device has the stronger photo-response in range from 600 nm to 800 nm, which is attributed to the higher extinction coefficients of *o*-F-ITIC. A little change in the intrinsic properties (e.g., in bandgaps and energy levels), as revealed by the comparison of isomers *o*-F-ITIC and *m*-F-ITIC, could be responsible, to some degree, for the observed difference in the photovoltaic performance; however, it is still insufficient to explain this. Therefore, we propose that the different fluorine positioning in the side chains of the F-ITIC acceptors induces different intermolecular interaction with the donor counterpart, resulting in the surprisingly large discrepancy between the devices based on *o*-F-ITIC and *m*-F-ITIC.

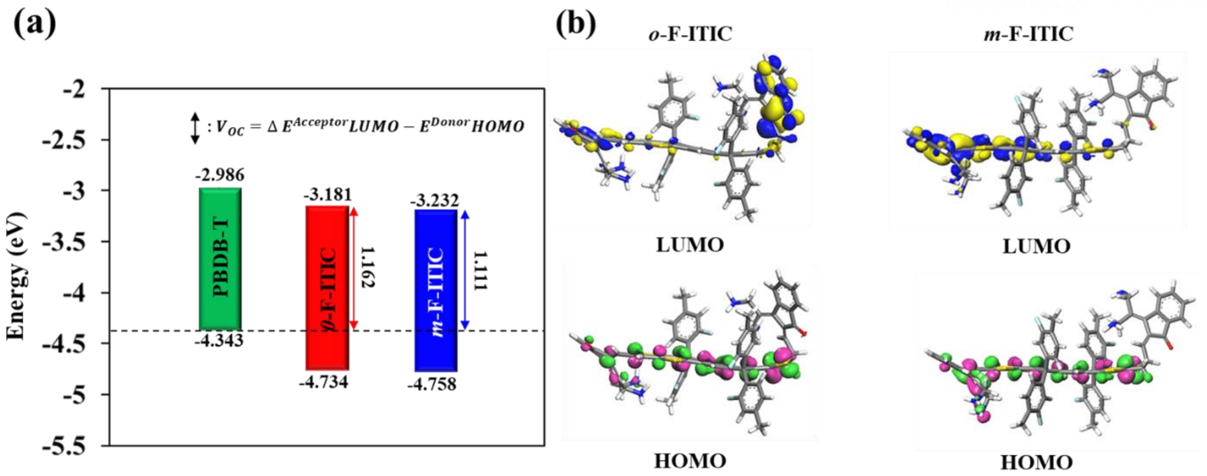

Figure 4.4. (a) Energy diagram of the PBDB-T, o-F-ITIC, and m-F-ITIC. (b) Electron density distributions of HOMO and LUMO for optimized o-F-ITIC and m-F-ITIC. Gray, yellow and light blue represents carbon, sulfur and fluorine atoms, respectively.

Computational Study

The origin of difference in V_{OC} values is not yet clear at the current stage. Therefore, we carried out an additional density functional theory (DFT) calculations (GGA/PBE).[50] For both F-ITICs, in addition to the similar electron density distributions, the calculated energy levels show the same trend as observed in the CV and UPS data. The somewhat higher-lying HOMO level of *o*-F-ITIC is partially correlated with the higher V_{OC} in o-F-ITIC-based device (**Figure 4.4**). To understand the overall picture of the donor–acceptor intermolecular interactions and/or arrangements, we carried out an in-depth simulation study. First, by using all-atom molecular dynamics (AAMD), we predicted the stacked structures of the intermolecular complex formed between the F-ITIC acceptors and PBDB-T donor (**Figure 4.5a** and **4.5b**), showing a closer interaction between PBDB-T and *o*-F-ITIC with each other by ~0.11 nm relative to the PBDB-T and *m*-F-ITIC case (**Figure 4.6a**). Here, the trimer repeating units as a model of PBDB-T polymer was set up for the AAMD study. In addition, the intermolecular interaction behaviors were further traced by the radial distribution function (RDF), where each main backbone of PBDB-T and F-ITICs was arbitrarily divided into two constituting components [i.e., electron-rich donor–electron-deficient acceptor moieties, such as benzodithiophene (BDT)–dithienylbenzodithiophenedione (BDD) and IDT–DCI building units] (see **Figure 4.5c**). For the PBDB-T:*o*-F-ITIC-based stacking state, the BDT, rather than *BDD*, unit of PBDB-T closely interacted with the DCI units of *o*-F-ITIC, whereas more interaction between the BDD of PBDB-T and DCI units of *m*-F-ITIC was observed in the *m*-F-ITIC-based device (**Figure. 4.5d** and **4.5e**). Such different arrangements were furthermore shown by the binding configurations of the favorable DCI–BDT and DCI–BDD complexes formed from each of *o*-F-ITIC- and *m*-F-ITIC-stacked structures, respectively (**Figure 4.5f** and **4.5g**). Note also that we observed face-to-face alignment between DCI of *o*-F-ITIC and BDT molecular planes (plane angle = ~97°) compared to the DCI of *m*-F-ITIC and BDD cases (plane angle = ~70°).

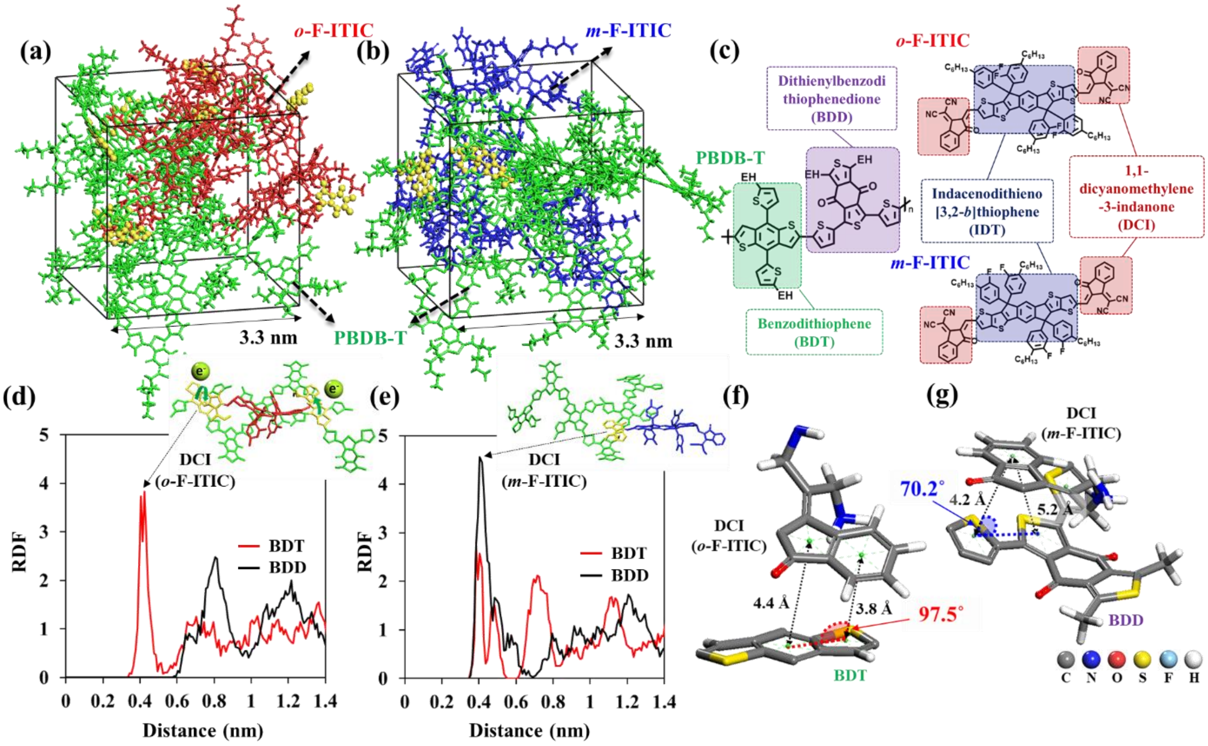

Figure 4.5. Final configurations of (a) PBDB-T:*o*-F-ITIC and (b) PBDB-T:*m*-F-ITIC from AAMD simulation. Stacked DCI and BDT are shown in yellow color. (c) Division into two constituent components by the electron-rich donor and electron-deficient acceptor moieties of PBDB-T, *o*-F-ITIC and *m*-F-ITIC. RDF between the backbone of PBDB-T and the DCI unit of (d) *o*-F-ITIC and (e) *m*-F-ITIC. Stacking states of PBDB-T and F-ITICs are shown and black arrows indicate the stacking sites. Stacking states between (f) the BDT unit of PBDB-T and the DCI unit of *o*-F-ITIC and (g) the BDD unit of PBDB-T and the DCI unit of *m*-F-ITIC.

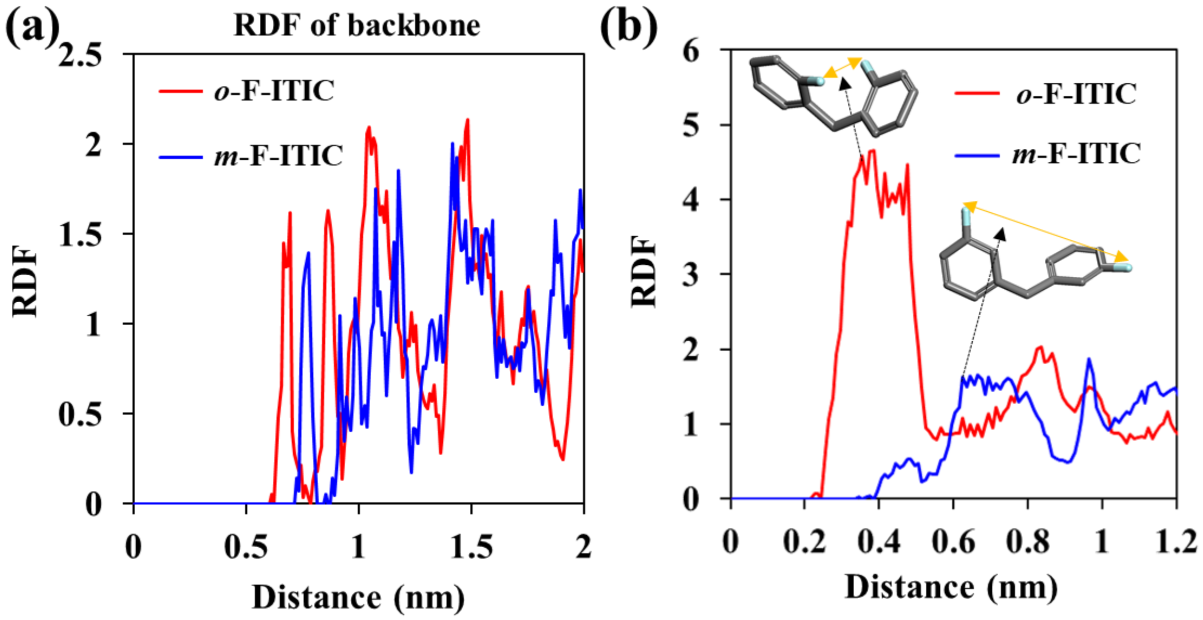

Figure 4.6. (a) Radial distribution function (RDF) of backbone of PBDB-T and F-ITICs; (b) RDF of fluorine atoms in o-F-ITIC and m-F-ITIC. Insets show the structure of fluorine atoms in o-F-ITIC and m-F-ITIC.

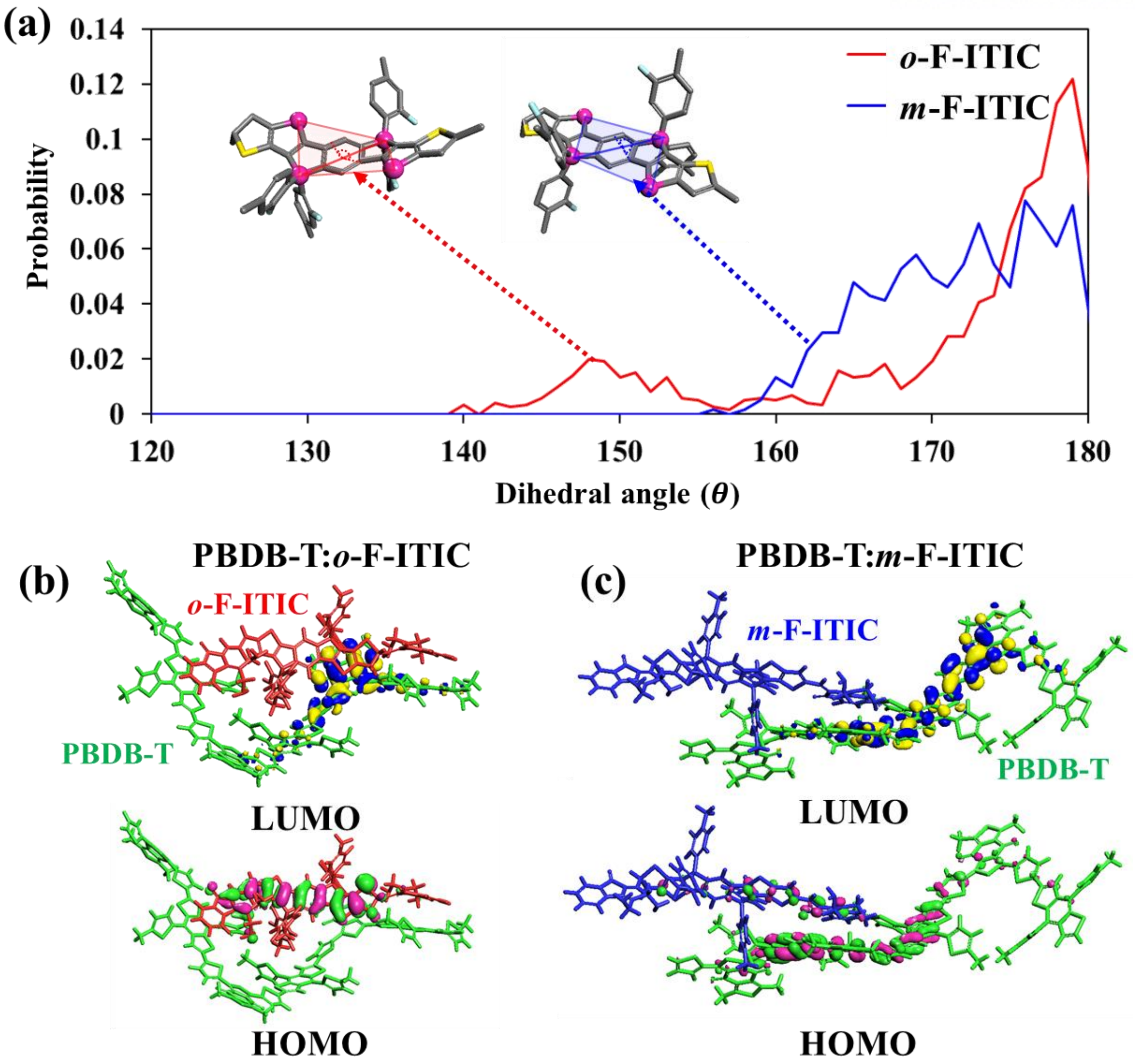

Figure 4.7. (a) Probability distribution of dihedral angles of the backbone of F-ITICs. Insets show the dihedral angles and dark pink indicates the atoms for measurement of dihedral angles. Grey, yellow and light blue represent carbon, sulfur and fluorine atoms, respectively. Electron density distributions of the HOMO and LUMO for optimized (b) PBDB-T:*o*-F-ITIC and (c) PBDB-T:*m*-F-ITIC.

The probability distribution of dihedral angles of the fused IDT core of the F-ITICs shows that the IDT core of *o*-F-ITIC has a wider range for the dihedral angles than that of *m*-F-ITIC (**Figure 4.7a**). This observation can be reasonably explained by the relatively high repulsive force between neighboring *ortho*-fluorine atoms on the side chains of the *o*-F-ITIC, which are at a closer distance than *meta*-fluorine ones in the *o*-F-ITIC case (**Figure 4.6b**). Therefore, the IDT core backbone of *o*-F-ITIC favors a slightly curved structure, thereby providing the unique parallel-like DCI–BDT packing, as observed in the stacked structure. In contrast, the relatively unbent IDT core of *m*-F-ITIC did not encourage a parallel-like DCI–BDD stacking structure with PBDB-T. These behavioral characteristics helped to understand why a higher population of the DCI–BDT stacked complex was observed in the configuration of PBDB-T:*o*-F-ITIC versus DCI–BDD of PBDB-T:*m*-F-ITIC (see the yellow-colored molecules in **Figure 4.5a** and **4.5b**). Furthermore, such varied configurations influence the electron density distributions of HOMO and LUMO for the optimized stack structures. For PBDB-T:*o*-F-ITIC, the LUMO is mainly localized on PBDB-T, whereas the HOMO is concentrated on *o*-F-ITIC. On the other hand, PBDB-T:*m*-F-ITIC has both LUMO and HOMO more distributed on PBDB-T units (**Figure 4.7b** and **4.7c**). Superficially, relative to PBDB-T:*m*-F-ITIC, the PBDB-T:*o*-F-ITIC system is expected to be favorable for charge transfer.

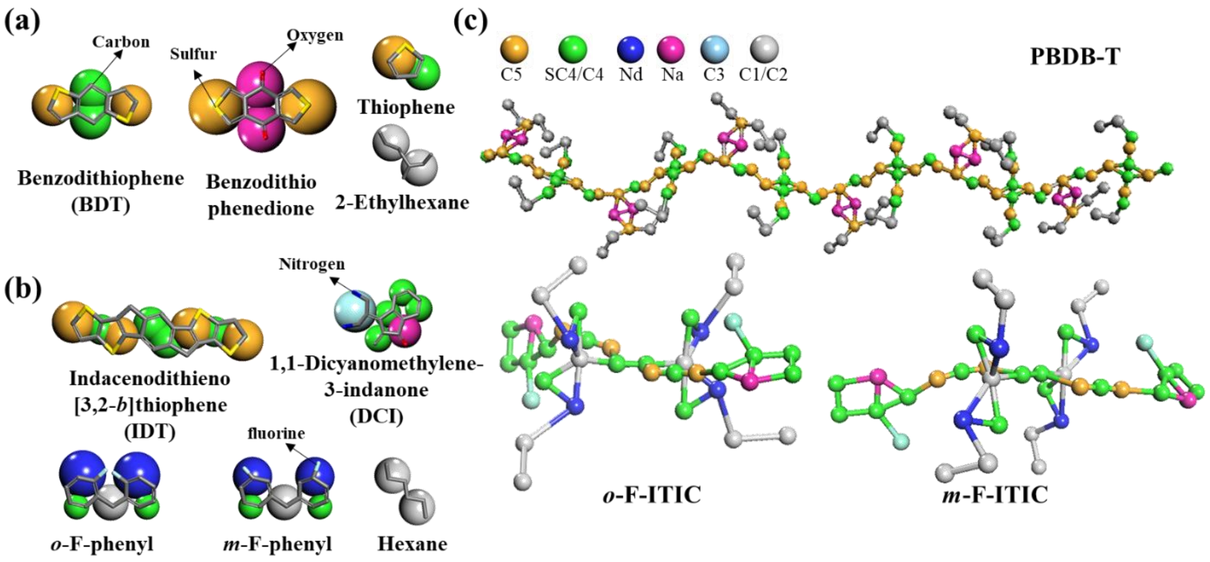

Figure 4.8. Coarse-grained models of (a) PBDB-T and (b) F-ITICs. (c) PBDB-T and F-ITICs are shown with constituent CG beads. Martini bead types for CG beads are shown in the figure and hydrogen atoms are not shown in all atom model for clarity.

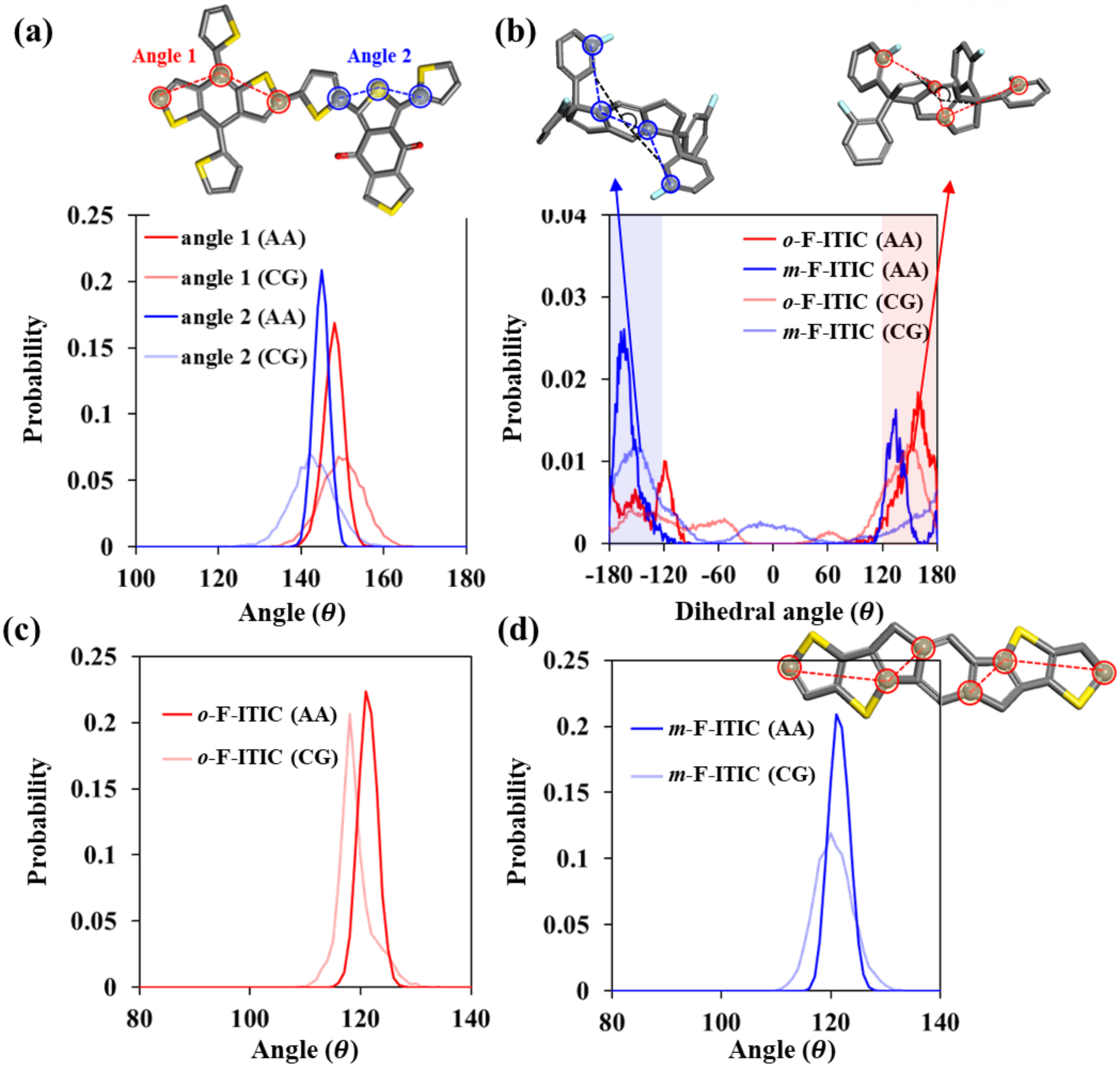

Figure 4.9. (a) Probability distributions of angles in backbone of PBDB-T and angles are shown above the graph. (b) Probability distributions of dihedral angles of o-F-ITIC and m-F-ITIC. Insets show the dihedral angle. Probability distributions of angles in backbone of (c) o-F-ITIC and (d) m-F-ITIC. Angles are shown above the graph. AA and CG represent the results of allatom and coarse-grained model, respectively.

To gain more insights into the macroscopic morphology induced by the PBDB-T:F-ITICs complexes, we investigated, through the coarse-grained molecular dynamics (CGMD) using Martini force field, where the PBDB-T chains containing six repeating units were used for CGMD model.[51] The CG models and their structural properties (e.g., various angle distributions in the backbones of each molecule) are described in detail (**Figure 4.8** and **4.9**). The number densities of both stacked structures, which represent the number of CG beads projected on the *x*-*y* plane per unit area, are shown in **Figure 4.10a** and **4.10**, which indicate that PBDB-T:*o*-F-ITIC has larger interface areas with a higher density compared to PBDB-T:*m*-F-ITIC. Additionally, the average surface areas are estimated to be 178.1 nm^2 and 163.5 nm^2 for PBDB-T:*o*-F-ITIC and PBDB-T:*m*-F-ITIC, respectively (**Figure 4.10c**), wherein the PBDB-T backbone is less folded in the PBDB-T:*o*-F-ITIC, which is evidenced by a comparison of the end-to-end distance of PBDB-T in the stacked structures (**Figure 4.10d**).

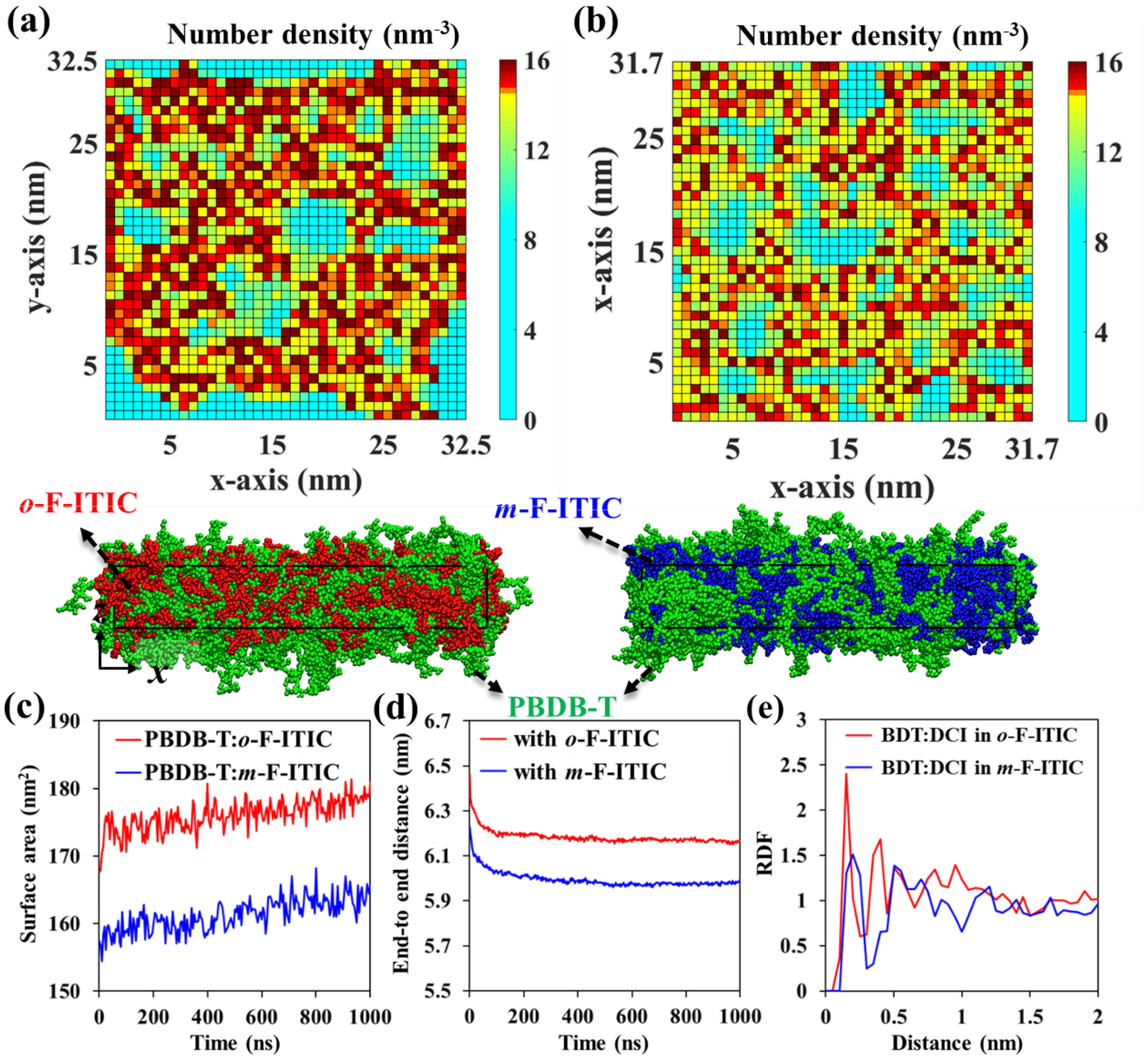

Figure 4.10. The 2-dimensional number density and morphology of thin films of (a) PBDB-T:*o*-F-ITIC and (b) PBDB-T:*m*-F-ITIC from CGMD simulation. Thickness of thin films was ~5.5 nm. (c) Solvent-accessible surface area between the backbones of PBDB-T and F-ITICs. (d) End-to-end distance of PBDB-T in the thin film with F-ITICs. (e) RDF of DCI of F-ITICs and BDT of PBDB-T in thin films.

Additionally, as shown in **Figure 4.10e**, the CGMD-derived RDF result provides further confirmation of a stronger DCI–BDT interaction in PBDB-T:*o*-F-ITIC found through the AAMD analysis. Collectively, the thorough theoretical studies demonstrate that changing the position of the fluorine atom within the side chains of the acceptors significantly influences the intermolecular stacking arrangement when admixed with the counterpart donor polymer, giving rise to significant difference in the BHJ device performances, as the most likely factor in differentiating charge carrier dynamics (e.g., exciton dissociation, charge transport, and charge recombination).

Charge Generation, Dissociation, and Transport Properties

To better understand this significant difference between the devices based on the two isomers *o*-F-ITIC and *m*-F-ITIC, the carrier hole (μ_h) and electron (μ_e) mobilities of all blends were first estimated by using the space charge limited current (SCLC) method (**Figure 4.11a**).[52-54] Despite the observation of similar μ_h values for both the blends (~5.0×10^{-4} cm^2 V^{-1} s^{-1}), the μ_e value (4.1×10^{-4} cm^2 V^{-1} s^{-1}) of the *o*-F-ITIC blend film is almost an order of magnitude higher than that for the *m*-F-ITIC-based one (3.7×10^{-5} cm^2 V^{-1} s^{-1}). Consequently, the μ_h/μ_e ratios are more balanced for the *o*-F-ITIC blend film (1.32) compared to the *m*-F-ITIC film (13.8). These features should be very beneficial in not only promoting charge carrier transport to the electrodes but also reducing the build-up of space charges. Note that we also measured the μ_es of the neat F-ITIC films, revealing the *o*-F-ITIC ($\mu_e = 4.8 \times 10^{-4}$ cm^2 V^{-1} s^{-1}) versus *m*-F-ITIC ($\mu_e = 9.4 \times 10^{-5}$ cm^2 V^{-1} s^{-1}).

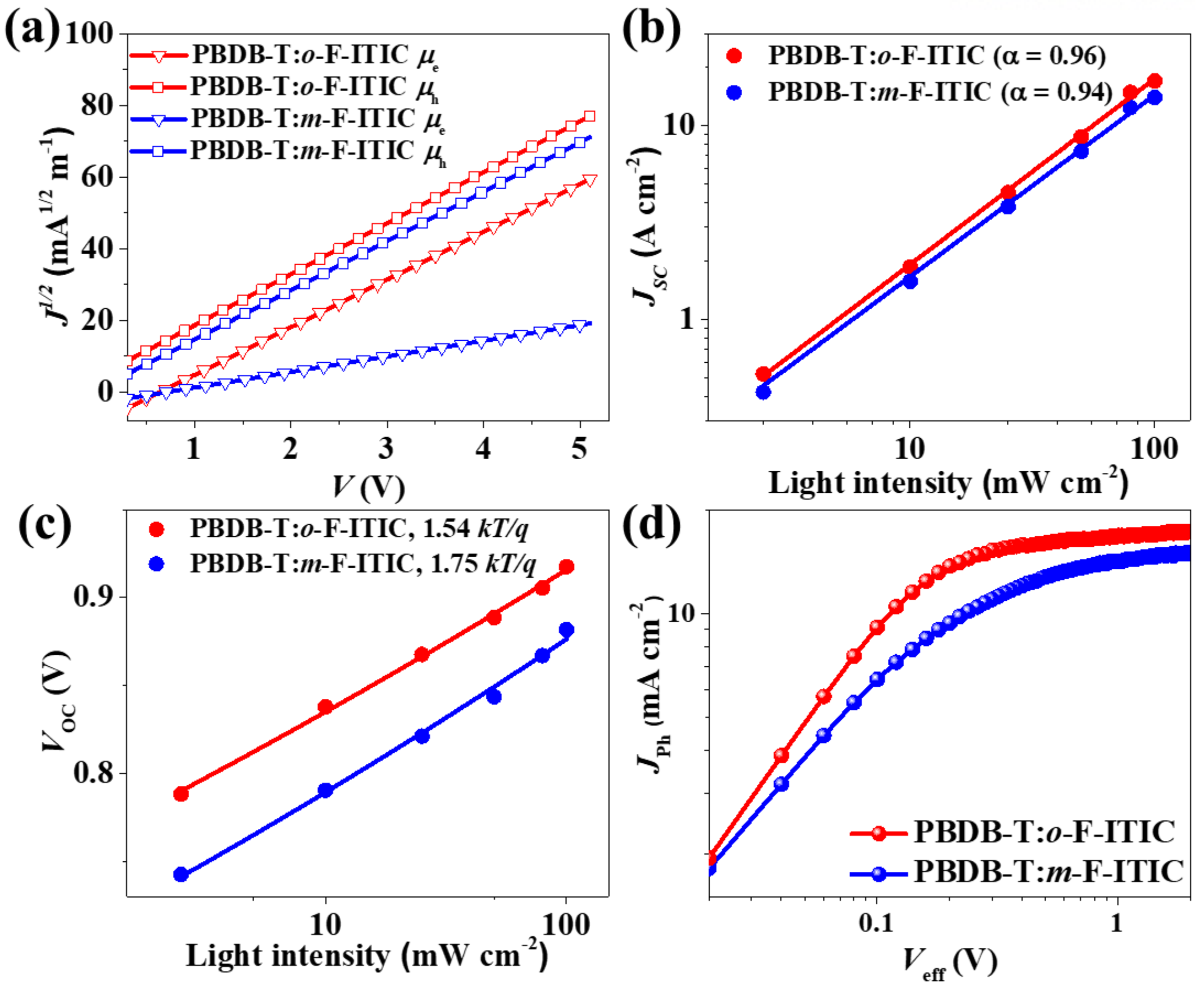

Figure 4.11. (a) Electron-only and hole-only SCLC fitting of PBDB-T:F-ITIC photovoltaic cells. (b) J_{SC} as a function of light intensity and the corresponding α values of PBDB-T:o-F-ITIC (α = 0.96) and PBDB-T:m-F-ITIC (α = 0.94). (c) V_{OC} as a function of light intensity and the corresponding slope values of PBDB-T:o-F-ITIC (1.54 κ*T*/q) and PBDB-T:m-F-ITIC (1.75 κ*T*/q). (d) J_{Ph} versus V_{eff} characteristics of the optimized devices with PBDB-T:F-ITICs.

The charge recombination mechanism in the devices was evaluated by analyzing their *J*–*V* characteristics as a function of light intensity (*P*) (**Figure 4.11b**). In general, the J_{SC} and *P* values follow the power-law functional relationship $J_{SC} \propto P^{\alpha}$, where *α* represents the exponential factor related to bimolecular recombination.[55, 56] The *α* values of *o*-F-ITIC- and *m*-F-ITIC-based devices are 0.96 and 0.94, respectively, suggesting that the bimolecular recombination is somewhat more suppressed in the *o*-F-ITIC-based device. This correlates well with the charge carrier transport properties discussed earlier. Additionally, the V_{OC} dependence on *P* could be expressed by the natural logarithmic formula of $V_{OC} \propto n(\kappa T/q)\ln P$, where κ, *T*, and *q* are the Boltzmann constant, temperature, and elementary charge, respectively. As shown in **Figure 4.11c**, the fitted *n* for the *o*-F-ITIC- and *m*-F-ITIC-based OSCs are 1.54 and 1.75, respectively, indicating that the geminate or Shockley–Read–Hall recombination occurs to a somewhat reduced extent in the *o*-F-ITIC-based device.[55, 56]

Furthermore, photogenerated current density (J_{ph}) versus effective voltage (V_{eff}) curves were plotted to evaluate the exciton dissociation and charge collection in the two devices (**Figure 4.11d**). The J_{ph} ($J_{ph} = J_L - J_D$) is obtained by subtracting the current density in the dark (J_D) from the current density under light (J_L); V_{eff} is defined as $V_0 - V_a$, where V_0 and V_a can be obtained during test J_L and J_D.[57, 58] J_{ph} reaches the saturation value (J_{sat}) at $V_{eff} > 1.0$ V for all devices, at which point, all photogenerated excitons dissociate into free charge carriers and collect at the electrodes. A higher J_{sat} value for the *o*-F-ITIC-based device is observed, indicating an enhancement in charge generation. The charge recombination probability (J_{ph}/J_{sat}) can be extracted from $J_{ph} - V_{eff}$ under the short-circuit condition. Under the short-circuit condition, the J_{ph}/J_{sat} values in the *o*-F-ITIC-based and the *m*-F-ITIC-based systems are 98% and 94%, respectively, implying that the *o*-F-ITIC-based device reduces geminate recombination loss.[57, 58] Furthermore, at the maximum power output condition, the *o*-F-ITIC-based device (89%) also shows a higher J_{ph}/J_{sat} than that of the *m*-F-ITIC-based device (68%). These results confirm that better exciton dissociations and charge carrier extractions occur in the *o*-F-ITIC-based device relative to the *m*-F-ITIC-based device. Overall, the superior charge generation, dissociation, and transport properties of the *o*-F-ITIC-based OSC are in accordance with the enhanced J_{SC} and *FF* values. Considering that such electrical discrepancy between the devices based on isomers *o*-F-ITIC and *m*-F-ITIC should have a strong correlation with the different BHJ blend morphologies, as evidenced by the afore-mentioned simulation studies, detailed investigations on the morphological characteristics of the two blends are conducted and discussed in the following section.

Morphological Characterization

First, the surface and bulk morphologies of the blend films were examined by using atomic force spectroscopy (AFM) and scanning transmission electron microscopy (STEM) measurements. The AFM images, as shown in **Figure 4.12a** and **4.12e**, reveal that the *o*-F-ITIC-based blend has a slightly smoother surface with a smaller root-mean square (RMS) of 1.79 nm (versus 2.03 nm for the *m*-F-ITIC-based blend). This could be the result of the different intermolecular interactions and aggregations of the two acceptor isomers with the PBDB-T counterpart donor. From the STEM images, shown in **Figure 4.12c** and **4.12g**, the *o*-F-ITIC-based blend shows a finely distributed fibril-like structure, indicating that *o*-F-ITIC was well spread in the PBDB-T polymer matrix. In contrast, some *m*-F-ITIC aggregates appear as dark spots in the TEM image of the *m*-F-ITIC-based blend. The obvious difference in the blend morphologies is further elucidated by the energy dispersive X-ray analysis (EDAX) (**Figure 4.12d** and **4.12h**), wherein, relative to *m*-F-ITIC, the greenish-dots derived from fluoride atoms of the *o*-F-ITIC acceptor are well dispersed throughout. The finely intermixed morphology between PBDB-T and *o*-F-ITIC components can induce large donor-acceptor interface areas, as confirmed by the CGMD results discussed earlier, thereby facilitating favorable photocurrent generation and transport and leading to an improved performance of the *o*-F-ITIC-based OSC.

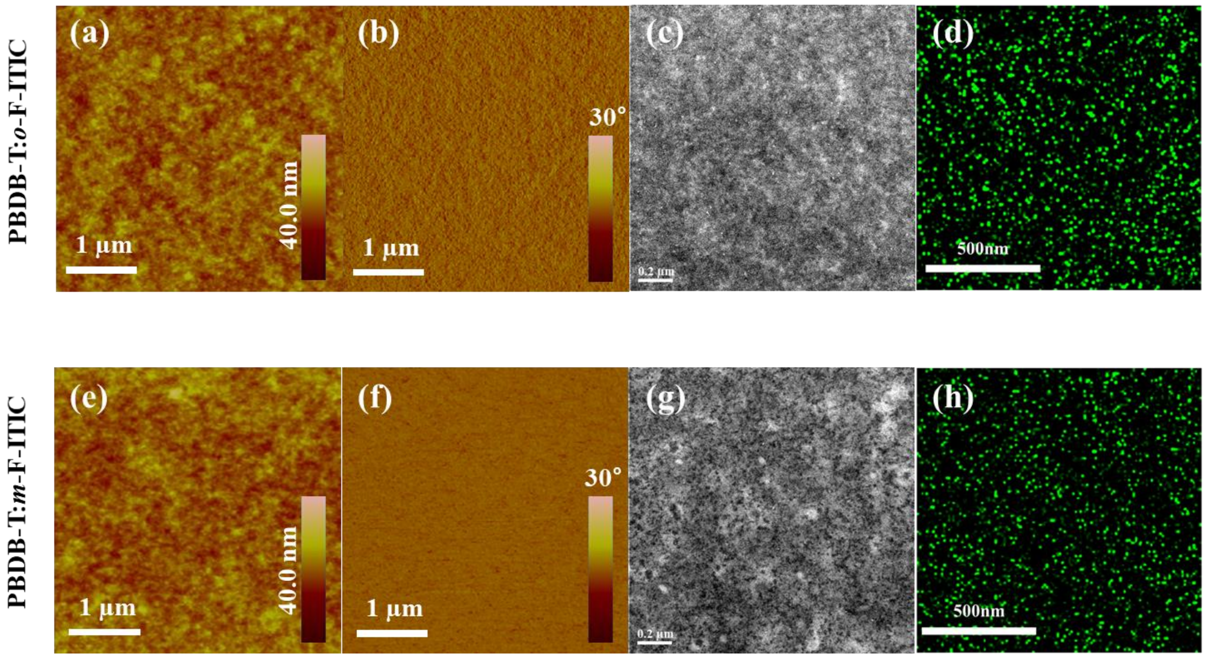

Figure 4.12. AFM, STEM, and EDAX elemental mapping of fluorine element with blend films composed of PBDB-T:*o*-F-ITIC (a-d) and PBDB-T:*m*-F-ITIC (e-h), respectively.

Molecular ordering and interchain organization of PBDB-T and F-ITICs for neat and blend films were further investigated by using the grazing-incidence wide-angle (GIWAXS) analysis.[59] As shown in **Figure 4.13a** and **4.13b**, both neat F-ITIC acceptor films exhibit the in-plane (IP) lamellar (100) scattering and a strong out-of-plane (OOP) π-π stacking (010) peak, implying a preferential face-on crystalline orientation. It is interesting to note that the calculated π-π stacking distance of the *o*-F-ITIC film (3.6 Å) is smaller than that of *m*-F-ITIC (4.1 Å), partially explaining the observed higher μ_es of *o*-F-ITICs relative to *m*-ITIC in both neat and blend cases. Moreover, a closer look reveals a more-resolved anisotropic IP lamellar peak in the *o*-F-ITIC film, which is most likely related to the different self-organization behaviour as a function of the fluorine position on the side chains. Note also that the crystallite coherence lengths (CCL$_{010}$) calculated by using the Scherrer equation[60] are 2.14 nm for the *o*-F-ITIC film and 1.03 nm for the *m*-F-ITIC film, which signifies a higher crystalline feature of *o*-F-ITIC. One can conclude that *o*-F-ITIC has quite more ordered molecular packing with the higher crystalline feature, which is favorable for electron transport. On the other hand, the azimuthal (100) peak and the OOP π-π stacking (010) peak were observed in the neat PBDB-T film reported in our previous work.[61]

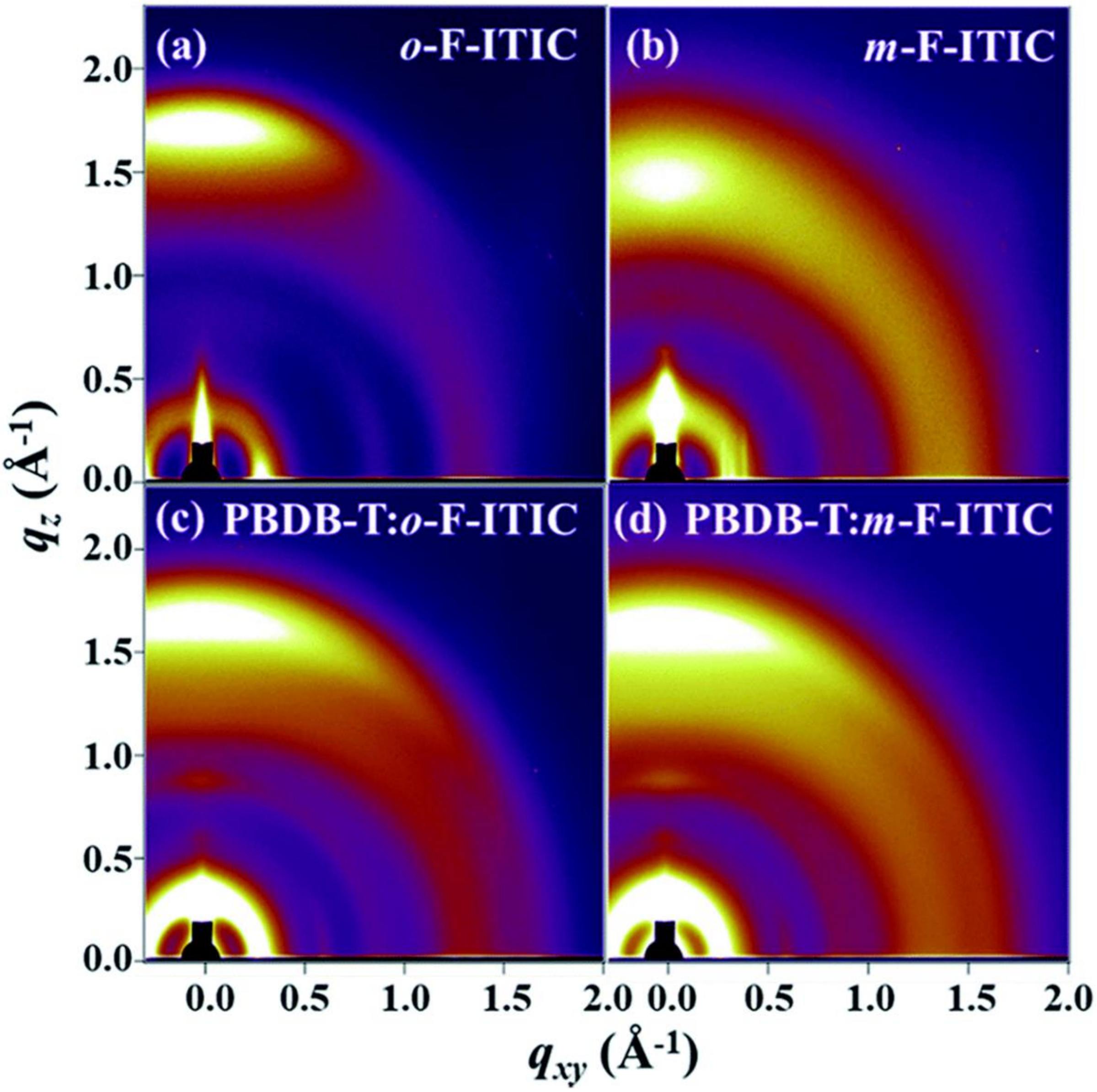

Figure 4.13. 2D GIWAXS images with films composed of (a) *o*-F-ITIC, (b) *m*-F-ITIC, (c) a blend of PBDB-T:*o*-F-ITIC, and (d) a blend of PBDB-T:*m*-F-ITIC, respectively.

Both the blend films produced an OOP (010) π-π stacking peak centered at 1.6–1.7 Å^{-1} with an arc-like lamellar (100) peak at 0.29 Å^{-1}. Looking cursorily at the images in **Figure 4.13c** and **4.13d**, it is rather difficult to make out the difference between GIWAXS pattern comparisons for both the blends because of the overlaps of the peaks induced by two PBDB-T and F-ITICs. However, on a closer examination of the GIWAXS parameters, it can be found that the PBDB-T:*o*-F-ITIC blend shows a slightly larger CCL_{010} together with a smeller π-stacking distance compared to that of PBDB-T:*m*-F-ITIC. This trend provides the evidence for the enhanced phase purity between PBDB-T and *o*-F-ITIC induced by the well-intermixed blend morphology, which is consistent with the afore-mentioned morphological and theoretical results.

Photophysics

The exciton generation and charge transfer of photo-induced carriers were further investigated by transient absorption (TA) measurements. The TA spectra of the neat films were first collected by employing two distinct pump wavelengths of 500 nm and 710 nm for the PBDB-T donor and F-ITIC acceptors, respectively, which allowed the temporal evolution of the TA signals to be extracted for the individual component (see **Figure 4.14**). Next, the pump-induced differential change in the probe transmission, $\Delta T/T = (T_{\text{pump-on}} - T_{\text{pump-off}})/T_{\text{pump-off}}$, was measured. At each selected excitation, the PBDB-T donor and F-ITIC acceptors gave broad photo-induced absorptions centered at ~640 nm and ~730 nm, respectively (**Figure 4.16a**). With excitation at 710 nm, no bleaching signal was found in the neat PBDB-T, which was only excited at 500 nm; however, both the neat F-ITIC acceptors gave bleaching signals at ~650 nm and ~730 nm (**Figure 4.14** and **4.15**). For both the blends excited at 710 nm, in addition to the signals of F-ITIC acceptors, bleaching signals below 640 nm derived from the PBDB-T were observed (**Figure 4.16b**). In both blends, we observed an increase in the bleaching signals of PBDB-T (<640 nm), accompanied by the decay of the signals of F-ITICs. It is apparent on the shorter time scale TA data in the blend films with respect to the corresponding neat F-ITIC acceptors (**Figure 4.17a** and **4.17b**), which is indicative of the faster hole transfer in the blends. The early-stage decay kinetics of excitons are also characterized by an exponential fit, as shown in **Figure 4.16c**. A shorter decay lifetime parameter (2.9 ps) is observed for the *o*-F-ITIC-based blend (versus 4.2 ps for the *m*-F-ITIC-based blend), thereby suggesting its more efficient hole transfer process.

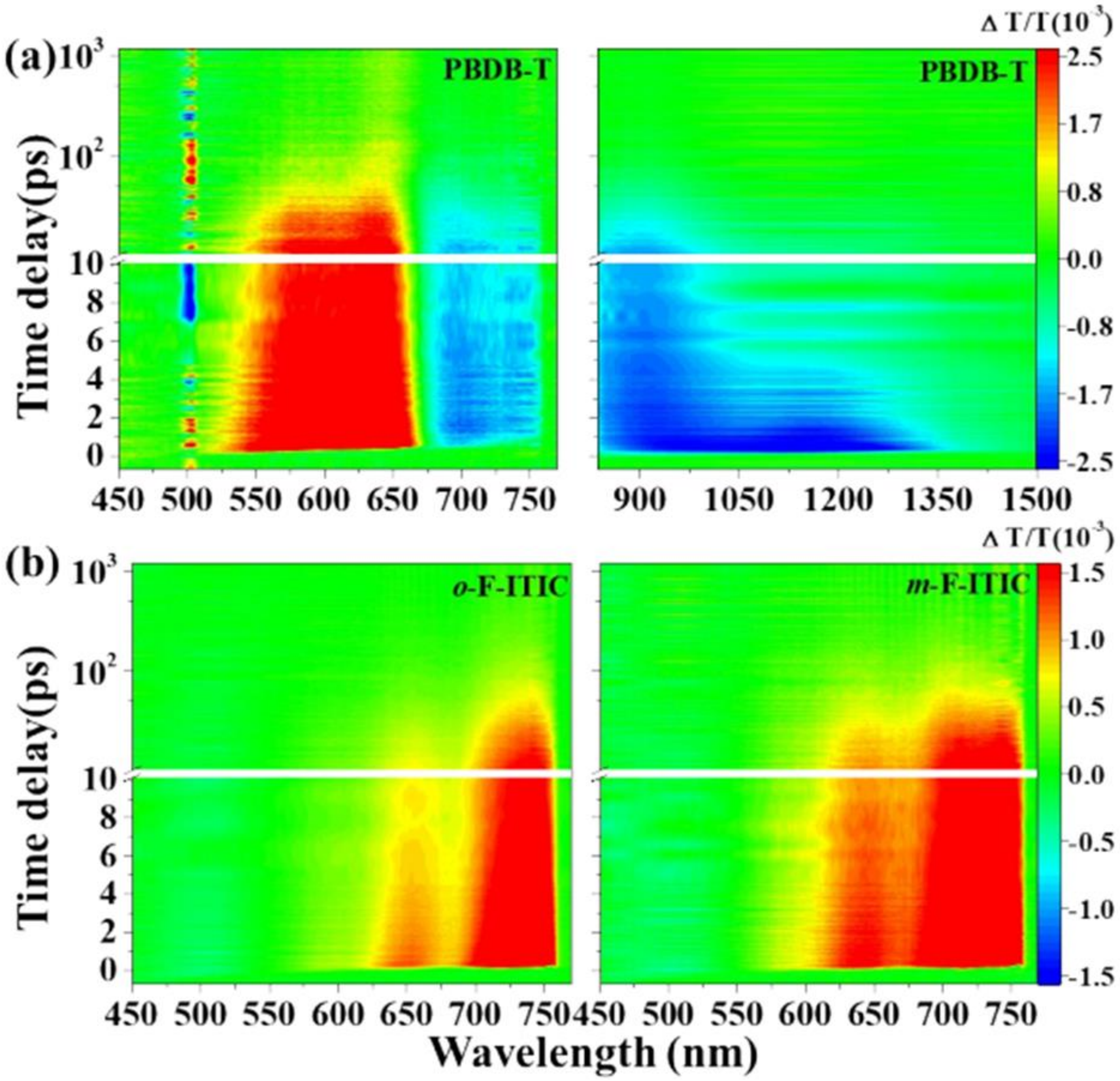

Figure 4.14. TA signal recorded from (a) the neat film of PBDB-T excited by 500 nm and (b) the neat film of o-F-ITIC and m-F-ITIC excited by 710 nm.

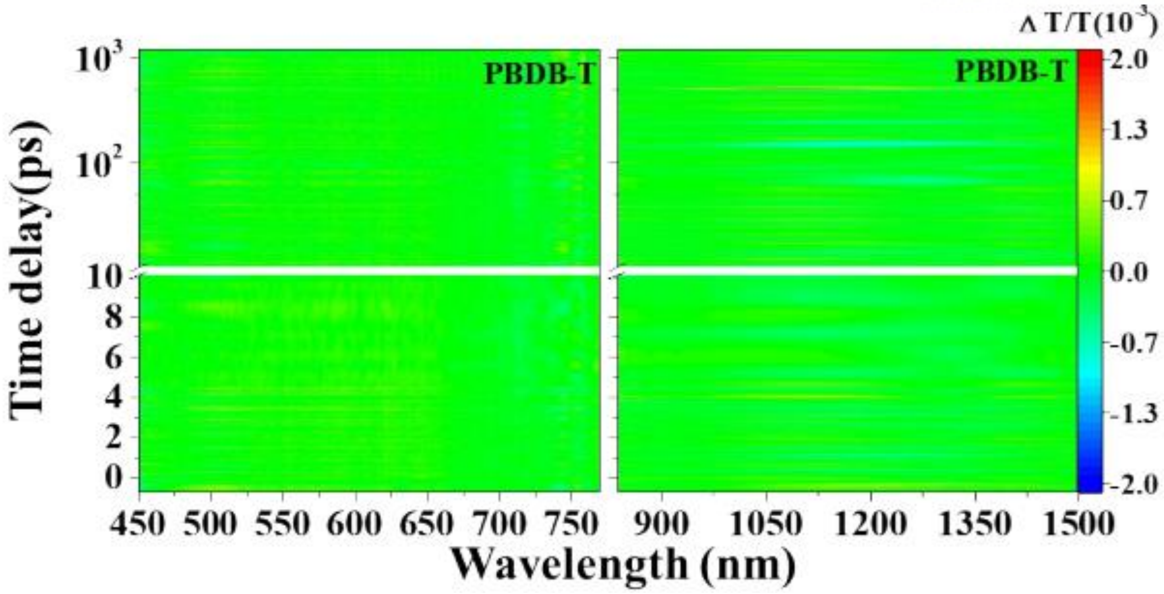

Figure 4.15. TA signal recorded from the neat film of PBDB-T excited by 710 nm.

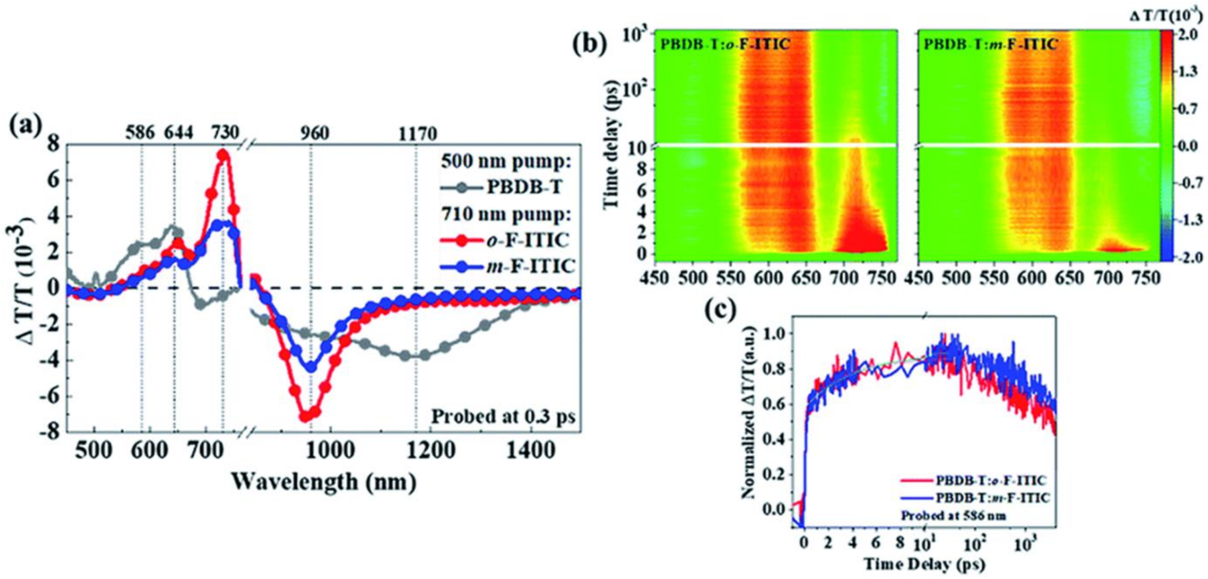

Figure 4.16. (a) TA spectra from the neat PBDB-T and F-ITICs collected at an excitation pump wavelength of 500 nm and 710 nm, respectively. (b) TA signal and (c) TA dynamics curves probed at 586 nm recorded from the films of PBDB-T:F-ITIC blends excited at a pump wavelength of 710 nm.

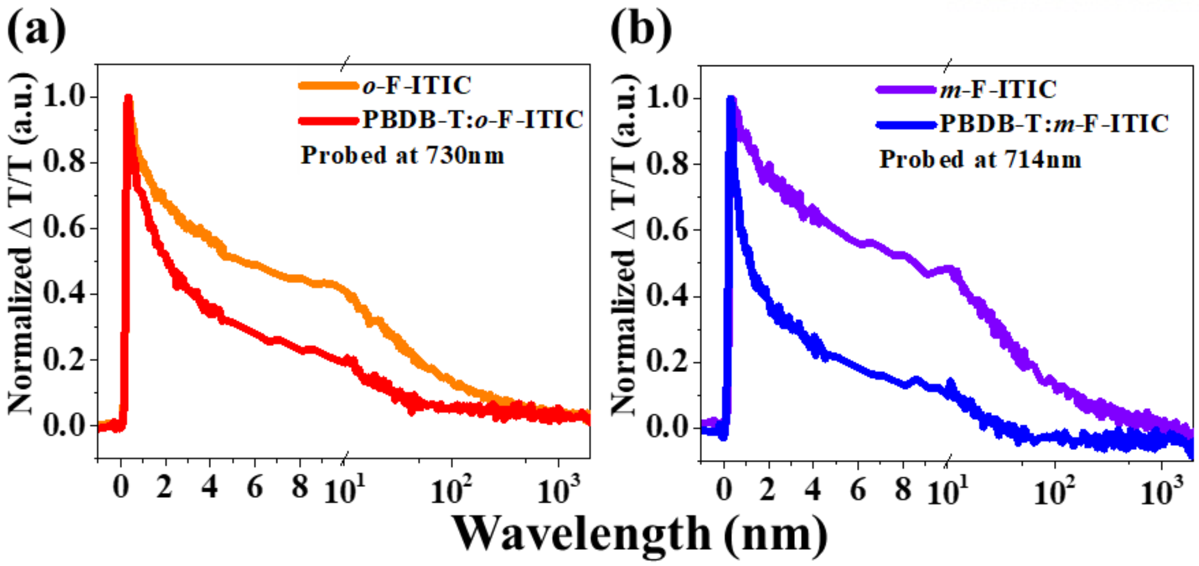

Figure 4.17. TA dynamics (a) probed at 730 nm recorded from the films of neat o-F-ITIC and blend PBDB-T:o-F-ITIC and (b) probed at 714 nm recorded from the films of neat m-F-ITIC and blend PBDB-T:m-F-ITIC.

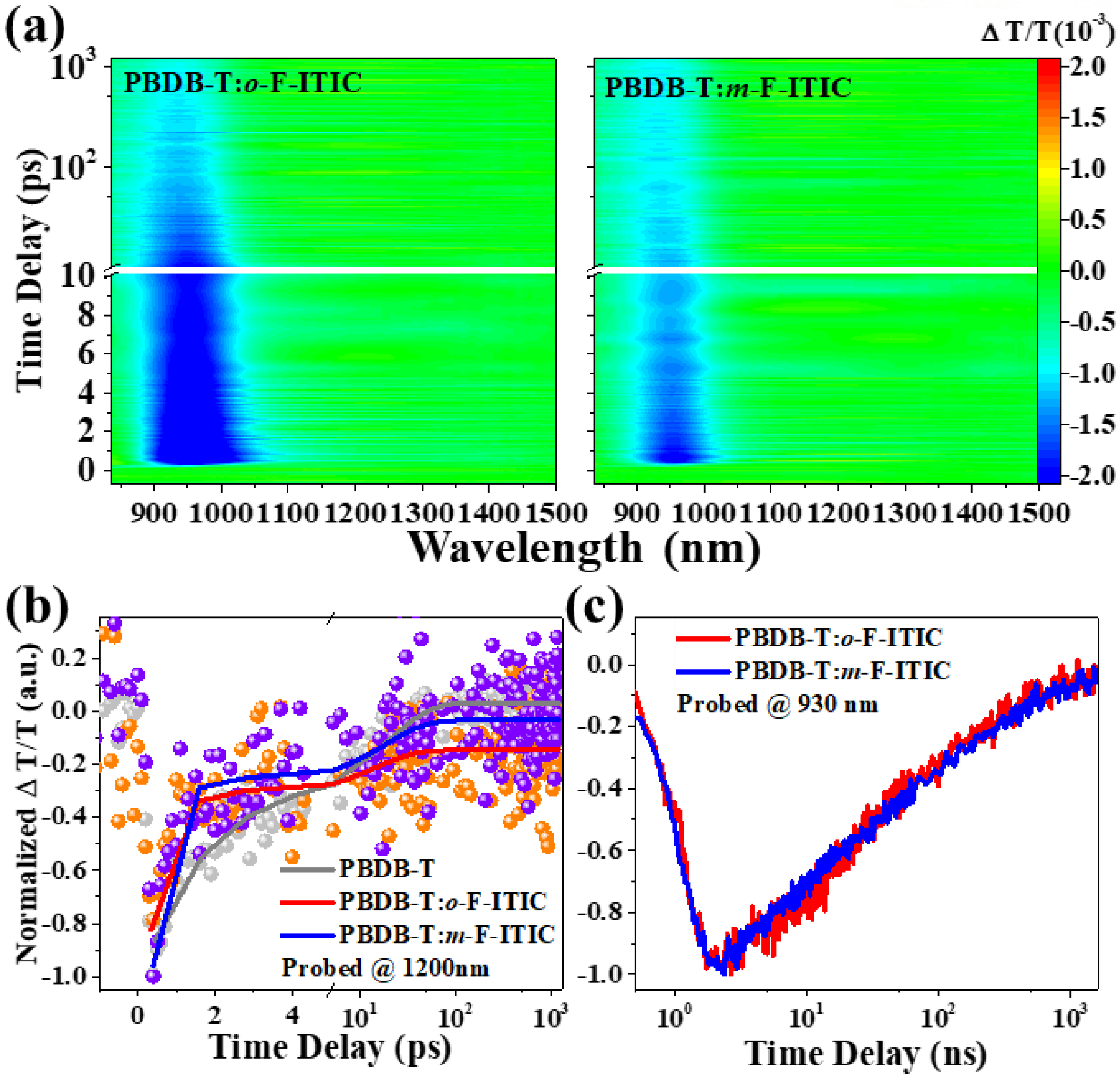

Figure 4.18. (a) TA signal recorded from the films of PBDB-T:F-ITIC blends excited at 500 nm. (b) TA dynamics curves probed at 1200 nm recorded from the films of neat PBDB-T and blend PBDB-T:F-ITICs. (c) Nanosecond-resolved dynamics for the polaron ESA band of PBDB-T:F-ITIC blend films probed at 930 nm with bi-exponential fitting.

Revisiting the TA data shown in **Figure 4.16a**, the neat PBDB-T and F-ITICs clearly featured very broad excited state absorption (ESA) peaks centered at ~960 nm and ~1200 nm, respectively. Therefore, we measured the TA spectra of both the blends (PBDB-T:*o*-F-ITIC and PBDB-T:*m*-F-ITIC) with the donor excited at 500 nm to further investigate the charge transfer between the donor and acceptor components. In both the blends, as shown in **Figure 4.18a**, only the ESA signal at ~960 nm, mainly assigned to F-ITICs, appeared without the signal at ~1170 nm seen in the neat film of PBDB-T (**Figure**

4.14a), thereby suggesting proper electron transfer from photo-excited PBDB-T to the F-ITIC acceptors. Note that PBDB-T:*o*-F-ITIC shows a higher intensity ESA signal than that of PBDB-T:*m*-F-ITIC, which is consistent with the trend of the bleaching signals induced by the blends excited at 710 nm. Moreover, both the blends exhibited a shorter bi-exponential fitting decay lifetime of the ESA signals around 1200 nm (0.36–0.41 ps) than that of the neat PBDB-T donor film (1.52 ps) (**Figure 4.18b**), which is again similar to the above TA data with the excitation at 710 nm. However, a very small difference between the lifetimes of two blends makes it difficult for us to conclude that the higher PCE of PBDB-T:*o*-F-ITIC is stemmed from this process just from our fitting results of the electron transfer rate. Therefore, we further analyzed the polaron lifetimes of both blend films from the polaron ESA band probed at 930 nm by using the nanosecond-resolved TA measurement (**Figure 4.18c**). Here, compared to the *m*-F-ITIC-based one (10.95 ns and 214.68 ns), the *o*-F-ITIC-based blend clearly exhibited longer polaron lifetimes (20.88 ns and 257.23 ns), which implied an increased polaron generation in this device through the reduced recombination mechanism, which may explain the reason why the EQE curve of PBDB-T:*o*-F-ITIC exceeds that of PBDB-T:*m*-F-ITIC around 500 nm.

4.3 Conclusion

In summary, this study provides the synthesis and characterization of two new ITIC-based isomeric acceptors (*o*-F-ITIC and *m*-F-ITIC) with fluorine atoms at *ortho* and *meta* positions within the side chains, with the aim to study the fluorine-positioning effect on the intermolecular interaction with the donor counterpart (PBDB-T) strongly associated with BHJ OSC performances. We observe a significant difference between the OSCs based on the two isomers, which makes the different donor–acceptor intermolecular interactions and/or arrangements evident. In particular, the PBDB-T:*o*-F-ITIC device (PCE = 11.11%) outperforms the PBDB-T:*o*-F-ITIC device (PCE = 8.90%), with all its photovoltaic parameters higher than those of PBDB-T:*m*-F-ITIC. From detailed simulation studies, we found that the PBDB-T:*o*-F-ITIC system has a closer donor–acceptor interaction with a tightly stacked parallel-like DCI–BDT complex, leading to larger interfacial areas with a higher density, compared to PBDB-T:*m*-F-ITIC possessing a favorable DCI–BDD complex. These results correlate quite well with the observation of enhanced electrical characteristics (*e.g.*, charge transport, generation, and recombination loss) in PBDB-T:*o*-F-ITIC, attributed to the well-intermixed blend morphology. Moreover, it appears from TA spectra that PBDB-T:*o*-F-ITIC has more efficient hole/electron transfer and separation processes relative to PBDB-T:*m*-F-ITIC. The theoretical and experimental results presented here demonstrate that even changing only the position of a single atom (popularly called constitutional isomerism) in the side chains can significantly affect the donor–acceptor interaction properties in blends. This finding can open new pathways to evaluate the structure–property–performance relationships.

4.4 Experimental Section

Materials and Characterization

All starting materials were purchased from Aldrich and Acros and used without further purification. All solvents are of ACS grade unless otherwise noted. Diethyl-2,5-bis(thieno[3,2-*b*]thiophene-2-yl)terephthalate (**2**),[62] 1,1-dicyanomethylene-3-indanone (DCI),[63] and poly[(2,6-(4,8-bis(5-(2-ethylhexyl)thiophen-2-yl)-benzo[1,2-*b*:4,5-*b'*]dithiophene))-*alt*-(5,5-(1',3'-di-2-thienyl-5',7'-bis(2-ethylhexyl)benzo[1',2'-*c*:4',5'-*c*']dithiophene-4,8-dione))] (PBDB-T) were prepared according to the reported procedures.[64] ^{1}H NMR and ^{13}C NMR spectra were recorded on a VNMRS 400 MHz spectrophotometer using $CDCl_3$ as solvent and tetramethylsilane (TMS) as the internal standard. UV-vis spectra were recorded on a Cary 5000 (Varian USA) spectrophotometer. For UV-vis spectra of F-ITICs, the solutions (2.00 mg ml^{-1} in chloroform) were used and the films were prepared by deposition from the 20 mg ml^{-1} concentrated chlorobenzene solution via spin-casting method at 1000 rpm. The optical bandgaps were estimated from absorption onset of the as-cast thin films. Cyclic voltammetry (CV) measurements were performed on Solartron electrochemical station (METEK, Versa STAT3) with a three-electrode cell in a 0.1 M tetra-*n*-butylammonium hexafluorophosphate (n-Bu_4NPF_6) solution in acetonitrile at a scan rate of 100 mV s^{-1} at room temperature under argon. A Ag/Ag^+ electrode, a platinum wire, and a platinum electrode were used as the reference electrode, counter electrode, and working electrode, respectively. The Ag/Ag^+ reference electrode was calibrated using a ferrocene/ferrocenium redox couple as an external standard, whose oxidation potential is set at 4.8 eV with respect to a zero vacuum level. The HOMO energy levels were obtained from the equation HOMO (eV) = $-(E_{(ox)}^{onset} - E_{(ferrocene)}^{onset} + 4.8)$. The LUMO levels of polymers were obtained from the equation LUMO (eV) = $-(E_{(red)}^{onset} - E_{(ferrocene)}^{onset} + 4.8)$. The UPS measurement was carried out using an AXIS-NOVA (Kratos, Inc.) with a base pressure of 4.2×10^{-9} Torr. AFM was collected using a Bruker Dimension Icon Atomic Force Microscope with an RTESP-150 probe in the standard tapping mode. The GIWAXS was conducted at PLS-II 6D UNIST-PAL beamline of the Pohang Accelerator Laboratory in Korea. The X-rays coming from the in vacuum undulator were monochromated ($\lambda = 1.10994$ Å) using a double crystal monochromator and focused both horizontally and vertically (450 (H) × 60 (V) μm^2 in FWHM (full width at half maximum) @sample position) using K-B type mirrors. The GIWAXS sample stage was equipped with a 7-axis motorized stage for the fine alignment of sample, and the incidence angle of X-ray beam was set to be 0.13° for the neat and blend films. The GIWAXS patterns were recorded with a 2D CCD detector (Rayonix SX165) and X-ray irradiation time was 6–9 s, dependent on the saturation level of the detector. Diffraction angles were calibrated using a sucrose standard (Monoclinic, P21, a = 10.8631 Å, b = 8.7044 Å, c = 7.7624 Å, β = 102.938°) and the sample-to-detector distance was ≈231 mm. STEM and EDAX measurement was performed on the JEOL USA JEM-2100F Transmission

Electron Microscope, with samples prepared under the same condition of the optimized active layer in device on PEDOT:PSS. The transient absorption (TA) was performed using a regenerative amplifier (Libra, Coherent, 1 kHz, 90 fs) with tunable wavelength and analyzed using a highspeed charge-coupled device (S11071-1104, Hamamatsu) with a monochromater (Acton 2358, Princeton Instrument) at 1 kHz enabled by a custom-built board from Entwicklungsbuero Stressing. The angle between the polarizations of the pump and probe beam was set at the magic angle.

Synthesis

1-Bromo-2-fluoro-4-hexylbenzene (1a): To a two-necked round-bottomed flask were added $CuCl_2$ (75 mg, 0.56 mmol), 1-bromo-4-(bromomethyl)-2-fluorobenzene (3.0 g, 11 mmol) and THF (50 mL). The reaction mixture was cooled in a dry ice-acetone bath at -78°C, *n*-pentylmagnesium bromide solution (1.0 M in THF, 15 ml, 15 mmol) and 1,3-butadiene (2.0 M in THF, 5.6 ml, 11 mmol) were introduced into the reaction mixture in a sequence. The reaction mixture was warmed to room temperature and stirred for 15 h. The reaction was quenched with 1N HCl solution, and then the products were extracted with ethyl acetate several times. The organic layer was collected and dried by $MgSO_4$, and then the volatiles were removed under reduced pressure. The resulting crude mixture was purified by column chromatography using hexane as eluent, yielding a colorless oil (2.0 g, 69%). ^{1}H NMR (400 MHz, $CDCl_3$, δ): 7.40 (dd, 1H), 6.93 (dd, 1H), 6.83 (m, 1H), 2.56 (t, 2H), 1.58 (q, 2H), 1.38-1.20 (m, 6H), 0.88 (t, 3H). ^{13}C NMR (100 MHz, $CDCl_3$, δ): 161.01, 131.71, 128.58, 127.01, 119.32, 118.74, 31.68, 30.67, 29.18, 28.55, 22.65, 13.61. MALDI-TOF-MS *m/z*: $[M]^+$ = 258.11; calcd 258.04.

4-Bromo-2-fluro-1-hexylbenzene (1b): 1b was synthesized through the same synthetic route of 1a, and 4-bromo-1-(bromomethyl)-2-fluorobenzene was used, yielding a colorless oil (1.5 g, 52%). ^{1}H NMR (400 MHz, $CDCl_3$, δ): 7.18 (m, 2H), 7.04 (t, 1H), 2.58 (t, 2H), 1.57 (q, 2H), 1.36-1.25 (m, 6H), 0.88 (t, 3H). ^{13}C NMR (100 MHz, $CDCl_3$, δ): 162.31, 159.94, 131.71, 127.18, 119.00, 118.75, 31.77, 30.07, 29.08, 28.77, 22.75, 14.21. MALDI-TOF-MS *m/z*: $[M]^+$ = 258.10; calcd 258.04.

o-F-IT: To a solution of 1a (2.0 g, 7.72 mmol) in THF (20 mL) at -78°C was added *n*-BuLi solution (2.5 M in hexane, 3.1 ml, 7.8 mmol) and the reaction mixture was kept at -78°C for 1 h. A solution of compound 2 (1.6 g, 3.2 mmol) in THF (40 ml) was added, and then the reaction mixture was warmed to room temperature and stirred overnight. The reaction was quenched with water, and then the products were extracted with ethyl acetate several times. The organic layer was collected and dried by $MgSO_4$, and then the volatiles were removed under reduced pressure. The resulting crude mixture was re-dissolved in AcOH (40 ml), and then concd. H_2SO_4 (0.80 ml) was added by dropwise. The resulting mixture was refluxed for 3 h. Then the mixture was poured into water and extracted twice with ethyl acetate. The organic layer was collected and dried by $MgSO_4$, and then the volatiles were removed under reduced pressure. The crude products were purified by column chromatography using hexane/DCM as eluent, yielding a light-yellow solid (1.0 g, 29%). ^{1}H NMR (400 MHz, $CDCl_3$, δ): 7.75 (s, 2H), 7.29 (s, 4H), 6.91 (d, 4H), 6.76 (m, 8H), 2.54 (t, 8H), 1.69-1.45 (m, 8H), 1.39-1.14 (m, 24H), 0.85 (t, 12H). ^{13}C NMR (100 MHz, $CDCl_3$, δ): 159.78, 152.43, 145.55, 144.62, 141.84, 137.54, 133.77, 129.76, 126.91, 120.61, 120.45, 120.25, 117.16, 114.89, 114.69, 62.67, 31.78, 30.14, 29.31, 28.94, 22.72, 14.22. MALDI-TOF-MS *m*/*z*: $[M]^+$ = 1090.33; calcd 1090.43.

m-F-IT: *m*-F-IT was synthesized through the same synthetic route of *o*-F-IT, and compound 1b was used, yielding a light-yellow solid (0.80 g, 23%). ^{1}H NMR (400 MHz, $CDCl_3$, δ): 7.50 (s, 2H), 7.28 (m, 2H), 7.25 (m, 2H) 7.18 (m, 8H), 7.04 (m, 4H), 2.54 (t, 8H), 1.69-1.45 (m, 8H), 1.39-1.14 (m, 24H), 0.85 (t, 12H). ^{13}C NMR (100 MHz, $CDCl_3$, δ): 159.42, 152.31, 145.12, 144.77, 142.02, 137.17, 133.53, 129.67, 126.08, 120.94, 120.45, 117.65, 114.12, 113.95, 113.71, 62.65, 31.78, 30.14, 29.31, 28.95, 22.71, 14.23. MALDI-TOF-MS *m*/*z*: $[M]^+$ = 1090.34; calcd 1090.43.

o-F-IT-CHO: A Vilsmeier reagent, which was prepared with $POCl_3$ (0.30 mL) in DMF (3.0 mL), was added to a solution of *o*-F-IT (1.0 g, 0.92 mmol) in 1,2-dichloroethane (30 mL) under the protection of argon. The resulting mixture was stirred at 85°C overnight, the reaction was quenched with water and then extracted with chloroform. The organic layer was dried with $MgSO_4$ and the solvent removed under reduced pressure. The resulting crude mixture was purified by column chromatography using hexane/ethyl acetate as eluent, yielding a yellow solid (0.62 g, 59%). ^{1}H NMR (400 MHz, $CDCl_3$, δ): 9.89 (s, 2H), 7.96 (s, 2H), 7.85 (s, 2H), 6.93 (m, 4H), 6.80 (m, 8H), 2.54 (t, 8H), 1.69-1.45 (m, 8H), 1.39-1.14 (m, 24H), 0.85 (t, 12H). ^{13}C NMR (100 MHz, $CDCl_3$, δ): 159.78, 152.43, 145.55, 144.62, 141.84, 137.54, 133.77, 129.76, 126.91, 120.61, 120.45, 120.25, 117.16, 114.89, 114.69, 62.67, 31.78, 30.14, 29.31, 28.94, 22.72, 14.22. MALDI-TOF-MS *m*/*z*: $[M]^+$ = 1090.33; calcd 1090.43.

m-F-IT-CHO: *m*-F-IT-CHO was synthesized through the same synthetic route of *o*-F-IT-CHO, yielding a light-yellow solid (0.57 g, 54%). ^{1}H NMR (400 MHz, $CDCl_3$, δ): 9.89 (s, 2H), 7.94 (s, 2H), 7.62 (s, 2H), 7.20 (m, 8H), 7.07 (m, 4H), 2.54 (t, 8H), 1.69-1.45 (m, 8H), 1.39-1.14 (m, 24H), 0.85 (t, 12H). ^{13}C NMR (100 MHz, $CDCl_3$, δ): 182.99, 162.42, 154.03, 147.11, 145.77, 144.92, 142.17, 141.03, 136.67, 131.08, 129.94, 129.45, 123.65, 118.11, 114.95, 114.71, 62.74, 31.75, 30.11, 29.28, 28.92, 22.70, 14.22. MALDI-TOF-MS *m*/*z*: $[M]^+$ = 1146.33; calcd 1146.42.

o-F-ITIC: To a two-necked round-bottomed flask were added *o*-F-IT-CHO (0.30 g 0.26 mmol), 1,1-dicyanomethylene-3-indanone (0.26 g, 1.3 mmol), chloroform (30 mL), and pyridine (1.0 mL). The reaction mixture was stirred at 80°C overnight. After cooling to room temperature, the volatile was removed under reduced pressure and then re-dissolved in 5.0 mL of chloroform. The concentrated mixture was precipitated in methanol (200 mL) and filtered. The residue was purified by column chromatography using hexane/chloroform as eluent, yielding a dark blue solid (0.12 g, 30%). ^{1}H NMR (400 MHz, $CDCl_3$, δ): 8.84 (s, 2H), 8.68 (d, 2H), 8.31 (s, 2H), 7.92 (d, 2H), 7.89 (s, 2H), 7.75 (m, 4H), 7.00 (m, 4H), 6.84 (m, 8H), 2.55 (t, 8H), 1.67-1.48 (m, 8H), 1.40-1.19 (m, 24H), 0.85 (m, 12H). ^{13}C NMR (100 MHz, $CDCl_3$, δ): 188.56, 160.74, 159.69, 157.44, 157.23, 146.26, 141.56, 141.26, 140.19, 138.78, 137.99, 137.07, 135.57, 135.33, 134.88, 134.70, 133.73, 126.84, 125.60, 125.26, 124.06, 123.27, 122.48, 122.36, 120.93,114.78, 114.53, 70.47, 69.39, 39.19, 31.68, 29.71, 24.50, 22.73, 14.14. EA: Anal. calcd. for $C_{53}H_{42}N_4O_2S_2$: C, 75.27; H, 5.24; N, 3.74; Found: C, 75.12; H, 5.21; N, 3.64. MALDI-TOF-MS m/z: [M]+ = 1090.33; calcd 1090.43.

m-F-ITIC: *m*-F-ITIC was synthesized through the same synthetic route of *o*-F-ITIC, yielding a dark blue solid (0.11 g, 28%). ^{1}H NMR (400 MHz, $CDCl_3$, δ): 8.88 (s, 2H), 8.70 (d, 2H), 8.23 (s, 2H), 7.92 (d, 2H), 7.76 (m, 4H), 7.60 (s, 2H), 7.17 (m, 8H), 7.01 (m, 4H), 2.59 (t, 8H), 1.68-1.51 (m, 8H), 1.41-1.18 (m, 24H), 0.85 (m, 12H). ^{13}C NMR (100 MHz, $CDCl_3$, δ): 188.07, 160.53, 156.48, 154.23, 150.38, 146.48, 143.93, 142.66, 141.86, 140.21, 139.82, 138.02, 137.49, 137.07, 136.88, 135.28, 134.57, 132.44, 130.29, 128.04, 126.05, 125.02, 124.47, 121.33, 118.69, 114.77, 114.71, 69.60, 63.98, 38.95, 31.59, 29.66, 24.35, 22.65, 14.09. EA: Anal. calcd. for $C_{53}H_{42}N_4O_2S_2$: C, 75.27; H, 5.24; N, 3.74; Found: C, 75.02; H, 5.12; N, 3.65. MALDI-TOF-MS *m/z*: [M]+ = 1146.33; calcd 1146.42.

Device fabrication and characterization

The patterned ITO glass substrates (15 Ω^{-1}) were cleaned by ultrasonic treatment in detergent, distilled water, acetone, and isopropyl alcohol, then dried in an oven for overnight at 70 °C. The cleaned ITOs were treated with oxygen plasma for 5 min and then a thin PEDOT:PSS (Bayer Baytron 4083) layer was deposited over ITO surface at 4000 rpm. After sequentially annealed at 130 °C for 10 min, the substrates were transferred to the nitrogen filled glove box. The mixed solutions of PBDB-T:F-ITICs (1:1,1.3:1,1.5:1 and 2:1 w/w) with donor concentration 10mg ml^{-1} in chlorobenzene containing 0%–2% (v/v) 1,8-diiodooctane were spin-coated on the top of the PEDOT:PSS coated ITO glass. Followed by a thermal annealing treatment at 60-180 °C for 10 min, then methanol solution of PDINO (1.0 mg mL^{-1}) was deposited onto the active layer with a spin rate of 3000 rpm for 30 s. Finally, 100 nm aluminum was thermally evaporated under vacuum ($<5.0 \times 10^{-5}$ Pa). The active area of each sample was 13.0 mm^2. The current density versus voltage (*J–V*) characteristics were recorded using a Keithley 2400 source under illumination of an AM 1.5G solar simulator with an intensity of 100 mW cm^{-2}. The external quantum efficiency (EQE) measurements were conducted using Model QEX7 by PV measurements Inc. (Boulder, Colorado) in ambient air. The thickness of the active layers was measured using a stylus profilometer (P6, KLA Tencor). The hole and electron mobilities were measured via using the space charge limited current (SCLC) method. Device structures are ITO/PEDOT:PSS/active layer/Au for hole-only devices and ITO/ZnO/active layer/PDINO/Al for electron-only devices, respectively. The SCLC mobilities were calculated using the Mott–Gurney equation:

$$J = \frac{9\varepsilon_r\varepsilon_0\mu V^2}{8L^3}$$

where ε_r is the relative dielectric constant of the organic semiconductor, ε_0 is the permittivity of empty space, μ is the mobility of zero-field, L is the thickness of the active layer, and $V = V_{\text{applied}} - V_{\text{built-in}} - V_{\text{series-resistance}}$ (the V_{bi} values are 0.2 V and 0 V for the hole-only and the electron-only devices, respectively), where V_{applied} is the voltage applied, and $V_{\text{built-in}}$ is the built-in voltage from the relative work function difference between the two electrodes. $V_{\text{series-resistance}}$ is the voltage caused by the series and contact resistance potential drop ($V_{\text{series-resistance}} = J \times R_{\text{series-resistance}}$). For convenience, the voltage drops caused by this resistance ($R_{\text{series-resistance}}$) was ignored.

Simulation details

Density function theory (DFT): DFT calculation using DMol^3 program was performed to obtain optimal molecular structures of PBDB-T (e.g., trimer), *o*-F-ITIC, and *m*-F-ITIC.[65, 66] For the frontier orbital (i.e., HOMO and LUMO) calculations, the aliphatic side chains were substituted with methyl group since the reduction of molecular model did not affect to vary the HOMO/LUMO energy levels.[67] Initial molecular structure for geometry optimization of PBDB-T:*o*-F-ITIC and PBDB-T: *m*-F-ITIC were from MD trajectory. We used the generalized gradient approximation (GGA) with the Perdew–Burke–Ernzerhof (PBE) functional,[50] which showed similar band gap results of PBDB-T and F-ITICs calculated by B3LYP functional.[5] Semi-empirical dispersion-correction by Tkatchenko and Scheffler's scheme and spin-polarized calculations with the DNP 4.4 basis set were included.[68] The convergence criteria for the geometry optimization were 1.0×10^{-5} Ha for energy, 0.002 Ha/Å for force, and 0.005 Å for displacement, respectively.

All-atom molecular dynamics (AAMD): All-atom molecular dynamics (AAMD) was performed with COMPASSⅡ force field to study stacking states of PBDB-T and F-ITICs.[69] Following the experimental condition, 4 PBDB-T (trimer) and 250 chlorobenzene molecules were packed in boxes of 4.5×4.5×4.5 nm^3 and 4 *o*-F-ITIC and *m*-F-ITIC were included, respectively. NPT (i.e., isothermal-isobaric) simulations were performed for 2 ns at 318 K and chlorobenzene molecules were removed to assume the evaporated state. Sequential NPT simulations were performed for 3 ns at 333 K and for 3 ns at 298 K. Time step was 1 fs and Berendsen barostat and thermostat were applied to control pressure and temperature. Radial distribution function and angle distribution analysis were done with the trajectory of final 2 ns. Trimer of PBDB-T was used, which was able to form stacking sites with F-ITICs, and we confirmed that interaction sites with F-ITICs were same compared to PBDB-T of eight repeat units.[70]

Coarse-grained molecular dynamics (CGMD): Coarse-grained molecular dynamics (CGMD) was performed with Martini force field to investigate the morphology of thin films with PBDB-T and F-

ITICs.[51] Coarse-grained bead mappings of PBDB-T and F-ITICs were performed to construct similar structure of atomic model (**Figure 4.8**). Monomer of PBDB-T was composed of 24 beads and number of monomers was 6 for thin film system. *o*-F-ITIC and *m*-F-ITIC were composed of 38 constituent CG beads, respectively. CG models of *o*-F-ITIC and *m*-F-ITIC were same, except angle potential model (**Figure 4.9**). For chlorobenzene, 3 CG beads were used in triangular shape. To keep planar structure of molecules, elastic bond and angle potential were applied by harmonic potential with force constant of 10000 kJ/mol.[71] Angle and dihedral angle distributions were obtained from NVT simulation for 5 ns in boxes of 40×40×40 nm^3, which were composed of one molecule of PBDB-T, *o*-F-ITIC and *m*-F-ITIC, respectively, and compared with all-atom model. Probability distributions of angle and dihedral angle were analyzed with the trajectory of final 2 ns. Simulation systems for investigating the morphology of thin film were composed of 72, 216, 10280 molecules of PBDB-T, F-ITICs and chlorobenzene in boxes of 30×30×5 nm^3. NPT simulations were performed for 100 ns at 318 K. Final configurations were replicated twice by *x*- and *y*-axis and chlorobenzene molecules were removed. NPT simulations were performed for 500 ns at 333 K and annealing treatment were done for 15 ns from 333 K to 298 K, sequentially, with 288 PBDB-T and 864 F-ITICs molecules. Interval of annealing temperature and simulation time were 10 K and 500 ps, respectively. Finally, NPT simulation was performed for 485 ns at 298 K. End-to-end distance of PBDB-T was calculated between the BDT CG beads at the end of polymer. Time step was 10 fs and Parrinello-Rahman barostat and velocity rescaling thermostat were used. The cut-off radius of van der Waals interaction was 1.2 nm and the GROMACS 5.0.6 package was used for CGMD simulations.[72]

4.5 References

1. Günes, S.; Neugebauer, H.; Sariciftci, N. S., Conjugated Polymer-Based Organic Solar Cells. *Chem. Rev.* **2007,** *107* (4), 1324.

2. Li, G.; Zhu, R.; Yang, Y., Polymer Solar Cells. *Nat. Photonics* **2012,** *6* (3), 153.

3. Lu, L.; Zheng, T.; Wu, Q.; Schneider, A. M.; Zhao, D.; Yu, L., Recent advances in bulk heterojunction polymer solar cells. *Chem. Rev.* **2015,** *115* (23), 12666-12731.

4. Liu, Y.; Zhao, J.; Li, Z.; Mu, C.; Ma, W.; Hu, H.; Jiang, K.; Lin, H.; Ade, H.; Yan, H., Aggregation and morphology control enables multiple cases of high-efficiency polymer solar cells. *Nat. Commun.* **2014,** *5*, 5293.

5. Huang, J.; Carpenter, J. H.; Li, C. Z.; Yu, J. S.; Ade, H.; Jen, A. K. Y., Highly Efficient Organic Solar Cells with Improved Vertical Donor–Acceptor Compositional Gradient Via an Inverted Off-Center Spinning Method. *Adv. Mater.* **2016,** *28* (5), 967.

6. Zhao, J.; Li, Y.; Yang, G.; Jiang, K.; Lin, H.; Ade, H.; Ma, W.; Yan, H., Efficient

Organic Solar Cells Processed from Hydrocarbon Solvents. *Nat. Energy* **2016,** *1* (2), 15027.

7. He, Z.; Xiao, B.; Liu, F.; Wu, H.; Yang, Y.; Xiao, S.; Wang, C.; Russell, T. P.; Cao, Y., Single-Junction Polymer Solar Cells with High Efficiency and Photovoltage. *Nat. Photonics* **2015,** *9* (3), 174.

8. Cho, H. J.; Kim, Y. J.; Chen, S.; Lee, J.; Shin, T. J.; Park, C. E.; Yang, C., Over 10% Efficiency in Single-Junction Polymer Solar Cells Developed from Easily Accessible Random Terpolymers. *Nano Energy* **2017,** *39*, 229.

9. Kumari, T.; Lee, S. M.; Yang, C., Cubic-Like Bimolecular Crystal Evolution and over 12% Efficiency in Halogen-Free Ternary Solar Cells. *Adv. Funct. Mater.* **2018,** *28* (19), 1707278.

10. Lin, Y.; Wang, J.; Zhang, Z. G.; Bai, H.; Li, Y.; Zhu, D.; Zhan, X., An Electron Acceptor Challenging Fullerenes for Efficient Polymer Solar Cells. *Adv. Mater.* **2015,** *27* (7), 1170.

11. Yao, H.; Chen, Y.; Qin, Y.; Yu, R.; Cui, Y.; Yang, B.; Li, S.; Zhang, K.; Hou, J., Design and Synthesis of a Low Bandgap Small Molecule Acceptor for Efficient Polymer Solar Cells. *Adv. Mater.* **2016,** *28* (37), 8283.

12. Holliday, S.; Ashraf, R. S.; Wadsworth, A.; Baran, D.; Yousaf, S. A.; Nielsen, C. B.; Tan, C.-H.; Dimitrov, S. D.; Shang, Z.; Gasparini, N.; Alamoudi, M.; Laquai, F.; Brabec, C. J.; Salleo, A.; Durrant, J. R.; McCulloch, I., High-Efficiency and Air-Stable P3HT-Based Polymer Solar Cells with a New Non-Fullerene Acceptor. *Nat. Commun.* **2016,** *7*, 11585.

13. Cui, Y.; Yang, C.; Yao, H.; Zhu, J.; Wang, Y.; Jia, G.; Gao, F.; Hou, J., Efficient Semitransparent Organic Solar Cells with Tunable Color enabled by an Ultralow-Bandgap Nonfullerene Acceptor. *Adv. Mater.* **2017,** *29* (43), 1703080.

14. Song, X.; Gasparini, N.; Ye, L.; Yao, H.; Hou, J.; Ade, H.; Baran, D., Controlling Blend Morphology for Ultrahigh Current Density in Nonfullerene Acceptor-Based Organic Solar Cells. *ACS Energy Lett.* **2018,** *3* (3), 669.

15. Li, Y.; Lin, J.-D.; Che, X.; Qu, Y.; Liu, F.; Liao, L.-S.; Forrest, S. R., High Efficiency Near-Infrared and Semitransparent Non-Fullerene Acceptor Organic Photovoltaic Cells. *J. Am. Chem. Soc.* **2017,** *139* (47), 17114.

16. Bin, H.; Zhang, Z.-G.; Gao, L.; Chen, S.; Zhong, L.; Xue, L.; Yang, C.; Li, Y., Non-Fullerene Polymer Solar Cells Based on Alkylthio and Fluorine Substituted 2D-Conjugated Polymers Reach 9.5% Efficiency. *J. Am. Chem. Soc.* **2016,** *138* (13), 4657.

17. Yu, T.; Xu, X.; Zhang, G.; Wan, J.; Li, Y.; Peng, Q., Wide Bandgap Copolymers Based on Quinoxalino [6, 5-f]. quinoxaline for Highly Efficient Nonfullerene Polymer Solar Cells. *Adv. Funct. Mater.* **2017,** *27* (28), 1701491.

18. Qin, Y.; Uddin, M. A.; Chen, Y.; Jang, B.; Zhao, K.; Zheng, Z.; Yu, R.; Shin, T.

J.; Woo, H. Y.; Hou, J., Highly Efficient Fullerene-Free Polymer Solar Cells Fabricated with Polythiophene Derivative. *Adv. Mater.* **2016,** *28* (42), 9416.

19. Park, G. E.; Choi, S.; Park, S. Y.; Lee, D. H.; Cho, M. J.; Choi, D. H., Eco-Friendly Solvent-Processed Fullerene-Free Polymer Solar Cells with over 9.7% Efficiency and Long-Term Performance Stability. *Adv. Energy. Mater.* **2017,** *7* (19), 1700566.

20. Bao, X.; Zhang, Y.; Wang, J.; Zhu, D.; Yang, C.; Li, Y.; Yang, C.; Xu, J.; Yang, R., High Extinction Coefficient Thieno[3, 4-b]thiophene-Based Copolymer for Efficient Fullerene-Free Solar Cells with Large Current Density. *Chem. Mater.* **2017,** *29* (16), 6766.

21. Zhang, Z. G.; Yang, Y.; Yao, J.; Xue, L.; Chen, S.; Li, X.; Morrison, W.; Yang, C.; Li, Y. J. A. C. I. E., Constructing a Strongly Absorbing Low-Bandgap Polymer Acceptor for High-Performance All-Polymer Solar Cells. **2017,** *56* (43), 13503-13507.

22. Liu, X.; Xie, B.; Duan, C.; Wang, Z.; Fan, B.; Zhang, K.; Lin, B.; Colberts, F. J.; Ma, W.; Janssen, R. A.; Huang, F.; Cao, Y., A High Dielectric Constant Non-Fullerene Acceptor for Efficient Bulk-Heterojunction Organic Solar Cells. *J.Mater. Chem. A* **2018,** *6* (2), 395.

23. Fei, Z.; Eisner, F. D.; Jiao, X.; Azzouzi, M.; Röhr, J. A.; Han, Y.; Shahid, M.; Chesman, A. S.; Easton, C. D.; McNeill, C. R.; Anthopoulos, T. D.; Nelson, J.; Heeney, M., An Alkylated Indacenodithieno [3, 2-b] thiophene-Based Nonfullerene Acceptor with High Crystallinity Exhibiting Single Junction Solar Cell Efficiencies Greater than 13% with Low Voltage Losses. *Adv. Mater.* **2018,** *30* (8), 1705209.

24. Lin, Y.; Zhao, F.; He, Q.; Huo, L.; Wu, Y.; Parker, T. C.; Ma, W.; Sun, Y.; Wang, C.; Zhu, D.; Heeger, A. J.; Marder, S. R.; Zhan, X., High-Performance Electron Acceptor with Thienyl Side Chains for Organic Photovoltaics. *J. Am. Chem. Soc.* **2016,** *138* (14), 4955.

25. Luo, Z.; Sun, C.; Chen, S.; Zhang, Z. G.; Wu, K.; Qiu, B.; Yang, C.; Li, Y.; Yang, C., Side-Chain Impact on Molecular Orientation of Organic Semiconductor Acceptors: High Performance Nonfullerene Polymer Solar Cells with Thick Active Layer over 400 nm. *Adv. Energy. Mater.* **2018**, 1800856.

26. Yang, Y.; Zhang, Z.-G.; Bin, H.; Chen, S.; Gao, L.; Xue, L.; Yang, C.; Li, Y., Side-Chain Isomerization on an n-type Organic Semiconductor ITIC Acceptor Makes 11.77% High Efficiency Polymer Solar Cells. *J. Am. Chem. Soc.* **2016,** *138* (45), 15011.

27. Zhang, C. e.; Feng, S.; Liu, Y.; Hou, R.; Zhang, Z.; Xu, X.; Wu, Y.; Bo, Z., Effect of Non-fullerene Acceptors' Side Chains on the Morphology and Photovoltaic Performance of Organic Solar Cells. *ACS Appl. Mater. Interfaces* **2017,** *9* (39), 33906.

28. Li, S.; Ye, L.; Zhao, W.; Liu, X.; Zhu, J.; Ade, H.; Hou, J., Design of a New Small-Molecule Electron Acceptor Enables Efficient Polymer Solar Cells with High Fill Factor. *Adv. Mater.*

2017, *29* (46), 1704051.

29. Li, R.; Liu, G.; Xiao, M.; Yang, X.; Liu, X.; Wang, Z.; Ying, L.; Huang, F.; Cao, Y., Non-Fullerene Acceptors Based on Fused-Ring Oligomers for Efficient Polymer Solar Cells via Complementary Light-Absorption. *J. Mater. Chem. A* **2017,** *5* (45), 23926.

30. Feng, H.; Qiu, N.; Wang, X.; Wang, Y.; Kan, B.; Wan, X.; Zhang, M.; Xia, A.; Li, C.; Liu, F.; Zhang, H.; Chen, Y., An ADA Type Small-Molecule Electron Acceptor with End-Extended Conjugation for High Performance Organic Solar Cells. *Chem. Mater.* **2017,** *29* (18), 7908.

31. Zhu, J.; Ke, Z.; Zhang, Q.; Wang, J.; Dai, S.; Wu, Y.; Xu, Y.; Lin, Y.; Ma, W.; You, W.; Zhan, X., Naphthodithiophene-Based Nonfullerene Acceptor for High-Performance Organic Photovoltaics: Effect of Extended Conjugation. *Adv. Mater.* **2018,** *30* (2), 1704713.

32. Jia, B.; Dai, S.; Ke, Z.; Yan, C.; Ma, W.; Zhan, X., Breaking 10% Efficiency in Semitransparent Solar Cells with Fused-Undecacyclic Electron Acceptor. *Chem. Mater.* **2017,** *30* (1), 239.

33. Dai, S.; Zhao, F.; Zhang, Q.; Lau, T.-K.; Li, T.; Liu, K.; Ling, Q.; Wang, C.; Lu, X.; You, W.; Zhan, X., Fused Nonacyclic Electron Acceptors for Efficient Polymer Solar Cells. *J. Am. Chem. Soc.* **2017,** *139* (3), 1336.

34. Li, S.; Ye, L.; Zhao, W.; Zhang, S.; Mukherjee, S.; Ade, H.; Hou, J., Energy-Level Modulation of Small-Molecule Electron Acceptors to Achieve over 12% Efficiency in Polymer Solar Cells. *Adv. Mater.* **2016,** *28* (42), 9423.

35. Zhang, Z.; Feng, L.; Xu, S.; Yuan, J.; Zhang, Z.-G.; Peng, H.; Li, Y.; Zou, Y., Achieving over 10% Efficiency in a New Acceptor ITTC and its Blends with Hexafluoroquinoxaline based Polymers. *J. Mater. Chem. A* **2017,** *5* (22), 11286.

36. Sun, J.; Zhang, Z.; Yin, X.; Zhou, J.; Yang, L.; Geng, R.; Zhang, F.; Zhu, R.; Yu, J.; Tang, W., High Performance Non-Fullerene Polymer Solar Cells Based on PTB7-Th as the Electron Donor with 10.42% Efficiency. *J. Mater. Chem. A* **2018,** *6* (6), 2549.

37. Yan, C.; Wang, W.; Lau, T.-K.; Li, K.; Wang, J.; Liu, K.; Lu, X.; Zhan, X., Enhancing the Performance of Non-Fullerene Organic Solar Cells via End Group Engineering of Fused-Ring Electron Acceptors. *J. Mater. Chem. A* **2018,** *6* (34), 16638.

38. Gao, W.; An, Q.; Ming, R.; Xie, D.; Wu, K.; Luo, Z.; Zou, Y.; Zhang, F.; Yang, C., Side Group Engineering of Small Molecular Acceptors for High-Performance Fullerene-Free Polymer Solar Cells: Thiophene Being Superior to Selenophene. *Adv. Funct. Mater.* **2017,** *27* (34), 1702194.

39. Yao, H.; Ye, L.; Hou, J.; Jang, B.; Han, G.; Cui, Y.; Su, G. M.; Wang, C.; Gao, B.; Yu, R.; Zhang, H.; Yi, Y.; Woo, H. Y.; Ade, H.; Hou, J., Achieving Highly Efficient

Nonfullerene Organic Solar Cells with Improved Intermolecular Interaction and Open-Circuit Voltage. *Adv. Mater.* **2017,** *29* (21), 1700254.

40. Beljonne, D.; Cornil, J.; Muccioli, L.; Zannoni, C.; Brédas, J.-L.; Castet, F., Electronic Processes at Organic−Organic Interfaces: Insight from Modeling and Implications for Opto-electronic Devices. *Chem. Mater.* **2010,** *23* (3), 591.

41. Graham, K. R.; Cabanetos, C.; Jahnke, J. P.; Idso, M. N.; El Labban, A.; Ngongang Ndjawa, G. O.; Heumueller, T.; Vandewal, K.; Salleo, A.; Chmelka, B. F.; Amassian, A.; Beaujuge, P. M.; McGehee, M. D., Importance of the Donor: Fullerene Intermolecular Arrangement for High-Efficiency Organic Photovoltaics. *J. Am. Chem. Soc.* **2014,** *136* (27), 9608.

42. Meager, I.; Ashraf, R. S.; Mollinger, S.; Schroeder, B. C.; Bronstein, H.; Beatrup, D.; Vezie, M. S.; Kirchartz, T.; Salleo, A.; Nelson, J.; McCulloch, I., Photocurrent Enhancement from Diketopyrrolopyrrole Polymer Solar Cells through Alkyl-Chain Branching Point Manipulation. *J. Am. Chem. Soc.* **2013,** *135* (31), 11537.

43. Gao, J.; Dou, L.; Chen, W.; Chen, C. C.; Guo, X.; You, J.; Bob, B.; Chang, W. H.; Strzalka, J.; Wang, C.; Li, G.; Yang, Y., Improving Structural Order for a High-Performance Diketopyrrolopyrrole-Based Polymer Solar Cell with a Thick Active Layer. *Adv. Energy. Mater.* **2014,** *4* (5), 1300739.

44. Osaka, I.; Saito, M.; Koganezawa, T.; Takimiya, K., Thiophene–Thiazolothiazole Copolymers: Significant Impact of Side Chain Composition on Backbone Orientation and Solar Cell Performances. *Adv. Mater.* **2014,** *26* (2), 331.

45. Dang, D.; Chen, W.; Himmelberger, S.; Tao, Q.; Lundin, A.; Yang, R.; Zhu, W.; Salleo, A.; Müller, C.; Wang, E., Enhanced Photovoltaic Performance of Indacenodithiophene-Quinoxaline Copolymers by Side-Chain Modulation. *Adv. Energy. Mater.* **2014,** *4* (15), 1400680.

46. Wang, J.-L.; Liu, K.-K.; Hong, L.; Ge, G.-Y.; Zhang, C.; Hou, J., Selenopheno [3, 2-b] thiophene-Based Narrow-Bandgap Nonfullerene Acceptor Enabling 13.3% Efficiency for Organic Solar Cells with Thickness-Insensitive Feature. *ACS Energy Lett.* **2018,** *3* (12), 2967-2976.

47. Lee, J.; Ko, S. J.; Seifrid, M.; Lee, H.; Luginbuhl, B. R.; Karki, A.; Ford, M.; Rosenthal, K.; Cho, K.; Nguyen, T. Q., Bandgap Narrowing in Non-Fullerene Acceptors: Single Atom Substitution Leads to High Optoelectronic Response Beyond 1000 nm. *Adv. Energy Mater.* **2018,** *8* (24), 1801212.

48. Huang, C.; Liao, X.; Gao, K.; Zuo, L.; Lin, F.; Shi, X.; Li, C.-Z.; Liu, H.; Li, X.; Liu, F., Highly efficient organic solar cells based on S, N-heteroacene non-fullerene acceptors. *Chem. Mater.* **2018,** *30* (15), 5429-5434.

49. Iwasaki, T.; Imanishi, R.; Shimizu, R.; Kuniyasu, H.; Terao, J.; Kambe, N., Copper-

Catalyzed Alkyl–Alkyl Cross-Coupling Reactions Using Hydrocarbon Additives: Efficiency of Catalyst and Roles of Additives. *J. Org. Chem.* **2014,** *79* (18), 8522.

50. Perdew, J. P.; Burke, K.; Ernzerhof, M., Generalized gradient approximation made simple. *Phys. Rev. Lett.* **1996,** *77* (18), 3865.

51. Marrink, S. J.; Risselada, H. J.; Yefimov, S.; Tieleman, D. P.; De Vries, A. H., The MARTINI Force Field: Coarse Grained Model for Biomolecular Simulations. *J. Phys. Chem. B* **2007,** *111* (27), 7812.

52. Guo, X.; Zhou, N.; Lou, S. J.; Smith, J.; Tice, D. B.; Hennek, J. W.; Ortiz, R. P.; Navarrete, J. T. L.; Li, S.; Strzalka, J.; Chen, L. X.; Chang, R. P. H.; Facchetti, A.; Marks, T. J., Polymer Solar Cells with Enhanced Fill Factors. *Nat. Photonics* **2013,** *7* (10), 825.

53. Bartesaghi, D.; del Carmen Pérez, I.; Kniepert, J.; Roland, S.; Turbiez, M.; Neher, D.; Koster, L. J. A., Competition between Recombination and Extraction of Free Charges Determines the Fill Factor of Organic Solar Cells. *Nat. Commun.* **2015,** *6*, 7083.

54. Schilinsky, P.; Waldauf, C.; Brabec, C. J., Recombination and Loss Analysis in Polythiophene Based Bulk Heterojunction Photodetectors. *Appl. Phys. Lett.* **2002,** *81* (20), 3885.

55. Cowan, S. R.; Roy, A.; Heeger, A. J., Recombination in Polymer-Fullerene Bulk Heterojunction Solar Cells. *Phys. Rev. B* **2010,** *82* (24), 245207.

56. Kyaw, A. K. K.; Wang, D. H.; Gupta, V.; Leong, W. L.; Ke, L.; Bazan, G. C.; Heeger, A. J., Intensity Dependence of Current–Voltage Characteristics and Recombination in High-Efficiency Solution-Processed Small-Molecule Solar Cells. *ACS nano* **2013,** *7* (5), 4569.

57. Lenes, M.; Morana, M.; Brabec, C. J.; Blom, P. W., Recombination-Limited Photocurrents in Low Bandgap Polymer/Fullerene Solar Cells. *Adv. Funct. Mater.* **2009,** *19* (7), 1106.

58. He, Z.; Zhong, C.; Huang, X.; Wong, W. Y.; Wu, H.; Chen, L.; Su, S.; Cao, Y., Simultaneous Enhancement of Open-Circuit Voltage, Short-Circuit Current Density, and Fill Factor in Polymer Solar Cells. *Adv. Mater.* **2011,** *23* (40), 4636.

59. Rivnay, J.; Mannsfeld, S. C.; Miller, C. E.; Salleo, A.; Toney, M. F., Quantitative Determination of Organic Semiconductor Microstructure from the Molecular to Device Scale. *Chem. Rev.* **2012,** *112* (10), 5488.

60. Lilliu, S.; Alsari, M.; Bikondoa, O.; Macdonald, J. E.; Dahlem, M. S., Absence of Structural Impact of Noble Nanoparticles on P3HT: PCBM Blends for Plasmon-Enhanced Bulk-Heterojunction Organic Solar Cells Probed by Synchrotron GI-XRD. *Sci. Rep.* **2015,** *5*, 10633.

61. Jeong, M.; Chen, S.; Lee, S. M.; Wang, Z.; Yang, Y.; Zhang, Z. G.; Zhang, C.; Xiao, M.; Li, Y.; Yang, C., Feasible D1–A–D2–A Random Copolymers for Simultaneous High-Performance Fullerene and Nonfullerene Solar Cells. *Adv. Energy. Mater.* **2018,** *8* (7), 1702166.

62. Xu, Y. X.; Chueh, C. C.; Yip, H. L.; Ding, F. Z.; Li, Y. X.; Li, C. Z.; Li, X.; Chen, W. C.; Jen, A. K. Y., Improved Charge Transport and Absorption Coefficient in Indacenodithieno [3, 2-b] thiophene-based Ladder-Type Polymer Leading to Highly Efficient Polymer Solar Cells. *Adv. Mater.* **2012,** *24* (47), 6356.

63. Shang, Y.; Wen, Y.; Li, S.; Du, S.; He, X.; Cai, L.; Li, Y.; Yang, L.; Gao, H.; Song, Y., A triphenylamine-containing donor− acceptor molecule for stable, reversible, ultrahigh density data storage. *J. Am. Chem. Soc.* **2007,** *129* (38), 11674.

64. Jeong, M.; Chen, S.; Lee, S. M.; Wang, Z.; Yang, Y.; Zhang, Z. G.; Zhang, C.; Xiao, M.; Li, Y.; Yang, C., Feasible D1–A–D2–A Random Copolymers for Simultaneous High-Performance Fullerene and Nonfullerene Solar Cells. *Adv. Energy Mater.* **2018,** *8* (7), 1702166.

65. Delley, B., An all-electron numerical method for solving the local density functional for polyatomic molecules. *J. Chem. Phys.* **1990,** *92* (1), 508.

66. Delley, B., From molecules to solids with the DMol 3 approach. *J. Chem. Phys.* **2000,** *113* (18), 7756.

67. Brandt, R. G.; Yue, W.; Andersen, T. R.; Larsen-Olsen, T. T.; Hinge, M.; Bundgaard, E.; Krebs, F. C.; Yu, D., An isoindigo containing donor–acceptor polymer: synthesis and photovoltaic properties of all-solution-processed ITO-and vacuum-free large area roll-coated single junction and tandem solar cells. *J. Mater. Chem. C* **2015,** *3* (8), 1633.

68. Tkatchenko, A.; Scheffler, M., Accurate molecular van der Waals interactions from ground-state electron density and free-atom reference data. *Phys. Rev. Lett.* **2009,** *102* (7), 073005.

69. Rigby, D.; Sun, H.; Eichinger, B., Computer simulations of poly (ethylene oxide): force field, pvt diagram and cyclization behaviour. *Polym. Int.* **1997,** *44* (3), 311.

70. Han, G.; Guo, Y.; Ma, X.; Yi, Y., Atomistic Insight Into Donor/Acceptor Interfaces in High-Efficiency Nonfullerene Organic Solar Cells. *Solar RRL* **2018,** *2* (11), 1800190.

71. Periole, X.; Cavalli, M.; Marrink, S.-J.; Ceruso, M. A., Combining an elastic network with a coarse-grained molecular force field: structure, dynamics, and intermolecular recognition. *J. Chem. Theory Comput.* **2009,** *5* (9), 2531.

72. Van Der Spoel, D.; Lindahl, E.; Hess, B.; Groenhof, G.; Mark, A. E.; Berendsen, H. J., GROMACS: fast, flexible, and free. *J. Comput. Chem.* **2005,** *26* (16), 1701.

Chapter 5 Acknowledgements

First of all, I’m thoroughly grateful for instruction of my supervisor Prof. Changduk Yang, who gave me inspiration and compliment during my Ph.D. course in UNIST. Under his passionate teaching, I have been able to learn and experience various organic materials with extensive organic synthetic skills for optoelectronic application such as OPVs and OFETs. Moreover, He lavish his time on lesson to fundamental knowledges of organic chemistry, as well as cherishing my personality to be a great scientist. Also, I’d like to take this opportunity to acknowledge my committee advisors Prof. Jin Young Kim, Prof. Sung You Hong, Prof. Hyesung Park, and Prof. BongSoo Kim. They are devoted guidance and support including professional discussions and collaboration opportunities.

Besides, I’d like to thank to acquaintances who always help and support me during my Ph. D course. First of all, I appreciate to ATOMS members who are my colleges of Prof. Changduk Yang’s group in UNIST. The alumna members including Dr. Jonggi Kim, Dr. Yi HO Kim, Prof. Junghoon Lee, Dr. Gyungsik Kim, Dr. Kyu Cheol Lee, Prof. Shanshan Chen, and Dr. Tanya Kumari, always have given me useful advices in my research works and collaboration. Sang Myeon Lee, So-Huei Kang, Byongkyu Lee, Mingyu Jung, Yongjoon Cho, Sungwoo Jung, Jiyeon Oh, Seonghun Jeong, and Seoyoung Kim who are the junior members together make an effort to be a better ATOMS research group. On the other hand, I’d like to express my gratitude to my research colleagues and collaborated group members such as Eun Min Go (Prof. Sang Kyu Kwak’s lab), Je Min Yu (Prof. Ji-Wook Jang’s lab), Dr. Jeff L. Hermandez, Ian Pelse (Prof. John R. Reynolds’ group), Dr. Tomasz Marszalek (Dr. Wojciech Pisula’s group), and Dr. Eun-Sol Shin (Prof. Yong Young Noh’s lab).

In the end, I really numberless appreciate to my father, mother, sisters and relatives.

I would like to really thank everyone once more.

감사의 글

우선, 저의 박사 학위 기간동안 끊임없이, 이 글을 쓰고 있는 동안에도 불철주야 저에게 많은 가르침과, 지도편달을 아끼시지 않은 저의 지도 교수님 양창덕 교수님께 감사의 인사를 드리고 싶습니다. 부족한 점이 많고 아직 덜 성장하지 않은 저를 사제의 연을 넘어선 아버지와 같은 보살핌으로서 가르침을 전달해주신 그 마음에 고마운 마음을 항상 간직하며 살고 있습니다. 특히나 개성이 강하고 고집이 센 저에게 연구의 길과 목표에 관해서 저의 견해를 충분한 존중을 해주시면서, 또한 제 자신이 잘 될 수 있게 올바른 방향으로 매번 이끌어 주기위한 조언과 지식을 전달해 주신 점에 깊은 감사를 표하고 싶습니다.

다음으로는 제가 학위 기간을 무사히 마칠 수 있도록 가장 가까이에서 도움과 지원을 아끼지 않은 우리 연구실 구성원들께 감사의 인사를 드리고 싶습니다. 제가 처음 입학했을 때, 아무것도 모르던 저를 도와주시고 가르쳐 주셨던 지금은 자리에 없지만, 먼저 졸업하신 김종기 박사님, 김이호 박사님, 이정훈 박사님, 김경식 박사님, 이규철 박사님께 깊은 감사를 드리고 싶습니다. 또, 낯선 타국 생활이지만 학위 과정내내 같이 힘을 내며 노력을 아끼지 않은 Shanshan Chen 박사님, Tanya Kumari 박사님 두 분께도 감사의 인사를 전합니다. 그리고 지금도 같이 생활하면서 지내는 구성원들, 묵묵히 책임감을 가지고 일하는 소희, 깊이 있고 소신 있는 학문을 연구하는 병규, 매사에 최선을 다하고 랩을 위해 희생을 마다하지 않는 민규, 늦은 시간까지 노력하며 연구에 매진하는 용준, 항상 밝고 건강한 모습으로 잘 지내며 실험실에 서포팅을 잘해주는 성우 지연, 그리고 1 년 밖에 못 보았지만 항상 열심히 노력하는 서영, 성훈 두 막내 연구원까지 모두에게 고마운 마음과 부족한 선배로서 미안한 마음을 표하고 싶습니다. 마지막으로, 같이 들어오고 같이 졸업하는 가장 오랜 친구이자 동료, 상면이에게도 감사의 인사를 전함과 동시에 고생 많았다는 말을 전하고 싶습니다. 연구실 처음 들어와서 막내 생활부터 고학년 선배 생활까지 힘든 와중에도, 동기인 상면이가 있었기에, 많은 도움과 위로를 통해 힘든 학위과정내내 잘 버티며 여기까지 오지 않았나 생각이 많이 듭니다. 앞으로도 더 잘 될 거라 믿어 의심치 않으며 오래오래 봤으면 좋겠습니다.

매번 유쾌하신 모습으로 밝게 가르침을 전달해 주신 김진영 교수님, 점잖고 헤아릴 수 없을 정도로 유기화학에 깊은 지식을 보여주시는 홍성유 교수님, 소자 분야에 학문적 조예가 깊어 연구에 혜안을 제시해주시는 박혜성 교수님, 박사학위 심사에서 많은

조언과 학문 지도를 해주신 김봉수 교수님께 잘 배웠습니다 라는 감사의 인사를 드리고 싶습니다. 또, 같이 공동연구를 진행하며, 늦은 밤까지 많은 조언과 도움을 마다하지 않으셨던 곽상규 교수님, 바쁘신 와중에도 틈틈이 논문 지도편달을 해주신 포항공대 노용영 교수님, 연구뿐만 아니라 저의 장래와 인생에 관련해서도 걱정을 해주시는 장지욱 교수님께도 감사의 인사를 드리고 싶습니다.

마지막으로 학위과정 중 저의 든든한 버팀목이 되어준 가족과 친구들에게 감사를 전하고 싶습니다. 친구들 마굿간 상혁이, 동현이, 여문이, 정길이, 수곤이, 진석이, 덕규까지 벌써 10 년 넘게 보고 있는데 매번 고마움을 느낍니다. 그리고 못난 아들 뒷바라지하느라 아픈 몸으로 일하시는 아버지, 매일 매일 걱정해주시는 어머니, 힘든일 없니 하고 물어봐주는 누나 와 매형 그리고 자기가 더 바쁘고 힘들텐데 괜찮냐고 물어봐주는 효열이 까지 모두 사랑합니다. 감사합니다.

Appendix

Permission from all cited journal in this dissertation

Chapter 2. *J. Mater. Chem. C*, **2020**, 8, 296.

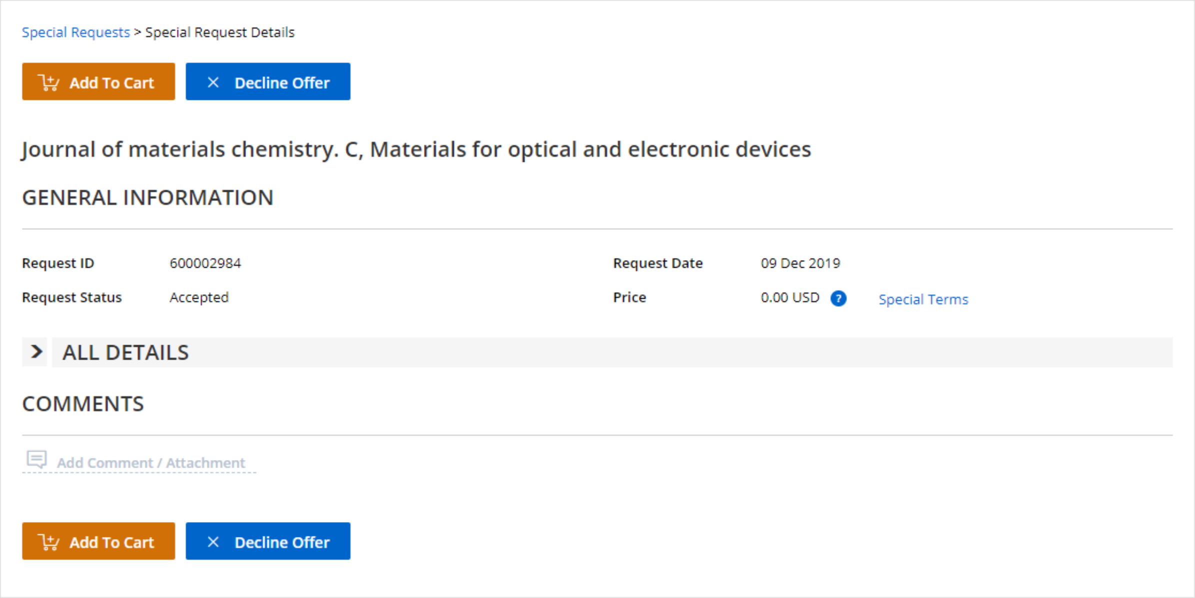

Journal of materials chemistry. C, Materials for optical and electronic devices

GENERAL INFORMATION

Request ID	600002984	Request Date	09 Dec 2019
Request Status	Accepted	Price	0.00 USD

Chapter 3.1. *Macromolecular Chem. Phys.*, **2015,** *216*, 1244.

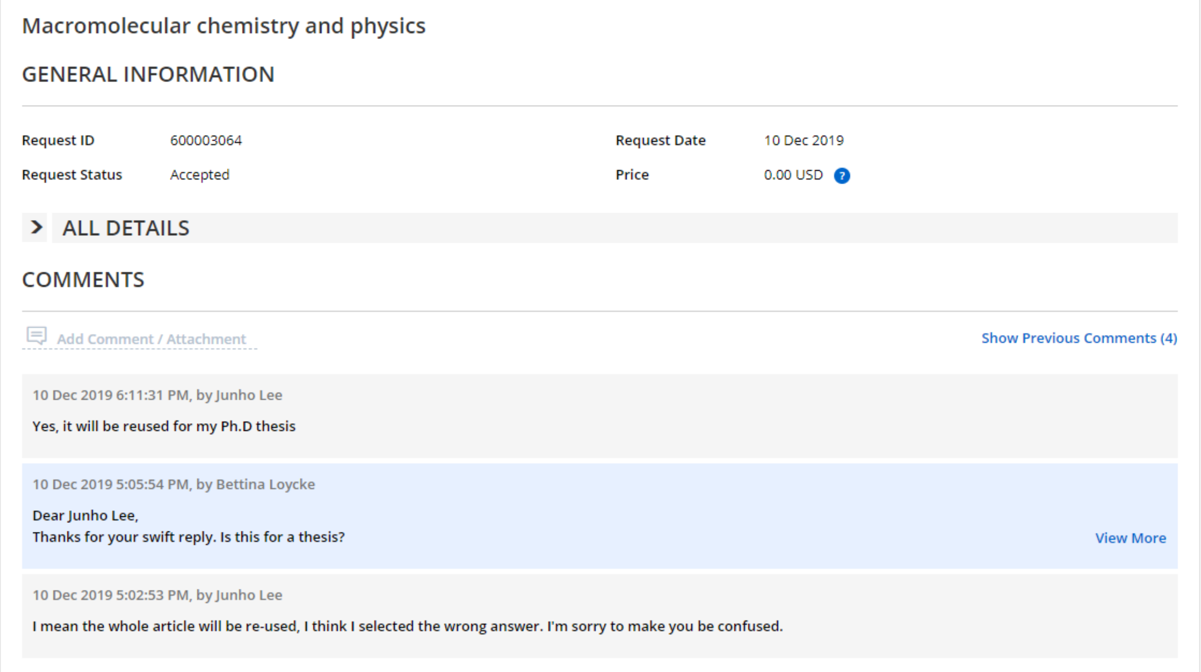

Macromolecular chemistry and physics

GENERAL INFORMATION

Request ID	600003064	**Request Date**	10 Dec 2019
Request Status	Accepted	**Price**	0.00 USD

COMMENTS

10 Dec 2019 6:11:31 PM, by Junho Lee

Yes, it will be reused for my Ph.D thesis

10 Dec 2019 5:05:54 PM, by Bettina Loycke

Dear Junho Lee,
Thanks for your swift reply. Is this for a thesis?

10 Dec 2019 5:02:53 PM, by Junho Lee

I mean the whole article will be re-used, I think I selected the wrong answer. I'm sorry to make you be confused.

Chapter 3.2. *J. Mater. Chem. C*, **2018,** *6*, 10532.

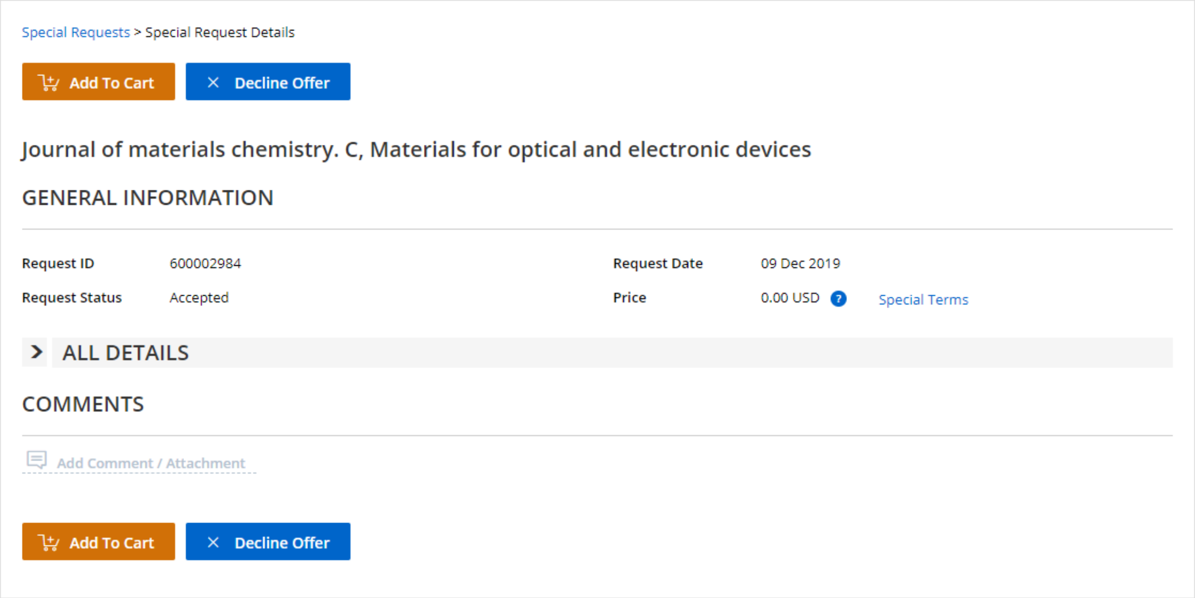

Journal of materials chemistry. C, Materials for optical and electronic devices

GENERAL INFORMATION

Request ID	600002984	**Request Date**	09 Dec 2019
Request Status	Accepted	**Price**	0.00 USD ? Special Terms

> ALL DETAILS

COMMENTS

Chapter 4. *J. Mater. Chem. A*, **2019,** *7*, 18468.

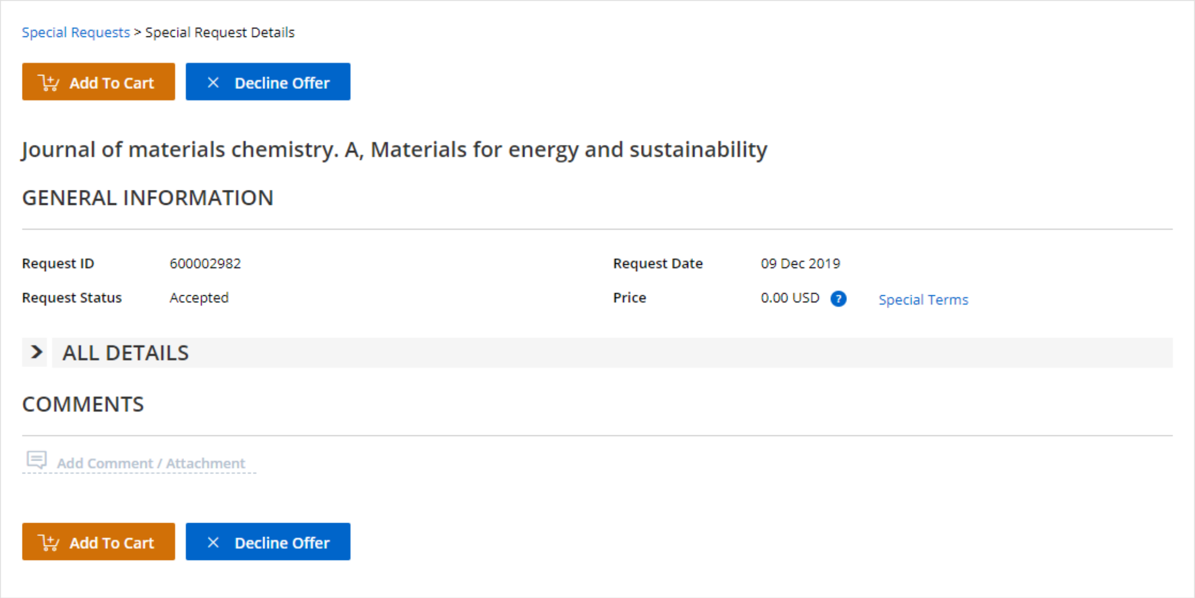

Special Requests > Special Request Details

Journal of materials chemistry. A, Materials for energy and sustainability

GENERAL INFORMATION

Request ID	600002982	**Request Date**	09 Dec 2019	
Request Status	Accepted	**Price**	0.00 USD	Special Terms

COMMENTS